Simulations of early universe phase transitions and gravitational waves

Daniel Cutting

Submitted for the degree of Doctor of Philosophy

University of Sussex

30th June 2020

Declaration

I hereby declare that this thesis has not been and will not be submitted in whole or in part to another University for the award of any other degree.

The work in this thesis has been completed in collaboration with Elba Granados Escartin, Mark Hindmarsh, and David Weir, and is comprised of the following papers:

- D. Cutting, M. Hindmarsh and D. J. Weir, "Gravitational waves from vacuum first-order phase transitions: from the envelope to the lattice", *Phys. Rev.*, vol. D97, no. 12, p. 123 513, 2018. DOI: 10.1103/PhysRevD.97.123513. arXiv: 1802.05712 [astro-ph.CO]

  In this paper I developed the code that was used to perform the 3d lattice simulations. The envelope approximation simulations were performed using a code developed by David Weir. I conducted the exploratory and final production runs that were used in the paper. I also carried out the data analysis and created all of the plots used in the paper. I wrote the first draft of the paper, with further edits made collaboratively with David Weir and Mark Hindmarsh. David Weir and Mark Hindmarsh gave advice and supervised the project throughout.

- D. Cutting, M. Hindmarsh and D. J. Weir, "Vorticity, kinetic energy, and suppressed gravitational wave production in strong first order phase transitions", Jun. 2019. arXiv: 1906.00480 [hep-ph]

  For this paper, I used a code that was created by David Weir. I made extensive modifications to the code such that it could be used within the parameter space explored in this paper. I conducted all exploratory and final production runs. I produced all plots and performed the relevant data analysis. The first draft was written by me and then edited by David Weir and Mark Hindmarsh. David Weir and Mark Hindmarsh gave advice and supervised the project throughout.

- D. Cutting, E. G. Escartin, M. Hindmarsh and D. J. Weir, "Gravitational waves from vacuum first order phase transitions II: from thin to thick walls", May 2020. arXiv: 2005.13537 [astro-ph.CO]

The initial exploratory work for this project was conducted by Elba Granados Escartin under my supervision. This involved creating a 1d code for exploring the scalar field dynamics during the expansion of isolated bubbles of the true vacuum. After this, 3d simulations were performed using the same code as in Ref. [1]. The exploratory simulation runs were completed by Elba Granados Escartin and myself. I performed the production runs. I analysed the data presented in the paper and created all of the plots. I wrote the first draft, with further edits suggested by David Weir and Mark Hindmarsh. David Weir and Mark Hindmarsh gave advice and supervised the project throughout.

I have led or corroborated all the original research presented in this thesis.

Signature:

Daniel Cutting

UNIVERSITY OF SUSSEX

Daniel Cutting, Doctor of Philosophy

Simulations of early universe phase transitions and gravitational waves

Summary

Upcoming space based gravitational wave observatories like the Laser Interferometer Space Antenna (LISA) will provide a new window into early universe physics. While the results from ground-based detectors have largely concerned astrophysical objects such as black holes and neutron stars, future space-based gravitational wave observatories will be able to observe far earlier times in the history of the universe than are directly accessible through the electromagnetic spectrum. LISA in particular will be sensitive to the detection of a stochastic gravitational wave background from a first-order cosmological phase transition around the electroweak scale.

In cosmological phase transitions, an effective scalar field passes from a false vacuum state to the true vacuum. If the transition is first-order, this occurs through the nucleation of bubbles of the true vacuum. These bubbles expand and, upon collision, produce gravitational waves. The focus of this thesis is to better characterise the gravitational wave signal from a first-order phase transition using numerical simulations.

Within this thesis, I study both vacuum and thermal first-order phase transitions. In a vacuum phase transition, bubble walls accelerate to ultra-relativistic speeds. In this case, the gradients in the scalar field during bubble collisions form the dominant source of gravitational waves. I perform full 3D classical lattice field theory simulations, compute the gravitational wave signature and compare it to previously used techniques such as the envelope approximation. I further extend this work to investigate whether the shape of the effective potential of the scalar field can affect the final gravitational wave signal.

In thermal phase transitions, the bubbles of the true vacuum nucleate in the presence of a relativistic plasma. As the bubbles expand, friction between the outward propagating bubble wall and the plasma causes shells of fluid to form around the bubble wall. The dominant source of gravitational waves from thermal transitions is shear-stress that remains in the fluid after the transition completes. While simulations of weak and intermediate strength phase transitions have been conducted, I perform the first 3D simulations of a strongly first-order phase transition and provide results for the generation of vorticity, formation of heated droplets, and the effect that this has on the gravitational wave signal.

Acknowledgements

If I were to list everyone who has contributed to this thesis in some small way, then the acknowledgments would easily be the longest section. What follows is my attempt to thank as many people as space allows.

I am forever indebted to my supervisor, Prof. Mark Hindmarsh, for inducting me into the world of research. His guidance, physical insight and overwhelming patience have been instrumental in my work. The depth and breadth of his knowledge of physics will continue to inspire me.

I would also like to thank Dr. David Weir for his supervision throughout my PhD. His immeasurable kindness and expertise in numerics have both been extremely valuable and I feel immensely privileged to have recieved his support.

I extend my gratitude to Prof. Kari Rummukainen and Prof. Stephan Huber for their discussions and advice during my PhD and for sharing their vast knowledge of first-order phase transitions.

It has been a pleasure to work alongside the members of the Theoretical Particle Physics group at Sussex. In particular, I would like to thank Jonathan Manuel, Djuna Croon, Chris Harman, Gustavo Medina Vasquez, Yannick Kluth, and Andy Bond for sharing an office with me over the years. The laughter and discussions I have shared in their company enabled me to persevere on long and frustrating days.

Jonathan Manuel deserves a special mention for being the other member of the "bubble boys", a name we have accepted if not enthusiastically endorsed. He has been an excellent companion on the journey from complete confusion to becoming fully fledged researchers.

During my PhD, I have been lucky enough to have had a second home at the University of Helsinki. It has been a privilege to spend time there and I have a deep gratitude to the entirety of the Helsinki Institute of Physics for making me feel so welcome within the department. Some of the best time in my PhD has been that spent in Helsinki with my colleagues Chloe Gowling, Elba Granados Escartin, Oliver Gould, Anna Kormu, Asier Lopez-Eiguren, Reuben Mitchell, Saga Säppi, Satumaaria Sukuvaara, Sara Tähtinen, Tuomas Tenkanen, Essi Vilhonen, and Severino Zeni.

I would also like to thank my collaborators at APC in Paris: Pierre Auclair, Chiara

Caprini, and Danièle Steer. While this thesis does not contain any of our ongoing work, I have learnt a lot working together and I look forward to our future collaboration.

To my friends Thomas Helfer, James Widdicombe, Katy Clough, and Josu Aurrekoetxea, I owe a deep thanks for welcoming me into their community early on in my PhD when I complained that I had few colleagues working on numerics. I have learnt lots from all of you, especially back when I was too afraid to ask my supervisors how to configure a makefile!

Becoming friends with Arianna Renzini has been a high point of my PhD. I could not think of a better person with whom to share the stress of our first postdoctoral application season.

To Erika, Rodrigo, Saana, Salla, Moritz, and Zac, I could not have wished for a better friendship group in Helsinki. I've not had such a tight bond form with a group of people so quickly in a very long time and I cannot wait to see you all again.

I must mention my friends from my undergraduate years and the everpresent GC. When I started my degree, I had no idea that I would be making friends that I would talk to every day four years after I graduated. Thank you for keeping me sane and for always being there when I need to vent about all the injustice in our world.

Giles, Frank, Aisha, Sally, and David of the Brittin-Snell family deserve their own chapter of acknowledgement for all the encouragement and support they have given me throughout my PhD. I have felt so warmly embraced into the family and could not be more proud of this fact.

My own family, Amber, Tim, Tass, and Mimbi, have always believed in me and encouraged me in all aspects of life. Their love has shaped me into who I am today. They inspire me and I will be forever grateful for the values they have instilled in me.

To my partner, Eva, this thesis is as much your accomplishment as it is mine. Without you it would not exist and your love is the bedrock upon which it has been built.

Contents

List of Tables

List of Figures

Chapter 1

Introduction

1.1 Prelude

Phase transitions are ubiquitous within nature. From the transitions familiar from everyday life, such as between solid, liquid and gaseous states, to more exotic transitions such as the quantum condensation of bosonic fluids and the emergence of superconductivity, phase transitions occur in a wide range of fields within physics.

Phase transitions can occur within cosmological contexts as well. Cosmological phase transitions can be dramatic events in which regions of the universe transition from one ground state to another. During a cosmological phase transition, an effective scalar field, or order parameter, changes its vacuum expectation value (VEV). If the phase transition is first-order, then two ground states for the order parameter exist simultaneously for some temperature range. In a cosmological first-order[1] phase transition, the scalar field is initially trapped in a metastable false vacuum state, separated from the true vacuum state by a barrier in the potential [4–6]. The scalar field can either tunnel through the barrier quantum mechanically or thermally fluctuate over the barrier in some local region. When this happens a bubble of the true vacuum state nucleates. If the bubble is sufficiently large, the pressure arising from the potential energy difference between phases will overcome the surface tension and the bubble will expand.

Alternatively, if there is no potential barrier separating the two states, then the transition between ground states can occur smoothly, with the order parameter continuously changing between the high-temperature (symmetric) state and the low-temperature (broken) state. If accompanied by an infinite correlation length, this form of transition is known as second-order, otherwise it is called a crossover.

[1] The Ehrenfest classification scheme, from which the name first-order originates, dictates that the order of the phase transition is given by the lowest discontinous derivative of the order parameter. Rather than focusing on the technical definition, we instead outline the important qualitative features in each type of transition.

Early studies involved deriving the nucleation rate of bubbles per unit volume, first in vacuum and then at finite temperatures [4, 5, 7, 8]. These studies established the importance of the bounce solution. The bounce solution gives the critical bubble profile corresponding to the most likely field configuration into which a bubble will nucleate.

As the early universe cooled, a number of cosmological phase transitions could have taken place. Indeed, within the Standard Model, we are aware of two occasions during which a phase transition could have occurred, namely when the electroweak symmetry was broken and the Higgs field obtained a VEV and during the QCD transition between a quark-gluon plasma and a hadron gas.

First-order phase transitions provide a departure from thermal equilibrium. This is one of the three Sahkarov conditions required for baryogenesis; the process in which the baryon asymmetry was generated in the early universe [9]. The other Sahkarov conditions require violation of C and CP symmetry and the presence of baryon number violating processes. The electroweak phase transition can fulfil all three of the Sahkarov conditions providing it was first-order. The mechanism of generating the baryon asymmetry during the electroweak phase transition is known as electroweak baryogenesis [10–12]. Electroweak baryogenesis motivated many early studies into the electroweak phase transition; for a review of the current the state of the field, see Refs. [13, 14]. The strength of a first-order phase transition is sometimes parameterised by the ratio of potential energy released during the transition compared to the radiation energy at the time of transition. Electroweak baryogenesis typically requires that the electroweak phase transition is strong in addition to being first-order [15–18].

Unfortunately, in the Standard Model, neither the electroweak or QCD phase transition is expected to be first-order; electroweak symmetry breaking takes place as a crossover [19, 20], as does the QCD transition absent large quark chemical potentials in the early universe [21].

While there are no cosmological first-order phase transitions in the Standard Model, there are many well motivated extensions which can generate one. There are numerous beyond the Standard Model (BSM) theories which can modify the electroweak phase transition such that it becomes first-order, for example by adding an extra singlet [22–28] or doublet [29–31]. Other extensions giving a first-order electroweak phase transition can provide dark matter candidates [32–36].

Extensions in BSM models can give rise to first-order phase transitions other than the electroweak phase transition. For example, some models include first-order phase

transitions in a hidden sector [37–43] or cause the QCD phase transition to become first-order [44, 45]. In models which introduce warped extra-dimensions, it is possible to obtain extremely strong first-order phase transitions [46–52].

While many of the above scenarios can produce potentially observable collider signatures, others remain out of reach of current and near-future collider experiments. Fortunately, there exists another feature of cosmological first-order phase transitions that we have not yet mentioned: the generation of gravitational waves [53, 54]. When the bubbles of the true vacuum state collide, transverse traceless modes of shear-stress are generated from gradients in the scalar field, which in turn source gravitational waves [55, 56]. Furthermore, many cosmological phase transitions are thermal, where the transition occurs in the presence of a cosmological plasma to which the scalar field is coupled. In thermal transitions, the plasma is stirred up by the expanding bubbles and transverse-traceless modes of shear-stress in the plasma source gravitational waves.

One of the first studies of gravitational waves from cosmological phase transitions discussed how sound waves in the plasma in a thermal transition could source gravitational waves [54]. Other initial studies focused instead on transitions occurring in vacuum [55]. The envelope approximation was developed [57], in which the shear-stress in a transition was assumed to be located in an infinitesimally thin shell at the bubble wall and to disappear upon collision. This was first applied to transitions in vacuum and later to thermal transitions with a cosmic plasma [58, 59]. The envelope approximation is still often used in vacuum transitions and thermal transitions in which the bubble wall 'runs away' and accelerates until collision.

Numerical simulations of thermal phase transitions have revealed that after the bubbles have finished colliding, motion in the cosmic plasma forms a long lasting source of gravitational waves which dominates the overall gravitational wave signal [60–63]. The initial propagation of the cosmic plasma for weaker transition strengths is well modelled by a superposition of sound waves [64, 65]. The scalar field contribution to the gravitational wave background in a thermal transition is well matched by the envelope approximation [66]. Eventually the sound waves are expected to decay and to be typically followed by a period of freely decaying turbulence which would also source gravitational waves [53, 58, 67–73].

The recent direct detection of gravitational waves from a binary black hole merger [74] by the Laser-Interferometer Gravitational Wave Observatory (LIGO) has been heralded as the advent of a new era of gravitational wave astronomy. Upcoming space based gravitational wave observatories like the Laser Interferometer Space Antenna (LISA) promise to

do the same for cosmology [75] (for an excellent review of cosmological gravitational wave backgrounds see Ref. [76]). For first-order phase transitions, LISA is of particular interest as its frequency window corresponds to roughly where an electroweak scale first-order phase transition is expected to peak [77].

While it may be disappointing that we do not expect a first-order phase transition in the Standard Model, it does raise the exciting prospect that the detection of the gravitational wave signal from a first-order transition is a smoking gun for BSM physics. Indeed, many of the extensions to the Standard Model listed above can only realistically be detected through the gravitational wave signal from a first-order transition.

The study of gravitational waves from cosmological phase transitions has progressed substantially in recent years, however there remain many areas that require progress. In particular, there have been limited simulations of strongly first-order thermal phase transitions. The decay of sound waves, generation of vorticity and subsequent development of turbulence is not well understood. The use of the envelope approximation for runaway thermal transitions and vacuum transitions has not been directly tested by simulations.

It is crucial to accurately characterise the gravitational wave signal produced by a first-order phase transition in order to obtain any future detection. It is my hope that the work in this thesis contributes to this in some small way.

1.2 Outline of this thesis

This thesis consists of a short review of cosmological phase transitions and their gravitational wave signatures, and a collection of articles completed during the course of my doctoral candidacy. The central theme of the collected articles is the characterisation of the gravitational wave background emerging from cosmological phase transitions using numerical simulations. The layout of the thesis is as follows:

- Given the that gravitational waves form an integral part of this thesis, it would be remiss to not begin with a brief introduction to general relativity. I provide this in Chapter 2, in which I introduce the space-time metric and Einstein's field equations. I detour briefly into the realm of cosmology, presenting the Friedmann-Lemaître-Robertson-Walker metric and showing the variation of the scale factor during matter and radiation domination. I conclude the chapter with a quick review of linearised gravity and gravitational waves.

- In Chapter 3, I review the basics of cosmological phase transitions and the gravit-

ational wave signatures emerging from them. Here I outline the effective potential and show how the decay rate of the false vacuum can be calculated. Next I review the dynamics of first-order phase transitions, starting with thermal transitions. It is possible to model thermal transitions using a coupled field-fluid system. I describe the field-fluid model and the corresponding equations of motion. When the bubbles expand, qualitatively different fluid shells develop around the expanding bubble wall depending on the wall velocity. The reaction front can be classified as a detonation, deflagration or hybrid. I discuss how the energy budget of a transition is distributed and outline the dynamics specific to runaway thermal transitions and vacuum transitions. Finally, the chapter is concluded by outlining the different sources of gravitational waves during a first-order phase transition and the gravitational wave power spectra they produce.

- In Chapter 4, I present the first paper of the thesis, Ref. [1]. In this paper, we conduct lattice field theory simulations of many bubbles in a vacuum transition with a quartic potential. We perform simulations with up to 4096 bubbles using a variety of different nucleation rates and several different choices for the potential parameters. We analyse the scalar field power spectrum, compute the resulting gravitational wave power spectrum, and compare this to the so called envelope approximation. After the bubbles finish colliding, there is a period of oscillation of the scalar field and we discuss the consequences of this period for the gravitational wave signal.

- Chapter 5, contains Ref. [3], which is a follow up study to Ref. [1]. We expand on the former work by exploring deeper the parameter space of the quartic potential. The dependence of the dynamics of the scalar field on the potential can be reduced into a single parameter $\overline{\lambda}$ which determines the thickness of the critical bubble wall and how close degenerate the minima are relative to the potential barrier. We perform simulations spanning a wide range of the possible $\overline{\lambda}$ values and calculate the power spectrum of the transverse-traceless shear stress, which tells us about the instantaneous sourcing of gravitational waves. The gravitational wave power spectrum is fitted with a broken power law, and the power law exponents, peak frequency, and peak amplitude are tracked throughout the simulations for each $\overline{\lambda}$. This is then compared to the fits of the envelope approximation and the bulk flow model.

- In Chapter 6, we turn our attention towards thermal transitions. We conduct the

first 3D simulations of strongly first-order phase transitions. We perform a scan across a series of wall velocities and transition strengths, with both deflagrations and detonations represented. Particular attention is given to the generation of vortical modes in the fluid velocity. The kinetic energy in the fluid is calculated after the transition and compared to the expected value estimated from the asymptotic profile of an expanding bubble. During the transition, hot droplets of the metastable state can form and we discuss their effect on the gravitational wave signal.

- Finally, in Chapter 7, I draw conclusions from the articles presented in the thesis and lay out future directions for research.

Chapter 2

A brief primer on general relativity

General relativity is an elegant theory in which the forces of gravitation we experience are due to the curvature of space and time. It is built on a key assumption known as the equivalence principle. The equivalence principle is sometimes given in two parts. First, the *weak equivalence principle* states that locally there can be no distinction between gravitational mass and inertial mass. In other words, for any gravitational field, at any point in spacetime, there exists a locally inertial reference frame in which the laws of motion can be constructed in the absence of gravity. The *strong equivalence principle* extends this to all laws of nature, so that in each inertial reference frame all of special relativity applies.

A key quantity in general relativity is the metric, $g_{\mu\nu}$. This is a symmetric rank-two tensor which describes the geometry of spacetime. The interval between two points in spacetime can be defined as

$$ds^2 = g_{\mu\nu} dx^\mu dx^\nu, \tag{2.1}$$

with dx^μ infinitesimal coordinate displacements. If $ds^2 < 0$, the interval is called timelike, whereas if $ds^2 > 0$ the interval is termed spacelike. Timelike intervals can correspond to trajectories taken by massive particles, and massless particles travel along lightlike trajectories where $ds^2 = 0$. As information cannot propagate faster than the speed of light, any event separated by a spacelike interval is acausal.

If the spacetime is flat, then the spacetime interval is given by

$$ds^2 = -dt^2 + dx^2 + dy^2 + dz^2. \tag{2.2}$$

This is referred to as Minkowski space, and has the corresponding Minkowski metric

$$\eta_{\mu\nu} = \begin{pmatrix} -1 & 0 & 0 & 0 \\ 0 & 1 & 0 & 0 \\ 0 & 0 & 1 & 0 \\ 0 & 0 & 0 & 1 \end{pmatrix}, \tag{2.3}$$

where we are using the $(-+++)$ convention for the metric, which we will continue to use throughout this thesis. In Minkowski space, the interval separating two events is independent of the inertial frame of reference.

The time as measured by a clock traversing a timelike wordline is referred to as the proper time. The proper time is defined using a specified coordinate system, and is therefore a Lorentz scalar. The proper time interval separating two events along a timelike path P is given by

$$\Delta\tau = \int_P \sqrt{-g_{\mu\nu}dx^\mu dx^\nu}. \tag{2.4}$$

From the weak equivalence principle, we know that locally there exists a coordinate frame in which a free particle will follow a straight world line. In this frame, a massive particle will follow the trajectory

$$\frac{d^2x^\mu}{d\tau^2} = 0, \tag{2.5}$$

with τ the proper time. From the existence of this frame, it can be deduced that, in general, free particles in a gravitational field will follow the curvature of spacetime along geodesics such that

$$\frac{d^2x^\mu}{ds^2} + \Gamma^\mu_{\alpha\beta}\frac{dx^\alpha}{ds}\frac{dx^\beta}{ds} = 0. \tag{2.6}$$

Here $\Gamma^\mu_{\alpha\beta}$ is the Levi-Civita connection, where the connection coefficients are also known as Christoffel symbols of the second kind,

$$\Gamma^\mu_{\alpha\beta} = \frac{1}{2}g^{\mu\nu}\left(\partial_\alpha g_{\nu\beta} + \partial_\beta g_{\alpha\nu} - \partial_\nu g_{\alpha\beta}\right). \tag{2.7}$$

Using the Levi-Cevita connection we can construct the Riemann curvature tensor,

$$R^\mu_{\nu\alpha\beta} = \partial_\alpha\Gamma^\mu_{\nu\beta} - \partial_\beta\Gamma^\mu_{\nu\alpha} + \Gamma^\mu_{\alpha\gamma}\Gamma^\gamma_{\nu\beta} - \Gamma^\mu_{\beta\gamma}\Gamma^\gamma_{\alpha\nu}. \tag{2.8}$$

The Riemann curvature tensor is so named as it encapsulates the deviation of the metric from being locally isometrically flat. Another way of stating this is that $R^\mu_{\nu\alpha\beta}$ measures the deviation in orientation of a vector when parallel transported along a loop on a curved manifold. If $R^\mu_{\nu\alpha\beta} = 0$, then the vector will remain parallel to its original direction when returned to its initial position. This is however not true in general for a curved manifold.

The Ricci tensor is then given by a contraction of the first and third indices of the Riemann tensor, $R_{\mu\nu} = R^\alpha_{\mu\alpha\nu}$, and the Ricci scalar is found by contracting the indices on the Ricci tensor, $R = R^\mu_\mu$.

So – we have introduced the metric tensor from which we can derive the curvature of spacetime. All that remains is to understand how the metric evolves. In general relativity,

the evolution of the metric in the presence of matter and radiation is determined by Einstein's field equations

$$R_{\mu\nu} - \frac{1}{2} g_{\mu\nu} R = 8\pi G T_{\mu\nu}, \tag{2.9}$$

where G is the gravitational constant. The Einstein field equations relate the behaviour of the curvature of spacetime corresponding to $R_{\mu\nu}$, R, and $g_{\mu\nu}$ to the matter and radiation content of the universe, which is encoded by the energy-momentum tensor $T_{\mu\nu}$. This constant effectively dictates the intrinsic energy density of the vacuum. When provided with an initial set of values for $g_{\mu\nu}$ and $T_{\mu\nu}$, the evolution of the metric is determined at all times.

2.1 Cosmology

Modern cosmology is founded on the Copernican principle, sometimes called the cosmological principle. This states that the region of the universe in which we find ourselves is statistically representative of the universe as a whole; we do not occupy a special place in the universe. From this principle we infer two of the key tenets of cosmology. The first is that the universe is homogenous, which means any chosen region looks the same as any other. The second is that the universe is isotropic, meaning that our observations of the universe should be equivalent in every direction. Our experience tells us that this is not true on small scales. Our Solar System is certainly different from interstellar space, and when looking towards the centre of the Milky Way we see very different conditions to those when looking out of the galactic plane. It is only on large enough scales that the statistical principles of homogeneity and isotropy stand. The distribution of galaxies on scales of $\gtrsim 100\,\mathrm{Mpc}$ is roughly uniform. The Cosmic Microwave Background very closely obeys a thermal blackbody spectrum which tells us that the early universe was very homogenous and isotropic.

An exact solution to Einstein's field equations in which the universe is taken to be homogenous and isotropic is given by the Friedmann-Lemaître-Robertson-Walker (FLRW) metric

$$ds^2 = -dt^2 + a(t)^2 \left(\frac{dr^2}{1 - kr^2} + r^2 d\Omega \right). \tag{2.10}$$

We can see that there is an overall scale factor $a(t)$ applied to the spatial components of the metric. The scale factor tracks the expansion of the universe such that $a(t')/a(t)$ represents the factor by which a given volume changes in size between times t and t'. By convention the scale factor at the present cosmic time, a_0, is normalised to unity. The

factor k represents the curvature of spatial slices at constant cosmic time. If $k < 0$ the spatial slice has an open spatial curvature in which the angle between initially parallel lines diverge due to the geometry. On the other hand if $k > 0$ the spatial curvature is closed and so parallel lines would eventually converge. Finally, $k = 0$ represents flat universes, in which initially parallel lines remain parallel.

The spatial coordinates in the FLRW metric r and Ω are known as comoving coordinates. Observers moving purely due to the expansion of the universe are at rest in comoving coordinates, and percieve the universe to be isotropic. The comoving distance

$$d\Sigma = \left(\frac{dr^2}{1 - kr^2} + r^2 d\Omega \right), \tag{2.11}$$

factors out the expansion of the universe. The proper distance between two points at a given cosmic time is $a(t)d\Sigma$. With a_0 normalised to unity, the comoving distance and proper distance between two points are equal at the present cosmic time.

The FLRW metric is used within cosmology to describe the background metric of our universe, with the structure that we see today forming via perturbations from this metric.

In the study of cosmology on large scales, the particle content of the universe is often modelled as a perfect fluid. A perfect fluid has no heat conduction or viscosity. This is typically a good approximation for the universe on large scales, as the mean free path of the particle content is small in comparison to the length scales of interest. A perfect fluid is described by the following energy-momentum tensor,

$$T_{\mu\nu} = (\rho + p) U_\mu U_\nu + p g_{\mu\nu} \tag{2.12}$$

with ρ the energy density, p the pressure, and U^μ the four-velocity of the fluid.

By applying Einstein's field equations to the FLRW metric with $T_{\mu\nu}$ given as above by a perfect fluid, we arrive at the Friedmann equations,

$$H^2 = \frac{8\pi}{3} G\rho - \frac{k}{a^2} \tag{2.13}$$

$$\dot{H} + H^2 = -\frac{4\pi G}{3} (\rho + 3p) \tag{2.14}$$

where $H = \dfrac{\dot{a}}{a}$ is the Hubble parameter. Sometimes Eq. (2.13) and Eq. (2.14) are called the first and second Friedmann equations respectively. They can be combined to provide the continuity equation,

$$\dot{\rho} + 3H(\rho + p) = 0. \tag{2.15}$$

Upon rearranging the first Friedmann equation we see that

$$\rho - \frac{3H^2}{8\pi G} = \frac{3H^2}{8\pi G} \frac{k}{(aH)^2}, \tag{2.16}$$

which allows us to identify the critical energy density corresponding to a flat universe with $k = 0$,

$$\rho_{\rm c} = \frac{3H^2}{8\pi G}. \tag{2.17}$$

Observations tell us that the value of $\rho/\rho_{\rm c}$ today is very close to 1 and therefore to a very good approximation the background curvature of the present day universe is flat. For the rest of this thesis the approximation $k = 0$ will be taken.

Taking a barotropic equation of state $p = w\rho$ for the perfect fluid allows us to further simplify the Friedmann equations. For $w \neq -1$, we find from the conservation equation that

$$\rho \propto a^{-3(w+1)} \tag{2.18}$$

which upon substitution into Eq. (2.13) gives

$$a(t) \propto t^{2/3(w+1)}. \tag{2.19}$$

In the case where $w = -1$ we instead find that ρ is constant in time, and therefore

$$a(t) \propto e^{Ht}. \tag{2.20}$$

Using the relations above we can show how the universe scales during matter and radiation domination. Non-relativistic particles or dust have negligible pressure compared to their energy density and so can be modelled with $w = 0$, giving

$$\rho_{\rm m} \propto a^{-3}. \tag{2.21}$$

As a result the scale factor grows as $a(t) \propto t^{2/3}$ during matter domination.

Massless and ultra-relativistic particles or radiation have $w = 1/3$, and so their energy density follows

$$\rho_{\rm r} \propto a^{-4}. \tag{2.22}$$

As the energy density of radiation dilutes with a higher power of the scale factor than matter, it dominates the early universe. During radiation domination the scale factor grows as

$$a(t) \propto t^{1/2}. \tag{2.23}$$

2.2 Gravitational waves

One of the most intriguing predictions of general relativity is the existence of gravitational waves. These ripples in spacetime carry information about the variation of the

curvature of the universe outwards from their source. Gravitational waves are small perturbations in the metric that propagate at the speed of light. Proposed originally in 1905 by Henri Poincaré, in 1916 Einstein predicted that, according to his general theory of relativity, gravitational waves must exist. It was not until 100 years later in 2016 that the first gravitational waves would be detected by the Laser Interferometer Gravitational-Wave Observatory or LIGO [74]. The first gravitational wave ever detected was produced during a black hole binary merger. In this event two black holes with masses close to 30 times that of the Sun collided and merged, radiating away several times the mass energy of the Sun in gravitational waves.

Many events have been observed since, and the era of gravitational wave astronomy has clearly begun. Gravitational waves hold great promise for probing cosmology. Already the detection of gravitational waves emitted during the coalescence of two neutron stars and the observation of the resulting electromagnetic counterpart [78, 79] have greatly constrained a range of modified gravity theories that predicted gravitational waves travel slower than the speed of light [80]. Future detectors could well lead to a revolution in cosmology as the gravitational wave band becomes further explored.

In this section we give a brief introduction to gravitational waves. We mostly follow the treatment in Ref. [81], though Refs. [82–84] are also useful.

In order to study gravitational waves, we begin by linearising gravity. Consider the metric of a flat Minkowski spacetime $\eta_{\mu\nu}$ which has been perturbed by a small fluctuation $h_{\mu\nu}$,

$$g_{\mu\nu} \approx \eta_{\mu\nu} + h_{\mu\nu}, \tag{2.24}$$

where $|h_{\mu\nu}| \ll |\eta_{\mu\nu}|$ for each μ and ν. Here $\eta_{\mu\nu}$ represents the background, and the fluctuation $h_{\mu\nu}$ corresponds to the variation of the metric due to the propagating gravitational wave.

Up to linear order in h, we may write the Ricci tensor as

$$R_{\mu\nu} = \frac{1}{2}\left(\partial^\alpha\partial_\mu\overline{h}_{\alpha\nu} + \partial^\alpha\partial_\mu\overline{h}_{\mu\alpha} + \Box\overline{h}_{\mu\nu} + \frac{1}{2}\eta_{\mu\nu}\Box\overline{h}\right), \tag{2.25}$$

where $\Box = \partial_\mu\partial^\mu$ is the D'Alembertian, and we have utilised the trace-reversed metric perturbation,

$$\overline{h}_{\mu\nu} = h_{\mu\nu} - \frac{h}{2}\eta_{\mu\nu}. \tag{2.26}$$

Contracting the indices of the Ricci tensor provides us with the Ricci scalar,

$$R = \partial^\alpha\partial^\beta\overline{h}_{\alpha\beta} + \frac{1}{2}\Box\overline{h}, \tag{2.27}$$

and then from the Ricci tensor and the Ricci scalar we can write out the Einstein field equations

$$\Box\overline{h}_{\mu\nu} + \eta_{\mu\nu}\partial^{\alpha}\partial^{\beta}\overline{h}_{\alpha\beta} - \partial^{\alpha}\partial_{\mu}\overline{h}_{\alpha\nu} - \partial^{\alpha}\partial_{\nu}\overline{h}_{\alpha\mu} = -16\pi G T_{\mu\nu}. \tag{2.28}$$

To continue, we must fix a gauge condition. The Einstein field equations are simplified by applying the Lorentz gauge $\partial^{\alpha}\overline{h}_{\alpha\beta} = 0$, upon which they reduce to

$$\Box\overline{h}_{\mu\nu} = -16\pi G T_{\mu\nu}. \tag{2.29}$$

We can clearly see that we have been left with a wave equation for $\overline{h}_{\mu\nu}$ with a source term arising from the energy-momentum tensor.

In order to consider a gravitational wave propagating in vacuum, far from its source, we set $T_{\mu\nu} = 0$, giving us the empty space equation for a gravitational wave

$$\Box\overline{h}_{\mu\nu} = 0. \tag{2.30}$$

Up until now, we have not fully exploited the gauge freedom of our system. Let us consider a general infinitesimal coordinate transform of the form $x'^{\mu} \to x^{\mu} + \xi^{\mu}(x)$. To linear order in h and ξ, the metric perturbation transforms as

$$h'_{\mu\nu}(x') = h_{\mu\nu}(x) - \partial_{\mu}\xi_{\nu} - \partial_{\nu}\xi_{\mu}, \tag{2.31}$$

and the trace-reversed perturbation as

$$\overline{h}_{\mu\nu}(x') = \overline{h}_{\mu\nu}(x) + \eta_{\mu\nu}\partial_{\alpha}\xi^{\alpha} - \partial_{\mu}\xi_{\nu} - \partial_{\nu}\xi_{\mu}. \tag{2.32}$$

The Lorentz gauge we have utilised is preserved providing

$$\Box\xi_{\nu} = 0. \tag{2.33}$$

We are free then to make a further gauge transformation of the form in Eq. (2.31) providing it also satisfies Eq. (2.33). This allows us to set a further four linear combinations of $\overline{h}_{\mu\nu}$ to zero. One such choice which is frequently taken is the transverse-traceless (TT) gauge, in which $\overline{h}_{0i} = 0$ and $\overline{h} = \overline{h}^{i}{}_{i} = 0$. Taken with the Lorentz gauge, this gives

$$\overline{h}^{TT}_{0\mu} = 0, \qquad \overline{h}^{TT} = 0, \qquad \partial^{i}\overline{h}^{TT}_{ij} = 0. \tag{2.34}$$

Note that in the transverse traceless gauge, $\overline{h}^{TT}_{\mu\nu} = h^{TT}_{\mu\nu}$. We have taken the 10 degrees of freedom originally present in the perturbation $h_{\mu\nu}$ and with the choice of the transverse-traceless gauge reduced this to 2 degrees of freedom. Upon this choice, the gauge freedom is saturated.

We can transform a given tensor into the transverse-traceless gauge by using a projector operator. We first define

$$P_{ij}(\mathbf{k}) = \delta_{ij} - \hat{k}_i \hat{k}_j, \tag{2.35}$$

which is an operator that projects an arbitrary vector to be orthogonal to a vector $\mathbf{k}$. P_{ij} is symmetric, transverse ($\hat{k}^i P_{ij}(\mathbf{k}) = 0$), has trace $P_{ii} = 2$, and as a projector satisfies $P_{ik}P_{ij} = P_{ij}$. Using P_{ij}, we are able to define the projector onto symmetric, transverse-traceless rank-two tensors,

$$\Lambda_{ij,lm}(\mathbf{k}) = P_{im}(\mathbf{k})P_{jl}(\mathbf{k}) - \frac{1}{2}P_{ij}(\mathbf{k})P_{lm}(\mathbf{k}). \tag{2.36}$$

The tensor $\Lambda_{ij,kl}$ is transverse to $\mathbf{k}$ on all indices i, j, k, l and is traceless with respect to the contraction of either the first two indices, or the third and fourth indices. It is also symmetric under the exchange of (i, j) with (k, l). Finally, it can be shown that $\Lambda_{ij,lm}\Lambda_{lm,kl} = \Lambda_{ij,kl}$ as it should for a projector.

For a given metric perturbation h_{ij} with spatial wavevector $\mathbf{k}$, we can recover the transverse-traceless gauge using

$$h_{ij}^{TT}(\mathbf{k}) = \Lambda_{ij,lm}(\mathbf{k})h_{lm}(\mathbf{k}). \tag{2.37}$$

In order to find the energy-momentum that gravitational waves carry, it is necessary to consider perturbations around a more general dynamical curved background metic $\overline{g}_{\mu\nu}$, as otherwise we preclude the possibility that gravitational waves themselves curve the background space-time. In this case the total metric is described through

$$g_{\mu\nu} = \overline{g}_{\mu\nu} + h_{\mu\nu}, \qquad\qquad |h_{\mu\nu}| \ll 1. \tag{2.38}$$

This adds another layer of complexity. Previously when we were expanding around a flat background metric $\eta_{\mu\nu}$, it was clear what the perturbations to the metric were. With the background metric now curved and dynamical as well, we need to find a way to distinguish between the background metric and the fluctuations corresponding to the gravitational waves.

While in a general case there is no unique way to perform a separation as in Eq. (2.38), there are some scenarios in which a clear separation between background and perturbations can be made [85, 86]. For example, if there exists a natural separation of scales such that there exists a large spatial variation with length scale L_B, upon which there are small scale perturbations with a characteristic wave length λ such that

$$\frac{\lambda}{2\pi} \ll L_{\mathrm{B}}, \tag{2.39}$$

then $h_{\mu\nu}$ can be considered to be small scale perturbations on a larger smooth background.

A similar distinction can be made in frequency space. If the background metric has typical frequencies below a maximum frequency $f_{\rm B}$, whereas there are small fluctuations with a characteristic frequency f such that

$$f \gg f_{\rm B}, \tag{2.40}$$

then the perturbations $h_{\mu\nu}$ are small high frequency fluctuations about a larger slowly varying background.

In both of the scenarios described above we have two small parameters when expanding the Einstein equations around the background metric. One of these parameters is the typical amplitude of the fluctuation, $h = O(|h_{\mu\nu}|)$, and the other is either the ratio of $\lambda/2\pi L_{\rm B}$ or $f/f_{\rm B}$, depending on how the background and the metric perturbations are distinguished. In order to separate the effect of gravitational waves from the background we perform an average of physical quantities over a given length-scale l or time scale τ, such that $\lambda/2\pi \ll l \ll L_{\rm B}$ or $1/f \ll \tau \ll 1/f_{\rm B}$.

To find the energy-momentum tensor of the gravitational waves, it is necessary to expand the Einstein equations to second order in $h_{\mu\nu}$. At quadratic order in $h_{\mu\nu}$, the Ricci tensor can be written as,

$$R_{\mu\nu} = \overline{R}_{\mu\nu} + R^{(1)}_{\mu\nu} + R^{(2)}_{\mu\nu} + O(|h_{\mu\nu}|^3) \tag{2.41}$$

where $\overline{R}_{\mu\nu}$ contains only the background metric, and $R^{(1)}_{\mu\nu}$ and $R^{(2)}_{\mu\nu}$ are linear and quadratic in $h_{\mu\nu}$ respectively.

Averaging over the energy-momentum tensor allows us to define an effective energy-momentum tensor of matter $\overline{T}^{\mu\nu}$,

$$\langle T_{\mu\nu} - \frac{1}{2} g_{\mu\nu} T \rangle = \overline{T}_{\mu\nu} - \frac{1}{2}\overline{g}_{\mu\nu}\overline{T}, \tag{2.42}$$

where $\overline{T} = \overline{g}_{\mu\nu}\overline{T}^{\mu\nu}$ is the trace of $T^{\mu\nu}$, and the notation $\langle ... \rangle$ signifies to average over l or τ as appropriate. We can also define another tensor $t_{\mu\nu}$ constructed out of terms quadratic in h,

$$t_{\mu\nu} = -\frac{1}{8\pi G}\langle R^{(2)}_{\mu\nu} - \frac{1}{2}\overline{g}_{\mu\nu} R^{(2)} \rangle, \tag{2.43}$$

with $R^{(2)} = \overline{g}^{\mu\nu} R^{(2)}_{\mu\nu}$.

We can now write out a form of the Einstein equations that governs how the background metric $\overline{g}_{\mu\nu}$ evolves,

$$\overline{R}_{\mu\nu} - \frac{1}{2}\overline{g}_{\mu\nu}\overline{R} = 8\pi G \left(\overline{T}_{\mu\nu} + t_{\mu\nu}\right), \tag{2.44}$$

where $\overline{R} = \overline{g}^{\mu\nu} R_{\mu\nu}$. The evolution of the background metric is therefore determined in part through the energy-momentum tensor of matter, and in part due to $t_{\mu\nu}$ which is quadratic in $h_{\mu\nu}$ and depends only on the gravitational field.

In order to determine the energy-momentum tensor of gravitational waves from $t_{\mu\nu}$, we need to remove any spurious contributions from gauge modes. Considering gravitational waves propagating in vacuum, such that $\Box h^{TT}_{\mu\nu} = 0$, we find that after projecting into the transverse-traceless gauge

$$t^{\rm gw}_{\mu\nu} = \frac{1}{32\pi G} \langle \partial_\mu h^{TT}_{\alpha\beta} \partial_\nu h^{TT,\alpha\beta} \rangle. \tag{2.45}$$

We are now able to show the well known result that the energy density carried by gravitational waves in vacuum is given by

$$\rho_{\rm gw} = t^{00}_{\rm gw} = \frac{1}{32\pi G} \langle \dot{h}^{TT}_{ij} \dot{h}^{TT,ij} \rangle. \tag{2.46}$$

In a cosmological context, we often talk about the gravitational wave energy density parameter $\Omega_{\rm gw}$, defined as

$$\Omega_{\rm gw} = \frac{\rho_{\rm gw}}{\rho_{\rm c}}. \tag{2.47}$$

Finally, we note that gravitational waves produced during cosmological events in the early universe typically produce a gravitational wave background that is stochastic in nature, see e.g. Ref. [76]. This means that the amplitude of the metric perturbations $h_{\mu\nu}$ should be treated as a random variable, which can only be characterised statistically. As such, when considering a cosmological gravitational wave background, the relevant signal is the power spectrum of gravitational waves.

The spectral density of the time derivative of the metric perturbations $P_{\dot{h}}$ can be defined as

$$\langle \dot{h}^{TT}_{ij}(\mathbf{k}, t) \dot{h}^{TT}_{ij}(\mathbf{k}', t) \rangle = P_h(\mathbf{k}, t)(2\pi)^3 \delta(\mathbf{k} + \mathbf{k}'). \tag{2.48}$$

If the gravitational wave background is isotropic, then we can write the power spectrum of the gravitational wave energy density as

$$\frac{d\rho_{\rm gw}}{d\ln(k)} = \frac{1}{32\pi G} \frac{k^3}{2\pi^2} P_{\dot{h}}(k, t). \tag{2.49}$$

Dividing through by the critical energy density $\rho_{\rm c}$ we obtain the power spectrum of the gravitational wave energy density parameter,

$$\frac{d\Omega_{\rm gw}}{d\ln(k)} = \frac{1}{32\pi G \rho_{\rm c}} \frac{k^3}{2\pi^2} P_{\dot{h}}(k, t), \tag{2.50}$$

which we will refer to as the gravitational wave power spectrum.

Chapter 3

Cosmological first-order phase transitions

Cosmological first-order phase transitions are dramatic events in which the ground state of the early universe changes abruptly via the nucleation, expansion and collision of bubbles of the true vacuum state. They can have exciting consequences, ranging from baryogenesis to the production of gravitational waves. In this chapter we review the dynamics of first-order cosmological phase transitions and the resulting gravitational wave signatures they produce. We begin by outlining the basic features of first-order cosmological transitions and how to compute the bubble nucleation rate. We then discuss the dynamics of the phase transition after bubble nucleation. We conclude by summarising the mechanisms for production of gravitational waves from first-order phase transitions.

In a first-order phase transition, two local minima coexist in the effective potential of the order parameter describing the phase transition, where the effective potential is constructed from the tree level potential of the field and quantum and thermal corrections. The two minima correspond to a metastable, false vacuum state, and the true, stable vacuum state. Sometimes these are called the symmetric and broken phase respectively, in recognition of the symmetry-breaking processes undergone during a transition. The scalar field can cross the potential barrier into the new phase either due to thermal fluctuations or via quantum mechanical tunneling. When this occurs, a bubble of the true vacuum state forms, surrounded by the metastable state, with the region where the field varies between the two phases corresponding to the bubble wall. The potential energy difference between states creates an outward pressure on the bubble wall. If the initial bubble is larger than some critical size, this pressure overcomes the surface tension in the bubble, and the bubble will expand. A first-order phase transition therefore proceeds via the nucleation of bubbles, their subsequent expansion, and eventual collision. The phase transition concludes when long-range connectivity between percolating clusters of bubbles is established.

Cosmological first-order phase transitions can be described as thermal or vacuum transitions. Thermal phase transitions take place in the presence of a cosmic plasma. Bubbles

nucleate primarily through thermal fluctuations or thermally assisted tunneling [5]. After the bubbles nucleate and begin to expand, friction between the plasma and the bubble wall results in shells of fluid developing around the bubble wall. Typically, the friction between the plasma and bubble wall will reach an equilibrium with the pressure driving the expansion of the bubble, and the wall will accelerate up to a terminal velocity [87]. Once the wall has approached its terminal velocity, the free energy of the transition is predominantly distributed between heating the plasma and bulk fluid motion [88]. After the bubbles collide and eventually percolate, the fluid shells continue to propagate and remain a long lasting source of gravitational waves [60, 62, 63].

Interestingly, it has been claimed that if a thermal transition is sufficiently strong then the friction between the plasma and bubble wall is always less than the pressure driving the expansion. In this case the bubble wall undergoes a 'runaway' acceleration, and does not reach a terminal wall velocity before collision [89]. When this occurs the dynamics of the transition can be similar to vacuum transitions; the free energy of the transition is deposited predominantly into kinetic and gradient energy in the scalar field at the bubble wall and the dominant gravitational wave signal will once again be due to gradients in the scalar field during bubble collisions [88]. While next to leading order effects have shown that in most situations runaway transitions do not occur [87], it has been proposed that they can still exist in certain cases [90, 91], which we shall discuss in more detail later.

3.1 Decay of the false vacuum

Cosmological first-order phase transitions proceed through the nucleation of bubbles of the true vacuum state. In order to calculate the decay rate of the false vacuum, we first consider the Euclidean effective action for a single scalar field, which is given by

$$S_4 = \int_0^{1/T} d\tau \int d^3x \left[\frac{1}{2} \left(\frac{\partial \phi}{\partial \tau} \right)^2 + \frac{1}{2} \left(\nabla \phi \right)^2 + V(\phi, T) \right]. \tag{3.1}$$

Here $V(\phi, T)$ is the effective potential, T is the temperature, and ϕ corresponds to the classical background field, or order parameter, of the transition. The effective potential at one-loop level is of the form

$$V(\phi, T) = V_0(\phi) + V_1(\phi) + \Delta V_1^T(\phi, T), \tag{3.2}$$

where $V_0(\phi)$ is the tree level potential, $V_1(\phi)$ are the one-loop corrections at zero temperature, and $\Delta V_1^{(T)}(\phi, T)$ corresponds to the leading thermal corrections.

For the electroweak phase transition in Standard Model-like theories, $V_1(\phi)$ is given by [92]

$$V_1(\phi) = \sum_i \frac{g_i(-1)^{2s_i}}{4(4\pi)^2} m_i^4(\phi) \left[\ln\left(\frac{m_i^2(\phi)}{\Lambda}\right) + C_i \right], \tag{3.3}$$

where i sums over all particles in the theory, with g_i and s_i the degrees of freedom and spin of each particle. The mass of each particle $m_i(\phi)$ depends on the value of the order parameter. The renormalisation scale is given by Λ, with corresponding scheme dependent constants C_i.

The leading order thermal corrections are given by the free-energy of the Bose-Einstein and Fermi-Dirac distributions of particles obtaining a mass across the transition [93]

$$\begin{aligned} \Delta V_1^{(T)}(\phi, T) = & \sum_B \frac{g_B T^4}{2\pi^2} \int^\infty \mathrm{d}x x^2 \ln\left(1 - \exp\left(-\sqrt{x^2 + \frac{m_B^2(\phi)}{T^2}}\right)\right) \\ & - \sum_F \frac{g_F T^4}{2\pi^2} \int_0^\infty \mathrm{d}x x^2 \ln\left(1 + \exp\left(-\sqrt{x^2 + \frac{m_F^2(\phi)}{T^2}}\right)\right), \end{aligned} \tag{3.4}$$

where B and F indicate to sum over the bosons and fermions in the theory respectively.

The one-loop effective potential in the Standard Model-like theories at high temperature can be approximated by [5]

$$V(\phi, T) = \frac{1}{2} D(T^2 - T_0^2)\phi^2 - \frac{1}{3} A T \phi^3 + \frac{1}{4}\lambda\phi^4, \tag{3.5}$$

with D, T_0, A and λ parameters to be determined from the particle physics theory. Only bosons contribute to the value of A. This form of potential has been frequently used to approximate first-order phase transitions in realistic particle physics theories. For an excellent review on computing effective potentials with phase transitions and a focus on the Standard Model, see Ref. [94].

The qualitative behaviour of an effective potential of the form in Eq. 3.5 is shown in Fig. 3.1. At high temperatures, the background field is in the ground state corresponding to the symmetric phase at $\phi = 0$. As the temperature lowers, a second minima in the potential develops and at the critical temperature, T_c, the minima are degenerate. For temperatures lower than T_c, the broken phase minima becomes energetically favourable, though the field remains trapped in the metastable state. Once the temperature drops to $T = T_0$, the potential barrier separating the symmetric and broken phase disappears and the potential no longer supports a first-order transition. We denote the temperature at which the transition proceeds as the nucleation temperature T_n, with $T_0 < T_\mathrm{n} < T_\mathrm{c}$.

The onset of the transition can be defined using the temperature at which one bubble is nucleated per horizon volume on average,

$$N(T_\mathrm{o}) = \int_{T_\mathrm{o}}^{T_\mathrm{c}} \frac{dT}{T} \frac{\Gamma(T)}{H(T)^4} = 1. \tag{3.6}$$

with Γ the nucleation rate per unit volume. Sometimes the temperature $T_{\rm o}$ is also defined to be the nucleation temperature.

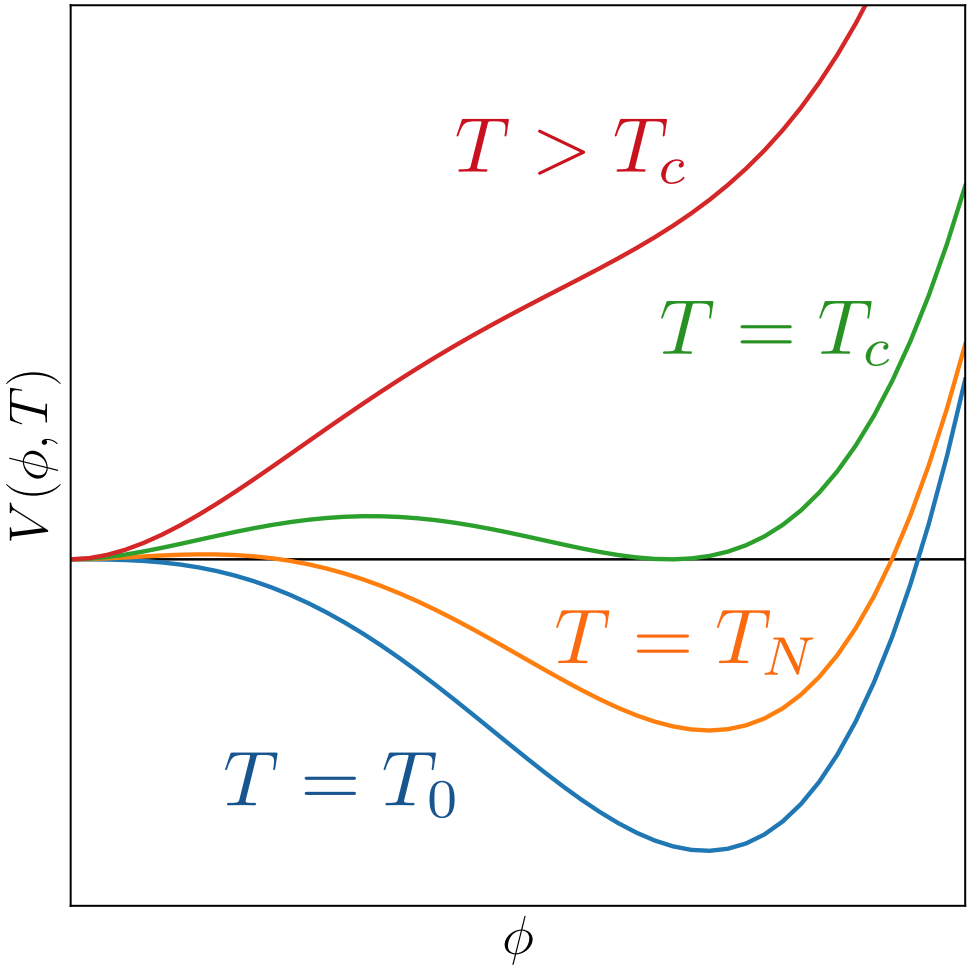

Figure 3.1: Qualitative behaviour of the high temperature effective potential for the electroweak phase transition in Standard Model-like theories. The critical temperature is given by $T_{\rm c}$, $T_{\rm n}$ is the nucleation temperature at which the transition proceeds, and T_0 is the temperature at which the barrier between vacua disappears.

In order to compute the decay rate of the vacuum, we must first find the tunneling solution of the scalar field. This is often referred to as the bounce solution. For vacuum transitions, or thermal transitions very close to $T = 0$, this can be found by assuming an O(4) symmetry of the tunneling solution. More precisely, the bounce solution ϕ is taken to be a function of only $\rho = \sqrt{r^2 + \tau^2}$, with $r^2 = |\mathbf{x}|^2$ the spatial distance from the bubble centre and τ the Euclidean time.

The tunneling solution is found by solving the Euclidean equation of motion,

$$\frac{d^2\phi}{d\rho^2} + \frac{3}{\rho}\frac{d\phi}{d\rho} = V'(\phi, 0), \tag{3.7}$$

with boundary conditions

$$\left.\frac{d\phi}{d\rho}\right|_{\rho=0} = 0, \qquad \lim_{\rho\to\infty}\phi(\rho) = \phi_{\rm s}, \tag{3.8}$$

and $\phi_{\rm s}$ the value of ϕ in the symmetric phase. The field profile for the critical bubble is found by analytically continuing the bounce solution at $\tau = 0$. The critical bubble gives the field profile into which the false vacuum is most likely to tunnel.

At high temperatures the four-dimensional action can be approximated by a three-dimensional action [5],

$$S_4 \approx \frac{1}{T}\int d^3x \left[\frac{1}{2}\left(\frac{\partial\phi}{\partial\tau}\right)^2 + \frac{1}{2}(\nabla\phi)^2 + V(\phi, T)\right] \equiv \frac{S_3}{T} \tag{3.9}$$

where S_3 is the three-dimensional action corresponding to the $O(3)$-symmetric bubble. Then, at high temperatures the bounce solution can be found by solving

$$\frac{\partial^2\phi}{\partial r^2} + \frac{2}{r}\frac{\partial\phi}{\partial r} = V'(\phi, T), \tag{3.10}$$

with boundary conditions $\phi \to \phi_{\rm s}$ at $r \to \infty$ and $\partial\phi/\partial r = 0$ at $r = 0$.

The total decay rate per unit volume of the false vacuum can typically be approximated as that of the dominant contribution from either thermally-induced tunneling or quantum tunneling,

$$\Gamma(t) \sim \max\left(\Gamma_{\rm QT}(t), \Gamma_{\rm therm}(t)\right). \tag{3.11}$$

The decay rate of the false vacuum due to quantum tunneling is approximately given by [4]

$$\Gamma_{\rm QT}(t) \sim R_{\rm c}^{-4}\left(\frac{S_4}{2\pi}\right)^2 e^{-S_4}, \tag{3.12}$$

whereas the thermally-induced decay rate is given by [5, 95]

$$\Gamma_{\rm therm}(t) \sim T^4\left(\frac{S_3}{2\pi T}\right)^{3/2} e^{-S_3/T}. \tag{3.13}$$

Here S_3 and S_4 correspond to the three-dimensional and four-dimensional actions for the O(3) and O(4)-symmetric bounce solutions and the typical radius of the nucleated bubble is $R_{\rm c}$. The quantum tunneling contribution dominates for vacuum transitions and at very low temperatures for thermal transitions with a barrier between vacua at $T = 0$. At high temperatures, the thermally induced tunneling rate dominates instead.

The nucleation rate per unit volume is frequently taken to be

$$\Gamma(t) = p_0 e^{-S_4(t)}, \tag{3.14}$$

where p_0 is constant. This often is a good approximation to first order as the prefactors in $\Gamma_{\rm QT}$ and $\Gamma_{\rm therm}$ vary much slower with respect to time than the exponential factor.

Often the phase transition completes in much less than a Hubble time in which case the expansion of the universe can be neglected. Then, the expected fraction of the universe remaining in the metastable state is given by [96]

$$h(t) = \exp\left(-\frac{4}{3}\pi v_{\rm w}^3 \int_{t_{\rm c}}^{t} dt' p_0 e^{-S_4(t')}(t-t')^3\right), \tag{3.15}$$

where $v_{\rm w}$ is the speed at which the bubble expands, and $t_{\rm c}$ is the time corresponding to $T = T_{\rm c}$. For convenience, we introduce $I(t) = -\ln h(t)$.

For many particle physics models with thermal transitions, the action S_4 is decreasing with time during the phase transition. Upon Taylor expanding the nucleation rate, we find that

$$\Gamma(t) = p_0 \exp\left(-S_{\rm f} + \beta(t-t_{\rm f}) + ...\right), \tag{3.16}$$

where $\beta = S_4'(t_f)$, $S_{\rm f} = S_4|_{t_{\rm f}}$ and $t_{\rm f}$ is some reference time. Neglecting higher order terms in the Taylor expansion,

$$I(t) = 8\pi p_0 \frac{v_{\rm w}^3}{\beta^4} e^{-S_{\rm f}+\beta(t-t_{\rm f})}. \tag{3.17}$$

Choosing the reference time $t_{\rm f}$ via $h(t_{\rm f}) = 1/e$, the volume fraction in the metastable state decreases as

$$h(t) = \exp\left(-e^{\beta(t-t_{\rm f})}\right), \tag{3.18}$$

and as such this scenario is sometimes called exponential nucleation, and β^{-1} approximately gives the transition duration. The time $t_{\rm f}$ is set by

$$8\pi p_0 \frac{v_{\rm w}^3}{\beta^4} e^{-S_{\rm f}} = 1. \tag{3.19}$$

The time $t_{\rm f}$ and corresponding temperature $T_{\rm f}$ are frequently used to define the nucleation temperature instead of $T_{\rm o}$. Choosing either $T_{\rm f}$ or $T_{\rm o}$ as $T_{\rm n}$ is equivalent to choosing whether the nucleation temperature is defined to be when most of the bubbles are nucleated or when the first bubble is nucleated.

The transition completes with the percolation of the bubbles of the true vacuum. The completion of the transition and percolation of the bubbles can be defined through the condition $h(t_{\rm p}) = 0$, which sets the percolation time $t_{\rm p}$ and the corresponding temperature $T_{\rm p}$.

In the above we have neglected the effect of the expansion of the universe. For very strong transitions in which the vacuum energy dominates, the metastable phase can begin to inflate. In this case, while the comoving fraction of the universe in the metastable phase tends towards zero, the fraction of the physical volume in the metastable phase can tend towards unity, and as such the phase transition never completes. This is the same issue that was faced in old inflation models that completed through a first-order phase transition [97]. For very strong transitions it is therefore necessary to carry out the above calculation including the effect of expansion, with $h(t)$ then giving the fraction of the comoving volume remaining in the metastable state. Furthermore, it is necessary to also check that at t_p not only is the condition $h(t_\mathrm{p}) = 0$ fulfilled, but also that the physical volume of the universe in the false vacuum, $\mathcal{V}_\mathrm{false} \propto a(t)^3 h(t)$, is decreasing. If this is true, then the transition completes. For more details on percolation in strong transitions and a calculation of $h(t)$ including expansion, see Ref. [98].

When assuming exponential nucleation, for a thermal phase transition in a radiation dominated epoch it is possible to determine T_o and T_p from the action using [99]

$$\left.\frac{S_3}{T}\right|_{T=T_\mathrm{o}} \simeq 141 + \log(p_0/T^4) - 4\log\left(\frac{T_\mathrm{o}}{100\,\mathrm{GeV}}\right) - \log\left(\frac{\beta}{100}\right), \tag{3.20}$$

$$\left.\frac{S_3}{T}\right|_{T=T_\mathrm{p}} \simeq 131 + \log(p_0/T^4) - 4\log\left(\frac{T_\mathrm{p}}{100\,\mathrm{GeV}}\right) - \log\left(\frac{\beta}{100}\right) + 3\log(v_\mathrm{w}), \tag{3.21}$$

where for the electroweak phase transition the factor $\log(p_0/T^4) \simeq -14$ [100].

The number density of bubbles n_b at a given time is found via

$$\frac{dn_\mathrm{b}}{dt} = h(t)\Gamma(t), \tag{3.22}$$

respecting that bubbles can only nucleate in the metastable phase. By integrating this equation, it can be shown that the asymptotic number density of bubbles for a transition with exponential nucleation is given by

$$n_\mathrm{b} = \frac{p_0}{\beta} e^{-S_\mathrm{f}} = \frac{\beta^3}{8\pi v_\mathrm{w}^3}. \tag{3.23}$$

From the number density of bubbles we can define the average separation between bubble centres,

$$R_* \equiv n_\mathrm{b}^{-1/3}, \tag{3.24}$$

which for exponential nucleation is given by

$$R_* = \frac{(8\pi)^{1/3} v_\mathrm{w}}{\beta}. \tag{3.25}$$

The average bubble separation is an important quantity for the generation of gravitational waves from first-order phase transitions. We shall see later that it sets both the peak length

scale and amplitude of the gravitational wave power spectrum, both in thermal transitions and those in vacuum.

It is possible to imagine scenarios in which S_4 reaches a minimum at some time t_0 during the transition. In this case, we can expand the action about the minimum,

$$\Gamma(t) = p_0 e^{-S_0 - \frac{1}{2}\beta_2^2 (t-t_0)^2 + \cdots}, \tag{3.26}$$

with $\beta_2 = S''(t_0)$. In this scenario, the metastable fraction decreases as

$$h(t) = \exp\left(-\frac{4\pi}{3} p_0 e^{-S_0} v_\mathrm{w}^3 \int_{t_\mathrm{c}}^{t} dt' e^{-\frac{1}{2}\beta_2^2 (t'-t_0)^2} (t-t')^3 \right). \tag{3.27}$$

In the limit where $p_0 e^{-S_0} v_\mathrm{w}^3 / \beta_2^4 \ll 1$ and $\beta_2 (t_0 - t_\mathrm{c}) \gg 1$, then at late times where $t \to \infty$, the metastable fraction asymptotes towards

$$h(t) \to \exp\left(\frac{4\pi}{3} \frac{\sqrt{2\pi}}{\beta_2} p_0 e^{-S_0} v_\mathrm{w}^3 (t-t_0)^3 \right). \tag{3.28}$$

In this case the asymptotic bubble density is given approximately by

$$n_\mathrm{b} \approx \frac{\sqrt{2\pi}}{\beta_2} p_0 e^{-S_0}. \tag{3.29}$$

This allows us to rewrite the asymptotic metastable fraction as

$$h(t) \to \exp\left(-\frac{1}{6} \beta_\mathrm{eff}^3 (t-t_0)^3 \right), \tag{3.30}$$

where $\beta_\mathrm{eff} = 8\pi n_\mathrm{b} v_\mathrm{w}^3$. Here we can clearly see that bubble nucleation will peak sharply around $t = t_0$, and so this situation is sometimes referred to as simultaneous nucleation.

3.2 Phase transition dynamics

3.2.1 Coupled field-fluid model

In thermal first-order phase transitions, bubbles of the true vacuum state nucleate in a hot relativistic plasma. In order to study this system, a coupled field-fluid model is typically utilised [96, 101]. The coupled field-fluid model consists of a perfect fluid and a scalar order parameter which communicate through a dissipative phenomenological friction term.

To introduce the model, we start by considering the energy-momentum tensor of relativistic plasma and the background scalar field driving the transition. The total energy-momentum tensor can be split into a pieces describing the field and the plasma,

$$T_{\mu\nu} = T_{\mu\nu}^\mathrm{field} + \sum_i T_{i,\mu\nu}^\mathrm{fluid}, \tag{3.31}$$

where subscript i runs over all the particle species in the plasma.

The background scalar field energy-momentum tensor is given by

$$T^{\rm field}_{\mu\nu} = \partial_\mu\phi\partial_\nu\phi - g_{\mu\nu}\left(\frac{1}{2}(\partial\phi)^2 - V(\phi)\right), \tag{3.32}$$

with $V(\phi) = V_0(\phi) + V_1(\phi)$ the classical potential.

The energy-momentum tensor for each particle species in the plasma is given by [102],

$$T^{\rm fluid}_{i,\mu\nu} = \int \frac{d^3k}{(2\pi)^3}k^\mu k^\nu \frac{1}{E_i} f_i(\mathbf{k},x)\Big|_{k_0=E}, \tag{3.33}$$

with $f_i(\mathbf{k},x)$ the particle distribution function, $E_i = k^2 + m_i^2$ the energy for each particle species, and m_i^2 the field dependent mass of each particle.

The total energy-momentum is conserved such that,

$$\partial^\mu T_{\mu\nu} = \partial^\mu \sum_i T^{\rm i,fluid}_{\mu\nu} + \partial^\mu T^{\rm field}_{\mu\nu} = 0. \tag{3.34}$$

Taking the divergence of field and fluid, and substituting into the equation above, we obtain the equation of motion for the background field,

$$\Box\phi + \frac{dV(\phi)}{d\phi} + \sum_i \frac{dm_i^2}{d\phi}\int \frac{d^3k}{(2\pi)^3}\frac{1}{2E_i} f_i(k,x) = 0. \tag{3.35}$$

The plasma particle distributions can be decomposed into an equilibrium population plus a deviation from equilibrium, $f_i(\mathbf{k},x) = f_i^{\rm eq}(E_i) + \delta f(\mathbf{k},x)$. The equilibrium population is given by $f_i^{\rm eq}(E_i) = 1/(\exp(E_i/T)\pm 1)$, with positive and negative signs corresponding to fermions and bosons respectively. Here we have neglected the chemical potential, μ, which is negligible in the early universe where the energy density is dominated by photons. Note that this also means that there is no conserved particle number in the plasma.

The finite-temperature effective potential of the background field obeys

$$\frac{\partial V(\phi,T)}{\partial\phi} = \frac{\partial V(\phi)}{\partial\phi} + \sum_i \frac{\partial m_i^2}{\partial\phi}\int \frac{d^3k}{(2\pi)^3}\frac{1}{2E_i} f_i^{\rm eq}(E_i) \tag{3.36}$$

and so the equation of motion for the background field can be rewritten as

$$\Box\phi + \frac{dV(\phi,T)}{d\phi} - \mathcal{K}(\phi) = 0, \qquad \mathcal{K}(\phi) = -\sum_i \int \frac{d^3k}{(2\pi)^3}\frac{1}{2E_i}\delta f_i(\mathbf{k},x). \tag{3.37}$$

From the equation of motion we obtain a clear picture of the behaviour of bubbles of the background field during the transition. The second term in the equation of motion shows us that expansion of the bubble wall is driven by a force arising from the latent heat of the transition. This is then opposed by the so-called friction term $\mathcal{K}(\phi)$. The form of $\mathcal{K}(\phi)$ shows us that friction arises from the deviation of particle distribution functions

from equilibrium. So, as the bubble expands due to a pressure difference arising from the latent heat, it disturbs the plasma from its equilibrium state, leading to a friction which opposes the motion of the bubble wall.

Further approximations are frequently used in order to simplify the field-fluid system. If the early universe plasma can be considered to be locally in equilibrium, it can be modelled as a perfect fluid. Then

$$T_{\mu\nu}^{\text{fluid}} = (\epsilon + p)U_\mu U_\nu + g_{\mu\nu}p, \tag{3.38}$$

with ϵ the internal energy density, p the pressure in the fluid, and $U = \gamma(1, \mathbf{v})$ the fluid four-velocity. The full energy-momentum tensor of the system is then given by

$$T^{\mu\nu} = \partial^\mu\phi\partial^\nu\phi - \frac{1}{2}g^{\mu\nu}\partial_\rho\phi\partial^\rho\phi + (\epsilon + p)U^\mu U^\nu + g^{\mu\nu}p. \tag{3.39}$$

The enthalpy density w, entropy density s, and internal energy density can all be calculated from the pressure,

$$w \equiv T\frac{\partial p}{\partial T}, \qquad s \equiv \frac{\partial p}{\partial T}, \qquad \epsilon \equiv T\frac{\partial p}{\partial T} - p. \tag{3.40}$$

The plasma can often be well approximated by a relativistic gas, in which case the equation of state is given by

$$p = aT^4 - V(\phi, T), \tag{3.41}$$

$$\epsilon = 3aT^4 + V(\phi, T) - T\frac{\partial V(\phi, T)}{\partial T}, \tag{3.42}$$

$$w = \epsilon + p, \tag{3.43}$$

with $a = \pi^2 g_*/90$ and g_* the effective degrees of freedom. The effective degrees of freedom quantify the contribution of the internal degrees of freedom of the particle species in the plasma to the energy density or pressure at a given temperature. The effective degrees of freedom contributing to the pressure, $g_{*,p}$, can differ from those contributing to the energy density, $g_{*,\epsilon}$. However, $g_* = g_{*,\epsilon} = g_{*,p}$ is typically a good approximation.

In the fluid approximation, the strength of the transition can be defined as

$$\alpha_\theta = \left.\frac{\theta_{\text{s}} - \theta_{\text{b}}}{\epsilon_{\text{r}}}\right|_{T_{\text{n}}}, \tag{3.44}$$

where θ is the trace anomaly,

$$\theta = \frac{1}{4}(\epsilon - 3p), \tag{3.45}$$

and ϵ_{r} is the radiation energy density in the plasma. The s and b subscripts denote the symmetric and broken phases respectively. The trace anomaly of a pure radiation fluid in

which the particles are massless is zero. The interaction of the scalar field with the fluid breaks this and generates the trace anomaly. This can be seen through the entry of the effective potential into p and ϵ in Eq. 3.41 and Eq. 3.43.

The transition strength, along with the wall velocity, dictates the fluid profile of an expanding bubble. Therefore, it has a substantial effect on the resulting gravitational wave signal. Within the rest of this thesis, we will refer to transitions with $\alpha_\theta \sim 0.005$ as weak, $\alpha_\theta \sim 0.05$ as intermediate, and $\alpha_\theta \sim 0.5$ as strong.

Another frequently used definition of the transition strength is made using the potential energy difference between the metastable and true vacuum states,

$$\alpha_{\mathrm{V}} = \left.\frac{\Delta V(T)}{\epsilon_{\mathrm{r}}}\right|_{T=T_{\mathrm{n}}}, \tag{3.46}$$

where

$$\Delta V(T) = V(0,T) - V(\phi_{\mathrm{b}},T). \tag{3.47}$$

Yet another alternative definition of the transition strength is made using the latent heat density, $\mathcal{L}(T) = w(\phi_{\mathrm{s}},T) - w(\phi_{\mathrm{b}},T)$,

$$\alpha_{\mathcal{L}} = \left.\frac{\mathcal{L}(T)}{\epsilon_{\mathrm{r}}}\right|_{T_{\mathrm{n}}}. \tag{3.48}$$

These three different definitions are not interchangeable and can give substantially different results. At the critical temperature, $\alpha_{\mathcal{L}}$ is a factor of four larger than α_θ. The behaviour of $\alpha_{\mathcal{L}}$ at lower temperatures depends on the model. While α_{V} and α_θ converge for large transition strengths, they diverge for weaker transitions where T_{n} is close to the critical temperature. The definition in Eq. 3.44 is typically used to calculate the gravitational wave power spectrum.

When working with the fluid approximation, a simplified model for $\mathcal{K}(\phi)$ can be taken such that

$$\mathcal{K}(\phi) = \eta(\phi,T,v_{\mathrm{w}})U^\mu\partial_\mu\phi, \tag{3.49}$$

where η is a phenomenological friction parameter which encapsulates the microphysics at the scale of the bubble wall. In principle η can depend on the background field value, the temperature, and the bubble wall velocity v_{w}. The form of η is typically determined by matching to previous results using the Boltzmann equations for $f_i(\mathbf{k},x)$ [102–105] or the relaxation time approximation [106]. It is also possible to compute η explicitly from the microphysics in specific particle physics models [107–109].

In numerical simulations of the field-fluid system, simple forms of η have been utilised, such as

$$\eta(\phi,T,v_{\mathrm{w}}) = \text{const} \quad \text{and} \quad \eta(\phi,T,v_{\mathrm{w}}) = \tilde{\eta}\frac{\phi^2}{T}, \tag{3.50}$$

where $\tilde{\eta}$ is a dimensionless constant. While these are clearly substantial simplifications to the behaviour shown in Eq. 3.37, the exact form of η is not expected to dramatically affect the large scale behaviour of the field or fluid once a terminal wall velocity has been reached. Indeed, as ϕ is constant both inside and outside of the bubble, $\mathcal{K}(\phi)$ tends asymptotically to zero away from the bubble wall. The form of η is therefore only expected to modify the scalar field and plasma profile in close proximity to the phase boundary.

Note that the field dependent friction parameter shown in Eq. 3.50 depends on the background value of ϕ. A more physical choice motivated by the fluctuation-dissipation theorem would be to scale the friction parameter with the variance of the field, $\eta \sim \langle(\phi - \phi_0)^2\rangle$, with ϕ_0 some background field value. We leave the study of this form of friction coupling to future studies.

With the above simplifications, the divergences of the field and fluid energy momentum tensors are given by

$$[\partial_\mu T^{\mu\nu}]_{\text{field}} = (\partial_\mu \partial^\mu \phi)\partial^\nu \phi - \frac{\partial V}{\partial \phi}\partial^\nu \phi = \eta(\phi, T, v_{\text{w}}) U^\mu \partial_\mu \phi \partial^\nu \phi, \tag{3.51}$$

$$[\partial_\mu T^{\mu\nu}]_{\text{fluid}} = \partial_\mu[(\epsilon + p)U^\mu U^\nu] + \partial^\nu p + \frac{\partial V}{\partial \phi}\partial^\nu \phi = -\eta(\phi, T, v_{\text{w}}) U^\mu \partial_\mu \phi \partial^\nu \phi. \tag{3.52}$$

From these it is simple to find the equation of motion for the background field ϕ,

$$-\ddot{\phi} + \nabla^2 \phi - \frac{\partial V}{\partial \phi} = \eta(\phi, T, v_{\text{w}})\gamma(\dot{\phi} + v^i \partial_i \phi), \tag{3.53}$$

the fluid energy density $E = \gamma\epsilon$,

$$\dot{E} + \partial_i(E v^i) + p[\dot{\gamma} + \partial(\gamma v^i)] - \frac{\partial V}{\partial \phi}\gamma(\dot{\phi} + v^i \partial_i \phi) = \eta(\phi, T, v_{\text{w}})\gamma^2(\dot{\phi} + v^i \partial_i \phi)^2, \tag{3.54}$$

and the fluid momentum density $Z_i = \gamma^2 w v_i$,

$$\dot{Z} + \partial_j(Z_i v^j) + \partial_i p + \frac{\partial V}{\partial \phi}\partial_i \phi = -\eta\gamma(\dot{\phi} v^j + \partial_j \phi)\partial_i \phi. \tag{3.55}$$

This form of the equations of motion for the field and fluid are well formulated for numerical simulations. Combined with an effective potential and an equation of state, it is possible to solve the above equations to study the evolution of the scalar field and the fluid during a first-order phase transition.

A model frequently used in analyses of first-order phase transitions is the bag model. The bag model employs a simplified choice of the equation of state which fixes $\theta_{\text{b}} = 0$ and θ_{s} a non-zero constant. This leads to the following pressure and internal energy densities in the broken and symmetric phases,

$$p_{\text{s}} = a_{\text{s}} T_{\text{s}}^4 - \theta_{\text{s}}, \qquad \epsilon_{\text{s}} = 3a_{\text{s}} T_{\text{s}}^4 + \theta_{\text{s}}, \tag{3.56}$$

$$p_{\text{b}} = a_{\text{b}} T_{\text{b}}^4, \qquad \epsilon_{\text{b}} = 3a_{\text{b}} T_{\text{b}}^4. \tag{3.57}$$

In order to perform numerical simulations using the bag model, a must be expressed as a function of ϕ. If we take a quartic shaped potential for the zero temperature potential,

$$V(\phi) = \frac{1}{2}M^2\phi^2 + \frac{1}{3}\mu\phi^3 + \lambda\phi T^4 - \tilde{V} \tag{3.58}$$

with $\tilde{V}$ a constant chosen such that $V(\phi_\mathrm{b}) = 0$, then a convenient choice for $a(\phi)$ is

$$a(\phi) = a_s - \frac{\Delta V}{T_c^4}\left[3\left(\frac{\phi}{\phi_\mathrm{b}}\right)^2 - 2\left(\frac{\phi}{\phi_\mathrm{b}}\right)^3\right], \tag{3.59}$$

with $\Delta V = V(0) - V(\phi_\mathrm{b})$. From considering the pressure at $T = 0$, we can identify that $\theta_\mathrm{s} = \Delta V$. Grouping all field dependent terms together, we see that the temperature dependent potential is given by

$$V(\phi, T) = V(\phi) + \Delta V\left(\frac{T}{T_\mathrm{c}}\right)^4\left[3\left(\frac{\phi}{\phi_\mathrm{b}}\right)^2 - 2\left(\frac{\phi}{\phi_\mathrm{b}}\right)^3\right]. \tag{3.60}$$

Our choice of $a(\phi)$ fixes ϕ_b to be constant at all temperatures, which, while unphysical, is convenient in a toy model utilised for simulations. It also enforces that the symmetric and broken phase in the potential become degenerate at $T = T_\mathrm{c}$ as they should.

3.2.2 Fluid shell profiles

In thermal transitions, expanding bubbles interact with the surrounding plasma, perturbing it and causing shells of fluid to develop around the bubble wall. It is typically assumed that the expanding bubbles and the surrounding fluid shells have a spherical symmetry until they collide.

For bubbles that reach a terminal wall velocity, there is no characteristic length scale in the fluid flow. The fluid profile around an expanding bubble should therefore be self-similar, such that there the fluid profile is related to itself at two different positions or times. In this case, the fluid shell tends to an asymptotic profile in which the fluid velocity, temperature, and enthalpy depend only on the similarity variable ξ. Here $\xi = r/t$, where r is the radius from the bubble centre and t the time since the bubble nucleated. Solving for the asymptotic profile for a given transition strength and wall velocity is possible by matching junction conditions across the bubble wall, see e.g Refs. [6, 65, 67, 88, 110]. To find the asymptotic profiles of the fluid around an expanding bubble in this thesis we use `PTtools`, which is a currently unreleased python module created for this purpose [65].

The bubble wall in a thermal phase transition is analogous to a reaction front. The plasma outside the bubble has more potential energy compared to the plasma inside the bubble as it is in the metastable false vacuum state. This makes it comparable to the

unburnt mixture ahead of a flame front. Inside the bubble, the potential energy has been released and the plasma is in the true ground state, similar to the burnt mixture in a chemical reaction. Two different types of reaction front can be distinguished, named detonations and deflagrations. Denoting the fluid directly ahead and behind the reaction front with + and − subscripts respectively, detonations are characterised by

$$p_+ < p_-, \qquad \tilde{v}_+ > \tilde{v}_-, \qquad \tilde{v}_+ > c_{s,+}, \tag{3.61}$$

whereas for deflagrations

$$p_+ > p_-, \qquad \tilde{v}_+ < \tilde{v}_-, \qquad \tilde{v}_+ < c_{s,+}, \tag{3.62}$$

where $\tilde{v}$ is the fluid velocity in the wall frame, given by the transformation

$$\tilde{v} = \frac{v - v_\mathrm{w}}{1 - v_\mathrm{w} v}, \tag{3.63}$$

and $c_{s,\pm}$ are the local speeds of sound in the fluid. Note that detonations always move supersonically relative to the fluid ahead of the bubble wall, whereas deflagrations always move subsonically.

Reaction fronts can be classified as weak, strong, or the special separating case known as Chapman-Jouguet. For a weak reaction front, $\tilde{v}_+$ and $\tilde{v}_-$ are either both locally subsonic, or supersonic. For strong reaction fronts, $\tilde{v}_+$ and $\tilde{v}_-$ instead lie on opposite sides of $c_{s,\pm}$. Chapman-Jouguet reaction fronts are the separating case, in which either $\tilde{v}_+ = c_{s,+}$ or $\tilde{v}_- = c_{s,-}$. It can be shown that strong deflagrations and weak detonations are not physically possible [110]. Chapman-Jouguet detonation reaction fronts propagate at the minimum possible velocity, called the Chapman-Jouguet velocity c_J. For a cosmological phase transition, c_J can be expressed as a function of α_V [88],

$$c_\mathrm{J} = \frac{\sqrt{\alpha_\mathrm{V}(2 + 3\alpha_\mathrm{V})} + 1}{\sqrt{3}(1 + \alpha_\mathrm{V})}. \tag{3.64}$$

Depending on the terminal wall velocity it is possible to obtain qualitatively different fluid shell solutions. In Fig. 3.2, we show the different behaviour of the fluid profiles schematically. The bubble wall is indicated by the black solid lines, and in colour is shown the asymptotic fluid velocity profile in the plasma flame, normalised to the peak fluid velocity in the profile v_peak. If the bubble wall moves slower than c_s, the fluid profile will form into a subsonic deflagration. If the bubble wall moves faster than c_J, the reaction front will form a detonation. For speeds between c_s and c_J, supersonic deflagrations form.

We show the asymptotic fluid profiles as functions of the similarity variable ξ for a detonation, supersonic deflagration, and subsonic deflagration in Fig. 3.3. In a detonation,

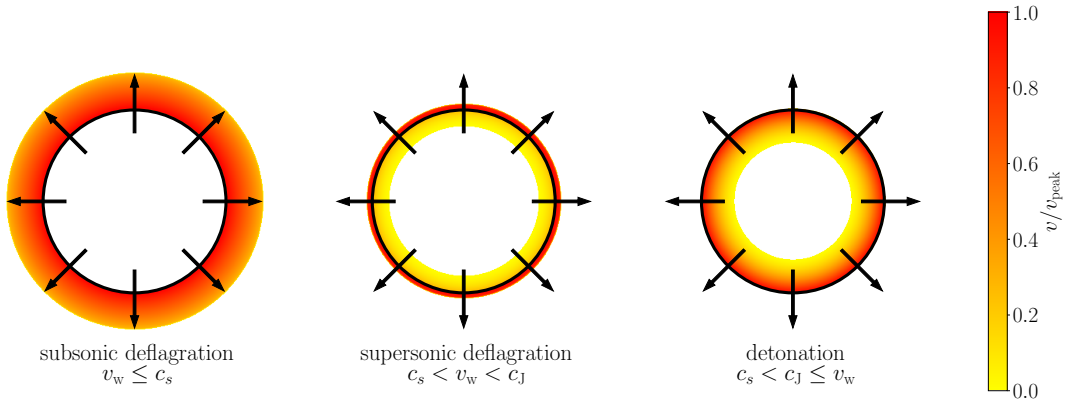

Figure 3.2: A diagram of the different possible fluid shells. The black circles indicate the position of the bubble walls. In colour is the asymptotic fluid velocity profile in the plasma frame, normalised by the peak fluid velocity in the flow, v_{peak}. The bubble wall and fluid are moving radially outwards from the bubble centre. The fluid velocity profiles are calculated for a transition in the bag model with $\alpha_\theta = 0.5$ and wall velocities given by $v_w = 0.44$, $v_w = 0.72$, and $v_w = 0.92$ from left to right.

the bubble wall travels supersonically. The fluid ahead of the bubble wall is at rest and at the nucleation temperature before meeting the bubble wall. As the fluid crosses the bubble wall, it is compressed, heated, and accelerated. The fluid then decelerates and cools in a rarefaction wave as it moves towards the bubble centre, eventually coming to a rest at $\xi = c_{s,-}$.

In a deflagration, the fluid ahead of the wall has time to react to the motion of the bubble wall before crossing the phase boundary. In this case the fluid ahead of the bubble wall is pushed radially outwards at a precompression front, where it is heated and accelerated until it reaches a peak fluid velocity at the phase boundary. The precompression front travels at a speed v_{sh}, which can either be equal to the sound speed, or supersonic. If the precompression front is supersonic, then it forms a shock front over which the fluid velocity is discontinuous. Once the fluid crosses the phase boundary, it is decelerated, and cooled.

If the deflagration is subsonic, then the fluid in the plasma frame is at rest inside bubble, in which case $\tilde{v}_- < c_{s-}$. On the other hand, if the bubble wall is moving supersonically, then the deflagration will be a Chapman-Jouguet deflagration, where $\tilde{v}_- = c_{s,-}$. This means that in the plasma rest frame, the fluid leaves the reaction front into the broken phase with a non-zero exit velocity. The exit velocity is larger for faster bubble walls. In a supersonic deflagration, the fluid decelerates in a rarefaction wave after entering the

bubble, eventually coming to a rest at $\xi = c_{s,-}$. As supersonic deflagrations have a leading precompression front, as well as a trailing pressure wave, they are sometimes referred to as hybrids.

The possibility of obtaining a supersonic deflagration in a physical transition is still debated [88, 111, 112]. It is possible to solve the junction conditions across the phase boundary for a bubble wall moving with a velocity between c_s and c_J, but this only shows that a static solution with that terminal wall velocity is possible. Numerical simulations of isolated expanding bubbles exploiting spherical symmetry have been conducted in Ref. [113]. Here the potential was modelled using the high temperature approximation in Eq. 3.5. The friction parameter $\eta(\phi, T, v_w)$ was taken to be a constant, and treated as a free parameter within the study. It was found that it was only for a very finely tuned region in η that the wall velocity corresponded to a supersonic deflagration. Typically the bubble wall velocity had a discontinuity in η corresponding $c_s \lesssim v_w \lesssim c_J$.

Interestingly, the existence of supersonic deflagrations appears to depend on the form of the potential and the equation of state in the model. To show this we perform a series of simulations of expanding isolated bubbles. The simulations evolve an initial bubble of the true vacuum using a spherical symmetric formulation of Eqs. 3.53–3.55. Following Ref. [113], $\eta(\phi, T, v_w)$ is taken to be a constant and treated as a free parameter. We study two different choices for the effective potential. The first is the high temperature approximation in Eq. 3.5 and the second is the bag model described at the end of Section 3.2.1. For each potential choice, we perform a scan across η for $\alpha_\theta = \{0.005,\ 0.05,\ 0.5\}$. After evolving the expanding bubble for $tT_c = 10000$, we estimate the terminal wall velocity v_w.

In Fig. 3.4, we show how v_w varies with η for each α_θ in both potential choices. For the high temperature approximation, when scanning across η there is a jump in the wall velocity that spans where supersonic deflagrations are expected. After checking fluid profiles it can also be seen that none of the resulting fluid flows have the features of supersonic deflagrations. On the other hand, in the bag model it can be seen that there are values of η which produce profiles with $c_s \leq v_w < c_J$. Upon inspection, these fluid profiles possess the features of supersonic deflagrations.

3.2.3 Energy budget

In a phase transition, potential energy is converted into thermal energy, kinetic energy in the fluid, and motion in the bubble wall. Taking the energy momentum tensor for the

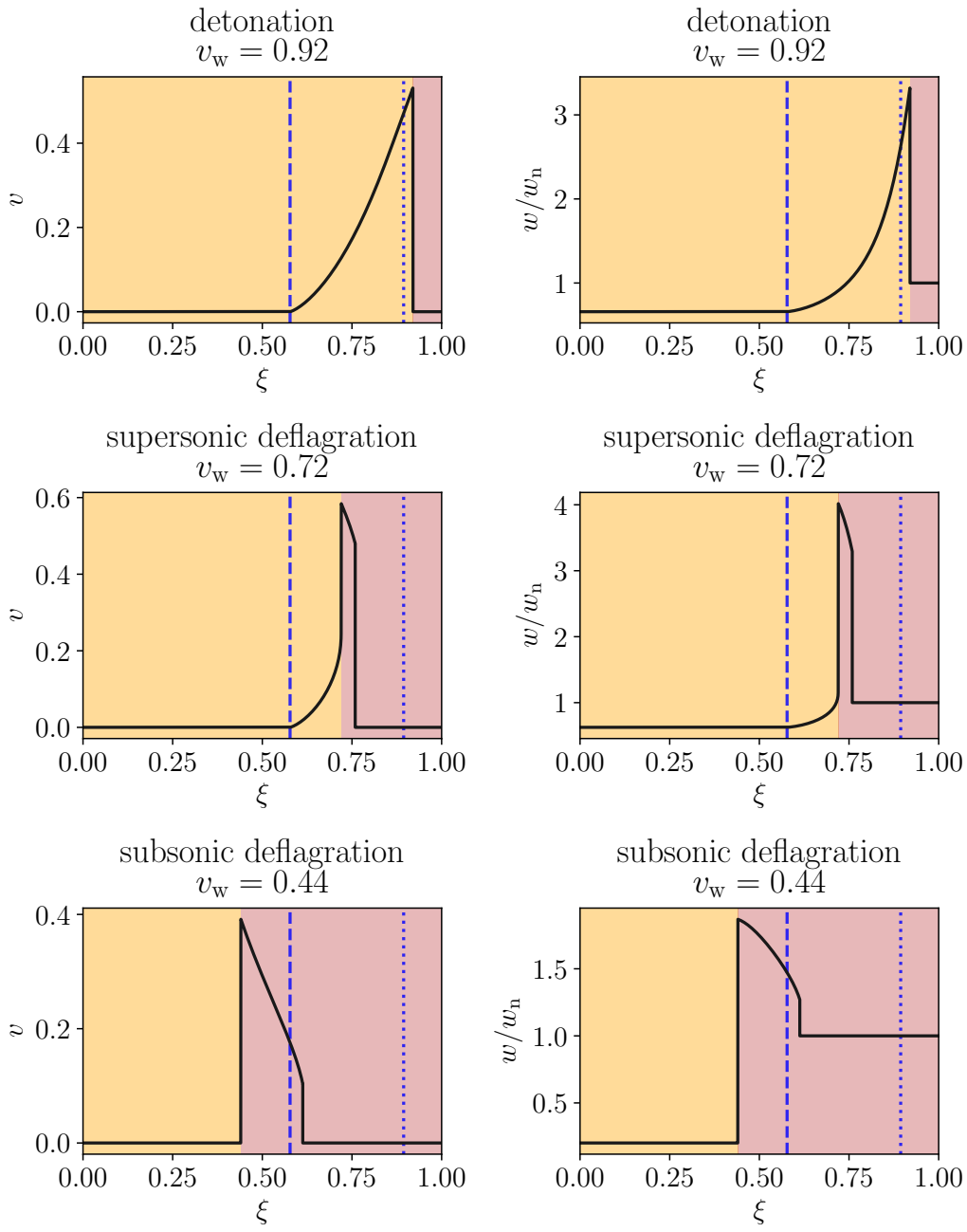

Figure 3.3: Asymptotic fluid profiles in the bag model for a transition with $\alpha_\theta = 0.5$. From top to bottom we show a detonation, a supersonic deflagration or hybrid, and a subsonic deflagration. The left panel shows the fluid velocity profile, and the right panel shows the enthalpy, normalised by the enthalpy at the nucleation temperature in the symmetric phase. The inside of the bubble is shaded in orange, whereas the outside is shaded red. The dashed vertical blue line indicates the speed of sound c_s, whereas the dotted vertical blue line shows the Chapman-Jouguet velocity c_J.

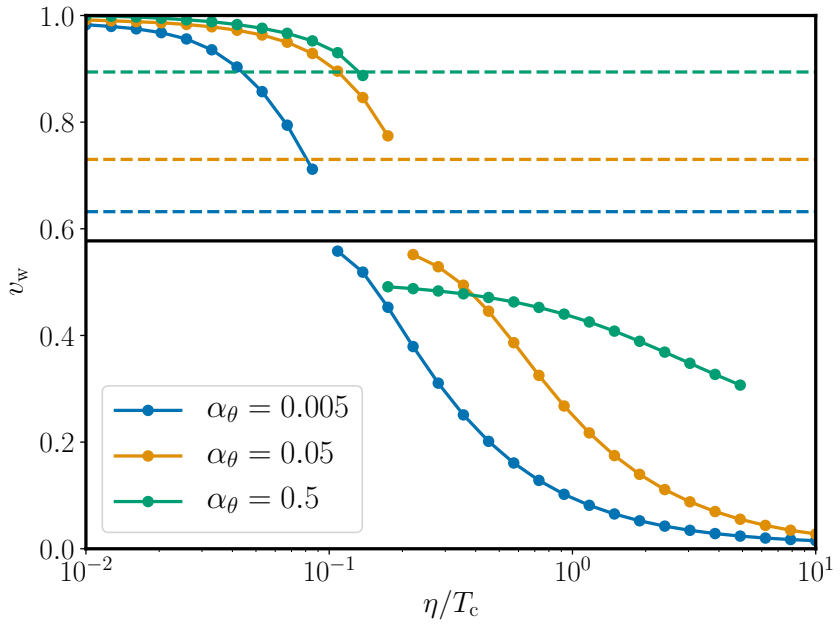

(a) High temperature approximation

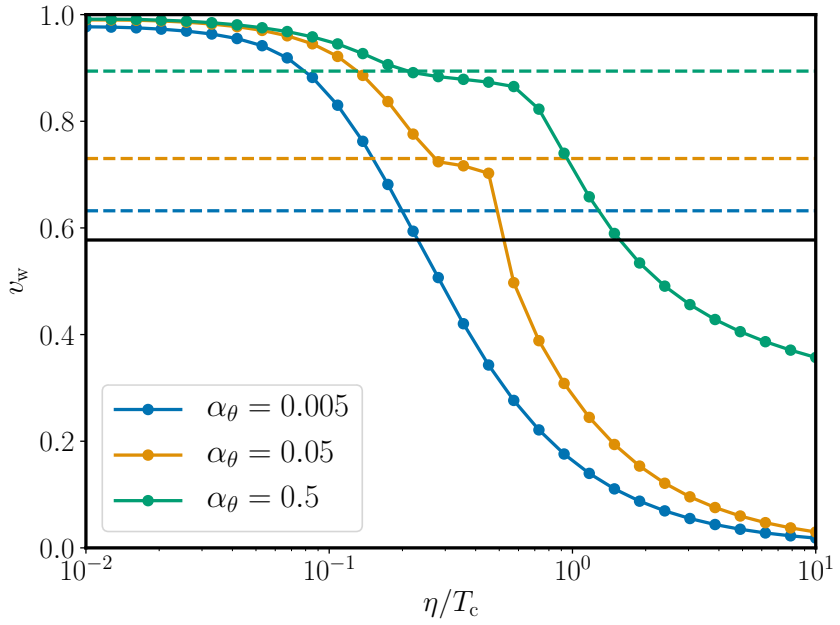

(b) Bag model

Figure 3.4: Wall velocities of expanding bubbles when using a constant friction parameter η. The top plot uses the high temperature approximation in Eq. 3.5 for the effective potential, whereas the bottom plot uses the bag model. The black solid lines show the speed of sound c_s and the dashed line coloured lines show the Chapman-Jouguet velocity c_J for each α_θ. The simulations used to obtain these results exploit a spherical symmetry. The lattice spacing is $\Delta x T_c = 0.5$, the timestep $\Delta t T_c = 0.05$. The wall velocity is calculated at $t T_c = 10000$, where t is the time after bubble nucleation.

combined field-fluid system given in Eq. 3.39, the energy density of the system is given by

$$T_{00} = w\gamma v^2 + \frac{3}{4}w + \theta + \frac{1}{2}\left((\dot{\phi})^2 + (\nabla\phi)^2\right). \tag{3.65}$$

From this we can identify the following constituents of the total energy density

$$e_{\mathrm{K}} = w\gamma v^2, \qquad e_{\mathrm{Q}} = \frac{3}{4}w, \qquad e_\theta = \theta, \qquad e_{\mathrm{D}} = \frac{1}{2}(\nabla\phi)^2, \qquad e_{\mathrm{F}} = \frac{1}{2}(\dot{\phi})^2. \tag{3.66}$$

Here e_{K} is the fluid kinetic energy density, e_{Q} the thermal energy density, e_θ the trace anomaly or potential energy density available in the transition, e_{D} the scalar field gradient energy, and e_{F} the scalar field kinetic energy. Both e_{D} and e_{K} will typically be associated with the bubble wall.

Conservation of energy dictates that the change in e_{Q}, e_{K}, e_{D} and e_{F} must come from the available potential energy in the trace anomaly. In other words,

$$\Delta e_{\mathrm{Q}} + \Delta e_{\mathrm{K}} + \Delta e_{\mathrm{D}} + \Delta e_{\mathrm{F}} = -\Delta e_\theta, \tag{3.67}$$

where Δe_i denotes the difference between the volume averaged energy density component measured shortly before the start of the transition and shortly after the transition completes. The kinetic energy in the fluid before the transition is close to zero, as the plasma is at rest. In thermal transitions in which the bubble wall reaches a terminal velocity before colliding, the energy deposited into the scalar field is negligible, such that Δe_{F} and Δe_{D} can be taken to be zero.

Understanding how the potential energy is distributed during the transition is important, as only the energy converted into fluid kinetic energy and gradients in the scalar field will contribute to producing a gravitational wave signal. This can be seen from considering the source of gravitational waves, the transverse-traceless projection of the energy momentum tensor T_{ij}^{TT}. Taking the energy momentum tensor in Eq. 3.39,

$$T_{ij}^{TT} = \Lambda_{ij,lm} T_{lm}, \tag{3.68}$$

$$= \Lambda_{ij,lm}\left(\partial_l\phi\partial_m\phi - \frac{1}{2}g_{lm}\partial_\rho\phi\partial^\rho\phi + wU_lU_m + g_{lm}p)\right), \tag{3.69}$$

$$= \Lambda_{ij,lm}\left(\partial_l\phi\partial_m\phi + wU_lU_m\right), \tag{3.70}$$

where in the last line we have exploited that $\Lambda_{ij,lm}$ removes the trace of T_{lm}. Motivated by the combination in Eq. 3.70, we refer to τ_{ij}^{ϕ} and τ_{ij}^{f} as source tensors for the scalar field and the fluid respectively, where

$$\tau_{ij}^{\phi} = \partial_i\phi\partial_j\phi, \qquad\qquad \tau_{ij}^{\mathrm{f}} = wU_iU_j. \tag{3.71}$$

Note that taking the trace of the source tensors results in $\tau_{ii}^{\phi} = 2e_{\rm D}$ and $\tau_{ii}^{\rm f} = e_{\rm K}$.

We therefore define efficiency factors for the transformation of potential energy into fluid kinetic energy, thermal energy, and gradient energy in the scalar field. These are correspondingly given as,

$$\kappa_{\rm f} = \frac{\Delta e_{\rm K}}{|\Delta e_\theta|}, \qquad \kappa_{\rm Q} = \frac{\Delta e_{\rm Q}}{|\Delta e_\theta|}, \qquad \kappa_\phi = \frac{2\Delta e_{\rm D}}{|\Delta e_\theta|}, \tag{3.72}$$

where the factor of two in κ_ϕ reflects that the trace of the scalar field source tensor is $\tau_{ii}^{\phi} = 2e_{\rm D}$. For thermal transitions with a terminal wall velocity, $\kappa_\phi \ll 1$ and $\kappa_{\rm f} + \kappa_{\rm Q} \simeq 1$.

The kinetic energy fraction in the fluid is given by,

$$K = \frac{e_K}{\bar{\epsilon}}, \tag{3.73}$$

with $\bar{\epsilon}$ the average internal energy density after the transition. An important quantity in determining the gravitational wave signal produced by the fluid is the enthalpy-weighted mean square fluid 4-velocity,

$$\overline{U}_{\rm f}^2 = \frac{e_{\rm K}}{\overline{w}}, \tag{3.74}$$

with $\overline{w}$ the mean enthalpy density after the transition. Note that $K = \Gamma \overline{U}_{\rm f}^2$, where $\Gamma = \overline{w}/\bar{\epsilon}$ is the mean adiabatic index of the fluid in the broken phase.

If the wall reaches a terminal velocity, it is possible to estimate $\Delta e_{\rm Q}$, $\Delta e_{\rm K}$ and Δe_θ from the asymptotic profile around an expanding bubble [65, 88]. Then,

$$\Delta e_{\rm Q} = 4\pi \int_0^{\xi_{\rm max}} d\xi \xi^2 \frac{3}{4}(w - w_{\rm n}), \tag{3.75}$$

$$\Delta e_{\rm K} = 4\pi \int_0^{\xi_{\rm max}} d\xi \xi^2 w \gamma v^2, \tag{3.76}$$

$$\Delta e_\theta = 4\pi \int_0^{\xi_{\rm max}} d\xi \xi^2 (\theta - \theta_n), \tag{3.77}$$

where the intergral is performed up to the location of the bubble wall or the precompression front, $\xi_{\rm max} = \max(v_{\rm w}, v_{\rm sh})$.

From the relations above, it is also possible to compute $\kappa_{\rm f}$, κ_Q and $\overline{U}_{\rm f}$ from the asymptotic fluid profiles. In Fig. 3.5, we show plot $\kappa_{\rm f}(\alpha_\theta, v_{\rm w})$ and $\overline{U}_{\rm f}(\alpha_\theta, v_{\rm w})$ as computed in the bag model from the asymptotic fluid profiles. The efficiency at which potential energy is converted into fluid kinetic energy grows with increasing α_θ. We also see that for a given value of α_θ, the kinetic efficiency increases towards intermediate values of $v_{\rm w}$, peaking for wall velocities corresponding to supersonic deflagrations. In the bag model, $\overline{U}_{\rm f}^2 = \frac{3}{4}\kappa_{\rm f}\alpha_\theta$ and so the behaviour of $\overline{U}_{\rm f}^2$ is similar to that of $\kappa_{\rm f}$, with an enhanced growth towards larger values of α_θ. As the energy in the bubble wall in negligible for thermal transitions with terminal wall velocities, the thermal energy efficiency can be found from $\kappa_{\rm Q} = 1 - \kappa_{\rm f}$.

It has been shown from simulations of weak and intermediate thermal transitions that the values of $\overline{U}_{\rm f}$ found after the transition agree well with those computed from the asymptotic fluid profile [62, 63].

3.2.4 Runaway and vacuum transitions

The dynamics of runaway and vacuum transitions differ substantially from thermal transitions with terminal wall velocities. In a vacuum transition, all of the available potential energy is converted into gradient and kinetic energy in the scalar field, in which case $\kappa_\phi \simeq 1$. Likewise, for runaway thermal transitions, a significant portion of the available potential energy is converted into the motion of the bubble wall.

The possibility of runaway thermal transitions was originally proposed in Ref. [89], where the friction on a bubble wall moving at ultra-relativistic speeds with $\gamma_{\rm w} = 1/\sqrt{1-v_{\rm w}^2} \gg 1$ was calculated to leading order. At leading order, the pressure due to the flux of particles crossing the bubble was found to tend to a constant as $\gamma_{\rm w} \to \infty$,

$$p_{\rm fr,lo} = \sum_i N_i \int \frac{d^3k}{(2\pi)^3 2E_i} f_i^{\rm eq}(E_i)\Delta m^2 \simeq \sum_i c_i \frac{N_i \Delta m^2 T^2}{24}. \tag{3.78}$$

Here the sum $\sum_i$ is over all particle types, N_i corresponds to the number of internal degrees of freedom, $\Delta m_i^2 = m_{{\rm b},i}^2 - m_{{\rm s},i}^2$ is the mass difference between broken and symmetric phase, $c_i = 1$ (1/2) for bosons (fermions), and the energy is given by $E_i = k^2 + m_{\rm s,i}^2$.

As the pressure restraining the wall reached an asymptotic value rather than growing with increasing $\gamma_{\rm w}$, for sufficiently strong transitions it would then be possible for the bubble wall to continue to accelerate until collision, with $\gamma_{\rm w} \to \infty$. Significant amounts of the available potential energy could then be converted into the motion of the bubble wall.

The question of runaway bubble walls was revisited in Ref. [87], where the next-to-leading order effect on the friction was calculated. The dominant higher order effect is transition radiation from gauge bosons when they gain a mass at the phase transition boundary. The next-to-leading order contribution is then

$$\gamma_{\rm w} p_{\rm fr,nlo} \simeq \gamma_{\rm w} \sum_{i\in V} N_i g_i^2 \Delta m_i T^3, \tag{3.79}$$

where $\sum_{i\in V}$ indicates a summation over all gauge bosons, and g_i are the respective gauge coupling constants. As the next-to-leading order friction contribution grows with $\gamma_{\rm w}$, in many situations the bubble wall will instead reach a finite wall velocity, rather than exhibiting runaway behaviour. If this occurs a negligible amount of the latent heat is turned into gradient energy in the scalar field, such that $\kappa_\phi \simeq 0$.

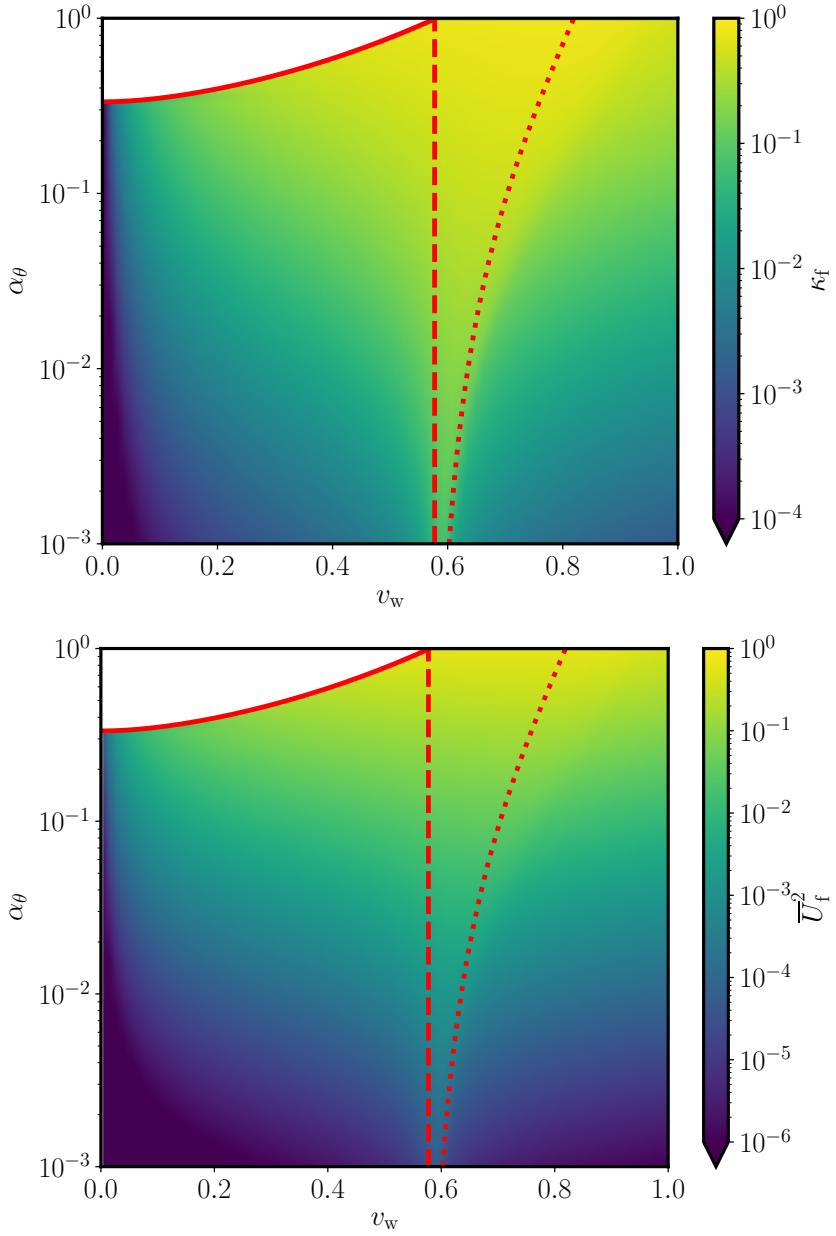

Figure 3.5: Variation of fluid kinetic energy efficiency, κ_f, and the enthalpy-weighted mean square fluid 4-velocity $\overline{U}_\mathrm{f}$ with the wall velocity v_w and transition strength α_θ. Both $\overline{U}_\mathrm{f}$ and κ_f have been calculated from the asymptotic fluid profile of an expanding bubble with strength α_θ and wall speed v_w. The bag model has been assumed in the calculation. Above the solid red line there are no solutions to the junction conditions across the bubble wall. The dashed red line indicates the speed of sound, c_s, which separates subsonic and supersonic deflagrations. The dotted red line indicates c_J, where fluid profiles with $c_\mathrm{J} \leq v_\mathrm{w}$ correspond to detonations.

Nonetheless, two possible scenarios have been proposed in which runaway behaviour may still occur in a thermal phase transition [90]. Firstly, if only scalars and fermions are involved in the transition radiation processes, then the next-to-leading order contribution to the friction would grow as at most $\ln\gamma$. This can occur if no gauge fields are present during the transition, such as during the spontaneous breaking of an approximate global symmetry in a hidden sector. In this case, it is possible that acceleration is able to continue until the eventual collision of the bubble walls. This possibility still needs to be investigated in specific models.

The other possibility is in the case of transitions with extreme supercooling, where $T_\mathrm{n} \ll \Delta m$. In this case, the next-to-leading order effect on the friction from the plasma may not be sufficient to hold back the bubble wall. This possibility has been investigated in detail for a variety of models [91].

In Ref. [91], the pressure difference across the wall was approximated by,

$$\Delta p = \Delta V - p_\mathrm{fr,lo} - \gamma_\mathrm{w} p_\mathrm{fr,nlo}, \tag{3.80}$$

where ΔV is the difference in the effective potential inside and outside the bubble wall. This approximation should be accurate provided $\Delta V > p_\mathrm{fr,lo}$.

The Lorentz factor corresponding to the terminal bubble wall velocity is then given by

$$\gamma_\mathrm{w,eq} = \frac{\Delta V - p_\mathrm{fr,lo}}{p_\mathrm{fr,nlo}}. \tag{3.81}$$

It was noted that, provided $\gamma_\mathrm{w} \gg 1$, the Lorentz factor corresponding to the terminal bubble wall velocity can be estimated to be

$$\gamma_\mathrm{w,eq} \simeq \frac{\alpha_\mathrm{V} - \alpha_\infty}{\alpha_\mathrm{eq}}, \tag{3.82}$$

where α_∞ and α_eq are the values of α_V at which ΔV is balanced by $p_\mathrm{fr,lo}$ and $p_\mathrm{fr,nlo}$ respectively. Note the absence γ_w from the next-to-leading order contribution. Estimates of α_∞ and α_eq are

$$\alpha_\infty \simeq \frac{p_\mathrm{fr,lo}}{\epsilon_\mathrm{r}}, \qquad\qquad \alpha_\mathrm{eq} \simeq \frac{p_\mathrm{fr,nlo}}{\epsilon_\mathrm{r}}. \tag{3.83}$$

With $\gamma_* \simeq R_*/2R_\mathrm{c}$ the typical expected Lorentz factor of the bubble wall upon collision when neglecting friction, it can be said that the runaway condition is fulfilled if $\gamma_* < \gamma_\mathrm{w,eq}$. In this case, the majority of the available potential energy is converted into the motion of the bubble wall. In the limit of $\gamma_w \gg 1$, the efficiency of converting potential energy into

gradient energy in the scalar field is [91],

$$\kappa_\phi \simeq \begin{cases} \dfrac{\gamma_{\rm w,eq}}{\gamma_*}\left[1-\dfrac{\alpha_\infty}{\alpha_{\rm V}}\left(\dfrac{\gamma_{\rm w,eq}}{\gamma_*}\right)^2\right], & \gamma_* > \gamma_{\rm w,eq}, \\ 1-\dfrac{\alpha_\infty}{\alpha_{\rm V}}, & \gamma_* \leq \gamma_{\rm w,eq}. \end{cases} \tag{3.84}$$

Therefore, for a given value of γ_*, there is a corresponding transition strength at which the runaway condition is fulfilled and κ_ϕ becomes substantial. However, the transition strength is not able to grow without limit for any given model. As mentioned in Section 3.1, if the vacuum energy begins to dominate then the universe in the metastable phase begins to inflate and the percolation of bubbles and completion of the phase transition is not guaranteed. For most models with a first-order thermal transition, there exists a maximal value of the transition strength for which percolation of the bubbles is possible [98]. For transition strengths above this maximal value, the vacuum energy dominates, the universe in the metastable phase expands faster than bubbles of the true vacuum can nucleate and the transition never completes.

The maximal value of the transition strength for many models is far below that at which runaway behaviour occurs and κ_ϕ becomes non-negligible. A class of models in which extremely large values of $\alpha_{\rm V}$ are attainable is the set of models with an approximate conformal symmetry. One result in Ref. [91] was that runaway behaviour could be achieved for a classically scale-invariant $U(1)_{\rm B-L}$ extension of the Standard Model, with $\kappa_\phi \simeq 1$ for sufficiently large $\alpha_{\rm V}$.

The dynamics of vacuum transitions and runaway thermal transitions with $\kappa_\phi \simeq 1$ are substantially different to that of thermal transitions with a terminal wall velocity. In this case, fluid effects can be neglected and only the scalar field dynamics need to be considered. After nucleation, the bubble will expand and reach ultra-relativistic speeds before collision. The vast majority of the energy density of the bubble will be located at phase boundary, which will be extremely thin relative to the radius of the bubble wall when it collides.

The dynamics of the scalar field upon collision has been studied previously through simulations of two colliding vacuum bubbles [55, 114–117]. When bubbles collide, the scalar field in the overlap region may rebound over the potential barrier and into the false vacuum. Whether this rebound occurs and the size of the rebound depends on the shape of the potential [115, 116], as well as the value of $\gamma_{\rm w}$ at collision. Waves of scalar field radiation are also dispersed from the collision region.

The so-called envelope approximation is often used to model the dynamics of the

scalar field during collisions when calculating the gravitational wave signal [57]. In the envelope approximation, the energy-momentum of the scalar field is modelled as being localised to an infinitesimally thin shell located at the bubble wall. Upon collision, the energy-momentum in the scalar field is assumed to disappear in the overlap region. This approximation is used frequently despite the dynamics described above. In Fig. 3.6 we depict the difference between the envelope approximation and a lattice simulation of a vacuum transition performed in Ref. [1].

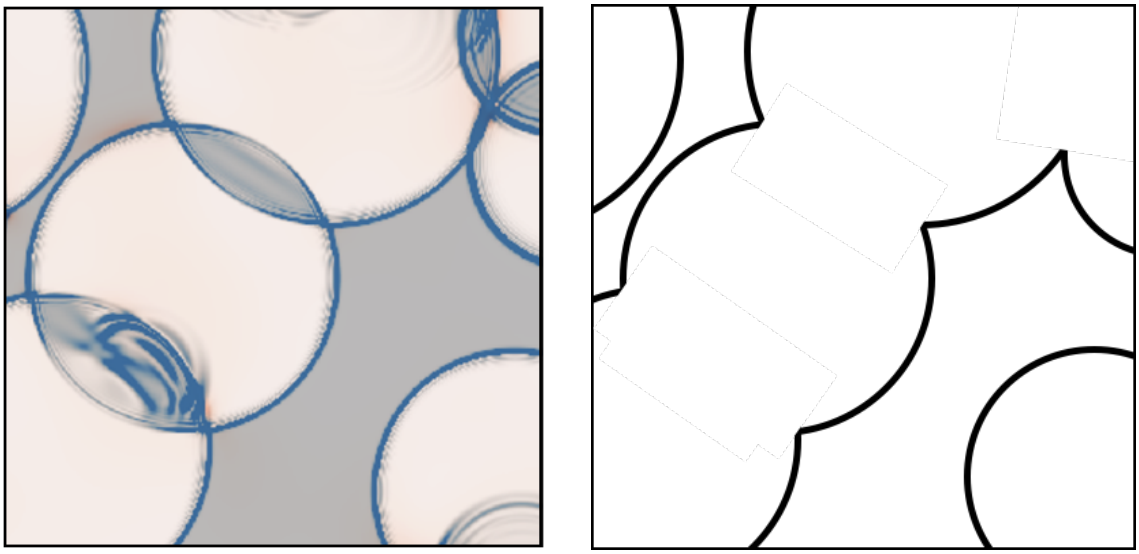

(a) Lattice simulation **(b)** Envelope approximation

Figure 3.6: Diagrams showing the difference in behaviour of the scalar field energy in a lattice simulation from Ref. [1] and the envelope approximation. In the left diagram we show a slice through a lattice simulation of a vacuum transition, where increasing values of the energy density are shown as varying from white to blue. In the right diagram, we show the behaviour of the energy density in the envelope approximation, where black lines indicate the location of infinitesimally thin shells of energy.

Lattice field theory simulations of many bubble collisions were conducted in Ref. [118]. In addition to the deviation from the envelope approximation in the overlap region, they also noticed that the scalar field continued to oscillate for a substantial time after all of the collisions had been completed. They dubbed this as a coalescence period after the completion of the transition and stated it had an important effect of the generation fo gravitational waves.

3.3 Gravitational wave signatures

The sources of gravitational wave generation during a first-order phase transition can be roughly split into three different processes. The first source of gravitational waves comes directly from the collision of bubble walls. When the bubble walls collide, spherical symmetry is broken and the shear-stress in the gradients of the scalar field source gravitational waves. This is typically a short lived source of gravitational waves.

In thermal phase transitions fluid shells develop around the bubble wall due to interactions between the scalar field and the plasma. After the bubble walls collide, these fluid shells continue to propagate in the form of sound waves. The shear-stress in the plasma sound waves is then a long lasting source of gravitational waves.

In addition to the generation of sound waves, thermal phase transitions may create turbulent flows. In the presence of a magnetic field, this could lead to magnetohydrodynamic turbulence. Both kinetic and magnetohydrodynamic turbulence can be sources of gravitational waves.

These sources may coexist, or form the dominant source at different stages of the phase transition. The total stochastic background should be approximately a linear superposition of the gravitational waves sourced by each of these processes,

$$\Omega_{\rm gw} \approx \Omega_{\phi} + \Omega_{\rm sw} + \Omega_{\rm turb}, \tag{3.85}$$

where Ω_{ϕ} is generated by colliding bubble walls, $\Omega_{\rm sw}$ by sound waves, and $\Omega_{\rm turb}$ by (magneto)hydrodynamic turbulence. The two LISA Cosmology Working Group reports on first-order phase transitions are excellent reviews for the generation of gravitational waves from each source [77, 90].

Two important parameters in deducing the peak frequency and amplitude of the gravitational wave power spectrum are the transition temperature at which gravitational waves are emitted T_* and the corresponding value of Hubble parameter H_*. Providing the transition is sufficiently fast, $T_* \simeq T_{\rm n}$ and $H_* \simeq H_{\rm n}$ are good approximations, and frequently taken.

The gravitational wave energy density after production is diluted during the expansion of the universe as radiation, such that $\rho_{\rm gw} \propto a^{-4}$, and the frequency of the radiation redshifts as a^{-1}. If the universe has expanded adiabatically since the phase transition, the entropy per comoving volume $S \propto a^3 g_s(T) T^3$ remains constant, where $g_s(T)$ are the effective entropic degrees of freedom at temperature T. Then the ratio of the scale factor

at the transition to the scale factor today is given by

$$\frac{a_*}{a_0} = \left(\frac{g_{s0}}{g_{s*}}\right)^{1/3} \frac{T_0}{T_s*}, \tag{3.86}$$

where subscripts 0 and $*$ correspond to quantities evaluated today and at the time of gravitational wave production respectively.

The gravitational wave energy density parameter at present day $\Omega_{\rm gw,0}$ can therefore be computed from $\Omega_{\rm gw}$ at the time of the transition through the relation

$$\Omega_{\rm gw,0} = \left(\frac{a_*}{a_0}\right)^4 \left(\frac{\rho_{c*}}{\rho_{c0}}\right)^2 \Omega_{\rm gw}, \tag{3.87}$$

$$= \Omega_{\rm rad,0} \frac{g_*}{g_0} \left(\frac{g_{s0}}{g_{s*}}\right)^{4/3} \Omega_{\rm gw}. \tag{3.88}$$

In the above equations, $\Omega_{\rm rad} = \rho_{\rm rad}/\rho_c$ is the radiation energy density parameter. We have also used that $\rho_{c*} \simeq \rho_{{\rm rad},*}$ for transitions occurring in the radiation era, and that the radiation energy density is given by $\rho_{\rm rad} = \pi^2 g T^4/30$. Taking the Plank best-fit value for $H_0 = 67.8 \pm 0.9\,{\rm km\,s^{-1}\,Mpc^{-1}}$ [119], the FIRAS temperature for the CMB $T_{\gamma,0} = 2.725 \pm 0.002\,{\rm K}$ [120], and setting $g_{s*} = g_*$, $g_0 = 2$, and $g_{s0} = 3.91$, we have

$$\Omega_{\rm gw,0} = (3.57 \pm 0.05) \times 10^{-5} \left(\frac{100}{g_*}\right)^{1/3} \Omega_{\rm gw}. \tag{3.89}$$

The peak frequency of the gravitational wave power spectrum $f_{\rm p}$ will also redshift from the time of production until today,

$$f_{\rm p,0} = f_{\rm p,*} \frac{a_*}{a_0}, \tag{3.90}$$

$$= 1.65 \times 10^{-7}\,{\rm Hz}\, \frac{f_{\rm p,*}}{H_*} \left(\frac{g_*}{100}\right)^{1/6} \frac{T_*}{1{\rm GeV}}. \tag{3.91}$$

3.3.1 Scalar field

The scalar field contribution to the gravitational wave power spectrum is often modelled using the envelope approximation [56–59, 66, 121, 122]. In the envelope approximation, the bubble walls are treated as infinitesimally thin and in regions where bubbles overlap the behaviour of the scalar field is completely ignored. The shear-stress of the bubble is considered to be located in the infinitesimally thin shells concentrated at the uncollided bubble walls. Bubble walls in the envelope approximation are set to expand at a constant velocity, which can be ultra-relativistic.

The envelope approximation has been studied using both numerical simulations [56–59, 66] and analytical techniques [121]. The most recent numerical study found that the

gravitational wave power spectrum emerging from the envelope approximation is given by [122]

$$\Omega_{\rm env,0}(f) = 3.63\times10^{-5}\Delta_{\rm env}\kappa^2\left(\frac{H_*}{\beta}\right)^2\left(\frac{\alpha_{\rm V}}{\alpha_{\rm V}+1}\right)\left(\frac{100}{g_*}\right)^{1/3}P_{\rm env}(f), \tag{3.92}$$

where $P_{\rm env}$ corresponds to the spectral shape of the power spectrum, $\Delta_{\rm env}$ is a function of the wall velocity, and κ corresponds to the efficiency in which vacuum energy is converted into energy density in the shell located at the bubble wall. The spectral shape is

$$P_{\rm env}(f) = \frac{(a+b)f_{env,0}^b f^a}{bf_{env,0}^{a+b}+af^{a+b}}, \tag{3.93}$$

where $f_{env,0}$ corresponds to the peak frequency of the spectrum today. This is given by

$$f_{env,0} = 2.62\times10^{-8}{\rm Hz}\left(\frac{f_{\rm env,*}}{\beta}\right)\left(\frac{\beta}{H_*}\right)\left(\frac{T_*}{1{\rm GeV}}\right)\left(\frac{g_*}{100}\right)^{1/6}. \tag{3.94}$$

The dependence of the peak frequency and peak amplitude of the gravitational wave power spectrum on the wall velocity is given by

$$\Delta_{\rm env} = \frac{0.44v_{\rm w}^3}{1+8.28v_{\rm w}^3}, \qquad f_{\rm env,*} = \frac{1.96}{1-0.051v_{\rm w}+0.88v_{\rm w}^2}. \tag{3.95}$$

The power law exponents in the spectral shape also depend on the wall velocity. If the bubble wall is extremely ultra-relativistic such that $v_{\rm w}\simeq1$, the power law exponents fitted by the data are $a=2.9$ and $b=0.9$. On the other hand, if $v_{\rm w}\ll1$, the power law exponents are $a=2.95$ and $b=1$.

The envelope approximation has historically been applied to gravitational waves sourced by a fluid, in which case $\kappa=\kappa_{\rm f}$, and to the gravitational waves sourced by the scalar field, in which case $\kappa=\kappa_\phi$. However, simulations of weak and intermediate thermal transitions shown that the envelope approximation does not accurately predict the gravitational waves sourced by the fluid [60]. The fluid contribution is better modelled as overlapping sound waves rather than infinitesimal shells of shear stress [64, 65]. The envelope approximation, therefore, is typically only used to model the contribution of the scalar field to the gravitational wave power spectrum, in which case $\Omega_\phi=\Omega_{\rm env}|_{\kappa=\kappa_\phi}$.

For thermal transitions in which the bubble wall reaches a finite velocity, it has been shown that the envelope approximation models the scalar field contribution to gravitational waves very accurately [66]. In these transitions, the amount of latent heat that is converted into scalar field gradient energy is negligible, and so $\kappa_\phi\ll1$ and $\Omega_\phi\ll\Omega_{\rm gw}$.

For vacuum transitions, the available vacuum energy is predominantly deposited into the gradients and kinetic energy of the scalar field. In this case $\kappa_\phi\simeq1$ and $\Omega_{\rm gw}\simeq\Omega_\phi$. For runaway thermal transitions, κ_ϕ can also be substantial and even approach unity, and

as such the contribution of the scalar field to the gravitational wave power cannot be neglected. In both these scenarios the bubble wall accelerates until collision, with $v_{\rm w} \simeq 1$. However, there have been limited tests for whether the envelope approximation applies within this regime.

One of the few studies of many bubble collisions in a vacuum transition using lattice field theory simulations showed a deviation from the envelope approximation [118]. In these simulations, two distinct phases were identified, a collision phase and a subsequent coalescence phase where the scalar field oscillates while relaxing into the true vacuum. It was shown that the gravitational wave spectrum produced during the collision phase was between two and three orders of magnitude smaller than the envelope approximation. There was no discussion of the UV power law, but it can be seen to be less steep than f^{-1}. During the coalescence phase it was claimed that gravitational waves continue to be sourced. The power spectrum was claimed to be amplified during the coalescence phase by more than an order of magnitude, with power deposited in higher frequency modes than those generated during bubble collisions.

We dispute the claims made in Ref [118] in Chapter 4 which contains the first paper of this thesis. In this paper, we test the envelope approximation for runaway and vacuum transitions and perform an investigation into the emergence of a coalescence phase and the effect it could have on the gravitational wave power spectrum. We do this by performing lattice field theory simulations of the collision of many vacuum bubbles in a transition with a quartic potential.

Other approximations for the gravitational wave production from the scalar field include the bulk flow model. Originally proposed as an extension to the envelope approximation [123], the bulk flow model modifies the behaviour of the infinitesimal shells of energy density after collision. Instead of disappearing immediately upon collision, the energy density in each shell subsequently decays with a characteristic timescale τ, where τ in principal depends on the source being modelled and the particle physics model. The envelope approximation then corresponds to setting $\tau = 0$, and free propagation of the shell after collision to $\tau = \infty$. Increasing τ has been shown analytically to decrease the infrared power law exponent from $a \simeq 3$ [123].

Numerical simulations of the bulk flow model with $\tau = \infty$ have also been conducted [122]. The gravitational wave power spectrum was found to be of the same form as Eq. 3.92, in which the dependence on the wall velocity was modified such that

$$\Delta_{\rm env} \to \Delta_{\rm bf} = \frac{0.0866 v_{\rm w}^3}{1 + 3.54 v_{\rm w}^3}, \qquad f_{{\rm env},*} \to f_{{\rm bf},*} = \frac{1.24}{1 - 0.047 v_{\rm w} + 0.58 v_{\rm w}^2}. \tag{3.96}$$

The power law exponents were also modified in comparison to the envelope approximation. When $v_{\rm w} \simeq 1$, the power law exponents fitted by the data are $a = 0.9$ and $b = 2.1$. For $v_{\rm w} \ll 1$, the exponents are instead $a = 0.95$ and $b = 2.9$.

Like the envelope approximation, the bulk flow model can in principle be applied to modelling the gravitational waves produced from the cosmic plasma in a thermal transition or those sourced from the scalar field driving the transition. It has been suggested that the gravitational wave power spectrum for vacuum and runaway transitions can depend on the shape of the effective potential [116]. In particular, behaviour like that seen in the bulk flow model might occur when the potential energy difference is large compared to the barrier between vacua. This is investigated in Chapter 5, in which a deeper exploration of the parameter space for the collision of many vacuum bubbles in a transition with a quartic potential is conducted.

3.3.2 Acoustic

During thermal phase transitions, the cosmic plasma is perturbed by the motion of the bubble walls. Fluid shells form around the expanding bubble walls, propagating either as subsonic deflagrations, hybrids, or detonations. After the bubbles have collided, these fluid shells continue to propagate, initially in the form of sound waves.

The transverse-traceless shear-stress in the sound waves source gravitational waves. The sound waves can continue to propagate in the fluid for a long time after the transition completes, and as such this acoustic phase can generate a substantial gravitational wave signal [60, 62, 63]. It is expected that eventually the sound waves will decay through the formation of shocks [124]. The shock formation time can be estimated to be $\tau_{\rm sh} \sim L_{\rm f}/\overline{U}_{\parallel}$, where $L_{\rm f}$ is the characteristic length scale of the sound waves and $\overline{U}_{\parallel}$ and $\overline{U}_{\perp}$ are the longitudinal and rotational projections of $\overline{U}_{\rm f}$. Note $\overline{U}_{\rm f}$ is originally defined in Eq. 3.74.

From simulations of weak and intermediate strength thermal transitions, it has been shown that the typical length scale of the sound waves resulting from a first-order phase transition is approximately the mean bubble separation, R_*, and that $\overline{U}_{\perp}$ is small after the transition [62, 63]. For the transition strengths considered, $\tau_{\rm sh}$ was much smaller than the duration of the simulations. Therefore, the formation of shocks and decay of sound waves after a first-order transition was not observed. It has been shown for a wide range of models with first-order phase transitions that typically $\tau_{\rm sh} < H_*^{-1}$ [125].

The gravitational wave power produced from sound waves is given by [62]

$$\Omega_{\rm sw} = 3\Gamma^2 \overline{U}_{\parallel}^4 \, (H_* \tau_v) \, (H_* \tau_{\rm c}) \, \tilde{\Omega}_{\rm gw}, \tag{3.97}$$

where $\tau_{\rm c}$ is the autocorrelation time of the source, $\tau_{\rm v}$ is the effective lifetime of the source and $\tilde{\Omega}_{\rm gw}$ is a dimensionless number that depends on the shape of the gravitational wave power spectrum.

Note that for sources that persist for longer than a Hubble time, the effective lifetime of the source is precisely H_*^{-1} due to the combination of expansion damping and decorrelation of the shear-stress [62]. Numerical simulations of weak and intermediate transitions have found that $\tilde{\Omega}_{\rm gw} \simeq 10^{-2}$. While the exact nature of the decay of sound waves needs further study, a conservative estimate for the source lifetime is $\tau_{\rm v} = \min(H_*^{-1}, \tau_{\rm sh})$. The autocorrelation time for sound waves is given by the sound-crossing time fo the flow length scale, $\tau_{\rm c} \sim R_*/c_{\rm s}$.

The LISA Cosmology Working Group reports [77, 90] provide an ansatz for the gravitational wave power spectrum produced from sound waves. The ansatz is based on the results of numerical simulations of weak and intermediate strength thermal transitions [62, 63]. These simulations use simultaneous nucleation, but it is expected they can be used to estimate the spectrum from exponential nucleation using Eq. 3.25 to convert R_* into β. The ansatz predicts that the gravitational wave spectrum from sound waves creates a broken power law, such that the present day spectrum is given by

$$\frac{d\Omega_{\rm sw,0}}{d\ln(f)} = 7.34 \times 10^{-5} \Gamma^2 \overline{U}_{\rm f}^4 \left(\frac{100}{g_*}\right)^{1/3} (H_* \tau_v) \left(\frac{H_* R_*}{c_{\rm s}}\right) \tilde{\Omega}_{\rm gw} C \left(\frac{f}{f_{\rm sw,0}}\right), \tag{3.98}$$

where the spectral shape is determined through,

$$C(s) = s^3 \left(\frac{7}{4+3s^2}\right)^{7/2}, \tag{3.99}$$

and the peak frequency at present day is

$$f_{\rm sw,0} \simeq 2.6 \times 10^{-7}\,{\rm Hz} \left(\frac{1}{H_* R_*}\right) \left(\frac{z_{\rm p}}{10}\right) \left(\frac{T_*}{1{\rm GeV}}\right) \left(\frac{g_*}{100}\right)^{1/6}. \tag{3.100}$$

The quantity $z_{\rm p}$ accounts for the location of the peak of the spectrum in kR_*, where in simulations it has been seen $z_{\rm p} \simeq 10$. When calculating the spectrum arising from sound waves for a transition in a particular particle physics model, $\overline{U}_{\rm f}$ is typically calculated from the asymptotic fluid profile for a bubble with a given wall speed and transition strength, as outlined in Section 3.2.3.

The behaviour of the sound waves has also been analytically studied using the sound shell model [64, 65]. In the sound shell model, the sound waves are treated as a superposition of overlapping fluid shells produced during the bubble expansion. The velocity power spectrum $\mathcal{P}_v$ takes the shape of a double broken power law with two length scales,

R_* and the thickness of the fluid shell at collision ΔR_*. The velocity power spectrum from transitions in the sound shell model follows

$$\mathcal{P}_v(k) \sim \begin{cases} (kR_*)^5, & k\Delta R_*, kR_*, \ll 1, \\ (kR_*)^1, & k\Delta R_* \ll 1 \ll kR_*, \\ (kR_*)^{-1}, & k\Delta R_*, kR_* \ll 1. \end{cases} \tag{3.101}$$

For a velocity power spectrum that goes as k^n, the gravitational wave power spectrum goes as k^{2n-1}. Therefore in the sound shell model,

$$\frac{d\Omega_{\rm sw}}{d\ln(k)} \sim \begin{cases} (kR_*)^9, & k\Delta R_*, kR_*, \ll 1, \\ (kR_*)^1, & k\Delta R_* \ll 1 \ll kR_*, \\ (kR_*)^{-3}, & k\Delta R_*, kR_* \ll 1. \end{cases} \tag{3.102}$$

These predictions match well to the numerical simulations conducted in Refs. [62, 63].

In Chapter 6, we perform the first 3D numerical simulations of strong thermal phase transitions. Prior to this, the results of weak and intermediate transitions had been used to extrapolate to larger transition strengths. We investigate the validity of this approach for strong transitions. In particular we test whether $\overline{U}_{\rm f}$ after the transition matches that predicted from the asymptotic fluid profile.

3.3.3 Turbulence

After a thermal phase transition, some of the kinetic energy may be in vortical modes, which can also source gravitational waves. Furthermore, it is possible further vorticity may be generated during the decay of sound waves as a result of non-linear effects such as the appearance of shocks.

The kinetic Reynolds number corresponds to the ratio of inertial to viscous forces and is given by $R_{\rm k} = vL_{\rm f}/\nu_{\rm k}$, where v is the fluid velocity, $L_{\rm f}$ the characteristic length scale in the fluid flow, and $\nu_{\rm k}$ is the kinematic viscosity. For low kinetic Reynolds numbers, viscous forces dominate and smooth laminar flows are expected, whereas at high kinetic Reynolds numbers chaotic turbulent flows predicted. The plasma in the early universe has a very high kinetic Reynolds number, on the order of 10^{13} during the electroweak epoch, and so turbulence is expected to develop after the sound waves decay [70]. The magnetic Reynolds number is given by $R_{\rm m} = vL_{\rm f}/\nu_{\rm m}$, with $\nu_{\rm m}$ the magnetic diffusivity. This is an analogue to the kinetic Reynolds number and gives an estimate of the relative effects of induction of a magnetic field in a flow compared to magnetic diffusion. $R_{\rm m}$ is

also very high in the early universe and so if a seed magnetic field is present before the transition, or the collision of bubbles themselves generate a magnetic field [126–130], then MHD turbulence is expected to develop.

Kinetic energy is injected into the fluid at the length scale associated with the mean bubble separation, $L_{\rm f} \simeq R_*$. A turbulent cascade should then set in after an eddy turnover time at this length scale, $\tau_{\rm turb} \sim L_{\rm f}/\overline{U}_\perp$. After the bubbles finish colliding, no more energy is injected at $L_{\rm f}$, and as such the turbulence decays. The turbulent flow will dissipate once the kinetic Reynolds number becomes of order one at the length scale of the fluid flow. It has been shown that this can occur over the course of many Hubble times [70], making the effective source lifetime $\tau_v \simeq H_*^{-1}$. The autocorrelation time of the fluid flow at a given length scale L is set by the eddy turn-over time at that scale, which for the intergral length scale corresponds to $\tau_{\rm turb}$.

If the turbulent flow lasts much longer than a Hubble time, with the autocorrelation time set to $\tau_{\rm c} = \tau_{\rm turb}$, the gravitational wave power should scale according to [90]

$$\Omega_{\rm turb} \propto \overline{U}_\perp^3 \, (H_* R_*) \, . \tag{3.103}$$

If the turbulence lifetime is instead much less than the Hubble time at nucleation, then the corresponding timescales are $\tau_{\rm v} \sim \tau_{\rm c} \sim \tau_{\rm turb}$ [70], and so

$$\Omega_{\rm turb} \propto \overline{U}_\perp^2 \, (H_* R_*)^2 \, . \tag{3.104}$$

The precise form of the gravitational wave power spectrum arising from a turbulent flow depends on the nature of the turbulent decay. Semi-analytic studies depend on assumptions both of a theoretical turbulence model and on a choice for the unequal-time correlators of the gravitational wave source. Typically, Kolmogorov turbulence [131] is taken to be the theoretical model (see e.g [58, 69, 70, 132, 133]) and the time dependence is modelled with the Gaussian Kraichnan decorrelation function [134]. Ref. [70] was used in the first LISA Cosmology Working Group report when modelling the gravitational wave source arising from a turbulent flow. In Ref. [70], Kolmogorov turbulence is assumed as the theoretical turbulence model, while the decorrelation is modelled using a top hat correlator that mimics the Gaussian Kraichnan decorrelation behaviour. The turbulence source was found to last many Hubble times, matching with the scaling relation in Eq. 3.103.

The contribution of MHD turbulence to the gravitational wave power spectrum was found to be

$$\frac{d\Omega_{\rm turb,0}}{d\ln(f)} = 7.29 \times 10^{-4} \left(\frac{H_*}{\beta}\right) \left(\frac{\kappa_{\rm turb}\alpha_\theta}{1+\alpha_\theta}\right)^{3/2} \left(\frac{100}{g_*}\right)^{1/3} v_{\rm w} S_{\rm turb}(f), \tag{3.105}$$

where $\kappa_{\rm turb} = \epsilon_{\rm turb}\kappa_{\rm f}$ is the efficiency of converting potential energy into turbulent kinetic energy and $S_{\rm turb}(f)$ dictates the spectral shape,

$$S_{\rm turb}(f) = \frac{(f/f_{\rm turb,0})^3}{(1+f/f_{\rm turb,0})^{11/3}\,(1+8\pi f/h_*)}. \tag{3.106}$$

Here $h_* = 1.6\times10^{-6}(T_*/1{\rm GeV})(g_*/100)^{1/6}$ is the Hubble parameter redshifted to today and the frequency $f_{\rm turb,0}$ is given by

$$f_{\rm turb,0} = 2.7\times10^{-7}{\rm Hz}\frac{1}{v_{\rm w}}\left(\frac{\beta}{H_*}\right)\left(\frac{T_*}{1{\rm GeV}}\right)\left(\frac{g_*}{100}\right)^{1/6}. \tag{3.107}$$

The shape of the power spectrum has the causal slope of $S(f)\propto f^3$ for frequencies smaller than h_*, while for $h_* \lesssim f \lesssim f_{\rm turb,0}$ the spectrum goes as $S(f)\propto f^2$. At large frequencies $f \gg f_{\rm turb,0}$, the shape is determined by the Kolmogorov turbulence model, such that $S(f)\propto f^{-5/3}$.

Note that helical turbulence was not considered as a possibility in Ref. [70], but it is has been shown that this can produce a polarised gravitational wave signal [135]. A detailed study of flows with both compressional and rotational modes and considering both helical and non-helical magnetic fields was performed in Ref. [72]. In Ref. [72], it was argued that the top hat decorrelator was unphysical and overproduces gravitational waves by up to an order of magnitude. Instead, the velocity decorrelation was modelled by the Kraichnan random sweeping hypothesis, where small scale fluctuations are advected by a large scale velocity field. It also investigated how the rotational and compressional modes may interact with each other and affect the resulting gravitational wave signal. The power laws of the spectrum and the peak shapes found in Ref. [72] depended on the fractional energy in rotational modes, $\epsilon_{\rm turb}$.

There have also been recent direct numerical simulations of the gravitational wave power spectrum arising from freely decaying (M)HD turbulence [73]. The simulations studied fully kinetic, helical, and non-helical turbulence. While the unequal-time correlators of the flow were not measured during these simulations, it was shown that at high frequencies $d\Omega_{\rm gw}/d\ln(f)\propto f^{-8/3}$. Furthermore, there were some indications that turbulent flows may be less efficient at producing gravitational waves that sound waves.

The initial proportion of the kinetic energy converted into vortical motion, $\epsilon_{\rm turb} = \overline{U}_\perp^2/\overline{U}_{\rm f}^2$, has been found to be on the order of $\epsilon_{\rm turb}\sim 0.05$ in simulations of weak and intermediate phase transitions [62, 63]. It is expected that $\epsilon_{\rm turb}$ may well be larger for stronger transitions and non-linear effects such as the formation of shocks may further increase the proportion or kinetic energy in turbulent flows. The efficiency of generating turbulent kinetic energy from decaying sound waves is an ongoing area of study.

In Chapter 6, we attempt to advance the understanding of the generation of rotational fluid flows from a first-order phase transition by performing the first simulations of strong phase transitions. We pay particular attention to how ϵ_{turb} depends on the wall velocity and transition strength.

Chapter 4

Gravitational waves from vacuum first-order phase transitions: from the envelope to the lattice

Daniel Cutting[a,b], Mark Hindmarsh[b] and David Weir[b]

[a] *Department of Physics and Astronomy, University of Sussex, Falmer, Brighton, BN1 9QH, U.K.*

[b] *Department of Physics and Helsinki Institute of Physics, PL 64, FI-00014, University of Helsinki, Finland*

Abstract

We conduct large scale numerical simulations of gravitational wave production at a first-order vacuum phase transition. We find a power law for the gravitational wave power spectrum at high wavenumber which falls off as $k^{-1.5}$ rather than the k^{-1} produced by the envelope approximation. The peak of the power spectrum is shifted to slightly lower wave numbers from that of the envelope approximation. The envelope approximation reproduces our results for the peak power less well, agreeing only to within an order of magnitude. After the bubbles finish colliding the scalar field oscillates around the true vacuum. An additional feature is produced in the UV of the gravitational wave power spectrum, and this continues to grow linearly until the end of our simulation. The additional feature peaks at a length scale close to the bubble wall thickness and is shown to have a negligible contribution to the energy in gravitational waves, providing the scalar field mass is much smaller than the Planck mass.

4.1 Introduction

The first direct detection of gravitational waves [74, 136] has brought in a new era of gravitational wave astronomy. Future space based gravitational wave observatories such as LISA [137] hold great promise for cosmology [76]. LISA's planned sensitivity band peaks at lower frequencies than ground based detectors. It therefore will have much greater sensitivity to gravitational waves originating from process in the very early universe. Cosmological first-order phase transitions are one such process, and LISA's sensitivity window allows it to probe electroweak phase transitions in many extensions of the Standard Model [77, 138].

In a cosmological first-order phase transition, the universe changes from a metastable high energy (symmetric) phase to a stable lower energy (broken) phase. This occurs through the quantum or thermal nucleation of bubbles of the broken phase [4–6], separated from the surrounding unbroken phase by a thin wall. These bubbles then expand, collide and eventually coalesce. This process generates shear stresses which in turn source gravitational waves [53, 54].

Early work focussed on characterising the signal from a phase transition that occurs in vacuum [55]. In such a transition, the bubble wall quickly accelerates to ultra-relativistic velocities.

A model of such a scenario was developed, termed the envelope approximation [57]. In this model, the shear stresses are assumed to be concentrated in an infinitesimally thin shell located at the bubble wall. Upon the collision of the bubble walls, the shear stress is assumed to dissipate, and so any regions where bubbles overlap are ignored. The characteristic gravitational wave power spectrum from the envelope approximation is a broken power law in wave number k, where the spectrum rises as k^3 from the low-wavenumber (IR) direction and falls off as k^{-1} in the high-wavenumber (UV) direction. The peak of the broken power law is associated with the length scale of the average bubble separation R_*.

Although the envelope approximation was originally created for bubbles expanding in vacuum it was quickly applied to thermal first-order phase transitions, in which the scalar bubbles expand in a hot plasma [58, 59, 122]. In this case frictional effects from the plasma typically cause the bubble wall to approach a terminal speed v_w. which is not generally ultra-relativistic. Then the majority of the energy liberated from the phase transition is deposited into heat or the bulk motion of the plasma, and the gravitational waves sourced from the shear stress in the scalar field are negligible. It was argued that, providing the

shear stress in the plasma is assumed to be in an infinitesimally thin envelope at the bubble wall, the envelope approximation can once again be applied [58]. Later modelling of bubble collisions introduced a thick fluid shell, and proposed that the velocity field should be Gaussian [68].

Large scale three-dimensional (3D) hydrodynamical simulations [60, 62, 63] have dramatically changed the picture. They show that the shear stresses do not disappear with the bubbles, and persist for long after the transition completes, in the form of sound waves. The envelope approximation is not a good description of total gravitational wave production, and predicts incorrectly both the amplitude and shape of the gravitational wave power spectrum. A better picture of the post-collision phase is one of many overlapping counter-propagating sound shells [64].

On the other hand, the envelope approximation does correctly describe the subdominant contribution to the power spectrum from the scalar field [66], and analytic studies within the envelope approximation have confirmed the broken power laws found from numerical simulations [121]. The envelope approximation can also accommodate the idea that fluid shells persist after collision [122, 123].

It is therefore widely believed that the envelope approximation describes the gravitational power in cases where the energy-momentum of the system is dominated by the scalar field, where the system is close to its vacuum state. In this paper, we investigate the quality of the envelope approximation with 3D numerical simulations of a first-order vacuum phase transition.

Classical lattice simulations of a vacuum phase transition have been used to study the power spectrum produced from bubble collisions before [55, 118]. A 1D simulation of the collision of two scalar field bubbles was carried out in Ref. [55]. and used to motivate the envelope approximation in Ref. [57].

In Ref. [118], it was claimed that the power spectrum produced from collisions in 3D simulations with several bubbles was several orders of magnitude smaller than that predicted by the envelope approximation. Furthermore, after the bubbles had finished colliding there appeared to be an additional phase of the transition in which the scalar field continued to oscillate around the true vacuum. During this oscillation phase the power spectrum continued to grow and the peak of the spectrum shifted towards a higher frequency.

Our numerical simulations adopt similar techniques. However, we are able to perform simulations with many more bubbles and higher wall velocities than Ref. [118].

The simulations solve the field equations for a scalar field sourcing gravitational waves in the linear approximation. The transition is modelled by introducing bubbles of the broken phase as initial conditions for the scalar field. This is done in three different ways, modelling three different histories of bubble nucleation. In simultaneous nucleation, we introduce all bubbles at the very start of the simulation. In exponential nucleation simulations, we introduce the bubbles with an exponentially increasing rate per unit volume. In constant nucleation, we introduce the bubbles at a constant rate.

We show power spectra for both the scalar field itself and also the resulting gravitational wave power spectrum for all nucleation types. We find that as we increase the wall velocity to ultra relativistic speeds, the slope of the gravitational wave power spectrum towards the UV becomes steeper than k^{-1}, and approaches $k^{-1.5}$. The peak amplitude and peak location are similar to those predicted by the envelope approximation. We provide a fit for the power spectrum generated from bubble collisions.

We also confirm the existence of a phase after the bubble collisions have finished, during which the scalar field oscillates around the true vacuum and continues to source gravitational waves. This creates an additional bump in the power spectrum that is associated with the mass scale of the scalar field. This continues to grow linearly until very late times, but we show that it has a negligible contribution to the power spectrum in comparison that of bubble collisions, providing that the mass of the scalar field is smaller than the Planck mass.

In the following section, we recap the dynamics of the scalar field during a vacuum phase transition. This includes the physics of the scalar field during bubble nucleation, expansion, and the eventual collision and oscillation phases of the transition. In Section 4.3 we describe how the scalar field sources gravitational waves, and also describe the envelope approximation. The numerical methods used to perform our simulations are discussed in Section 4.4. Our results are split into two parts; in Section 4.5, we present the behaviour of the scalar field within our simulations, and in Section 4.6, we analyse the gravitational wave power spectra from our simulations and compare them to the envelope approximation. Our conclusions are listed in Section 4.7.

4.2 Dynamics of vacuum transitions

4.2.1 Scalar field dynamics

In a first-order vacuum transition, bubbles of a new phase of a scalar field nucleate and then expand at ultra-relativistic speeds. At the interface between the two phases a bubble wall forms. In this region the scalar field varies smoothly between the two vacuum expectation values. Upon the collision and subsequently merger of the bubbles the shear stress of the system will source gravitational waves. The shear stress in a vacuum transition is predominantly due to gradients in the scalar field ϕ.

In this work, we study transitions in which the duration of the phase transition is much shorter than the Hubble time H_*^{-1} when the transition takes place. For such transitions the expansion of the universe can be neglected, and the equation of motion for the scalar field is simply given by

$$\Box\phi - V'(\phi) = 0, \tag{4.1}$$

where $V(\phi)$ is the effective potential of the scalar field. This is sufficient to investigate the envelope approximation, but may not give accurate results for transitions in which the universe enters an inflationary phase before bubbles start nucleating.

For these purposes it is sufficient to adopt a simple quartic form for the effective potential,

$$V(\phi) = \frac{1}{2}M^2\phi^2 + \frac{1}{3}\delta\phi^3 + \frac{1}{4}\lambda\phi^4, \tag{4.2}$$

where the presence of a cubic term allows us to ensure the transition is first-order. The value of the scalar field in the broken phase is then

$$\phi_{\rm b} = \frac{-\delta + \sqrt{\delta^2 - 4M^2\lambda}}{2\lambda}, \tag{4.3}$$

with mass

$$M_{\rm b} = \sqrt{-\delta\phi_{\rm b} - 2M^2}, \tag{4.4}$$

The potential difference between the two minima is given by

$$\rho_{\rm vac} = \frac{1}{12\lambda}\left(M_{\rm b}^4 - M^4\right). \tag{4.5}$$

By varying the couplings M^2, δ and λ we are able to change the potential difference $\rho_{\rm vac}$ between the two minima of our potential, and also the height of the potential barrier.

The total energy density in the scalar field ρ_ϕ can be split into three components,

$$\rho_\phi = \rho_{\rm K} + \rho_V + \rho_{\rm D}, \tag{4.6}$$

with the kinetic energy density,

$$\rho_{\rm K} = \frac{1}{2}\dot{\phi}^2, \tag{4.7}$$

the gradient energy density,

$$\rho_{\rm D} = \frac{1}{2}(\nabla\phi)^2, \tag{4.8}$$

and the potential energy density,

$$\rho_V = V(\phi) - V(\phi_{\rm b}). \tag{4.9}$$

4.2.2 Bubble nucleation

In a first-order vacuum transition, bubbles nucleate by quantum tunnelling through a potential barrier. This means that they nucleate as critical bubbles, O(4)-symmetric solutions to the Euclidean field equations [4, 5]. When the radius of the critical bubble is much larger than the thickness of the bubble wall the bubble is said to be in the thin wall limit. This occurs when $\rho_{\rm vac}$ is much smaller than the height of the potential barrier, or equivalently when the minima are close to degenerate. For our potential the minima are degenerate for

$$\delta = -\frac{3}{\sqrt{2}}M\sqrt{\lambda}. \tag{4.10}$$

When $\rho_{\rm vac}$ is much larger than the height of the potential barrier, the critical bubble is of a similar size to the radius. We leave the study of such bubbles to a later work.

The thin wall solution can be calculated analytically as a function of Euclidean radius, $r_{\rm E} = \sqrt{r^2 + \tau^2}$, where r is the spatial radius, and τ the Euclidean time. In the thin wall limit the scalar field profile of the critical bubble is given by

$$\phi_{\rm c}(r) = \frac{\phi_{\rm b}}{2}\left[1 - \tanh\left(\frac{r - R_{\rm c}^{\rm tw}}{l_0^{\rm tw}}\right)\right], \tag{4.11}$$

where l_0 is thickness of the bubble wall, which is given in the thin wall limit by

$$l_0^{\rm tw} = \frac{2}{\sqrt{V''(\phi_b)}}, \tag{4.12}$$

and $R_{\rm c}^{\rm tw}$ is the radius of the critical bubble. The radius of the critical bubble can be estimated by extremising the approximate expression for the Euclidean action

$$S_4 = 2\pi^2 R^3 \sigma^{\rm tw} - \frac{\pi^2}{2}R^4\rho_{\rm vac}, \tag{4.13}$$

where

$$\sigma^{\rm tw} = \frac{M^3}{3\lambda}, \tag{4.14}$$

is interpreted as the surface tension of the bubble. Then the critical radius is

$$R_{\rm c}^{\rm tw} = \frac{3\sigma^{\rm tw}}{\rho_{\rm vac}}. \tag{4.15}$$

At the point of time symmetry $\tau = 0$, the energy liberated from the vacuum is equal to the energy in the wall. Furthermore, the outward force on the bubble wall due to the pressure difference $\rho_{\rm vac}$ is equal and opposite to that caused by the surface tension.

Once the bubble has nucleated, the solution is found by the analytic continuation to Minkowski space, so that

$$\phi(r,t) = \begin{cases} \phi_{\rm c}(\sqrt{r^2 - t^2}), & r > t, \\ \phi_{\rm b}, & r \leq t. \end{cases} \tag{4.16}$$

The probability of nucleating a bubble per unit volume per unit time $p(t)$ is given by [5]

$$p(t) = p_{\rm n} \exp(-S_4). \tag{4.17}$$

Very often the Euclidean action decreases slowly in time due to a change in temperature or a background field. Then we may write

$$p(t) = p_f \exp[\beta(t - t_f)], \tag{4.18}$$

where $\beta = -\, d\ln p(t)/dt|_{t_f}$ and t_f is the time at which the fraction of the universe in the symmetric phase is $h(t_f) = 1/e$ [139]. The bubble number density can be shown to be

$$n_{\rm b} = \frac{1}{8\pi}\frac{\beta^3}{v_{\rm w}^3}, \tag{4.19}$$

where in the vacuum case $v_{\rm w}$ is very close to unity. We will refer to this case as exponential nucleation.

It is also possible that $S_4(t)$ has a minimum which is reached at time t_0 before a transition completes. Then the probability of nucleating a bubble per unit volume could be approximated by

$$p(t) = p_0 \exp[-\tfrac{1}{2}\beta_2^2 (t - t_0)^2], \tag{4.20}$$

where $\beta_2 = \sqrt{S''(t_0)}$. Nucleation is then concentrated around time t_0 [140]. The bubble density is

$$n_{\rm b} = \sqrt{2\pi}\frac{p_0}{\beta_2}. \tag{4.21}$$

We will refer to this case as simultaneous nucleation.

The last possibility we consider is if $S_4(t)$ tends to a constant (for a model with a constant nucleation rate see Ref. [141]). We would then expect bubbles to nucleate at a constant rate

$$p(t) = p_{\rm c}, \tag{4.22}$$

for which

$$n_{\rm b} = \frac{1}{4}\left(\frac{3}{\pi}\right)^{1/4}\Gamma\left(\frac{1}{4}\right)\left(\frac{p_{\rm c}}{v_{\rm w}}\right)^{3/4}. \tag{4.23}$$

We will refer to this as constant nucleation.

4.2.3 Bubble growth

If we consider a thin wall bubble then we can obtain an expression for the evolution of the bubble simply by considering energy conservation. The energy in the static bubble wall per unit area is simply $\sigma^{\rm tw}$. Then if the bubble wall is expanding at some velocity $v_{\rm w}$, the energy per unit area is given by $\sigma^{\rm tw}\gamma$ where γ is the wall's Lorentz factor. The total energy of an expanding bubble with radius R is then [4, 5]

$$E_{\rm bub} = 4\pi R^2\sigma^{\rm tw}\gamma - \frac{4}{3}\pi R^3\rho_{\rm vac}, \tag{4.24}$$

where we can define R to be the point in the scalar field profile such that $\phi(R) = \phi_b/2$. As we are considering vacuum decay, we expect $E_{\rm bub} = 0$. We therefore obtain that, for a bubble of radius R, the Lorentz factor of the bubble wall is given by

$$\gamma(R) = \frac{R\rho_{\rm vac}}{3\sigma^{\rm tw}} = \frac{R}{R_{\rm c}^{\rm tw}}. \tag{4.25}$$

We expect Eq. (4.25) to apply outside the thin wall limit by recalling that the solution of the classical field equations is simply the analytic continuation of the O(4)-symmetric bounce solution [4]. Then any point in the field profile of the critical bubble we define to be the critical radius $R_{\rm c}$ will expand out with a hyperboloid motion satisfying

$$R^2(t) - t^2 = R_{\rm c}^2, \tag{4.26}$$

which is equivalent to Eq. (4.25).

4.2.4 Bubble collision and oscillation phase

For bubbles with thin walls, after collision part of the overlap region rebounds and returns towards the false vacuum [115, 142]. In Fig. 4.1, we plot the variation during a collision of the scalar field along the collision axis connecting two bubble centres. At the collision point it can be seen that the scalar field oscillates between the true and false vacuum. These large amplitude oscillations are the source of scalar radiation moving at close to the speed of light, and can also induce rapid production of light particles through parametric resonance [143]. This rebounding and oscillation phase is something that is not accounted for within the envelope approximation. Away from the thin wall limit, the

scalar field in the overlap region is not able to return to the false vacuum, and instead will just oscillate around the true vacuum [115].

After this stage, the scalar field continues to oscillate around the true vacuum with large amplitude oscillations. In the absence of other interactions, scalar fields take a substantial time to thermalise [144–146].

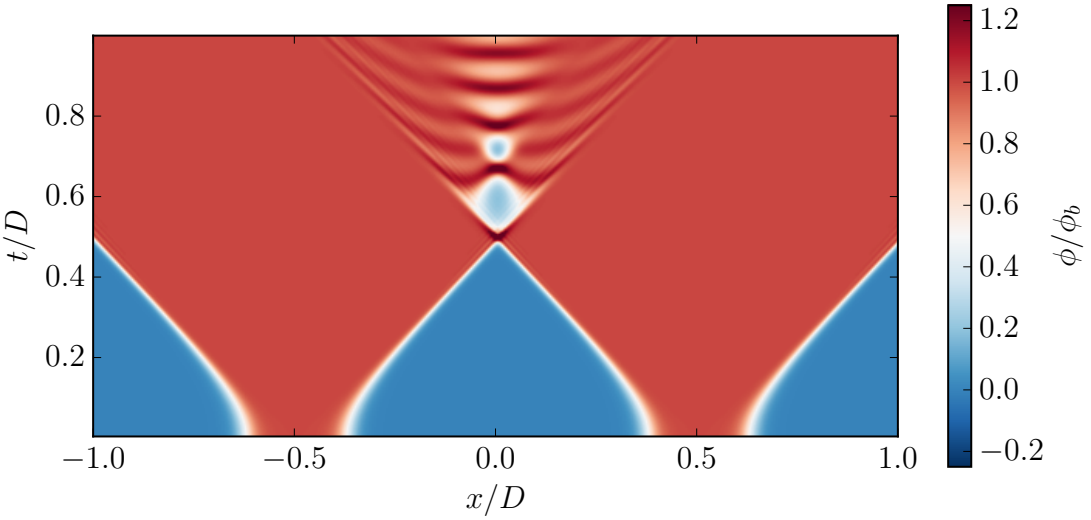

Figure 4.1: Values of the scalar field along the collision axis during a two bubble collision where $R_c M = 7.15$. Here the x axis is the collision axis which connects the two bubble centres. The y axis is time since the nucleation of the bubbles. The bubbles are separated by a distance D. This figure can be compared with Fig. 1 of [142] and Fig. 7 of [115].

4.3 Gravitational waves from a phase transition

In order to calculate the gravitational wave power spectrum, we need to find the transverse traceless (TT) metric perturbations h_{ij}^{TT} where

$$\Box h_{ij}^{TT} = -16\pi G T_{ij}^{TT}, \tag{4.27}$$

and T_{ij}^{TT} is the transverse traceless projection of the energy-momentum tensor,

$$T_{\mu\nu} = \partial_\mu\phi\partial_\nu\phi - \eta_{\mu\nu}\left(\frac{1}{2}(\partial\phi)^2 + V(\phi)\right), \tag{4.28}$$

where $\eta_{\mu\nu}$ is the Minkowski metric. The energy density in the gravitational waves can be defined as

$$\rho_{\rm gw}(\mathbf{x}, t) = \frac{1}{32\pi G}\dot{h}_{ij}^{TT}\dot{h}_{ij}^{TT}. \tag{4.29}$$

Note that an average over many wavelengths and periods may be needed in order to reduce fluctuations in this quantity.

We introduce an auxiliary tensor u_{ij} which satisfies [147]

$$\Box u_{ij} = -16\pi G(\partial_i\phi)(\partial_j\phi). \tag{4.30}$$

To obtain h_{ij}^{TT} we use the projector $\Lambda_{ij,lm}$ on u_{ij} in momentum space,

$$h_{ij}^{TT}(\mathbf{k},t) = \Lambda_{ij,lm}(\mathbf{k})u_{lm}(\mathbf{k},t), \tag{4.31}$$

where

$$\Lambda_{ij,lm}(\mathbf{k}) = P_{im}(\mathbf{k})P_{jl}(\mathbf{k}) - \frac{1}{2}P_{ij}(\mathbf{k})P_{lm}(\mathbf{k}), \tag{4.32}$$

and

$$P_{ij}(\mathbf{k}) = \delta_{ij} - \hat{k}_i\hat{k}_j. \tag{4.33}$$

We then define the spectral density of the time derivative of the metric perturbations $P_{\dot{h}}$ as

$$\langle \dot{h}_{ij}^{TT}(\mathbf{k},t)\dot{h}_{ij}^{TT}(\mathbf{k}',t)\rangle = P_{\dot{h}}(\mathbf{k},t)(2\pi)^3\delta(\mathbf{k}+\mathbf{k}'). \tag{4.34}$$

Therefore the power spectrum of gravitational wave energy density is

$$\frac{d\rho_{\rm gw}}{d\ln(k)} = \frac{1}{32\pi G}\frac{k^3}{2\pi^2}P_{\dot{h}}(\mathbf{k},t), \tag{4.35}$$

and by dividing through by the critical energy density ρ_c we obtain the power spectrum of the gravitational wave energy density parameter

$$\frac{d\Omega_{\rm gw}}{d\ln(k)} = \frac{1}{32\pi G\rho_c}\frac{k^3}{2\pi^2}P_{\dot{h}}(\mathbf{k},t). \tag{4.36}$$

4.3.1 Collision phase: envelope approximation

In the envelope approximation [57], the bubble walls are treated as infinitely thin, expanding with speed $v_{\rm w}$, and containing all the vacuum energy released by the transition. The overlap region of collided bubbles are ignored, and the gravitational waves from shear stress "envelope" calculated. The resulting spectrum was re-computed with many more bubbles in Ref. [59], and again in Ref. [122], for an exponential nucleation rate in both cases.

The gravitational wave power spectrum is well approximated by a broken power law

$$\frac{d\Omega_{\rm gw}^{\rm env}}{d\ln(k)} = \Omega_{\rm p}^{\rm env}\frac{(a+b)\tilde{k}^b k^a}{b\tilde{k}^{(a+b)} + ak^{(a+b)}}, \tag{4.37}$$

with power law exponents a and b, peak amplitude $\Omega_{\rm p}^{\rm env}$ and peak wavenumber $\tilde{k}$. The peak amplitude was found to be

$$\Omega_{\rm p}^{\rm env} \simeq \frac{0.44 v_w^3}{1 + 8.28 v_w^3} \left(\frac{H_*}{\beta}\right)^2 (\kappa_\phi \Omega_{\rm vac})^2 , \tag{4.38}$$

where the Hubble rate at the time of the transition H_*, the vacuum energy density parameter $\Omega_{\rm vac} = \rho_{\rm vac}/\rho_c$ and the bubble wall velocity $v_{\rm w}$. The peak frequency was estimated to be

$$\tilde{k}/\beta \simeq \frac{1.96}{1 - 0.051 v_{\rm w} + 0.88 v_{\rm w}^2}. \tag{4.39}$$

The efficiency factor κ_ϕ measures the fraction of vacuum energy that is converted to stress energy localised at the bubble wall. We define it as

$$\kappa_\phi = \frac{2\rho_D}{\rho_{\rm vac} - \rho_{\rm V}}. \tag{4.40}$$

For a vacuum phase transition $\kappa_\phi \simeq 1$.

The exponent for the broken power law on the low frequency side is expected to be $a = 3$ due to causality [71]. In Ref. [122], the power law exponents were found to be $a = 2.9$ and $b = 0.9$ for $v_{\rm w} \simeq 1$ and $a = 2.95$ and $b = 1$ for $v_{\rm w} \ll 1$. Furthermore, in Ref. [66], the envelope approximation was compared to lattice simulations of a scalar field with frictional effects chosen such that the bubble walls asymptotes a constant speed $v_{\rm w} = 0.44$. The gravitational wave power spectrum generated by stress energy in the scalar field was found to agree well with the envelope approximation. The power law exponents for the envelope approximation in this study were found to be $a = 2.98 \pm 0.02$ and $b = 0.62 \pm 0.05$ [66].

There is also some analytical understanding of the power spectrum produced under the envelope approximation. In Ref. [121], it is shown that the two point correlator of the energy-momentum tensor can be expressed as a 1-dimensional integral under the envelope approximation, also producing a broken power law with exponents $a = 3$ and $b = 1$.

It should be noted that while typically in a thermal phase transition friction effects from the plasma cause $v_{\rm w}$ to approach a constant, in a vacuum phase transition the bubble wall accelerates until collision with $v_{\rm w} \to 1$ and $\gamma \to \infty$. In this current work we shall check whether the formula is a good fit in the case where the bubble wall continues to accelerate until collision, reaching ultra-relativistic velocities.

4.3.2 Oscillation phase

Previous simulations of a vacuum first-order phase transition have observed that after all the bubble collisions have completed, the scalar field continues to oscillate, and the production of gravitational radiation continues [118].

The contribution to the gravitational wave power spectrum from this oscillation phase was seen to dominate that of the bubble collisions by more than an order of magnitude. The peak frequency moved towards the UV by an order of magnitude during the oscillation phase.

Providing the oscillations in the scalar field are non-linear [148] we would expect them to be a continuous source of gravitational waves, similar to acoustic waves in a thermal phase transition [62]. Eventually Hubble friction would damp out the oscillations.

A further goal of the current work is to investigate if we also see the growth of the gravitational wave power spectrum during an oscillation phase in our simulations.

4.4 Methods

To perform our study we perform a series of simulations solving the partial differential equations (4.1) and (5.35) on on a 3-dimensional lattice, using code built on the open source `C++` library `LATfield2` [149]. To compute derivatives we use a central finite difference method. For the Laplacian we use the minimal 7-point stencil made up of a central point and then an additional 2 points in each dimension. We choose our timestep Δt and lattice spacing Δx such that $\Delta t = 0.2\Delta x$. We advance in timestep by using the leapfrog algorithm.

Our simulations are on a cubic grid with L^3 grid sites, total volume $\mathcal{V} = (L\Delta x)^3$ and periodic boundary conditions. We begin each simulation by nucleating at least one bubble at the simulation time $t = 0$. The total number of bubbles nucleated by the end of the simulation is given by $N_{\rm b}$.

We use a shooting method to find the critical profile for specific values of M^2, δ and λ. We choose three profiles to simulate and give the parameters for these in Table 4.1. The resulting field profiles are modelled well by Eq. (5.25) with values for $R_{\rm c}$ and l_0 given in the first two columns. Note that they differ from the thin wall values due to the finite size of the bubble.

The value of $R_{\rm c}$ is given by the location in the numerical profile at which

$$\phi_c(R_{\rm c}) = \frac{\phi_{\rm b}}{2}. \tag{4.41}$$

Similarly, $l_0 = r^+ - r^-$ where

$$\phi_c(r^\pm) = \frac{\phi_{\rm b}}{2}\left(1 - \tanh\left(\pm 1/2\right)\right). \tag{4.42}$$

We nucleate bubbles with a critical profile inside our numerical simulation. Before nucleating the Nth bubble we check that, for all $n < N$, the distance between the Nth

$R_c M$	$l_0 M$	δ/M	λ	ϕ_b/M	ρ_{vac}/M^4	σ^{tw}/M^3	$l_0^{tw} M$	$R_c^{tw} M$
7.15	1.71	−1.632	0.5	2.45	0.495	2/3	1.42	4.04
14.3	1.83	−1.56	0.5	2.22	0.189	2/3	1.65	10.6
28.8	1.91	−1.528	0.5	2.11	0.0809	2/3	1.81	24.7

Table 4.1: Critical radii R_c and wall thicknesses l_0 that are used in our simulations. For each of these we give the potential parameters δ and λ used to derive them, the broken phase value of the scalar field ϕ_b and the vacuum energy density ρ_{vac}. We also list the surface tension σ^{tw}, wall thickness l_0^{tw} and critical radius R_c^{tw} as derived from the thin wall approximation.

and nth bubble centres r_n obeys the following relation

$$r_n^{sep} > R_c + \sqrt{R_c^2 + (t - t_n)^2}, \tag{4.43}$$

where t_n is the time at which the nth bubble nucleated. Providing this is satisfied for all bubbles, we nucleate a bubble by modifying $\phi \to \phi'$, where

$$\phi'(r) = \sqrt{\phi^2(r) + \phi_c^2(r)}. \tag{4.44}$$

We evolve the auxiliary metric tensor u_{ij} in real space at every timestep. At routine intervals we perform a Fourier transform of $\dot{u}_{ij}$, and then project the result according to Eq. (5.36) to find $\dot{h}_{ij}^{TT}(\mathbf{k}, t)$. From this we then calculate the gravitational wave power spectrum. It should be noted that in our units $G = 1$, though in general we plot quantities that do not depend on G.

We can nucleate bubbles simultaneously at the start of the simulation, or indeed with a nucleation rate throughout its duration. In order to compare with earlier studies using the envelope approximation, we nucleate bubbles with an exponentially increasing nucleation rate, using the algorithm given in Ref. [139]. Then the probability of nucleating a bubble per unit volume and time is given by Eq. (5.18). The parameters of the simultaneous nucleation runs are listed in Table 4.2, and those of the exponential nucleation runs in Table 4.3. We also perform two constant nucleation runs to check that this type of nucleation is consistent with our other results. The parameters of the constant nucleation runs are given in Table 4.4.

We also wish to study the gravitational wave power spectrum produced after the bubble collision phase is completed. In order to do this, we can simply turn on the evolution of u_{ij} once the bubbles have finished colliding. We employ this approach for a series of simultaneous nucleation simulations listed in Table 5.3.

$R_{\rm c}M$	γ_*	R_*M	N_b	$L\Delta xM$	L	ΔxM	$\gamma_*^{\rm lat}$
7.15	1.97	28.2	8	56.32	128	0.44	1.85
7.15	1.97	28.2	64	112.64	256	0.44	1.85
7.15	1.97	28.2	512	225.28	512	0.44	1.85
7.15	1.97	28.2	4096	450.56	1024	0.44	1.85
7.15	3.94	56.3	8	112.64	512	0.22	3.37
7.15	3.94	56.3	64	225.28	1024	0.22	3.37
7.15	3.94	56.3	512	450.56	2048	0.22	3.37
7.15	3.94	56.3	4096	901.12	4096	0.22	3.37
7.15	7.88	113.	8	225.28	2048	0.11	5.65
14.3	1.97	56.3	512	450.56	1024	0.44	1.87
28.8	1.96	113.	512	901.12	2048	0.44	1.89

Table 4.2: Parameters of the simultaneous nucleation simulations used within this paper. Listed here for each run is the critical radius $R_{\rm c}$, typical Lorentz factor at collision γ_*, average bubble separation R_*, number of bubbles $N_{\rm b}$, number of lattice points L^3, lattice spacing Δx, and effective γ_* as found on the lattice $\gamma_*^{\rm lat}$. Not given here are simulation runs where the metric perturbations are turned on after the bubbles have finished colliding, see Table 5.3.

$R_{\rm c}M$	γ_*	β/M	R_*M	N_b	$L\Delta xM$	L	ΔxM	$\gamma_*^{\rm lat}$
7.15	1.97	0.180	28.2	8	56.32	128	0.44	1.85
7.15	1.92	0.180	27.5	69	112.64	256	0.44	1.81
7.15	1.96	0.180	28.0	522	225.28	512	0.44	1.84
7.15	3.94	0.0625	56.3	8	112.64	512	0.22	3.37
7.15	4.09	0.0625	58.5	57	225.28	1024	0.22	3.55
7.15	7.57	0.0290	108.	9	225.28	2048	0.11	5.58

Table 4.3: Parameters of the exponential nucleation simulations used within this paper.

$R_{\rm c}M$	γ_*	$p_{\rm c}/M^4$	R_*M	N_b	$L\Delta xM$	L	ΔxM	$\gamma_*^{\rm lat}$
7.15	3.94	1.50×10^{-7}	56.3	64	225.28	1024	0.22	3.37
7.15	4.09	1.50×10^{-7}	56.3	510	450.56	2048	0.22	3.37

Table 4.4: Parameters of the constant nucleation simulations used within this paper.

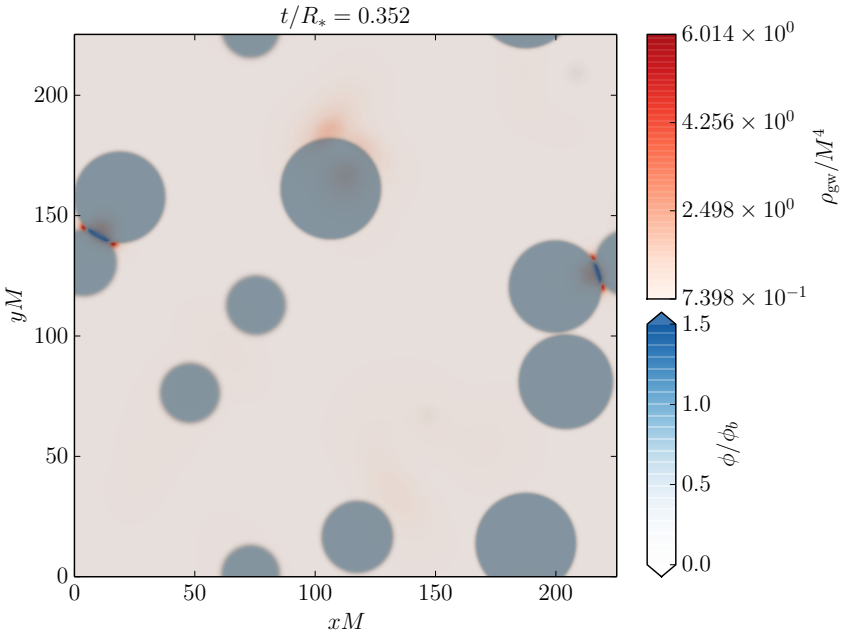
$t/R_* = 0.352$
6.014×10^0
4.256×10^0
2.498×10^0
7.398×10^{-1}
$\rho_{\rm gw}/M^4$
1.5
1.0
0.5
0.0
ϕ/ϕ_b
yM
xM
0
50
100
150
200

(a)

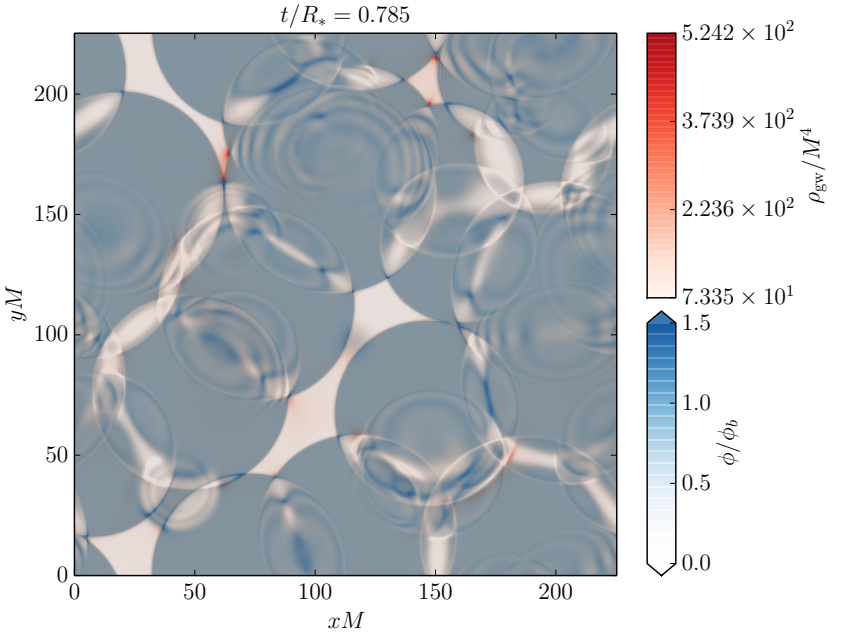
$t/R_* = 0.785$
5.242×10^2
3.739×10^2
2.236×10^2
7.335×10^1
$\rho_{\rm gw}/M^4$
1.5
1.0
0.5
0.0
ϕ/ϕ_b
yM
xM
0
50
100
150
200

(b)

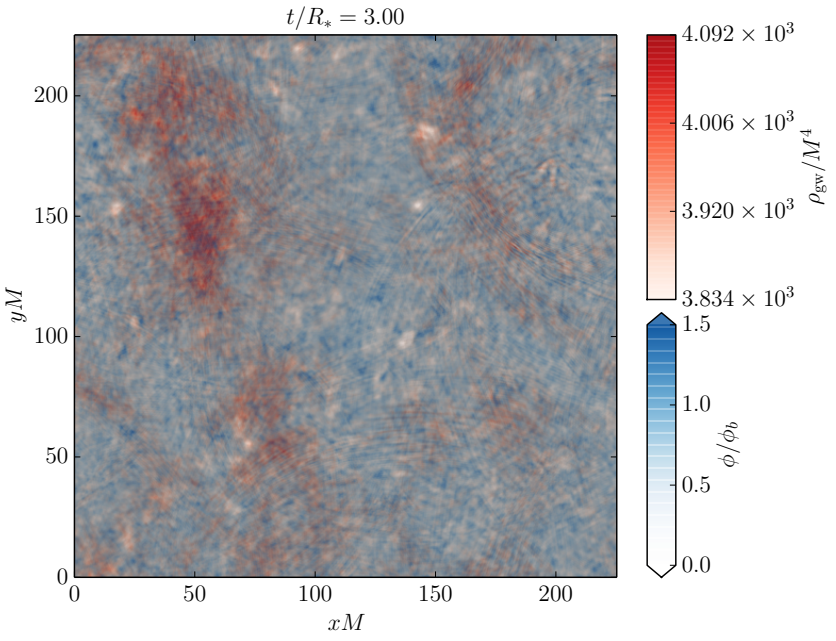

(c)

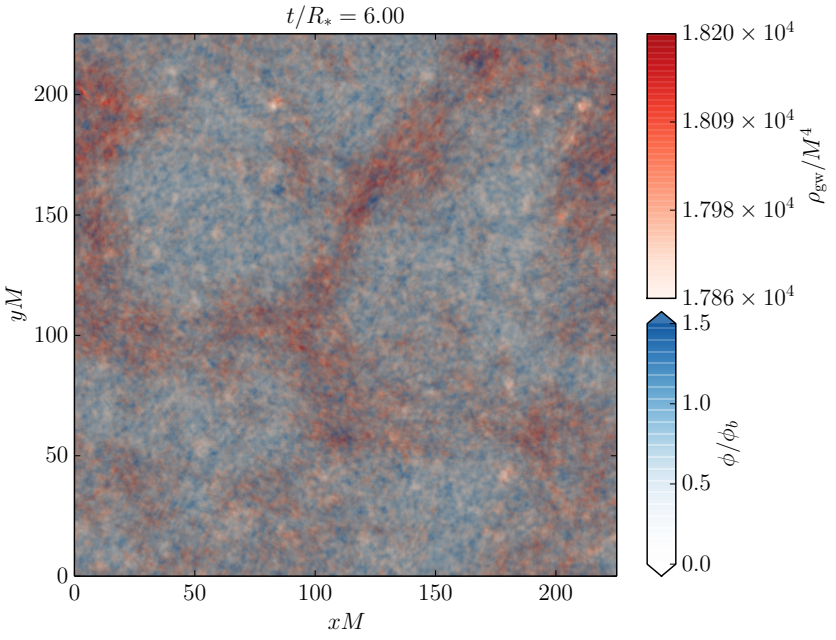

(d)

Figure 4.2: Slices through a simultaneous nucleation simulation with parameters $R_{\rm c}M = 7.15$, $N_{\rm b} = 64$ and $R_*M = 56.32$ showing the expansion (a), collision (b), and oscillatory (c and d) phase of the scalar field. The scalar field value is shown in blue, and the gravitational wave energy density is shown in red. Note that the range of the colourbar for the gravitational wave energy density changes for each plot. During the oscillatory phase the gravitational wave energy density becomes very uniform and the "hotspots" are deviations on the sub percent level. The full set of parameters for this run is shown in Table 4.2. A movie based on this simulation is included in the supplemental material.

$R_{\rm c}M$	γ_*	R_*M	N_b	$L\Delta xM$	L	ΔxM	$\gamma_*^{\rm lat}$
7.15	3.94	56.3	64	225.28	1024	0.44	3.37
14.3	1.97	56.3	512	450.56	1024	0.44	1.87
14.3	3.94	113.	8	225.28	1024	0.22	3.34
28.8	1.96	113.	64	450.56	1024	0.44	1.89

Table 4.5: Parameters of the simultaneous nucleation simulations where the metric perturbations are turned on at $t/R_* = 2.0$ at which point most of the bubbles have finished colliding. This is in order to see the shape of the power spectrum due to scalar field radiation during the oscillation phase.

There are a number of length scales within our simulation. The largest physical length scale within our system is the average separation between bubbles R_*. This is simply given by

$$R_* = \left(\frac{\mathcal{V}}{N_{\rm b}}\right)^{1/3}. \tag{4.45}$$

Much smaller than this length scale is the radius of the critical bubble $R_{\rm c}$, and the critical bubble wall width l_0. The critical bubble wall width is associated with the scalar field mass in the broken phase. Smaller still is the length scale of the Lorentz contracted bubble walls. We define $\gamma_* = R_*/2R_{\rm c}$ which is the expected Lorentz factor for a bubble with diameter R_*, and then define $l_* = l_0/\gamma_*$ as the width of the Lorentz contracted bubble wall with a diameter of R_*. It is crucial that we have a good resolution of the bubble walls up until they collide, and as such we need our lattice spacing $\Delta x \ll l_*$. Note that by obtaining different values of $R_{\rm c}$ we can vary R_* while keeping γ_* the same.

In most vacuum phase transitions we expect bubbles to expand to many times the size of the critical bubble, and therefore up to very high Lorentz factors. We also would like to have many bubbles within our simulation box to obtain an accurate ensemble. Hence, we need sufficiently large lattices to separate the scales

$$\Delta x \ll l_* \ll l_0 \lesssim R_{\rm c} \ll R_* \ll L\Delta x. \tag{4.46}$$

It is not possible to perform a simulation in which we achieve a realistic value for γ_* and a correct separation of scales. Instead, we perform multiple simulations with increasing values of γ_* to attempt to identify a trend as $\gamma_* \to \infty$.

For simulations with a given nucleation rate, we typically expect the first bubble nucleated to grow to a larger size than bubbles nucleated later, and so the wall of the first bubble when it collides will have γ greater than γ_*. Its bubble wall at collision will therefore be

thinner than l_*. This effect is particularly pronounced for simulations with an exponential nucleation rate where the first bubble nucleated often grows to be many times larger than the subsequent bubbles at collision time. For a simultaneous nucleation run the diameters of the bubbles will be more closely distributed around R_*, and so the thinnest wall at collision will be much closer to l_*.

For an exponential nucleation rate simulation we need a much finer lattice spacing in comparison to a simultaneous nucleation simulation with the same l_*. In practice, reducing the lattice spacing is too expensive and for large volumes we become unable to trust our results due to bad energy conservation.

4.5 Results: scalar field

As described in the previous section, the scalar field evolution can roughly be split into three stages, expansion, collision, and oscillation. Slices through a simultaneous nucleation simulation volume are shown in Fig. 4.2. During collision, we see many regions in which the scalar field is rebounding into the symmetric phase as described in Section 4.2.4. During the oscillation phase the scalar field becomes more homogeneous on large scales while the scalar field continues to oscillate on small wavelengths. This persists as long as the simulations run, for times that are many multiples of R_*.

In order to test for lattice effects, we study single bubbles, whose Lorentz factors should be related to their radius through Eq. (4.25). We find the volume by counting the number of lattice sites with $\phi > \phi_{\rm b}$, and then from this we are able to deduce the bubble radius R and the Lorentz factor factor of the wall γ.

We plot γ against R in Fig. 4.3. The lattice effects are easy to see, as γ is highly sensitive to small changes in velocity when $v_{\rm w} \to 1$. The bubble wall is stopped from contracting beyond a width which is representable on the lattice, and the bubble wall is unable to increase its velocity. The energy that is lost is transferred to small wavelength oscillations that follow behind the bubble wall. This effect has been seen previously in accelerating kinks on a lattice [150, 151].

If the deviation of γ from its theoretical value becomes sufficiently large then this can be associated with loss of energy conservation.

We plot the energy densities over time for a simultaneous nucleation phase transition in Fig. 4.4. As the bubbles expand the potential energy drops steeply and the kinetic and gradient energies increase. Initially the gradient energy and kinetic energy are roughly equal but when the bubbles begin to collide the kinetic energy becomes larger than the

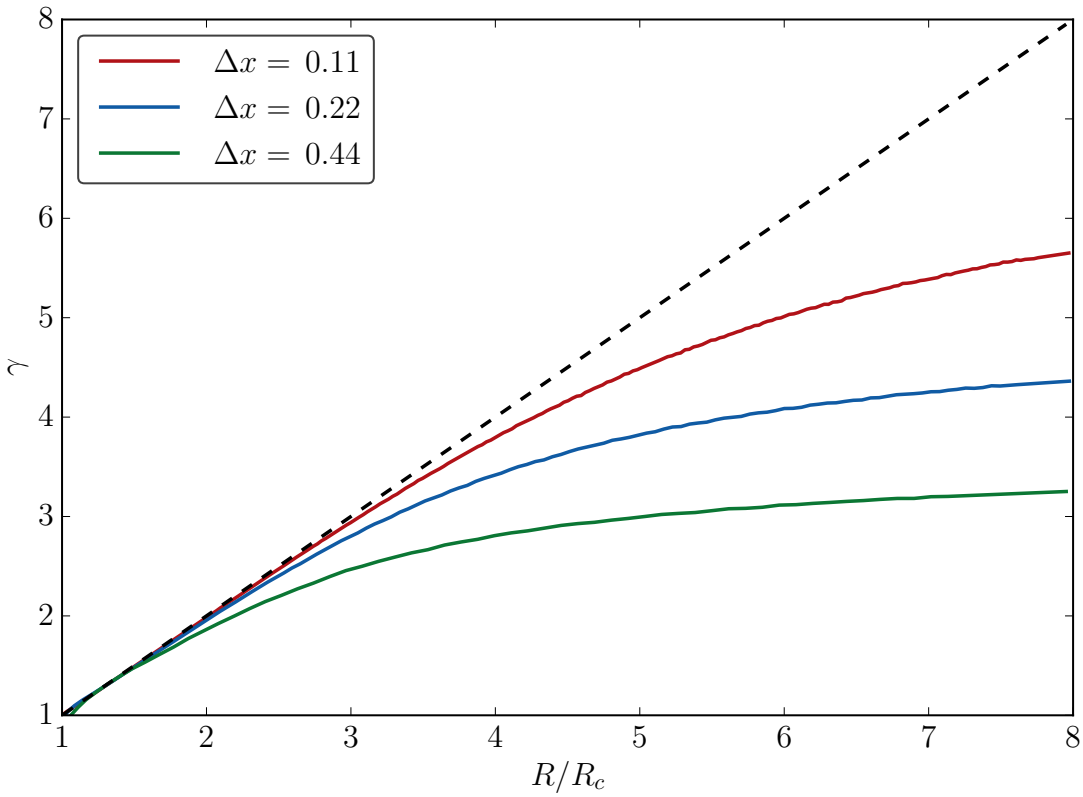

Figure 4.3: The Lorentz factor γ of the bubble wall for different values lattice spacings plotted against the radius of the bubble in units of the critical radius. This is for a bubble with $R_c M = 7.15$. The dashed black line shows $\gamma = R/R_c$.

gradient energy. Shortly after the phase transition enters the oscillation stage, with $\rho_V \neq 0$.

The energy conservation for a series of simulations with $L\Delta x = 225.28$ is given in Fig. 4.5. We can see that energy conservation is substantially better in the simultaneous nucleations in comparison to the exponential nucleation runs. This is what we expected due to the biggest bubble/thinnest wall effect mention in section 4.4. These are the largest volume simulation runs for exponential nucleation, and so have the worst energy violation of all simulations performed. Even in the worst case, energy conservation violation is still kept to $\lesssim 5\%$[1].

It should be noted that while energy conservation is a necessary constraint for correct evolution, it does not guarantee that the evolution matches that of the continuum. It is possible to maintain energy conservation perfectly but still have jumps in phase space arise due to lattice effects. One method to test if the evolution matches to the continuum

[1]It has been pointed out to the authors that measuring the total energy conservation of the system may be misleading. As the majority of the gravitational waves are produced in the collision regions of the bubbles, a better gauge would be to track the average energy loss on these collision surfaces. This was not tested in the current study, but could be employed as a test in future.

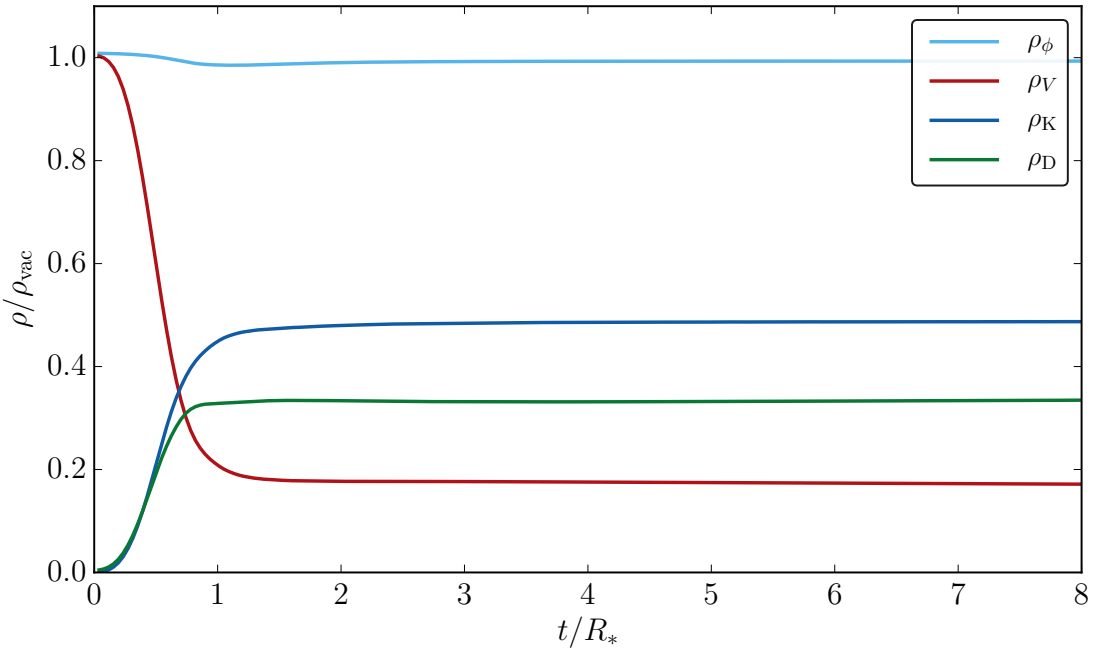

Figure 4.4: Energy densities in the scalar field over time for a simultaneous nucleation run with $R_c M = 7.15$, $R_* M = 56.3$ and $N_b = 4096$. The full set of parameters for this run is shown in Table 4.2.

limit is to perform lattice convergence tests and validate that observables like the power spectrum of the scalar field or gravitational waves converge with increasing resolution.

To monitor energy conservation in our multi-bubble simulations, we define a new parameter γ_*^{lat} which is the numeric value found for γ on the lattice when the bubble radius is $R = R_*$. This new parameter is listed for all simulation runs in their respective tables.

The power spectrum of the scalar field $\mathcal{P}_\phi$ can inform us about the length scales of the shear stresses sourcing gravitational waves. We plot $\mathcal{P}_\phi$ during the expansion, collision and oscillation phases for both a simultaneous and exponential nucleation run in Fig. 4.6. During expansion and collision $\mathcal{P}_\phi$ is peaked around R_*. During the oscillation phase $\mathcal{P}_\phi$ shifts so that its maximum is at a higher wavelength, closer to the scale associated with l_0. This can be understood as the structure of bubbles disappearing and being replaced with oscillating features around the mass scale of the scalar field.

The main differences in $\mathcal{P}_\phi$ between the simultaneous and exponential nucleation runs are during the expansion and collision phases. Identical bubbles are all spawned at the start of the simultaneous nucleation run, and so $\mathcal{P}_\phi$ has a larger magnitude at $t/R_* = 0.0$, and shows the characteristic "ringing" of the single-bubble power spectrum. These bubbles then expand in a uniform way, their geometries differentiating from each other only upon collision with another bubble. Comparatively, as more bubbles are spawned during the

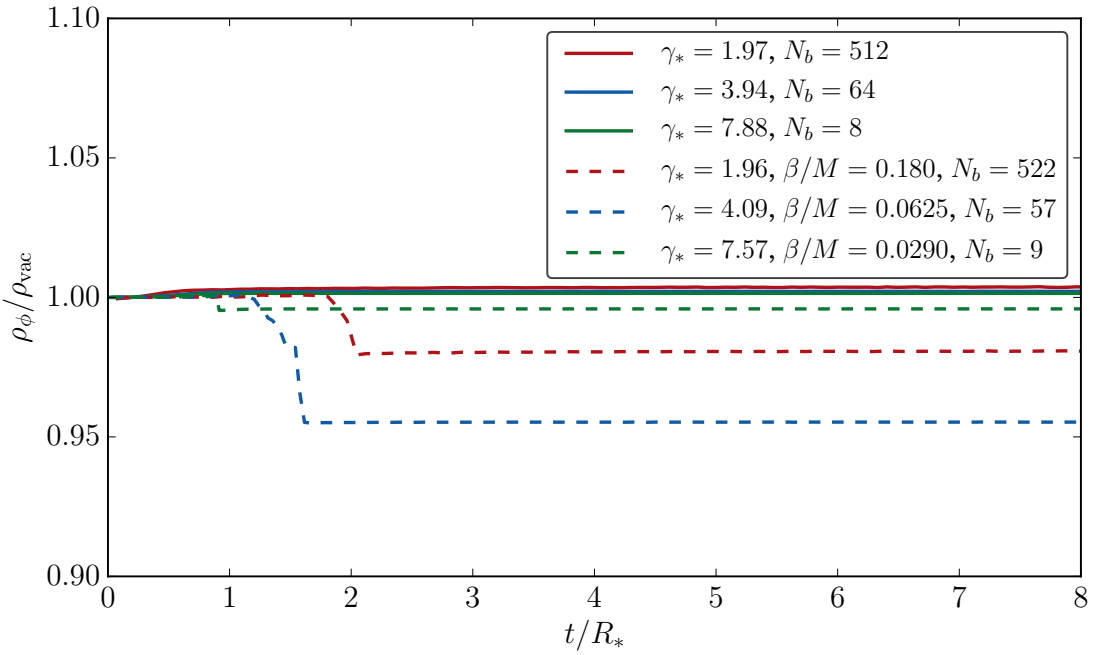

Figure 4.5: Energy conservation for several simulations of the same physical volume. Runs with exponential nucleation are plotted with dashed lines, and simultaneous nucleation runs are shown with solid lines. See Tables 4.2 and 4.3 for the full set of parameters of each run.

exponential nucleation run $\mathcal{P}_\phi$ becomes smoother on large scales and noisier on small scales as bubbles of varying sizes appear. The collision phase also lasts longer, and the distribution of bubbles is not as homogeneous as in a simultaneous nucleation run.

If we plot the late time scalar field power spectrum together on the same graph we can clearly see that during the oscillation phase the simultaneous and exponential nucleation runs settle into similar states. We do this for several values of γ_* in Fig. 4.7. In all cases, the scalar power spectra settle into similar states apart from lattice effects in the UV.

4.6 Results: gravitational waves

4.6.1 Simultaneous nucleation

In Fig. 4.2, we also show in shades of red the gravitational wave energy density $\rho_{\rm gw}(\mathbf{x}, t)$ sourced by the scalar field. To obtain $\rho_{\rm gw}$ in real space we first perform the Fourier transform of $\dot{u}_{ij}$, then project this to obtain $\dot{h}_{ij}^{TT}$ in k-space. Finally we perform the inverse Fourier transform to find $\dot{h}_{ij}^{TT}$ in real space. From this we then calculate $\rho_{\rm gw}(\mathbf{x}, t)$ using Eq. (5.33).

We can clearly see from Fig. 4.2 that during the collision phase hotspots in $\rho_{\rm gw}$ are

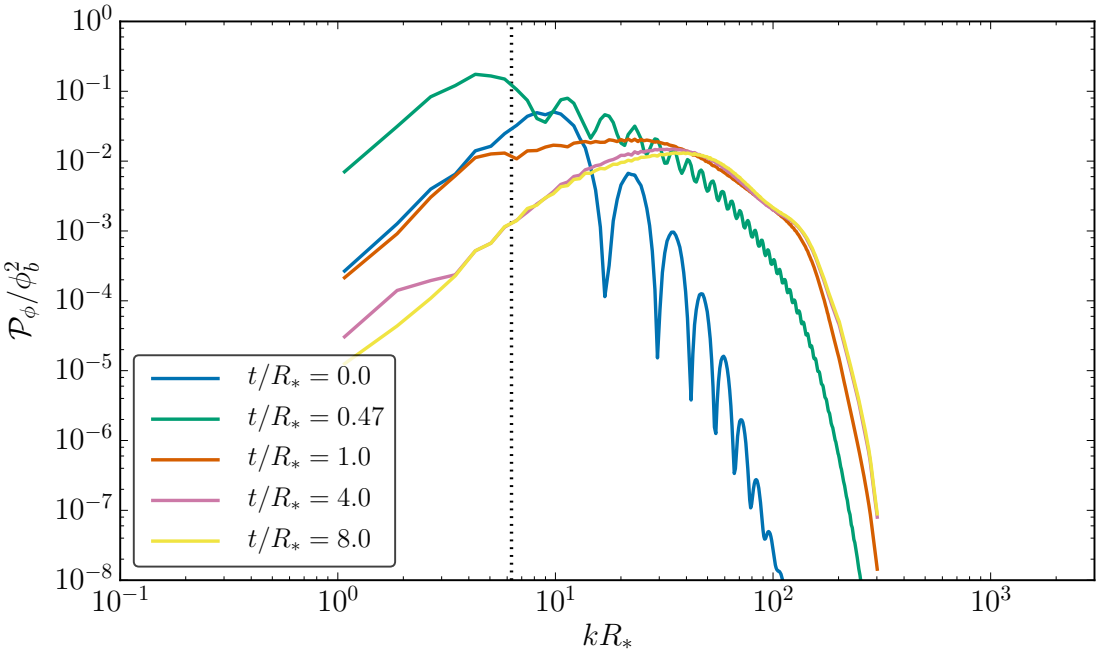

(a) Simultaneous

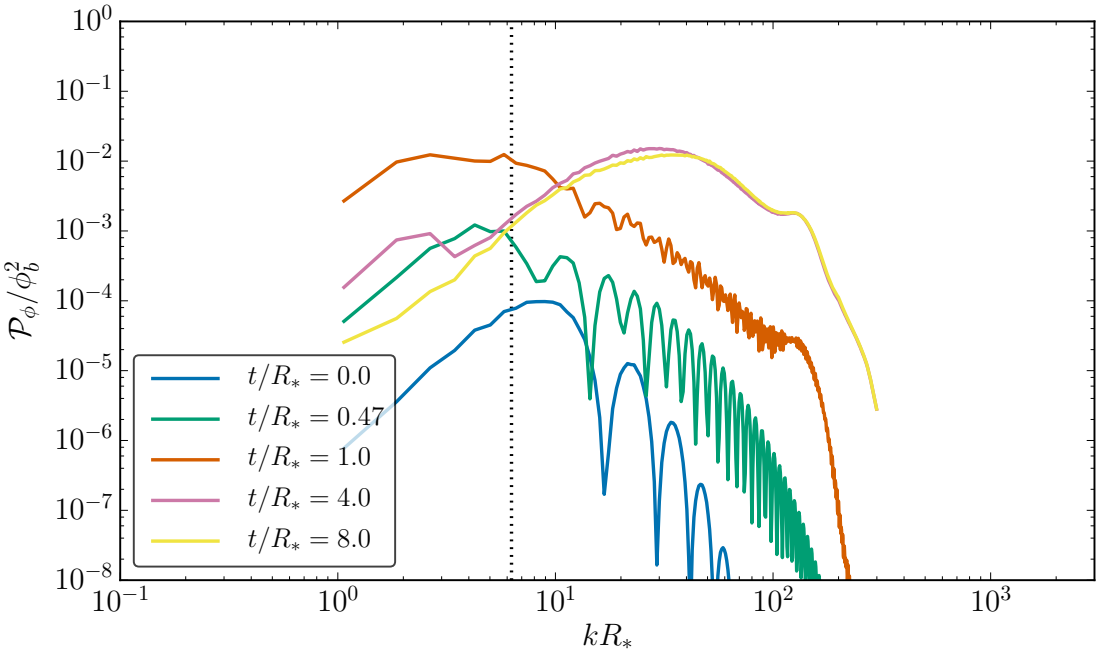

(b) Exponential

Figure 4.6: Scalar power spectra for simultaneous (top) and exponential (bottom) nucleation runs. Both simulations have $R_c M = 7.15$. The left plot has $N_b = 512$ and $\gamma_* = 1.97$, while the right plot has $N_b = 522$ and $\gamma_* = 1.96$. The full set of parameters of each run can be extracted from Tables 4.2 and 4.3. The initial configuration of the scalar field is seen at $t/R_* = 0$. The bubble expansion phase is seen for $t/R_* = 0.47$. The spectrum during bubble collision is seen at $t/R_* = 1.0$. The late time power spectrum after bubbles have collided is then shown at $t/R_* = 4.0$ and $t/R_* = 8.0$. The vertical black dotted line denotes $k = 2\pi/R_*$.

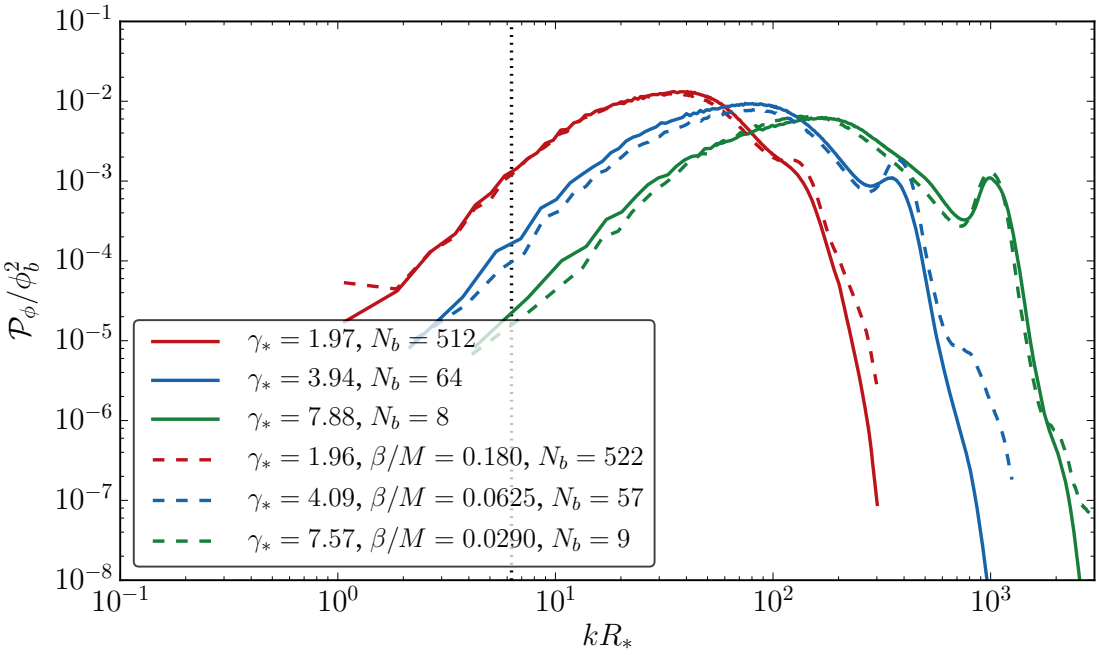

Figure 4.7: Comparison of the late time scalar power spectrum at $t/R_* = 8.0$ for both simultaneous (solid lines) and exponential (dashed lines) nucleation runs. All runs use bubbles with $R_c M = 7.15$. See Tables 4.2 and 4.3 for the full set of parameters of each run.

located in regions where bubbles are colliding. These are the locations where the spherical symmetry of the expanding bubbles is broken. During the oscillation phase the gravitational wave energy density becomes largely homogeneous with fluctuations on the percent level, though gravitational waves continue to be sourced.

In Fig. 4.8, we plot the gravitational wave power spectrum at several times over the duration of a simultaneous nucleation simulation with $\gamma_* \simeq 4$. As the bubbles begin to collide we begin to see a peak in the spectrum emerging near $k = 2\pi/R_*$, with a power law fall-off towards the UV. For this simulation we do not have a sufficient separation between R_* and $L\Delta x$ to estimate the power law towards the IR. As the collision phase completes this peak and the power law towards the IR persists, but a second peak associated with a much smaller length scale continues to grow. This second peak is due to gravitational waves sourced from oscillations in the scalar field with wavelengths close to the inverse mass of the scalar field.

In the same figure, we also plot the results of a numerical calculation in the envelope approximation, as detailed in [66], using the same bubble nucleation locations. The peak power in our simulation is closely reproduced by the envelope calculation, although the envelope calculation predicts that the peak is at higher frequency. The power law towards

the UV is somewhat steeper in the numerical simulations than in the envelope calculation.

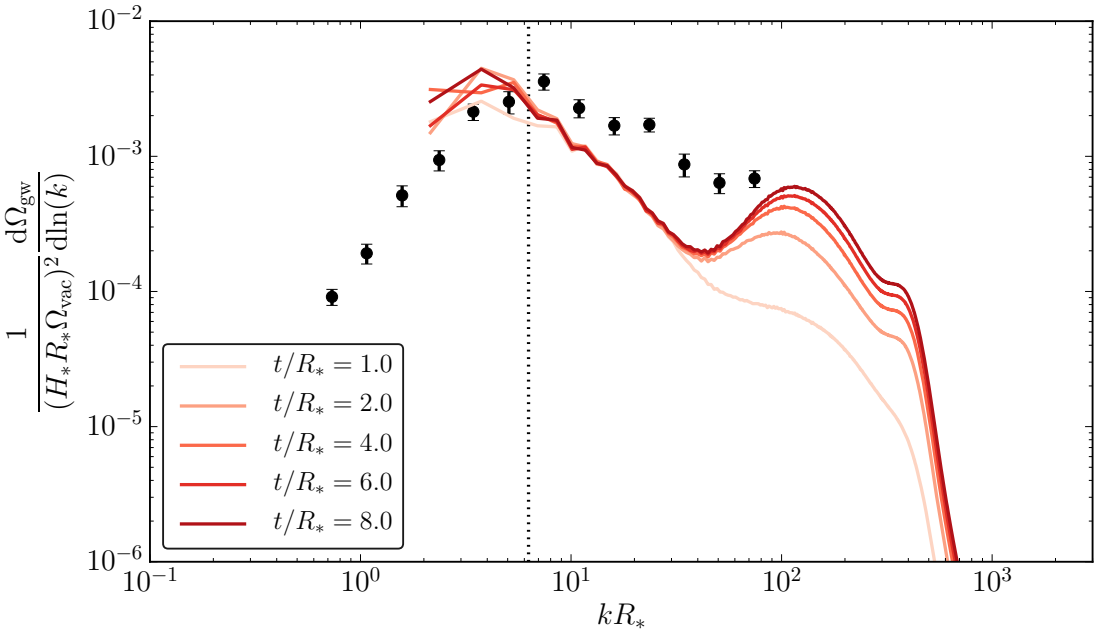

Figure 4.8: The gravitational wave power spectrum for the simultaneous nucleation run with $R_{\rm c}M = 7.15$, $N_b = 64$ and $\gamma_* = 3.94$ listed in Table 4.2. The vertical black dotted line marks where $k = 2\pi/R_*$. The black data points are the results for running a simulation with the envelope approximation with the same bubble locations and nucleation times.

We can show that the frequency of peak power is associated with the length scale of R_*, whereas the bump in the UV is associated with the length scale l_0. In Fig. 4.9, we plot the power spectra for three runs with different values of $R_{\rm c}$ and R_* but the same γ_*. It can be seen that the power peaks at $kR_* \simeq 3$, with a secondary peak at $kl_0 \simeq 3$.

In a realistic transition, the separation between R_* and l_0 will be many orders of magnitude, and we would expect the UV peak will be greatly suppressed due to the fall-off of the power spectrum with increasing k. We will estimate how large it can grow below.

Note that the power spectrum fluctuates due to the oscillations in the individual Fourier modes. In order to minimise this effect, in some plots we average over power spectra produced during an interval spanning several t/R_*. On these occasions the details are given in the caption of the figure.

We show the runs with $R_{\rm c}M = 7.15$ from Table 4.2 in Fig. 4.10. By increasing $N_{\rm b}$ while keeping R_* the same we are able to see further into the IR for a given γ_*. Apart from this increasing, $N_{\rm b}$ does not have a significant effect on the shape of the power spectrum,

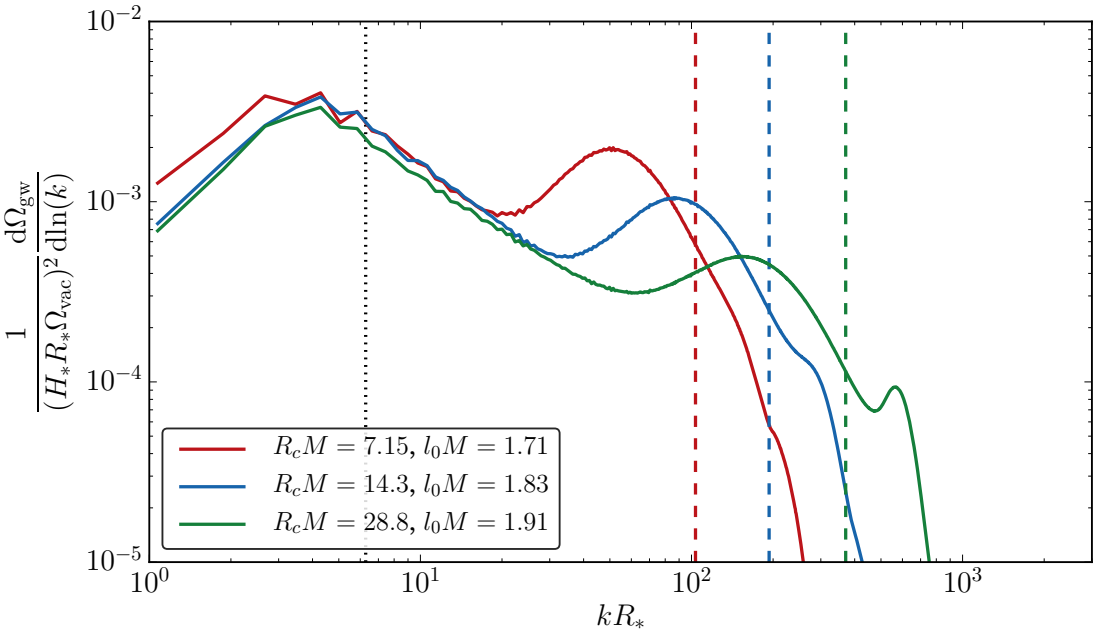

Figure 4.9: Gravitational wave power spectrum for several runs with different critical radius $R_{\rm c}$ and R_*. For each simulation the power spectra have been averaged over the interval $2.5 \leq t/R_* \leq 8.0$. All simulations shown have the same number of bubbles $N_b = 512$ and $\gamma_* \simeq 2$, with the full set of parameters listed in Table 4.2. We also plot the length scale associated with R_* as the vertical black dotted line, and the corresponding length scale for the initial wall width l_0 for each simulation as coloured dashed lines.

implying that $N_{\rm b} = 8$ is sufficient to measure the slope of the power law towards the UV. Increasing γ_* does not change the location or amplitude of the IR peak in respect to R_*. While the slope of the power spectrum towards the IR is in agreement with k^{-1} for $\gamma_* \simeq 2$, it appears steeper for $\gamma_* \simeq 4$ and $\gamma_* \simeq 8$. Between $\gamma_* \simeq 4$ and $\gamma_* \simeq 8$ the slope appears consistent.

4.6.2 Exponential and constant nucleation

In Fig. 4.11, we show the evolution of the power spectra for an exponential nucleation run with $\gamma_* \simeq 4$. Similar to in Fig. 4.8 we plot the results of a simulation using the envelope approximation as detailed in [66] using the same bubble nucleation locations and times.

For the exponential nucleation run we see that the envelope simulation gives an over-estimate of peak amplitude, but is still within an order of magnitude. From the full scalar field simulation we obtain a similar peak amplitude as in the simultaneous nucleation run shown in Fig. 4.8. This indicates that the scaling of gravitational wave production for

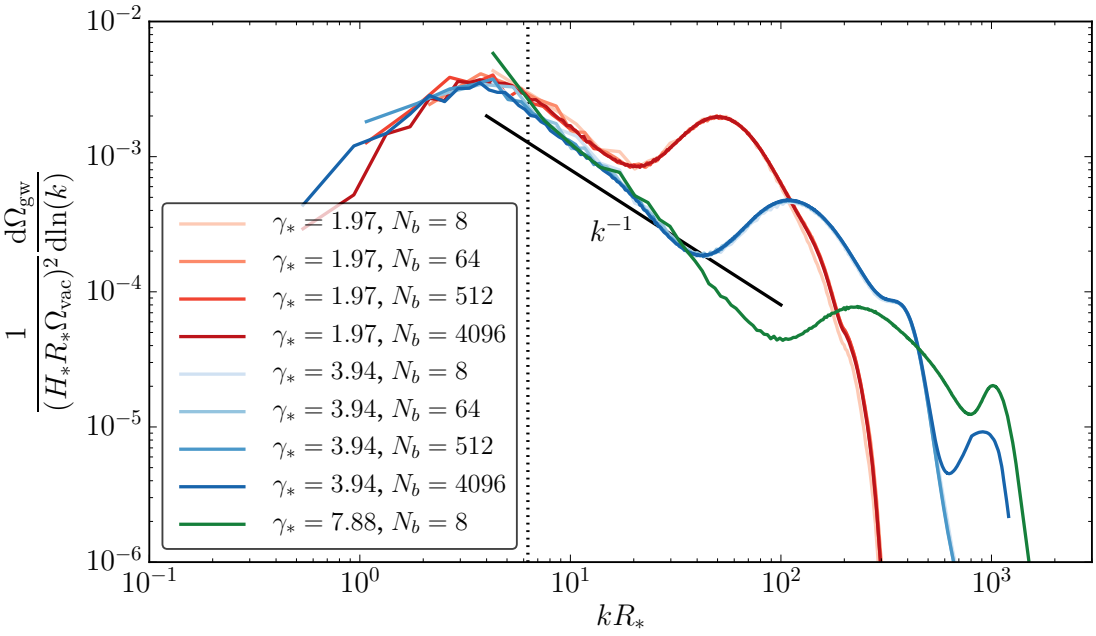

Figure 4.10: Gravitational wave power spectrum for all simultaneous bubble runs with $R_c M = 7.15$. The parameters for these runs are given in Table 4.2. For each simulation the power spectra have been averaged over the interval $2.5 \leq t/R_* \leq 8.0$. The solid black line shows a power law of k^{-1}. We plot as a vertical black dotted line the wave number $k = 2\pi/R_*$. See Table 4.2 for the full set of parameters of each run.

our simulations is governed by R_* rather than β. Once again the peak location is shifted slightly into the IR in comparison to the envelope simulation.

The power spectra for all exponential simulation runs are shown in Fig. 4.12. For similar γ_*, we see convergence to the resulting slope of the power spectra for even small numbers of bubbles, implying that even $N_b = 8$ creates a satisfactory ensemble.

All simulations seem to be consistent regarding the location and height of the peak in the IR and there is even agreement with the simultaneous nucleation runs. The slope of the power spectrum towards the IR is steeper than k^{-1} for $\gamma_* \simeq 4$ and $\gamma_* \simeq 8$, and appears consistent between them.

The two constant nucleation runs listed in Table 4.4 are found to produce power spectra that are consistent with the simultaneous and exponential nucleation runs. We plot the power spectra for the constant nucleation runs along with the other $\gamma_* \simeq 4$ runs in Fig. 4.15.

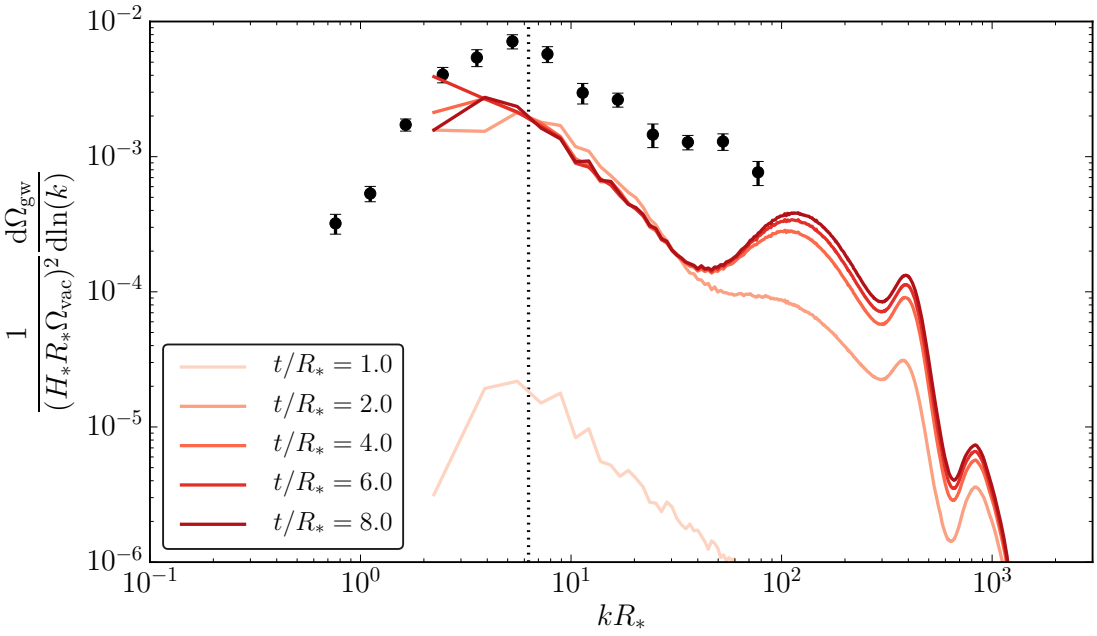

Figure 4.11: Gravitational wave power spectrum for the exponential nucleation run with $R_{\rm c}M = 7.15$, $N_b = 57$ and $\gamma_* = 4.09$ listed in Table 4.2. The vertical black dotted line marks where $k = 2\pi/R_*$. The black data points are the results for running a simulation with the envelope approximation with the same bubble locations and nucleation times.

4.6.3 Late time power spectrum

We are able to see the shape of the power spectrum generated during the oscillation phase by setting $u_{ij} = 0$ after the collision phase has completed. We chose a time $t/R_* = 2$ to set $u_{ij} = 0$. However for some simulations there appears to have been regions in which bubbles were still colliding at this time, and so a later time should have been chosen. For these simulations there is an uptick in the power spectrum in the IR, which can contribute significantly to the energy density. As the IR bins consist of only a few modes, there can be large oscillations in $\Omega_{\rm gw}$.

The evolution of the power spectrum from the oscillation phase is shown in Fig. 4.13. The spectrum consists of a bump in the UV corresponding to the length scale of l_0 and also a plateau extending from the bump up to just before the length scale of R_* in the IR. A similar shape can perhaps be discerned in Ref. [118], where the contribution to the total power spectrum from the oscillation phase appears to dominate. In the aforementioned study, the gravitational power spectrum from collisions was estimated to be between two and three orders of magnitude smaller than that predicted by the envelope approximation. The reason for this deficit is unclear. There was also a relatively small scale separation

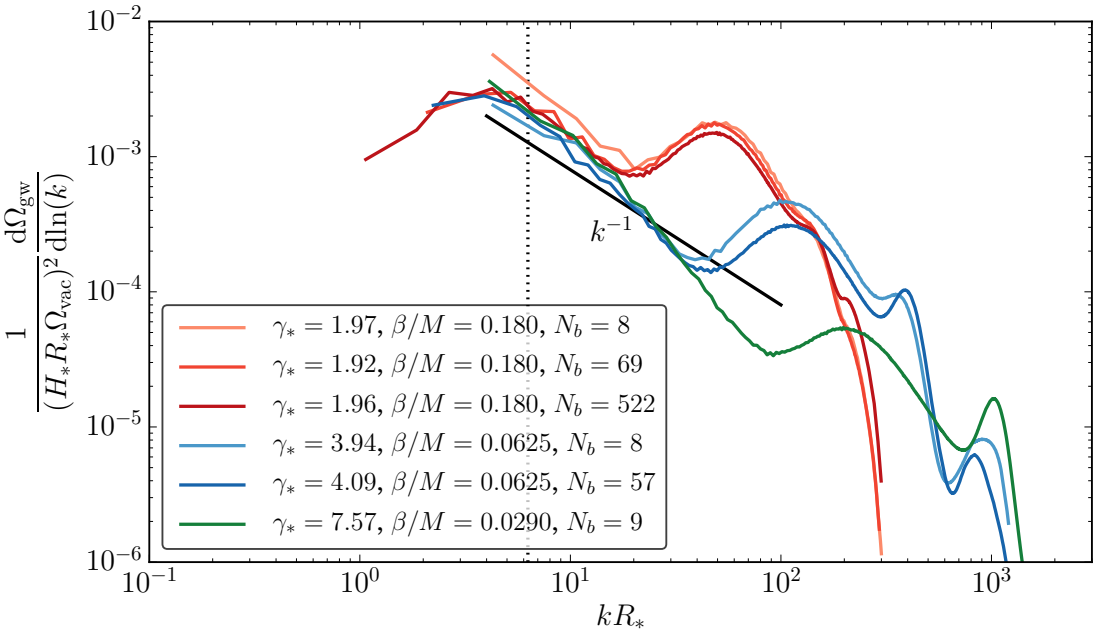

Figure 4.12: Gravitational wave power spectrum for all exponential nucleation runs with $R_{\rm c}M = 7.15$. The parameters for these runs are given in Table 4.3. For each simulation the power spectra have been averaged over the interval $2.5 \leq t/R_* \leq 8.0$. The solid black line shows a power law of k^{-1}. Also plotted as a vertical black dotted line is $kR_* = 2\pi$.

between R_* and l_0, as γ_* ranges between $\gamma_* \simeq 2$ and $\gamma_* \simeq 3$. Together these may explain why the contribution from the oscillation phase dominated that of bubble collisions.

We can see that the power spectrum continues to grow during the oscillation phase. One might conclude that the contribution from the oscillation phase would eventually dominate that from the bubble collisions. We therefore plot $\Omega_{\rm gw}$ for a set of simulations where the metric perturbations are turned on after $t/R_* = 2.0$ in Fig. 4.14. We are able to estimate the growth of $\Omega_{\rm gw}$ during the oscillation phase from these simulations. We find that

$$\frac{d\Omega_{\rm gw}^{\rm osc}}{dt} \sim 10^{-1} \frac{(H_* l_0 \Omega_{\rm vac})^2}{R_*}. \tag{4.47}$$

The largest amount of time that $\Omega_{\rm gw}^{\rm osc}$ can grow before the growth is cut off by expansion [62] is one Hubble time H_*^{-1}.

From our earlier plots we can estimate the contribution to $\Omega_{\rm gw}$ from the bubble collision phase is

$$\Omega_{\rm gw}^{\rm coll} \sim 10^{-3} (H_* R_* \Omega_{\rm vac})^2. \tag{4.48}$$

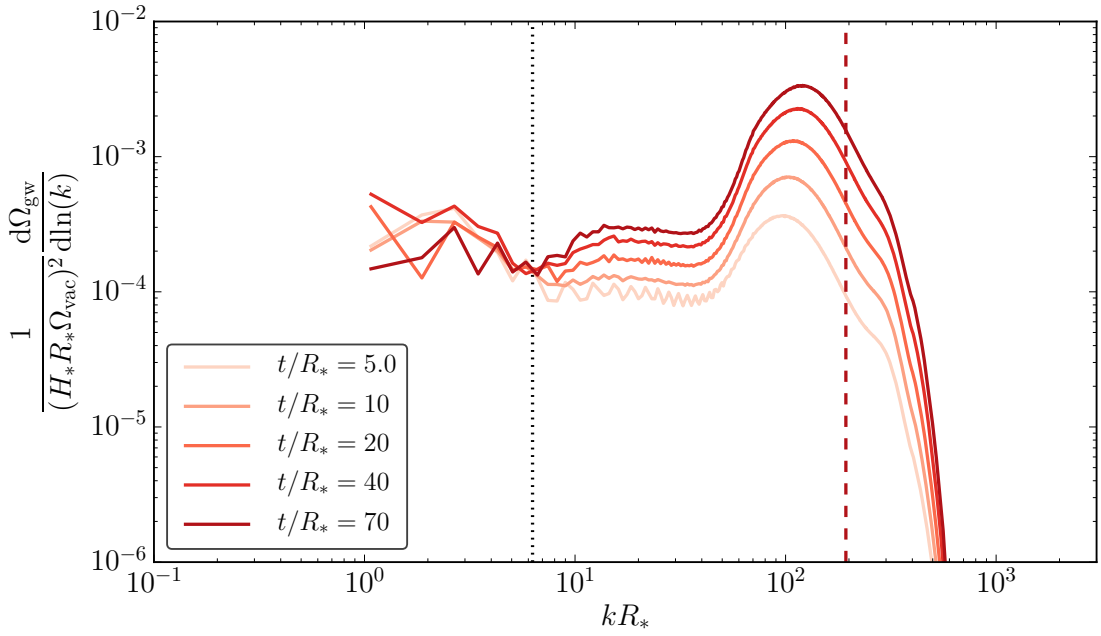

Figure 4.13: Late time power spectrum from gravitational waves generated from the oscillation stage. Metric perturbations are only turned on after $t/R_* = 2$. This is for the run with $R_{\rm c}M = 14.3$, $N_b = 512$ and $\gamma_* = 3.94$ listed in Table 5.3, where the full set of parameters of this run are given. The vertical black dotted line designates where $k = 2\pi/R_*$ and the dashed red line shows where $k = 2\pi/l_0$.

Therefore the ratio between these two contributions is

$$\frac{\Omega_{\rm gw}^{\rm coll}}{\Omega_{\rm gw}^{\rm osc}} \sim 10^{-2}(R_* H_*)^3 \frac{1}{(l_0 H_*)^2}, \tag{4.49}$$

$$\sim 10^{-3} \frac{H_*^3}{n_{\rm b}} \frac{(M_{\rm b} m_{\rm Pl})^2}{\rho_c}, \tag{4.50}$$

where $m_{\rm pl}$ is the Planck mass. For a vacuum dominated phase transition $\rho_c \sim \rho_{\rm vac} < \frac{1}{12\lambda} M_{\rm b}^4$.

$$\frac{\Omega_{\rm gw}^{\rm coll}}{\Omega_{\rm gw}^{\rm osc}} \gtrsim 10^{-1} \frac{H_*^3}{n_{\rm b}} \left(\frac{m_{\rm Pl}}{M_{\rm b}}\right)^2. \tag{4.51}$$

Providing that the mass scale of the phase transition is sufficiently smaller than the Planck scale, the contribution from the collision phase should dominate.

4.6.4 Fitting

In Fig. 4.15, we plot gravitational wave power spectra from all simultaneous, exponential and constant nucleation runs with $\gamma_* \simeq 4$. We can see that they seem to be consistent, indicating that nucleation rate makes little difference to the power spectra as a function

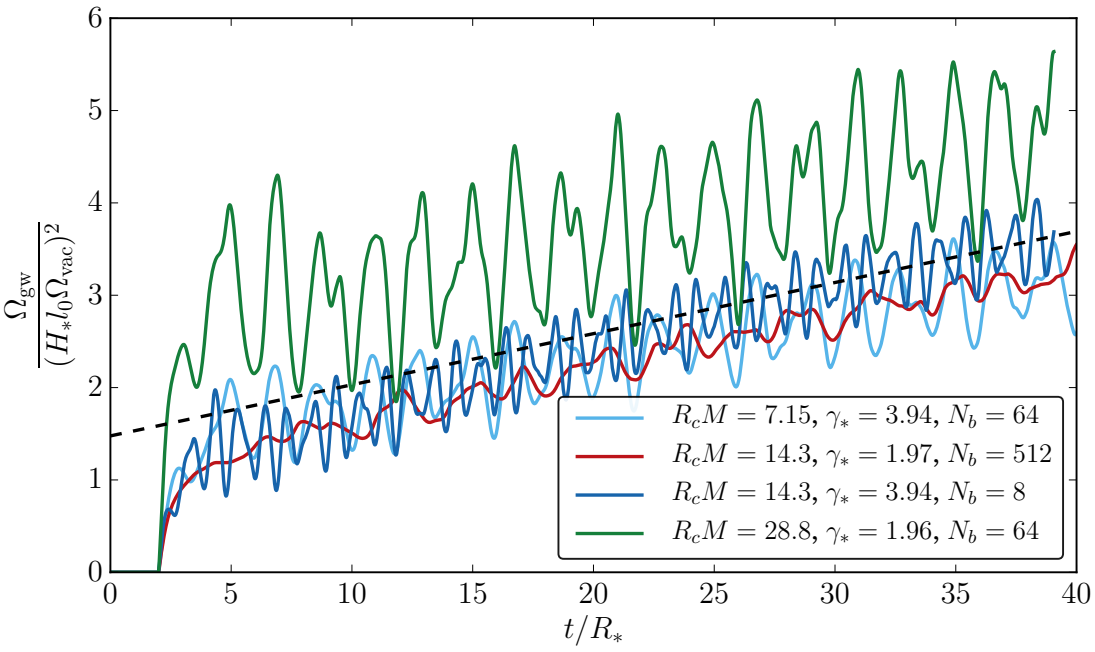

Figure 4.14: Total $\Omega_{\rm gw}$ from gravitational waves generated after $t/R_* = 2$ for a series of simulations with different $R_{\rm c}$, N_b and γ_*, see Table 5.3. The oscillations are due to ringing in the IR of the power spectrum. The dashed black line is a fit for the rate of increase of $\Omega_{\rm gw}$, with a slope of $d\Omega_{\rm gw}/dt = 0.06\,(H_* l_0 \Omega_{\rm vac})^2/R_*$.

of kR_*. We can therefore provide a fit for the gravitational wave power spectrum from collisions, applying to all nucleation histories.

The first two bins of the numerical power spectra contain very few modes and are expected to be significantly affected by finite size effects. To produce our fit we shall use the largest simultaneous nucleation simulation for $\gamma_* \simeq 4$ with $N_{\rm b} = 4096$ as this provides us with the largest dynamic range. This is the only simulation in which we can resolve the peak location after removing the first two bins.

Even so, we do not have sufficient dynamic range to be able to estimate the power law towards the IR. On causal grounds, though, it is expected that the IR power goes as k^3 [71]. Our peak is somewhat broader than previously seen in the envelope approximation.

We find a fit of the following form

$$\frac{d\Omega_{\rm gw}^{\rm fit}}{d\ln k} = \Omega_{\rm p}^{\rm fit} \frac{(a+b)^c \tilde{k}^b k^a}{(b\tilde{k}^{(a+b)/c} + a k^{(a+b)/c})^c}, \tag{4.52}$$

where we fix $a = 3$. Then we find that

$$\Omega_{\rm p}^{\rm fit} = (3.22 \pm 0.04) \times 10^{-3} \, (H_* R_* \Omega_{\rm vac})^2, \tag{4.53}$$

$$\tilde{k} R_* = 3.20 \pm 0.04, \tag{4.54}$$

$$b = 1.51 \pm 0.04, \tag{4.55}$$

$$c = 2.18 \pm 0.15, \tag{4.56}$$

with errors taken from the covariance matrix of the fit. We plot our fit in Fig. 4.15.

We provide the fit in terms of the mean bubble separation R_*, which has a clear definition in all nucleation histories, and is related to the nucleation probability through equations (4.21), (4.19) and (4.23), and the definition of $R_* = n_{\rm b}^{-1/3}$. For example, for exponential nucleation,

$$\beta = \frac{(8\pi)^{1/3} v_{\rm w}}{R_*}. \tag{4.57}$$

Using Eq. (4.57) with $v_{\rm w} = 0.97$ we find that

$$\frac{\Omega_{\rm p}^{\rm fit}}{\Omega_{\rm p}^{\rm env}} = 0.55, \tag{4.58}$$

and

$$\frac{\tilde{k}_{\rm fit}}{\tilde{k}_{\rm env}} = 1.0. \tag{4.59}$$

We plot both our fit and also the fit from the envelope approximation in Fig. 4.15.

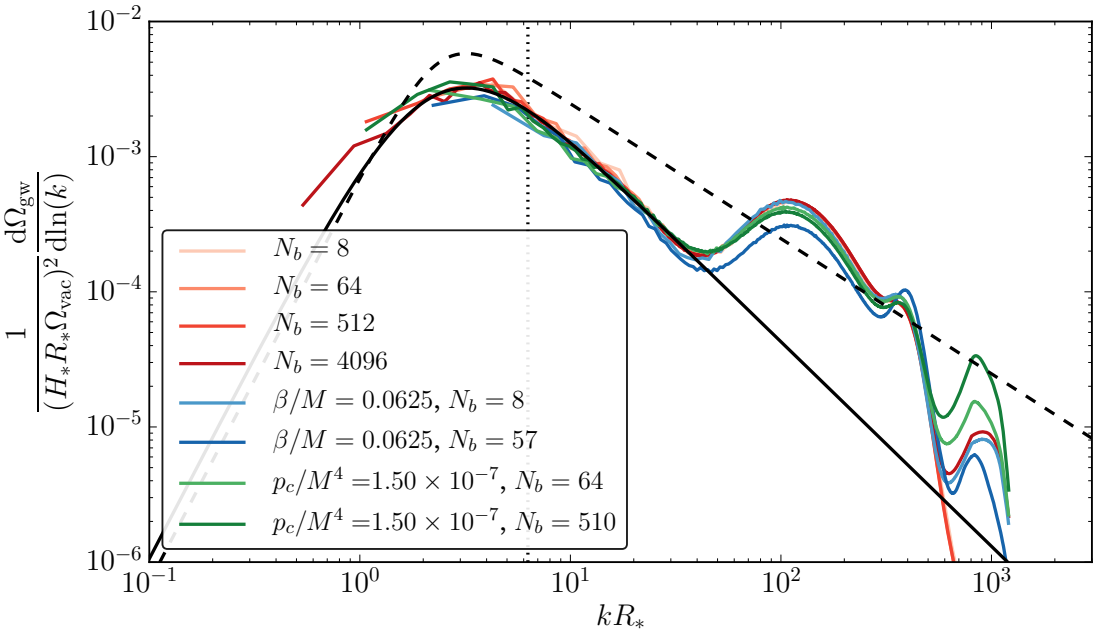

Figure 4.15: Scaled gravitational wave power spectrum for all simulations with $\gamma_* \simeq 4$. For each simulation the power spectra have been averaged over the interval $2.5 \leq t/R_* \leq 8.0$. Simultaneous nucleation runs are plotted in red, exponential nucleation in blue, and constant nucleation in green. From these simulation runs we make a fit for the gravitational wave power spectrum from bubble collisions given R_*, which is shown as the black solid line. The envelope approximation fit as given in [122] is shown as the dashed black line, where we have used Eq. (4.57) to convert between β and R_*.

4.7 Conclusions

We have performed the largest scale lattice simulations of a pure vacuum transition to date. In doing so we have been able to test the envelope approximation's description of the resulting gravitational wave power spectrum, at high bubble wall Lorentz factors γ_* and for many bubbles. We have simulated three different bubble nucleation histories, where bubbles are either nucleated simultaneously, with an exponentially increasing nucleation rate, or with a constant rate.

In our simulations, the peak gravitational wave power has approximate agreement with the most recent envelope approximation fit [122], to within a factor of two. The peak frequency in the envelope approximation fit has very good agreement with our results.

When the gravitational wave power is calculated using the envelope approximation's model of the actual bubbles of our simulation, the peak location is shifted towards slightly higher frequencies.

As we increase γ_* beyond $\gamma_* \simeq 2$ we find that the power law on the high frequency side of the peak becomes approximately $k^{-1.5}$, steeper than the k^{-1} predicted by the envelope approximation.[2] The power law on the low frequency side is consistent with the k^3 predicted by causality [71, 152], but we do not have sufficient dynamic range for an independent estimate. We provide a 3-parameter fit to our results Eq. (4.52).

In our simulations the overlap regions where bubbles have recently collided have extended regions in which the scalar field has large amplitude oscillations around the true vacuum, even returning to the false vacuum. These regions are not accounted for in the envelope approximation, and may be a source of its inaccuracy. Large amplitude nonlinear oscillations with wavelength of order the bubble wall width l_0 continue long after the bubbles finish colliding, which is also not included in the envelope approximation. These oscillations source gravitational waves which lead to an additional bump in the UV of the power spectrum at a frequency of order l_0^{-1}.

In the early universe, the gravitational wave source will eventually diminish due to thermalisation and Hubble expansion. We find that even if the bump continues to grow for as long as a Hubble time, H_*^{-1}, the power spectrum from the oscillation phase will be subdominant to that of bubble collisions providing that the mass of the scalar field is much less than the Planck mass.

In testing the envelope approximation and investigating the oscillatory phase of the scalar field, we have neglected the expansion of the universe, and therefore the fit we provide strictly applies only to transitions in which the duration is much shorter than the Hubble time H_*^{-1}. There is more work to do to study the case where the universe enters an inflationary phase before bubbles start nucleating.

Acknowledgements

We thank the Mainz Institute for Theoretical Physics (MITP) for its hospitality and support. We thank the LISA Cosmology Working Group for providing a forum to discuss our work, and extend further thanks to its coordinators Chiara Caprini and Germano Nardini. We are grateful to Stephan Huber, Ryusuke Jinno, and Kari Rummukainen for useful discussions, and to Nicola Hopkins for important contributions to this project in its early stages. Our simulations made use of the COSMOS Consortium supercomputer (within the DiRAC Facility jointly funded by STFC and the Large Facilities Capital Fund

[2] This steeper power law is closer to the $k^{-1.8}$ reported for two-bubble collisions [55, 57], widely taken to be the envelope approximation prediction before the work of Ref. [59].

of BIS) and the Finnish Centre for Scientific Computing CSC. DC (ORCID ID 0000-0002-7395-7802) is supported by an STFC Studentship. MH (ORCID ID 0000-0002-9307-437X) acknowledges support from the Science and Technology Facilities Council (grant numbers ST/L000504/1 and ST/P000819/1). DJW (ORCID ID 0000-0001-6986-0517) was supported by Academy of Finland grant no. 286769 and the Research Funds of the University of Helsinki.

Chapter 5

Gravitational waves from vacuum first-order phase transitions II: from thin to thick walls

Daniel Cutting[a,b], Elba Granados Escartin[b], Mark Hindmarsh[a,b] and David Weir[b,c]

[a] *Department of Physics and Astronomy, University of Sussex, Falmer, Brighton, BN1 9QH, U.K.*

[b] *Department of Physics and Helsinki Institute of Physics, PL 64, FI-00014, University of Helsinki, Finland*

[c] *School of Physics and Astronomy, University of Nottingham, Nottingham, NG7 2RD, U.K.*

Abstract

In a vacuum first-order phase transition, gravitational waves are generated from collision of bubbles of the true vacuum. The spectrum from such collisions takes the form of a broken power law. We consider a toy model for such a phase transition, where the dynamics of the scalar field depends on a single parameter $\overline{\lambda}$, which controls how thin the bubble wall is at nucleation and how close to degenerate the vacua are relative to the barrier. We extend on our previous work by performing a series of simulations with a range of $\overline{\lambda}$. The peak of the gravitational-wave power spectrum varies by up to a factor of 1.3, which is probably an unobservable effect. We find that the ultraviolet (UV) power law in the gravitational-wave spectrum becomes steeper as $\overline{\lambda} \to 0$, varying between $k^{-1.4}$ and $k^{-2.2}$ for the $\overline{\lambda}$ considered. This provides some evidence that the form of the underlying effective potential of a vacuum first-order phase transition could be determined from the gravitational-wave spectrum it produces.

5.1 Introduction

Upcoming space-based gravitational-wave detectors like the Laser Interferometer Space Antenna [137] (LISA) are anticipated to dramatically increase our capability to probe early universe cosmology through gravitational waves [76]. In particular, LISA will be sensitive to first-order cosmological phase transitions at the electroweak scale [77, 90].

In the Standard Model, the electroweak transition is a crossover [19, 20], and as such there are no first-order phase transitions at the electroweak scale. However, there are a multitude of well-motivated extensions to the Standard Model that produce first-order phase transitions, ranging from singlet extensions [25–28, 33], two-Higgs doublet models [29–31], models in which a conformal symmetry is spontaneously broken [46–52], to models with a phase transition in a hidden sector [37–43, 153, 154]. The gravitational wave signal generated by phase transitions in these Beyond the Standard Model extensions will enable LISA to detect or constrain their existence.

In a first-order cosmological phase transition, some effective scalar field is trapped in a metastable state (symmetric phase), separated by a potential barrier from the true vacuum state (broken phase) [4–6]. When the transition proceeds, bubbles of the true vacuum nucleate, expand and eventually collide, sourcing transverse-traceless modes of shear stress, which in turn source gravitational waves [53, 54]. The dynamics of the resulting phase transition can be split qualitatively according to whether the bubble wall reaches a terminal velocity before colliding, or whether the bubble wall continues to accelerate until collision. We denote these different transition types respectively as 'thermal' and 'vacuum-like'.

In a thermal phase transition, bubbles nucleate in the presence of a hot relativistic plasma made up of the early universe particle content. The friction felt between the plasma and the expanding bubble wall is sufficient to eventually result in the wall approaching a terminal wall velocity. Shells of hotter plasma develop around the expanding bubbles, and after collision continue to propagate as long-lasting sound waves. Eventually, the sound waves are expected to decay, and the flow may become turbulent [53, 67].

In a vacuum-like transition, the vacuum pressure driving the phase transition overcomes the resulting friction from the plasma and the bubble wall continues to accelerate before collision. An early study predicted that in most electroweak scale phase transitions the bubble wall would undergo 'run away' acceleration, provided sufficient supercooling [89]. More recently, it has been shown that if the scalar field couples to heavy gauge bosons, next-to-leading-order effects cause the friction to grow proportionally to the Lorentz factor γ of the bubble wall [87]. In this case, the runaway condition in Ref. [89]

is no longer fulfilled.

Several scenarios have been proposed that can still result in 'vacuum-like' behaviour. The friction term proportional to γ is generated by transition radiation of gauge bosons acquiring a mass as they cross the bubble wall. If the phase transition occurs in the absence of gauge fields, such as during the spontaneous breaking of an approximate global symmetry, then the dominant transition radiation process may grow as $\sim \log \gamma$ [90].

Alternatively, if there is an extreme level of supercooling, then there could be a sufficient dilution of the early universe plasma and resulting plasma friction to allow for the bubble walls to accelerate until collision. The levels of supercooling required for this to occur is large but can be achieved in transitions with a classically scale-invariant potential [91]. In other models, sufficient supercooling is difficult to achieve; at large supercooling the universe can start to inflate, meaning that the bubbles cannot percolate and the transition does not complete [98].

Finally, in a dark sector that is decoupled at the time of transition, runaway-type transitions are achieved more easily than in the visible electroweak sector [41].

The first attempts to model the gravitational-wave power spectrum from first-order phase transitions employed a seminumerical simulation method termed the 'envelope approximation'. In this calculation, the stress-energy is assumed to be located in an infinitesimally thin shell at the bubble wall which disappears upon collision [57]. This technique was first applied to vacuum transitions, and then to thermal transitions [58, 59, 122]. When the bubble wall velocity is ultra-relativistic the resulting gravitational-wave spectrum was shown to be a broken power law rising in the infrared (IR) and falling in the ultraviolet (UV) as approximately $k^{2.9}$ and $k^{-0.9}$, respectively. Analytic studies which build upon the envelope approximation have confirmed the broken power laws found from numerical simulations [121].

Extensions to the envelope approximation in which the shell of shear-stress continues to propagate after collision have also been studied [122, 123]. We will follow Ref. [122] in referring to this as the bulk flow model. Simulations of the bulk flow model with ultra-relativistic wall velocities have found power laws of approximately $k^{0.9}$ and $k^{-2.1}$.

Many developments have been made in the study of thermal phase transitions. 3D hydrodynamical simulations of weak and intermediate strength transitions [60–63] demonstrated that sound waves form the dominant contribution to the gravitational-wave signal and that while the contribution from bubble collisions is subdominant, for thermal phase transitions it is well represented by the envelope approximation [66]. Modelling has shown

weak and intermediate strength transitions are well represented shortly after the transition by a linear superposition of propagating sound waves [64, 65].

Simulations of stronger first-order phase transitions indicated that for walls moving slower than the speed of sound, the formation of hot droplets of the symmetric phase in the later stages of the collisions can significantly reduce the gravitational-wave signal [2]. The gravitational wave production in extremely strong phase transitions has also been studied using a combination of 1D simulations and modelling [155]. It has been shown that for almost all observable transitions, the timescale on which nonlinearities in the fluid are expected to play a role (given by the ratio of the bubble radius to the root-mean-square fluid velocity) is shorter than a Hubble time [125]. On longer timescales, the flow may become turbulent. The gravitational wave spectrum from freely decaying turbulence has been modelled [58, 68–72], and recently numerically simulated [73].

Full 3D lattice simulations have also been employed to test the envelope approximation within vacuum transitions [1, 118]. In Ref. [118], it was seen that after percolation, the gravitational-wave signal in a vacuum transition was amplified by more than an order of magnitude during a what was termed a period of coalescence. A more recent study by the present authors identified this growth of gravitational waves with oscillations of the scalar field around the true vacuum, producing gravitational waves peaked at the broken-phase mass scale [1]. With a realistic separation of scales between the mass scale and the mean bubble separation, the signal generated by these oscillations would be negligible in comparison to that from bubble collisions, and peak at too high a frequency to be observable. It also found that while the peak frequency and amplitude of the spectrum were roughly predicted by the envelope approximation, the UV power law was slightly steeper at around $k^{-1.5}$.

Early studies of two colliding bubbles in the thin wall limit demonstrated that the scalar field in the overlap region rebounds to the false vacuum, and can become temporarily trapped [55, 114, 156]. Further simulations have shown that far away from the thin wall limit, the trapping is reduced [115].

The question of trapping has recently been revisited in light of the recent interest in the dynamics of cosmological first-order phase transitions. In Ref. [116] the collision of two ultra-relativistic planar bubble walls was studied for a variety of potential shapes. Depending on the shape of the potential, it was seen that the scalar field could become trapped temporarily in the false vacuum in the collision region. The authors proposed that if trapping indeed occurred, then the gravitational-wave power spectrum should be given

by the envelope approximation, but if it did not then the bulk flow model should apply. This has been investigated by colliding two vacuum bubbles and measuring the resulting gravitational-wave power spectrum [117], where small changes were observed when varying the potential shape.

In this paper, we conduct a series of 3D lattice simulations of colliding vacuum bubbles, with the intention of exploring how modifying the shape of the effective potential changes the gravitational-wave spectrum. We consider a vacuum phase transition in a toy model with a quartic effective potential with a cubic term. We show that for this model, the effect of the potential on the scalar field dynamics can be shown to depend on a single parameter $\overline{\lambda}$. As $\overline{\lambda} \to 1$ the potential approaches thin-wall limit, whereas for $\overline{\lambda} \to 0$ the bubble wall becomes thick in comparison to the critical radius. We see that as $\overline{\lambda} \to 0$, less trapping occurs in the collision region. Our simulations span a range of $\overline{\lambda}$ and we analyse the effect changing $\overline{\lambda}$ has on the gravitational-wave power spectrum. The peak of the gravitational-wave power spectrum varies by a factor of up to 1.3 between the $\overline{\lambda}$ values we consider. We find that UV power law in the gravitational-wave spectrum becomes steeper as $\overline{\lambda} \to 0$, varying between $k^{-1.4}$ for $\overline{\lambda} = 0.84$ and $k^{-2.2}$ for $\overline{\lambda} = 0.07$.

We also find some evidence that the power law in the IR continues to evolve after the bubbles finish colliding. While at early times it is proportional to k^3 (as one would expect from causality [71]), it becomes shallower after the bubbles have finished colliding. By visualising our simulations, we can see that there are outward-propagating shells of transverse-traceless shear-stress that continue to propagate outwards This provides some evidence for the bulk flow model which assumes the continued outward propagation of shear-stress after bubbles have collided.

In Section 5.2 we discuss the dynamics of the scalar field, and how it varies according to the potential shape in our toy model. We illustrate how the variation of $\overline{\lambda}$ modifies the critical bubble profile, the evolution of an isolated bubble, and the dynamics of the scalar field in the overlap region of two colliding bubbles. We detail the linearised gravity approach we employ within our simulations in Section 5.3, and outline the current understanding of the gravitational-wave power spectrum produced in a vacuum transition. We describe the numerical methods we employ in our simulations in Section 5.4. The results we obtain are split into two sections, in Section 5.5 we show the behaviour of the scalar field and transverse traceless shear-stress, whereas in Section. 5.6 we analyse the resulting gravitational-wave power spectrum and provide a fit for the power spectrum over time for each $\overline{\lambda}$. Finally, in Section 5.7 we list our conclusions.

5.2 Scalar field dynamics

In a vacuum first-order phase transition, the universe transitions from a metastable false vacuum state into a true vacuum state. In a first-order phase transition, a potential barrier will separate these two states. Local patches of the universe will transition into the true vacuum state via quantum tunneling. These patches of the true vacuum state will form bubbles, with the interface between the true and false vacuum forming the bubble wall. After nucleating, these bubbles will expand, eventually reaching cosmological sizes and ultra-relativistic speeds before they collide.

We can describe the transition by using a scalar field order parameter ϕ which corresponds to the vacuum expectation value of the field transitioning. The equation of motion for this scalar field in our simulations is:

$$\Box\phi - V'(\phi) = 0, \tag{5.1}$$

where we choose the scalar field potential $V(\phi)$ to be given by

$$V(\phi) = \frac{1}{2}M^2\phi^2 + \frac{1}{3}\delta\phi^3 + \frac{1}{4}\lambda\phi^4. \tag{5.2}$$

Note here that we are neglecting the expansion of the universe in the dynamics of the scalar field. This is equivalent to making the assumption that the duration of the phase transition is much shorter than a Hubble time at the time of the transition H_*^{-1}.

This potential has a degenerate second ground state when the mass M is equal to the critical mass value,

$$M_{\rm c}^2 = \frac{2\delta^2}{9\lambda}. \tag{5.3}$$

It is useful to introduce the parameter $\overline{\lambda} = M^2/M_{\rm c}^2$. When $\overline{\lambda} < 1$ this potential has two ground states, one of which is metastable. The metastable state (or symmetric phase) is at $\phi = 0$ and the true vacuum state (or broken phase) is at

$$\phi_{\rm b} = \frac{3M_{\rm c}}{2\sqrt{2\lambda}}\left[1 + \sqrt{1 - 8\overline{\lambda}/9}\right], \tag{5.4}$$

The symmetric phase at $\phi = 0$ is separated from the broken phase at $\phi_{\rm b}$ by a potential barrier, which peaks at

$$\phi_{\rm max} = \frac{3M_{\rm c}}{2\sqrt{2\lambda}}\left[1 - \sqrt{1 - 8\overline{\lambda}/9}\right]. \tag{5.5}$$

The broken phase mass is given by

$$M_{\rm b} = \frac{3M_{\rm c}}{2}\sqrt{1 - \frac{8\overline{\lambda}}{9} + \sqrt{1 - \frac{8\overline{\lambda}}{9}}}. \tag{5.6}$$

Furthermore the potential difference between the two minima is given by

$$\rho_{\rm vac} = \frac{1}{12\lambda}\left(M_{\rm b}^4 - M^4\right), \tag{5.7}$$

and the height of the potential barrier $V_{\rm max} = V(\phi_{\rm max}) - V(0)$,

$$V_{\rm max} = \frac{M^6\left(M^2 + 2M_{\rm b}^2\right)}{\left(M^2 - M_{\rm b}^2\right)\left(M^2 + M_{\rm b}^2\right)^3}. \tag{5.8}$$

The total energy density in the scalar field ρ_ϕ can be split into three components,

$$\rho_\phi = \rho_{\rm K} + \rho_V + \rho_{\rm D}, \tag{5.9}$$

with the kinetic energy density,

$$\rho_{\rm K} = \frac{1}{2}\dot{\phi}^2, \tag{5.10}$$

the gradient energy density,

$$\rho_{\rm D} = \frac{1}{2}(\nabla\phi)^2, \tag{5.11}$$

and the potential energy density,

$$\rho_V = V(\phi) - V(\phi_{\rm b}). \tag{5.12}$$

We are free to rescale the potential by some constant value, and likewise the field, i.e $V \to V' = cV$ or $\phi \to \phi' = k\phi$. After accounting for this there are only two interesting dimensionless quantities that describe our potential which can affect the dynamics.

The first of these quantities is the ratio of $V_{\rm max}$ and $\rho_{\rm vac}$,

$$\frac{V_{\rm max}}{\rho_{\rm vac}} = \frac{\left(\sqrt{9-8\overline{\lambda}}-3\right)^2\left(4\overline{\lambda}+\sqrt{9-8\overline{\lambda}}-3\right)}{\left(\sqrt{9-8\overline{\lambda}}+3\right)^2\left(-4\overline{\lambda}+\sqrt{9-8\overline{\lambda}}+3\right)}. \tag{5.13}$$

The second is the ratio of $M_{\rm b}^2$ and M^2. This is given by

$$\frac{M_{\rm b}^2}{M^2} = \frac{4\overline{\lambda}}{9-8\overline{\lambda}+3\sqrt{9-8\overline{\lambda}}}. \tag{5.14}$$

Both of these ratios depend solely on $\overline{\lambda}$ rather than any other combination of the potential parameters.

Furthermore, we can reparameterize the scalar field as $\psi = \phi/\phi_{\rm b}$ and rewrite the coordinates $x'^\mu = x^\mu M$ in order to obtain the following equation of motion,

$$0 = M^2\phi_{\rm b}\left(\Box'\psi - \left(\psi - \frac{3\left(\sqrt{9-8\overline{\lambda}}+3\right)}{4\overline{\lambda}}\psi^2 + \frac{9-4\overline{\lambda}+3\sqrt{9-8\overline{\lambda}}}{4\overline{\lambda}}\psi^3\right)\right), \tag{5.15}$$

where $\Box' = \dfrac{\partial}{\partial x'^\mu}\dfrac{\partial}{\partial x'_\mu}$. Clearly the dynamics here depend only on the value of $\overline{\lambda}$.

In the limit of $\overline{\lambda} \to 1$ the minima of the potential become degenerate, and this corresponds to the thin wall limit of our potential. In the limit $\overline{\lambda} \to 0$ the potential barrier becomes infinitesimally small in comparison to the potential energy difference. We call this the thick wall limit. To see how varying $\overline{\lambda}$ affects the scalar field potential, see Fig. 5.1.

By varying $\overline{\lambda}$ between one and zero we are able to fully explore the physically meaningful parameter space of our potential.

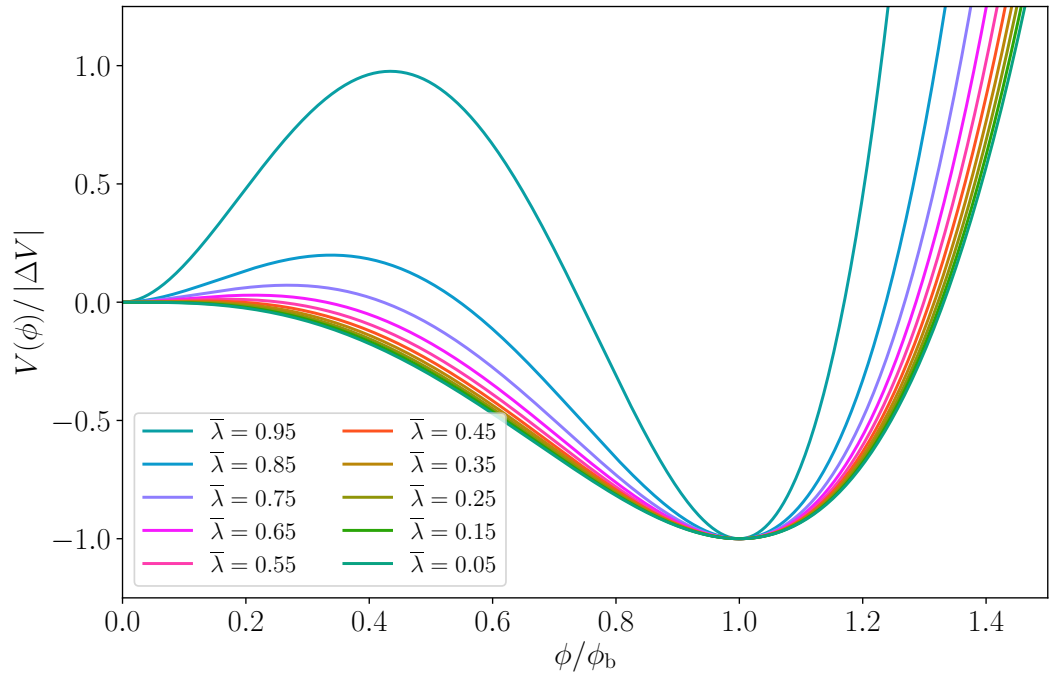

Figure 5.1: The effect on the potential due to the variation of $\overline{\lambda}$.

5.2.1 Nucleation

The probability of nucleating a bubble per unit volume per unit time $p(t)$ is given by [5]

$$p(t) = p_{\mathrm{n}} \exp(-S_4). \tag{5.16}$$

where S_4 is the Euclidean action,

$$S_4(\phi) = \int d^4x \left[\frac{1}{2} \left(\frac{d\phi}{dt} \right)^2 + \frac{1}{2} (\nabla\phi)^2 + V(\phi) \right]. \tag{5.17}$$

In the previous work Ref. [1], several nucleation scenarios were investigated. These were denoted exponential nucleation, simultaneous nucleation, and constant nucleation.

An exponential nucleation rate can occur if there is a change in temperature or background field. Then the Euclidean action decreases slowly in time resulting in the following

nucleation probability

$$p(t) = p_f \exp[\beta(t - t_f)], \tag{5.18}$$

where $\beta = -\, d\ln p(t)/dt|_{t_f}$ and t_f is the time at which the fraction of the universe in the symmetric phase is $h(t_f) = 1/e$ [96].

For an exponential nucleation rate, the number density of bubble nucleation sites at the end of the transition can be shown to be

$$n_{\rm b} = \frac{1}{8\pi}\frac{\beta^3}{v_{\rm w}^3}, \tag{5.19}$$

where for a vacuum transition the wall velocity $v_{\rm w}$ can be approximated to unity.

Simultaneous nucleation can occur if there is a minimum in $S_4(t)$ which is reached at time t_0 before a transition completes. Then the probability of nucleating a bubble per unit volume evolves as

$$p(t) = p_0 \exp[-\tfrac{1}{2}\beta_2^2(t - t_0)^2], \tag{5.20}$$

where $\beta_2 = \sqrt{S''(t_0)}$. Nucleation is then concentrated around time t_0 [140]. In the limit of $\beta_2 \to \infty$, the number density of nucleation sites tends towards

$$n_{\rm b} = \sqrt{2\pi}\frac{p_0}{\beta_2}. \tag{5.21}$$

A constant nucleation rate can occur if $S_4(t)$ tends to a constant, see e.g Ref. [141]. The nucleation probability in this scenario is then simply

$$p(t) = p_{\rm c}. \tag{5.22}$$

with the nucleation site number density given by

$$n_{\rm b} = \frac{1}{4}\left(\frac{3}{\pi}\right)^{1/4}\Gamma\left(\frac{1}{4}\right)\left(\frac{p_{\rm c}}{v_{\rm w}}\right)^{3/4}. \tag{5.23}$$

An important parameter for the gravitational wave power spectrum is the mean separation between bubble centres at the end of the transition, R_*. This is simply given by

$$R_* = \frac{1}{n_{\rm b}^{1/3}}. \tag{5.24}$$

5.2.2 Critical profile

During a vacuum phase transition, the critical profile corresponds to the most likely field configuration for a nucleated bubble. The profile of a vacuum bubble is invariant under four-dimensional Euclidean rotations [4], i.e it obeys an O(4) symmetry. We can

therefore express the field profile $\phi(\rho)$ as a function of a single variable $\rho = \sqrt{\tau^2 + r^2}$ with r the spatial radius from the bubble centre and τ the Euclidean time.

In the thin wall limit the scalar field profile of the critical bubble is given by

$$\phi_{\rm c}(r) = \frac{\phi_{\rm b}}{2}\left[1 - \tanh\left(\frac{r - R_{\rm c}^{\rm tw}}{l_{\rm w}^{\rm tw}}\right)\right], \tag{5.25}$$

where $l_{\rm w}^{\rm tw}$ is thickness of the critical bubble wall in the thin wall limit,

$$l_{\rm w}^{\rm tw} = \frac{2}{M_{\rm b}}, \tag{5.26}$$

and $R_{\rm c}^{\rm tw}$ is the radius of the critical bubble,

$$R_{\rm c}^{\rm tw} = \frac{3\sigma^{\rm tw}}{\rho_{\rm vac}}, \tag{5.27}$$

$$= \frac{12}{M\left(\frac{M_{\rm b}^4}{M^4} - 1\right)} \tag{5.28}$$

Here

$$\sigma^{\rm tw} = \frac{M^3}{3\lambda}, \tag{5.29}$$

is interpreted as the surface tension of the bubble. Note that both the combination $l_{\rm w}^{\rm tw} M$ and $R_{\rm c}^{\rm tw} M$ are constructed from quantities that depend only on $\overline{\lambda}$.

Taking inspiration from the thin wall approximation, we can define the "wall" of the bubble to correspond to the section of the field profile between $r_{\rm in}(t)$ and $r_{\rm out}(t)$ where $\phi(t, r_{\rm in}) = \phi_0(1 - \tanh(-1/2))/2$ and $\phi(t, r_{\rm out}) = \phi_0(1 - \tanh(1/2))/2$. Here ϕ_0 is the value of the scalar field at the centre of the critical bubble, $\phi_0 = \phi(0)$. We then say that the radius of the bubble $r_{\rm mid}(t)$ is defined by $\phi(t, r_{\rm mid}) = \phi_0/2$.

For potentials with $\overline{\lambda}$ close to 1, we find that the profile of the critical bubble is close to a hyperbolic tangent, as expected from Eq. 5.25. At the centre of the critical bubble the field sits very close to $\phi_{\rm b}$ As $\overline{\lambda}$ is reduced, we see a deviation of the critical bubble radius, $R_{\rm c}$ and initial wall width, $l_{\rm w}$, from those predicted in the thin wall limit. The lower the value of $\overline{\lambda}$, the smaller the critical radius of the bubble becomes in comparison to the thickness of the wall. For small values of $\overline{\lambda}$, the field profile can be approximated by a Gaussian, and the value of ϕ_0 decreases such that as $\overline{\lambda} \to 0$, we find that $\phi_0/\phi_{\rm b} \to 0$. We plot the critical bubble profile for a series of $\overline{\lambda}$ in Fig. 5.2. Note that with $\overline{\lambda}$ fixed, the profile $\phi/\phi_{\rm b}$ as a function of ρM is invariant under changes of the potential parameters.

5.2.3 Expansion

The energetically favourable state inside the bubble exerts an outward pressure on the bubble wall. Bubbles with the critical profile will begin to expand due to the pressure difference between the false and true vacuum states.

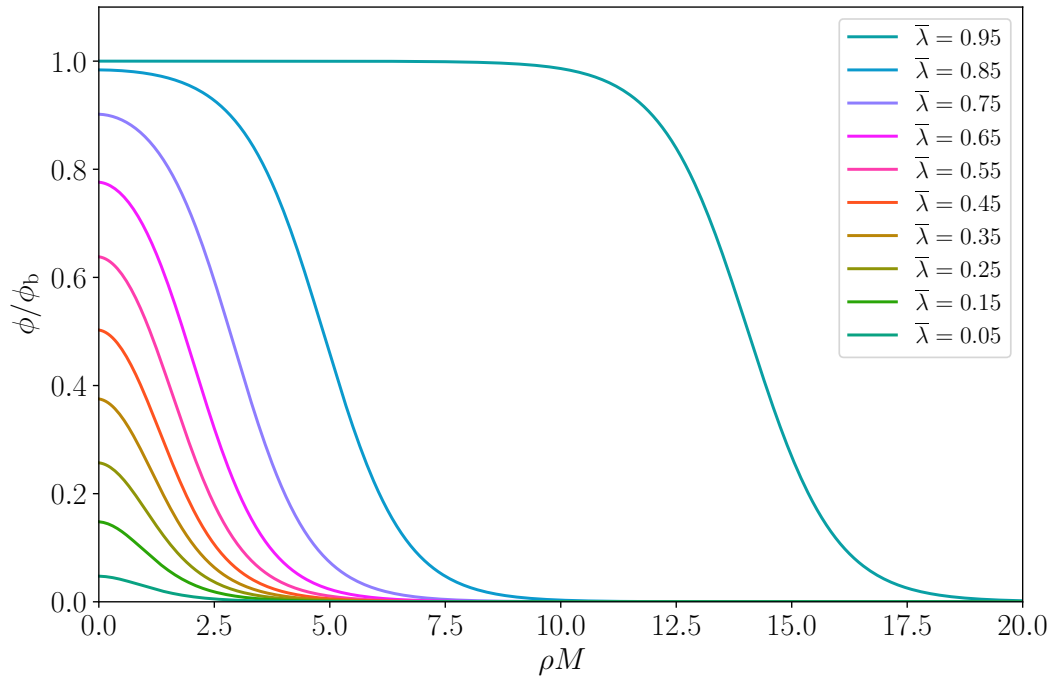

Figure 5.2: The critical profile for a series of potentials with different values of $\overline{\lambda}$.

As bubbles with high $\overline{\lambda}$ expand, the field profile inside the bubble remains close to ϕ_b. In the frame in which the center of the bubble is at rest, the bubble wall will become thinner due to Lorentz contraction. Thick wall bubbles have substantially different dynamics. For these the field at the centre of the bubble will move towards ϕ_b from its initial value of ϕ_0 as the bubble starts to expand. It will then proceed to oscillate around ϕ_b, resulting in outgoing waves of the scalar field following the bubble wall. We depict this behaviour for a thin wall bubble and a thick wall bubble in Fig. 5.3.

For times $t > 0$ and for $r \geq t$, the profile of the bubble should be given by $\phi(t, r) = \phi(\sqrt{r^2 - t^2})$. Therefore $r_{\text{out}}(t) = \sqrt{\rho_{\text{out}}^2 + t^2}$ and $r_{\text{in}}(t) = \sqrt{\rho_{\text{in}}^2 + t^2}$. We define the Lorentz factor of the bubble wall by measuring how much the wall contracts, $\gamma(t) = l_w(0)/l_w(t)$. This can be expressed as

$$\gamma(t) = \frac{\rho_{\text{out}} - \rho_{\text{in}}}{\sqrt{\rho_{\text{out}}^2 + t^2} - \sqrt{\rho_{\text{in}}^2 + t^2}}. \tag{5.30}$$

We show how γ increases for a series of $\overline{\lambda}$ at early times in Fig. 5.4. It can be clearly seen that as $\overline{\lambda} \to 0$, where ρ_{in} and ρ_{out} take smaller values, γ grows more rapidly.

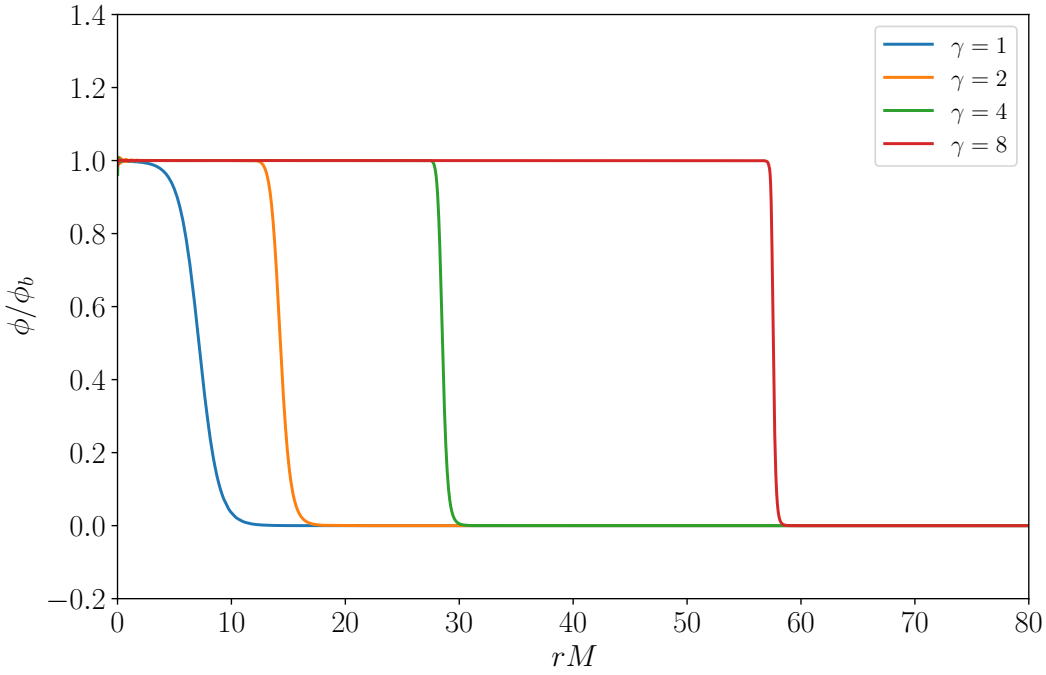

(a) $\overline{\lambda} = 0.84$

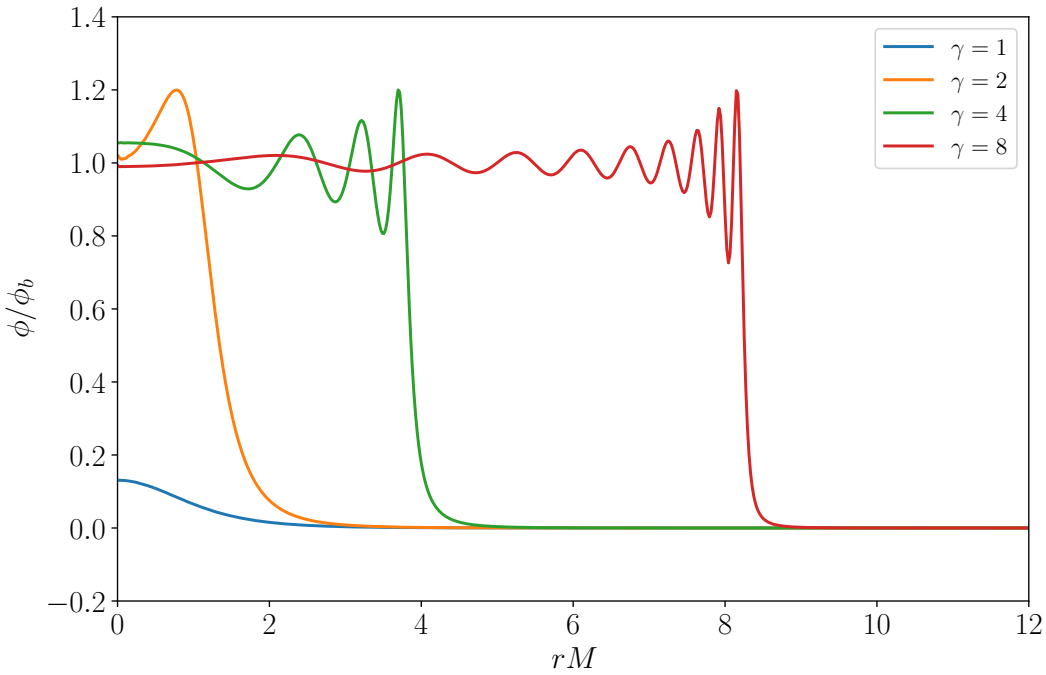

(b) $\overline{\lambda} = 0.07$

Figure 5.3: Field profiles of bubbles when the bubble walls have accelerated up to various γ factors. Note that $\gamma = 1$ corresponds to the critical bubble profile.

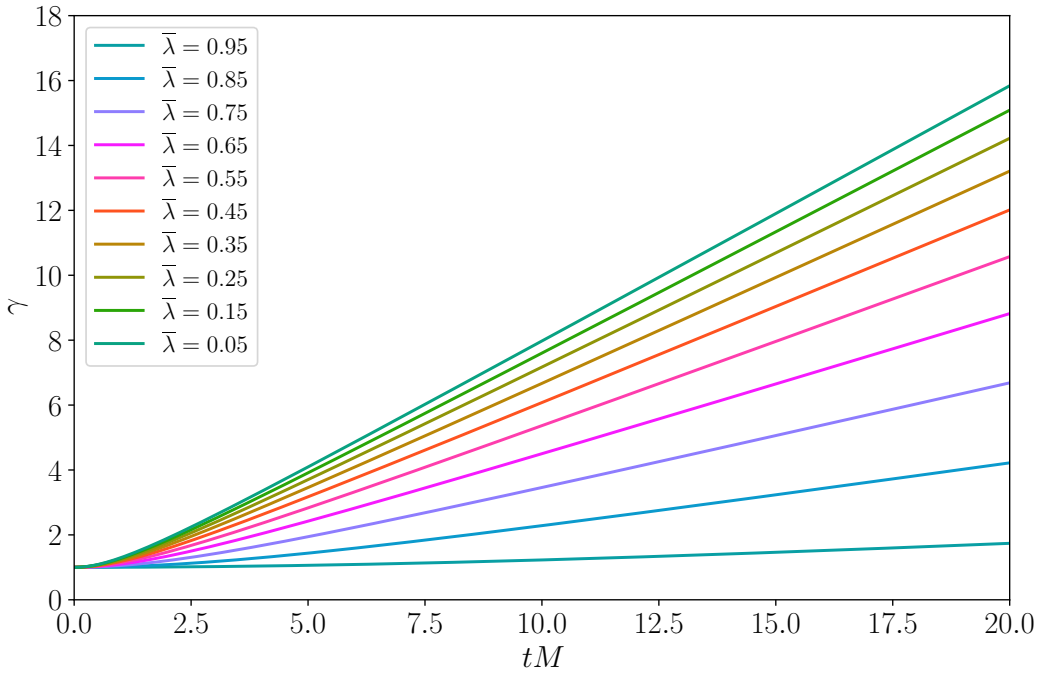

Figure 5.4: Evolution of γ as defined in Eq. 5.30 for a series of values of $\overline{\lambda}$.

5.2.4 Collision

When two true vacuum bubbles collide, the scalar field begins to oscillate in the region where the bubbles overlap. During this oscillation the scalar field will rebound towards the false vacuum [114, 115]. For thin wall potentials with $\overline{\lambda}$ closer to 1, the scalar field in the overlap region can rebound over the potential barrier and return to the false vacuum. This corresponds to the trapping discussed in Ref. [116]. On the other hand, for thick wall potentials with smaller $\overline{\lambda}$, the scalar field in the overlap region will instead oscillate around the true vacuum state. According to Ref. [116], this is where we would expect the bulk flow model to apply. The value of $\overline{\lambda}$ separating these behaviours has been demonstrated to depend on γ, see Fig. 13 of Ref. [116] for more details. We show both these behaviours in Fig. 5.5. In both cases, the oscillations produce scalar field radiation that is emitted at close to the speed of light. Neither of these effects is accounted for in the envelope approximation which instead assumes that all shear-stress disappears in the overlap region.

For all values of $\overline{\lambda}$, the scalar field will continue to oscillate around the true vacuum after the true vacuum bubbles have finished colliding. It is known that the thermalisation of scalar fields is a long-lasting process in the absence of other interactions [144–146].

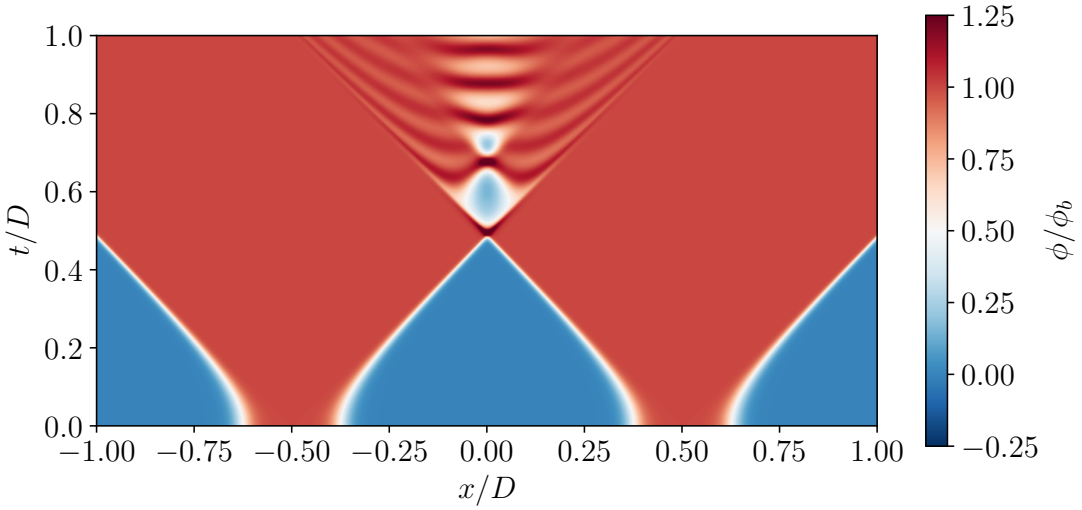

(a) $\overline{\lambda} = 0.84$

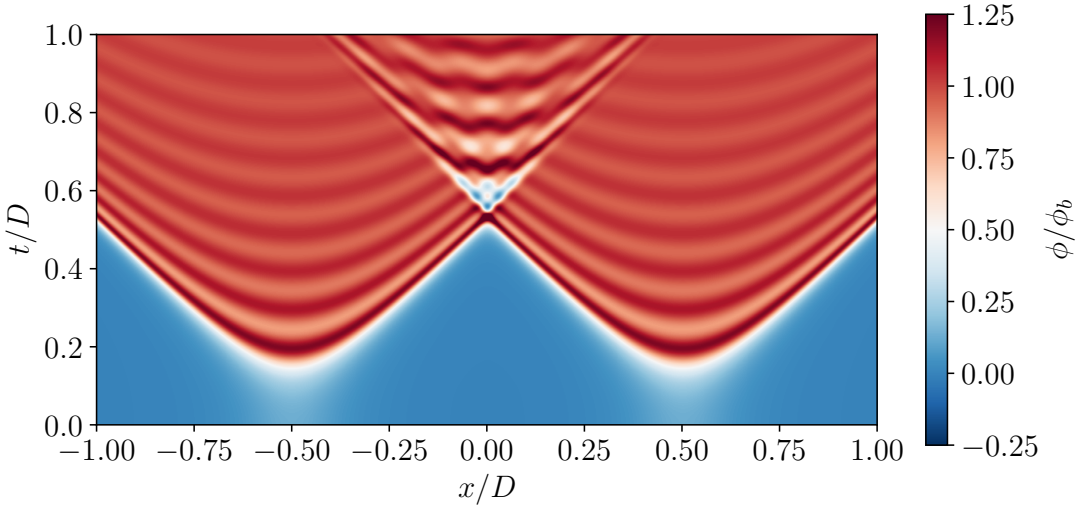

(b) $\overline{\lambda} = 0.07$

Figure 5.5: The collision of two bubbles of the true vacuum plotted for a thin wall (a) and thick wall (b) potential. The x axis corresponds to the line joining the two bubble centres, with D being the separation between bubbles. On the y axis we plot the time t since the bubbles were nucleated. For both these simulations, the bubbles collide when the Lorentz factors of the bubble walls are $\gamma = 4.0$.

5.3 Gravitational waves from a vacuum transition

In order to calculate the gravitational-wave power spectrum, we need to find the transverse traceless (TT) metric perturbations h_{ij}^{TT} where

$$\Box h_{ij}^{TT} = -16\pi G T_{ij}^{TT}, \tag{5.31}$$

and T_{ij}^{TT} is the transverse traceless projection of the energy-momentum tensor,

$$T_{\mu\nu} = \partial_\mu\phi\partial_\nu\phi - \eta_{\mu\nu}\left(\frac{1}{2}(\partial\phi)^2 + V(\phi)\right), \tag{5.32}$$

where $\eta_{\mu\nu}$ is the Minkowski metric.

The energy density in the gravitational waves can be defined as

$$\rho_{\rm gw}(\mathbf{x},t) = \frac{1}{64\pi G}\left(\dot{h}_{ij}^{TT}\dot{h}_{ij}^{TT} + (\nabla h_{ij}^{TT})(\nabla h_{ij}^{TT})\right), \tag{5.33}$$

Note that an average over many wavelengths and periods may be needed in order to reduce fluctuations in this quantity.

In general, while gravitational waves are being sourced $\langle(\dot{h}_{ij}^{TT})^2\rangle \neq \langle(\nabla h_{ij}^{TT})^2\rangle$. There is no unique local definition of the gravitational wave energy at source, but we found that defining the gravitational wave energy density through taking an average of the kinetic and gradient terms reduced oscillations in the gravitational wave power spectra and better tracked the eventual gravitational wave energy density once sourcing ceased. Note that for gravitational waves propagating in vacuum $\langle(\dot{h}_{ij}^{TT})^2\rangle = \langle(\nabla h_{ij}^{TT})^2\rangle$ and so our definition of the gravitational wave energy density reduces to the more familiar

$$\rho_{\rm gw}(\mathbf{x},t) = \frac{1}{32\pi G}\left(\dot{h}_{ij}^{TT}\dot{h}_{ij}^{TT}\right). \tag{5.34}$$

We introduce an auxiliary tensor u_{ij} which satisfies [147]

$$\Box u_{ij} = -16\pi G(\partial_i\phi)(\partial_j\phi). \tag{5.35}$$

To obtain h_{ij}^{TT} we use the projector $\Lambda_{ij,lm}$ on u_{ij} in momentum space,

$$h_{ij}^{TT}(\mathbf{k},t) = \Lambda_{ij,lm}(\mathbf{k})u_{lm}(\mathbf{k},t), \tag{5.36}$$

where

$$\Lambda_{ij,lm}(\mathbf{k}) = P_{im}(\mathbf{k})P_{jl}(\mathbf{k}) - \frac{1}{2}P_{ij}(\mathbf{k})P_{lm}(\mathbf{k}), \tag{5.37}$$

and

$$P_{ij}(\mathbf{k}) = \delta_{ij} - \hat{k}_i\hat{k}_j. \tag{5.38}$$

We then define the spectral density of the metric perturbations as

$$\langle h_{ij}^{TT}(\mathbf{k},t)h_{ij}^{TT}(\mathbf{k}',t)\rangle = P_h(\mathbf{k},t)(2\pi)^3\delta(\mathbf{k}+\mathbf{k}'). \tag{5.39}$$

Therefore the power spectrum of gravitational wave energy density is

$$\frac{d\rho_{\rm gw}}{d\ln(k)} = \frac{1}{64\pi G}\frac{k^3}{2\pi^2}\left(P_{\dot{h}}(\mathbf{k},t) + k^2 P_h(\mathbf{k},t)\right), \tag{5.40}$$

and by dividing through by the critical energy density ρ_c we obtain

$$\frac{d\Omega_{\rm gw}}{d\ln(k)} = \frac{1}{64\pi G\rho_c}\frac{k^3}{2\pi^2}\left(P_{\dot{h}}(\mathbf{k},t) + k^2 P_h(\mathbf{k},t)\right), \tag{5.41}$$

which we refer to as the gravitational-wave power spectrum.

5.3.1 Collision phase

Upon collision, the spherical symmetry of isolated bubbles is broken, and gravitational waves become sourced by the shear-stress located at the bubble walls. During the collision phase, gravitational waves are generated at large wavelengths associated with the scale of the bubble sizes at collision time.

This period has been studied both using lattice field theory simulations [1, 118] and using simplifying assumptions such as the envelope approximation [57, 59, 122] and bulk flow model [122, 123].

The envelope approximation [57] is based on two key assumptions. The first is that the shear-stress in the scalar field is entirely located in an infinitesimally thin shell located at the bubble wall. The second approximation is that when bubbles collide, the shear-stress is removed in the overlap region. Hence, to compute the transverse traceless shear-stress sourcing the gravitational waves, it is sufficient to consider the envelope from expanding bubbles. The gravitational-wave spectrum has been calculated for exponential nucleation rates using numerical simulations in Refs. [57, 59, 122].

The gravitational-wave power spectrum is well approximated by a broken power law

$$\frac{d\Omega_{\rm gw}^{\rm env}}{d\ln(k)} = \Omega_{\rm p}^{\rm env}\frac{(a+b)\tilde{k}^b k^a}{b\tilde{k}^{(a+b)} + ak^{(a+b)}}, \tag{5.42}$$

with power law exponents a and b, peak amplitude $\Omega_{\rm p}^{\rm env}$ and peak wavenumber $\tilde{k}$.

For a vacuum phase transition where the wall velocity approaches the speed of light, the power law exponents were found to be $a = 2.9$ and $b = 0.9$ [122]. The peak amplitude was given by

$$\Omega_{\rm p}^{\rm env} \simeq 4.7\times10^{-2}\left(\frac{H_*}{\beta}\right)^2\Omega_{\rm vac}^2, \tag{5.43}$$

where $\Omega_{\rm vac} = \rho_{\rm vac}/\rho_c$ is the vacuum energy density parameter. The peak wavenumber was estimated to be

$$\tilde{k}/\beta \simeq 1.07. \tag{5.44}$$

Note that the value of R_* that is expected for a vacuum transition with exponential nucleation rate is

$$R_* = \frac{(8\pi)^{1/3}}{\beta}. \tag{5.45}$$

Analytical investigations using the envelope approximation [121], have shown that the two-point correlator of the energy-momentum tensor can be expressed as a 1-dimensional integral. This then results in the gravitational-wave power spectrum being given by a broken power law with exponents $a = 3$ and $b = 1$.

In the bulk flow model, the envelope approximation is modified [122, 123]. The shear-stress during the transition is still considered to be located in an infinitesimally thin shell located at the bubble wall. However, in the bulk flow model, the shear-stress in the bubble wall is not assumed to disappear upon collision. Instead, the bubble wall continues to propagate but is no longer driven by the latent heat of the transition. The bubble wall energy density per surface element then decays as $e^{-(t-t_{\rm coll})/\tau}/R^2$, where R refers to the bubble radius and $t_{\rm coll}$ the time of collision. The value of τ indicates the typical damping timescale of the wall and should be determined from the particle physics model. The value of $\tau = 0$ corresponds to the envelope approximation, whereas $\tau = \infty$ corresponds to free propagation of the wall after collision. Analytical treatments for ultra-relativistic bubbles have shown that as $\tau \to \infty$, the IR power law in the gravitational-wave power spectrum becomes shallower than k^3, tending towards k^1 [123].

The gravitational-wave power spectrum in the bulk flow model with $\tau = \infty$ and an exponential nucleation rate has also been studied with numerical simulations [122]. The resulting fit for ultra-relativistic wall velocities was given in the same form as Eq. 5.42 with power law exponents $a = 0.9$ and $b = 2.1$. The peak amplitude was given as

$$\Omega_{\rm p}^{\rm bf} \simeq 6.4 \times 10^{-2} \left(\frac{H_*}{\beta}\right)^2 \Omega_{\rm vac}^2, \tag{5.46}$$

and peak wave number

$$\tilde{k}/\beta \simeq 0.809. \tag{5.47}$$

In Ref. [1], full lattice field theory simulations of colliding vacuum bubbles were conducted. The authors simulated the gravitational-wave power spectrum produced by colliding thin-wall bubbles, with $\overline{\lambda} \geq 0.84$. The bubbles were separated on average by a distance R_*, which is then the typical diameter of bubbles when they collide. The value of R_* in

each simulation was chosen so that the Lorentz factor of a bubble with diameter R_* was $\gamma_* = 4$. A number of different nucleation scenarios were investigated, which did not have a significant effect on the resulting spectrum.

In the aforementioned work, a fit for the spectrum resulting from bubble collisions was provided in the form

$$\frac{d\Omega_{\rm gw}^{\rm fit}}{d\ln k} = \Omega_{\rm p}^{\rm fit} \frac{(a+b)^c \tilde{k}^b k^a}{(b\tilde{k}^{(a+b)/c} + ak^{(a+b)/c})^c}, \tag{5.48}$$

where the value of a was fixed to $a = 3$. From the simulations conducted it was found that

$$\Omega_{\rm p}^{\rm fit} = (3.22 \pm 0.04) \times 10^{-3} \left(H_* R_* \Omega_{\rm vac}\right)^2, \tag{5.49}$$

$$\tilde{k} R_* = 3.20 \pm 0.04, \tag{5.50}$$

$$b = 1.51 \pm 0.04, \quad c = 2.18 \pm 0.15, \tag{5.51}$$

with H_* the Hubble parameter at the time of the transition. This corresponds to a slightly reduced total gravitational-wave power compared to the envelope approximation, and furthermore a slightly steeper UV power law. It was suggested that the deviation from the envelope approximation was due to the behaviour of the scalar field in the overlap regions. While the envelope approximation assumes that the shear-stress in the bubble wall disappears upon collision, lattice field theory simulations indicate that the scalar field oscillates in the overlap region during bubble collisions.

The fits provided for the gravitational-wave power spectrum arising from the bulk flow model and the envelope approximation are both taken from simulations using an exponential nucleation rate. Caution should be used when comparing them to the simulations in this paper which correspond to simultaneous nucleation scenario. While the gravitational-wave power spectrum from lattice simulations did not show a strong dependence on the nucleation scenario in Ref. [1], it has been shown that the envelope approximation peak frequency can be shifted by up to a factor of ~ 1.5 and the peak amplitude by a factor of ~ 3 when changing between exponential and simultaneous nucleation [66]. It has also been demonstrated that varying the nucleation rate in the envelope approximation can affect the shape of the power spectrum around the peak, with simultaneous nucleation creating a sharper peak than exponential nucleation [140].

In this work we intend to extend the results in Ref. [1] to potentials with much smaller $\overline{\lambda}$. The behaviour of the scalar field in the overlap region during bubble collisions varies depending on the value of $\overline{\lambda}$, as described in Section 5.2.4. If it is true that the deviation from the envelope approximation corresponds to the structure in overlap regions, the form

of the power spectrum may depend on the value of $\overline{\lambda}$. We will pay particular attention to whether there is a change in the total gravitational-wave power or the UV broken power law exponent due to a variation in $\overline{\lambda}$.

5.3.2 Oscillation phase

Once the bubbles have finished colliding in a vacuum first-order phase transition, the scalar field is left in an excited state. In this state, ϕ oscillates around the true vacuum value, $\phi_{\rm b}$, and as such we refer to this period as the oscillation phase. Eventually, these oscillations are expected to subside as the scalar field thermalises and Hubble friction damps away gradients in the field. In previous lattice field theory simulations, it has been shown that gravitational waves continue to be sourced during this period [1, 118].

In Ref. [118], this phase was referred to as a coalescence phase. It was posited that the gravitational waves produced during this period would dominate over those produced from bubble collisions, and will furthermore shift the peak of the power spectrum towards the UV. However, in Ref. [1] it was shown that the peak frequency of the gravitational-wave power spectrum generated during this phase was associated with the microphysics of the system, namely $l_{\rm w}$, rather than the cosmological scales that correspond to R_*. When the separation of these two scales was extrapolated from the simulations up to realistic values, the gravitational-wave power of the collision phase is expected to dominate. Furthermore, the peak frequency corresponding to the oscillation phase would be firmly out of range of any upcoming gravitational-wave detectors for any realistic early universe phase transition.

In this study we aim to resolve whether the result found in Ref. [1] extends to a wider range of $\overline{\lambda}$, or whether the gravitational-wave power or peak frequency changes for thick wall bubbles.

5.4 Methods

In order to conduct our simulations in this paper, we employ an updated version of the code used in Ref. [1]. This is a 3D classical lattice field theory code built using the `LATfield2` library in `C++` [149].

For each simulation, the fields are evolved on a lattice of L^3 points using a Crank-Nicholson leapfrog algorithm. We impose periodic boundary conditions, which corresponds to the approximation that the universe is isotropic and homogeneous at the scale of the simulation box. We use a 7 point stencil for the Laplacian operator. We pick an appropriate lattice spacing Δx and fix the timestep $\Delta t = \Delta x/5$. The final simulation time

is $t_{\rm fin}$.

In order to understand how the gravitational-wave power spectrum changes between thin and thick wall bubbles, we perform simulations with four different values of $\overline{\lambda}$. These, along with various corresponding parameters derived from the potential, are given in Table 5.1.

When choosing a lattice spacing, we perform a series of convergence tests for each set of simulations, which we detail in App. 5.8.1. For the largest simulation for each choice of $\overline{\lambda}$ we perform a low, medium and high resolution run with a factor of two smaller lattice spacing for each increase in resolution. The lattice spacing for the high resolution run is then used in the rest of the paper. For the gravitational wave power spectrum we take the uncertainty for each bin to be given by the difference of the power found in the high and medium resolution run. For the number of bubbles used in the largest simulations, the uncertainty in each bin arising from performing multiple realisations is very small for all but the most infrared modes, and can be neglected compared to the lattice uncertainty. For more information on the convergence rate, see App. 5.8.1.

To compare our choice of potential parameters with the quartic potential in Ref. [116], we use the conversion between $\overline{\lambda}$ and ϵ given below,

$$\epsilon = \frac{\left(\sqrt{9-8\overline{\lambda}}-3\right)^2\left(4\overline{\lambda}+\sqrt{9-8\overline{\lambda}}-3\right)}{8(9-8\overline{\lambda})^{3/2}}. \tag{5.52}$$

We list the corresponding values of ϵ for each $\overline{\lambda}$ in Table 5.1. In Fig. 13 of Ref. [116] it can be seen that trapping is exhibited for $\epsilon \gtrsim 0.6$ when $\gamma \simeq 4$. From this we infer that $\overline{\lambda} = 0.84$ and $\overline{\lambda} = 0.50$ exhibit trapping behaviour for $\gamma = 4.0$, whereas $\overline{\lambda} = 0.18$ and $\overline{\lambda} = 0.07$ do not.

In Ref. [1] a range of different nucleation rates were used. The nucleation rate did not appear to have a detectable effect on the gravitational-wave power spectrum. In order to limit the computational cost, we choose to study only simultaneous nucleation, where we nucleate all bubbles at the start of the simulation on the zeroth timestep. Bubbles are nucleated randomly in the symmetric phase, providing that for all $n < N$, the distance between the Nth and nth bubble centres r_n obeys the following relation

$$r_n^{\rm sep} > R_{\rm c} + \sqrt{R_{\rm c}^2 + (t-t_n)^2}, \tag{5.53}$$

where t_n is the time since nucleation of the nth bubble. For simultaneous nucleation $t_n = 0$ for all n. We nucleate a total of $N_{\rm b}$ bubbles in each simulation.

Bubbles are nucleated into the simulation with the corresponding critical profile. The

critical profile is found by using a shooting algorithm to determine the bounce solution for a given potential.

The average separation between bubbles is $R_* = (\mathcal{V}/N_\mathrm{b})^{1/3}$, where $\mathcal{V} = (L\Delta x)^3$ is the volume of the simulation. When bubbles collide, they will on average have a diameter of R_*, and so this quantity sets the length scale of the peak of the gravitational-wave power spectrum. In our simulations, we choose R_* such that the value of the Lorentz factor for a bubble of diameter R_* is $\gamma_* = 4$.

Once γ_* and $\overline{\lambda}$ are fixed, the combination $R_* M_\mathrm{b}$ is also determined uniquely. This is important as $R_* M_\mathrm{b}$ effectively dictates the separation between the length scales of the physics from bubble collisions and the microscopic physics from oscillations about the true vacuum. In a true vacuum phase transition, these scales would be separated by many orders of magnitude as $\gamma_* \to \infty$, but achieving this seperation of scales numerically is not possible.

To supplement our 3D simulations, we also perform a series of spherically symmetric 1D simulations of isolated bubbles. This enables us to study the effect of the lattice on the evolution of r_in, r_out, r_mid and γ. This analysis is provided in Appendix 5.8.1. We evaluate γ_* for an isolated bubble in both the 1D code and 3D code and list these values in Tables 5.2 & 5.3.

We also perform a series of simulations in order to understand the gravitational waves sourced by the oscillation phase of the scalar field. To do this we perform long-lasting simulations where the evolution of the metric perturbations is only turned on after the phase transition has completed, around $t/R_* = 2.0$. We list the simulations that we conduct to understand the gravitational waves sourced by the collision phase in Table 5.2, and for the oscillation phase in Table 5.3.

The simulations studying the collision phase all finish at $t/R_* = 8.0$, with the exception of the largest simulation with $\overline{\lambda} = 0.84$ and $N_\mathrm{b} = 512$ which terminates at $t/R_* = 7.0$ due to time limits imposed by the computing facilities utilised. The smaller but longer lasting simulations studying the oscillation phase terminate at $t/R_* = 40$.

5.5 Results: scalar field

During a vacuum first-order phase transition, the scalar field undergoes several phases of evolution. First occurs the nucleation and expansion of bubbles. Next, the bubbles begin to collide and the field oscillates in the overlap regions. Finally, the bubbles finish colliding, and the scalar field oscillates around ϕ_b as the field thermalises.

$\overline{\lambda}$	$R_{\rm c}M$	$l_{\rm w}M$	$R_{\rm c}^{\rm tw}M$	$l_{\rm w}^{\rm tw}M$	$\phi_0/\phi_{\rm b}$	$\phi_{\rm max}/\phi_{\rm b}$	$V_{\rm max}/\rho_{\rm vac}$	$M_{\rm b}^2/M^2$	ϵ
0.84	7.15	1.71	4.04	1.42	0.981	0.334	1.87×10^{-1}	1.99	1.6×10^{-1}
0.50	2.07	1.24	0.36	0.83	0.570	0.146	8.18×10^{-3}	5.84	8.1×10^{-3}
0.18	1.16	0.89	0.026	0.43	0.183	0.045	1.90×10^{-4}	21.46	1.9×10^{-4}
0.07	0.996	0.80	0.0031	0.25	0.066	0.016	8.21×10^{-6}	61.96	8.2×10^{-6}

Table 5.1: The values of $\overline{\lambda}$ used in our simulations. For each of these we give the critical radii, $R_{\rm c}$, and wall thicknesses, $l_{\rm w}$, that are used in our simulations, as well as their estimates in the thin wall approximation. We also supply the value of the scalar field at the centre of the bubble, ϕ_0, and the value of scalar field at the peak of the potential barrier, $\phi_{\rm max}$, both in terms of the broken phase value, $\phi_{\rm b}$. We also give the ratio of the height of the potential barrier, $V_{\rm max}$, compared to the potential energy difference, $\rho_{\rm vac}$, and the mass of the field in the broken phase, $M_{\rm b}$, compared to the symmetric phase mass, M. Finally we give the corresponding value of ϵ for comparison with the quartic potential in Ref. [116].

It is useful to investigate the evolution of the total, kinetic, gradient and potential energy densities of the scalar field. We show this for several simulations with a range of $\overline{\lambda}$ and $N_{\rm b} = 64$ in Fig. 5.6. There appears to be little variation in the mean energy densities for different $\overline{\lambda}$, nor any consistent trend as it changes. By tracking the evolution of ρ_V we can see that in all cases the bubbles finish colliding shortly after $t/R_* = 1$. Around this time the kinetic, gradient and potential energy densities settle to constant values. As ρ_V does not tend to zero at the end of the simulation, we know that the scalar field continues in the oscillation phase after the bubbles finish colliding. The scalar field does not thermalise during the duration of our simulations. We can also see that the total energy density in the scalar field ρ_ϕ is well conserved, with minimal energy being lost to the lattice.

It is perhaps not surprising that the relative contributions of gradient, kinetic and potential energy asymptote to a constant across simulations with different $\overline{\lambda}$ as from the equipartition theorem we expect that [157]

$$\langle \frac{1}{2}\partial_i\phi\partial^i\phi + V(\phi)\rangle = \langle \frac{1}{2}\dot{\phi}^2\rangle \tag{5.54}$$

once the system reaches equilibrium.

Further insight into the behaviour of the scalar field can be deduced from examining slices through the simulation box. In Appendix 5.8.2 we show slices of the scalar field for two simulations with $\overline{\lambda} = 0.07$ and $\overline{\lambda} = 0.84$ and $N_{\rm b} = 64$. We plot these slices at three

$\overline{\lambda}$	N_b	$R_* M_\mathrm{b}$	t_fin/R_*	L	$\Delta x M$	γ_*	$\gamma_{*,1\mathrm{D}}$	$\gamma_{*,3\mathrm{D}}$
0.84	8	80.66	8.0	1200	0.0952	4.000	3.958	3.984
0.84	64	80.66	8.0	2400	0.0952	4.000	3.958	3.984
0.84	512	80.66	7.0	4800	0.0952	4.000	3.958	3.984
0.50	8	40.53	8.0	800	0.0419	4.000	3.972	3.988
0.50	64	40.53	8.0	1600	0.0419	4.000	3.972	3.988
0.50	512	40.53	8.0	3200	0.0419	4.000	3.972	3.988
0.18	8	44.69	8.0	400	0.0482	4.000	3.927	3.966
0.18	64	44.69	8.0	800	0.0482	4.000	3.927	3.966
0.18	512	44.69	8.0	1600	0.0482	4.000	3.927	3.966
0.18	4096	44.69	8.0	3200	0.0482	4.000	3.927	3.966
0.07	8	65.54	8.0	800	0.0482	4.000	4.021	4.004
0.07	64	65.54	8.0	1600	0.0482	4.000	4.021	4.004
0.07	512	65.54	8.0	3200	0.0482	4.000	4.021	4.004

Table 5.2: Parameters of the simultaneous nucleation simulations used within this paper. Listed here for each run are the values of $\overline{\lambda}$, number of bubbles N_b, average bubble separation R_*, final simulation time t_fin, number of lattice points L^3, lattice spacing Δx, typical Lorentz factor at collision γ_*, the effective γ_* as found on the lattice in a 1D simulation $\gamma_{*,1\mathrm{D}}$ and in a 3D simulation $\gamma_{*,3\mathrm{D}}$. For details of the potential parameters for each $\overline{\lambda}$, see Table 5.1. Not given here are simulation runs where the metric perturbations are turned on after the bubbles have finished colliding, see Table 5.3.

$\overline{\lambda}$	N_b	$R_* M_\mathrm{b}$	t_fin/R_*	L	$\Delta x M$	γ_*	$\gamma_{*,1\mathrm{D}}$	$\gamma_{*,3\mathrm{D}}$
0.84	8	80.66	40.0	1200	0.0952	4.000	3.958	3.984
0.50	8	40.53	40.0	800	0.0419	4.000	3.972	3.988
0.18	8	44.69	40.0	400	0.0482	4.000	3.927	3.966
0.07	8	65.54	40.0	800	0.0482	4.000	4.021	4.004

Table 5.3: Parameters of the simultaneous nucleation runs where we turn the evolution of metric perturbations on well after the bubbles have finished colliding at $t/R_* = 2.5$. This allows us to study the gravitational-wave signal produced from the oscillation phase.

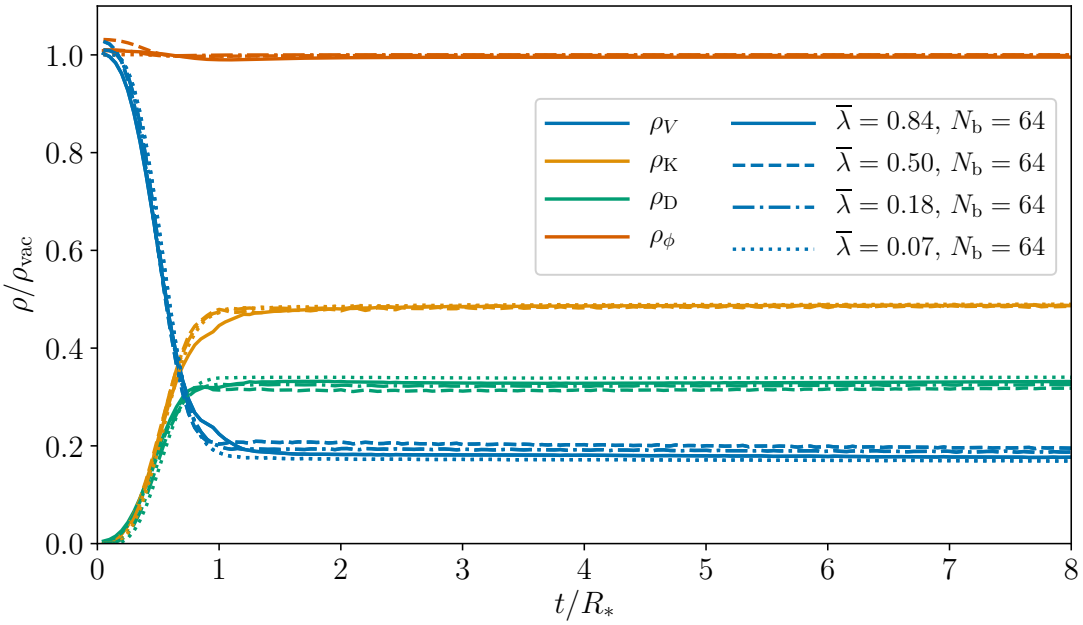

Figure 5.6: The evolution of mean energy densities corresponding to the scalar field for simulations with varying $\overline{\lambda}$.

different times, $t/R_* \in \{0.5,\ 1.0,\ 4.0\}$. These correspond to early on in the bubble collision phase, towards the end of this phase where most bubbles have finished colliding, and much later during the oscillation phase. These simulation slices confirm the behaviour outlined in Section 5.2.4. When $\overline{\lambda}$ is small, the expanding scalar field profile oscillates around $\phi_{\rm b}$ and the rebound in the overlap region towards the symmetric phase is minimal. For larger $\overline{\lambda}$, the rebound can be quite dramatic.

In Fig. 5.7 we show the power spectrum of the scalar field, $\mathcal{P}_\phi$ for two simulations with $\overline{\lambda} = 0.84$ and $\overline{\lambda} = 0.07$. We see that at early times while the bubble is expanding, the power spectrum is peaked around the scale of R_*. At later times, as the scalar field begins to oscillate, the peak wavenumber for the power spectrum increases, moving further towards the length scale associated with $M_{\rm b}$. It is interesting to note that the decay of power in the IR is not as rapid as one might initially expect. Although the bubbles have finished colliding around $t = R_*$, the power in the scalar field in the IR decays slower, reaching a minimum only after several t/R_*.

When trying to understand how the gradients in the scalar field source gravitational waves, it is useful to follow the evolution of T_{ij}^{TT}. The transverse traceless shear-stress tells us about the instantaneous source of gravitational waves at any given point in the simulation. By examining slices of the modulus of the transverse traceless shear-stress, $\sqrt{T_{ij}^{TT} T_{ij}^{TT}}$, we are able to determine also the location where gravitational waves are being

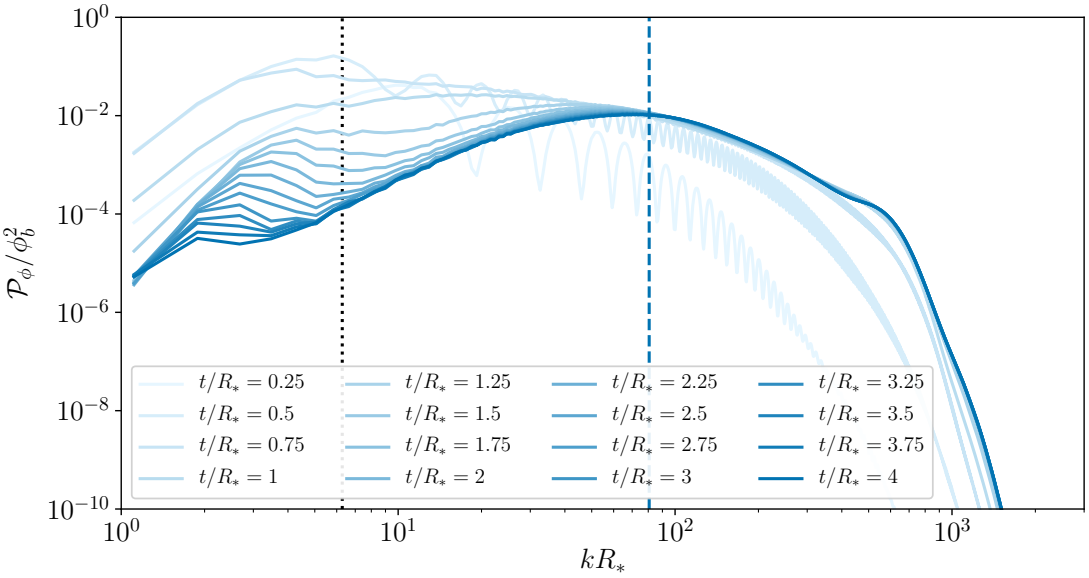

(a) $\overline{\lambda} = 0.84$, $N_\mathrm{b} = 512$

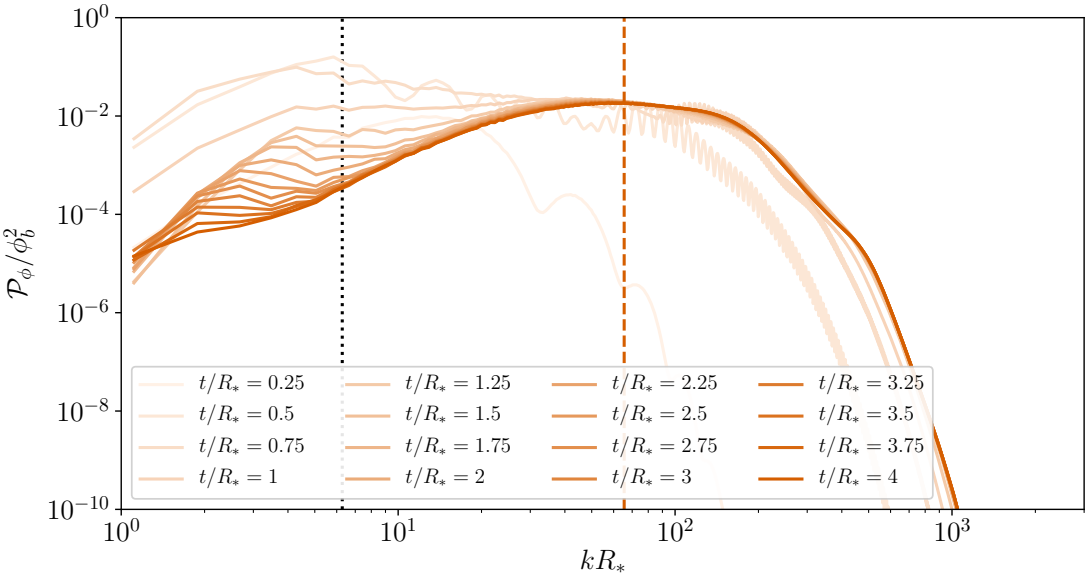

(b) $\overline{\lambda} = 0.07$, $N_\mathrm{b} = 512$

Figure 5.7: The power spectrum of the scalar field $\mathcal{P}_\phi$. In each plot darker shades indicate later times. The vertical black dotted line shows the location of $k = 2\pi/R_*$, whereas the vertical dashed coloured line shows the location of $k = M_\mathrm{b}$.

sourced. We show this alongside the scalar field slices in Appendix 5.8.2.

From the slices, we can see that, contrary to the prediction of the envelope approximation, there is substantial shear-stress in the overlap region of collided bubbles. This appears to be particularly true for potentials with smaller $\overline{\lambda}$. Furthermore, even after the final bubbles have finished colliding, waves of shear-stress previously associated with the bubble collisions propagate outwards with length scales of R_* or larger. This shows some similarity to that which is predicted in the bulk flow model. At later times the shear stress appears to have power on much smaller length scales.

It is useful to study the power spectrum of the transverse traceless shear-stress, $\mathcal{P}_T$. We plot the evolution of $\mathcal{P}_T$ for two simulations with $\overline{\lambda} = 0.07$ and $\overline{\lambda} = 0.84$ in Fig. 5.8. From $\mathcal{P}_T$, we can see that as the transition progresses, the shear-stress starts to grow as bubbles start to collide. Initially, there is substantial power in the IR, corresponding to typical length scales of the bubbles when they collide. At later times the power shifts more towards the UV, with a peak developing close to the scale associated with $M_{\rm b}$. This occurs as the scalar field has entered the oscillation phase of the transition.

Interestingly, we see that the power in the IR does not disappear immediately after the bubbles finish colliding, around $t/R_* = 1$. Instead the power slowly decreases for several t/R_*. This appears to agree with what we saw in the slices of $\sqrt{T_{ij}^{TT}T_{ij}^{TT}}$ in which the shear-stress associated with the bubble wall and collision regions continued to propagate for some time after the bubbles finished colliding, giving further support to the bulk flow model. Unfortunately, we cannot resolve a sufficient distance into the IR to see any fall off of the shear-stress corresponding to the causal interval.

From our smaller, but much longer simulations outlined in Table 5.3 we can show how $\mathcal{P}_T$ behaves at very late times. We plot the evolution of $\mathcal{P}_T$ up to $t/R_* = 40$ for two simulations with $N_{\rm b} = 8$ and for $\overline{\lambda} = 0.84$ and $\overline{\lambda} = 0.07$ in Fig. 5.9. It can clearly be seen that at very late times, the power spectrum settles into a shape with a characteristic power law of k^3 rising from the IR. In our simulations, we do not allow for the decay of the scalar field into other particles, and we also do not account for the damping of oscillations of the scalar field due to expansion. Both of these would reduce the power in T_{ij}^{TT}. It is still interesting to note however that the non-linear behaviour in the scalar field continues to source gravitational waves long after the collisions phase terminates.

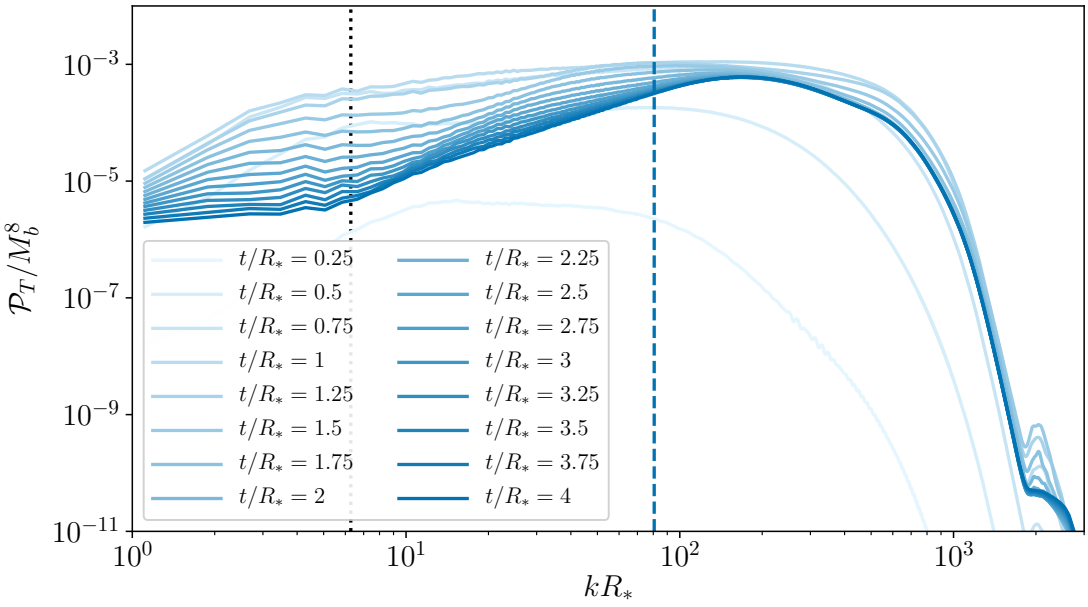

(a) $\overline{\lambda} = 0.84$, $N_\mathrm{b} = 512$

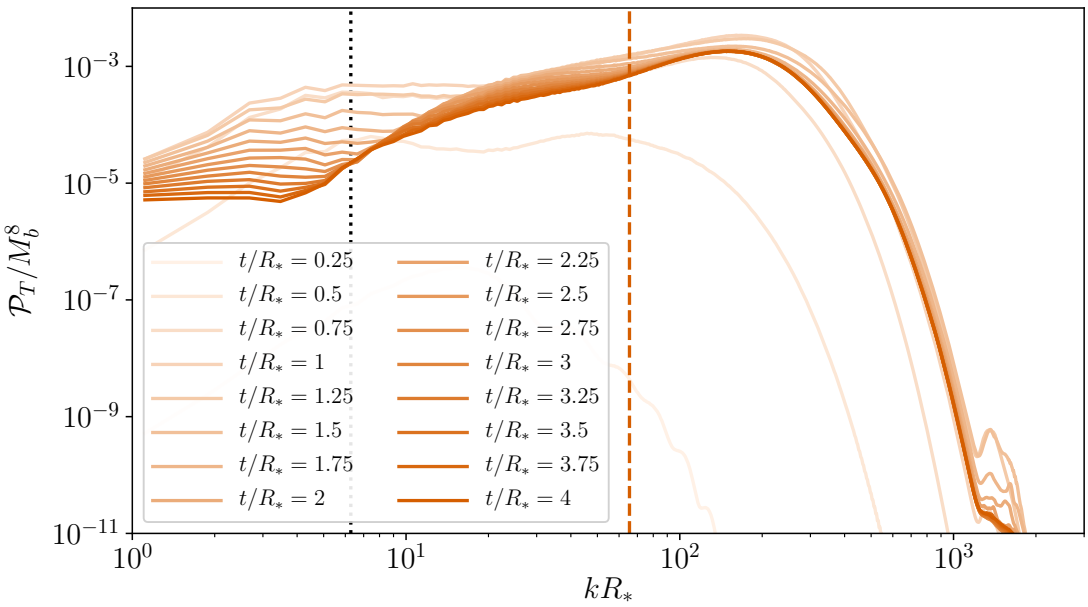

(b) $\overline{\lambda} = 0.07$, $N_\mathrm{b} = 512$

Figure 5.8: The power spectrum of the transverse traceless shear-stress T_{ij}^{TT}. In each plot darker shades indicate later times. The vertical black dotted line shows the location of $k = 2\pi/R_*$, whereas the vertical dashed coloured line shows the location of $k = M_\mathrm{b}$.

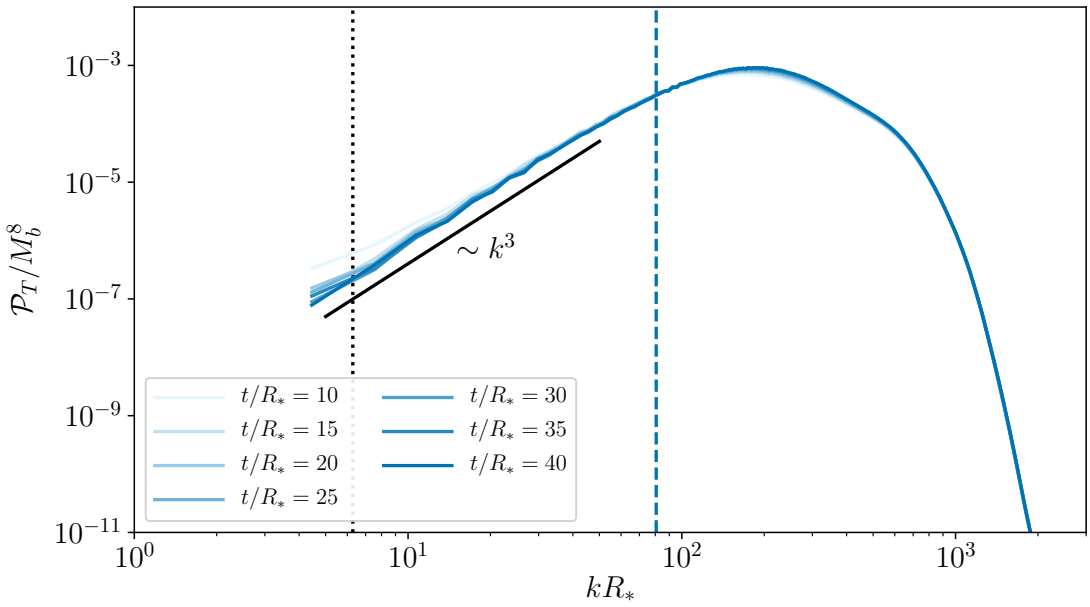

(a) $\overline{\lambda} = 0.84$, $N_\mathrm{b} = 8$

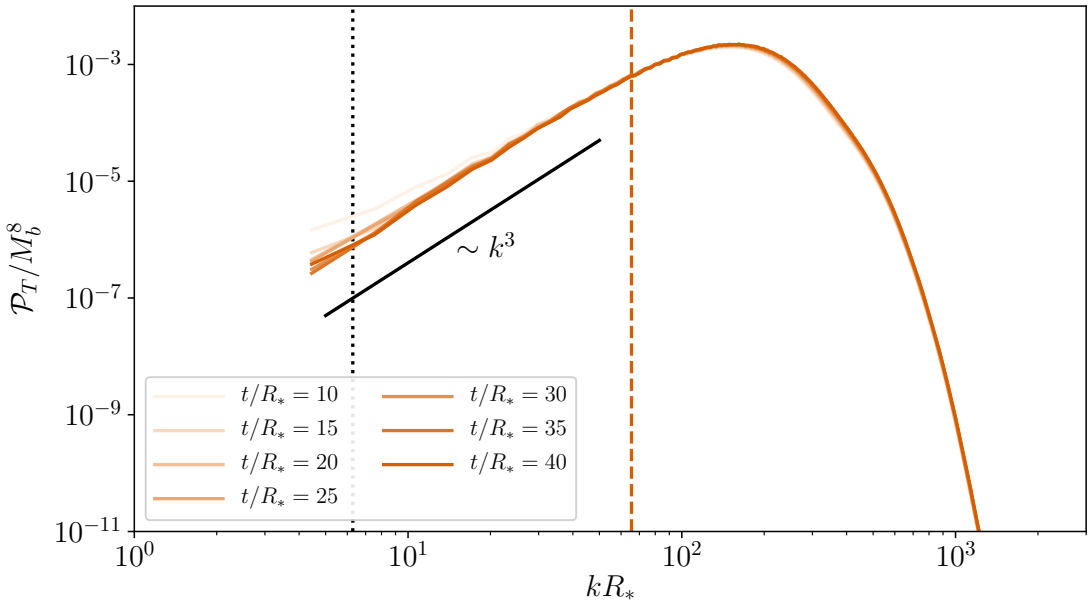

(b) $\overline{\lambda} = 0.07$, $N_\mathrm{b} = 8$

Figure 5.9: The power spectrum of the transverse traceless shear-stress T_{ij}^{TT} at very late times. In each plot darker shades indicate later times. The vertical black dotted line shows the location of $k = 2\pi/R_*$, whereas the vertical dashed coloured line shows the location of $k = M_\mathrm{b}$. The solid black line shows a power law of k^3.

5.6 Results: gravitational waves

We measure the gravitational-wave power spectrum produced during each simulation. We compare the resulting power spectra with the fit predicted from the previous work in Ref. [1], as well as the envelope approximation and bulk flow model fits using an exponential nucleation rate, as detailed in Section 5.3.1. In Fig. 5.10 we plot four snapshots showing the evolution of the gravitational-wave power spectrum (Eq. 5.41) for the largest simulations performed for each $\overline{\lambda}$. These simulations are listed in Table 5.2. The uncertainty for each power spectrum bin is given by the difference between its value in our high and medium resolution runs.

We see that early on in the collision phase at $t/R_* = 0.6$, the power spectrum is growing with a peak at $k \approx 2\pi/R_*$. At early times, for all $\overline{\lambda}$ there is a characteristic infrared power law in k with exponent ~ 3. Later in the collision phase at $t/R_* = 1.6$, most of the bubbles have finished colliding, and we see that for all $\overline{\lambda}$ the peak has shifted towards lower values of k, aligning with the peak locations predicted in Ref. [1] and earlier studies of the envelope approximation. The peak gravitational-wave power at this point seems very close to that predicted for an exponential nucleation rate in the envelope approximation for all $\overline{\lambda}$. With our limited resolution of the IR power law we see that it appears to still be roughly consistent with an exponent of ~ 3. The UV power laws vary between different $\overline{\lambda}$, with thicker potentials having steeper exponents. At later times in the collision phase, we see a rise in the first few bins for our gravitational-wave power spectra, consistent with the slow decay of the IR power in $\mathcal{P}_T$ shown in Fig. 5.8. The limited range we have in the IR makes it difficult to be conclusive about this. The peak location appears to remain fixed. We also see for each simulation the steady growth of a bump in the power spectrum towards the UV, associated with the length scale of $k \sim M_\mathrm{b}$, consistent with that seen in Ref. [1].

We first turn our attention to understanding the evolution of the UV bump in the power spectrum. This is made up of gravitational waves sourced during the oscillation phase, where the scalar field is oscillating around the scale of M_b. In order to see the shape of the power spectra produced from these oscillations, we conduct a series of long-lasting simulations where we only turn on the evolution of the metric perturbations at $t/R_* = 2.5$, long after the last bubbles have collided. These simulation runs are listed in Table 5.3.

We plot the resulting power spectra for $\overline{\lambda} = 0.84$ and $\overline{\lambda} = 0.07$ in Fig. 5.11. We see that for both $\overline{\lambda}$ the power spectra are characterised by a plateau in the IR, presumably turning over at wavelengths larger than we can access within our simulations, and a growing bump

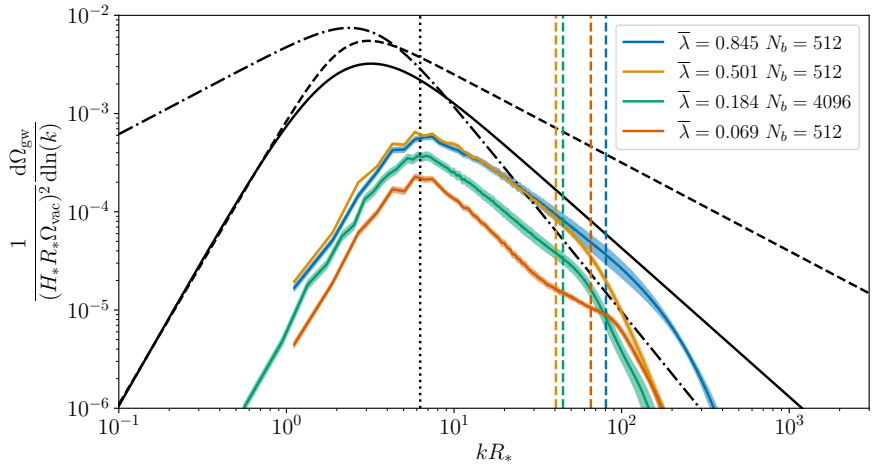

(a) $t/R_* = 0.60$

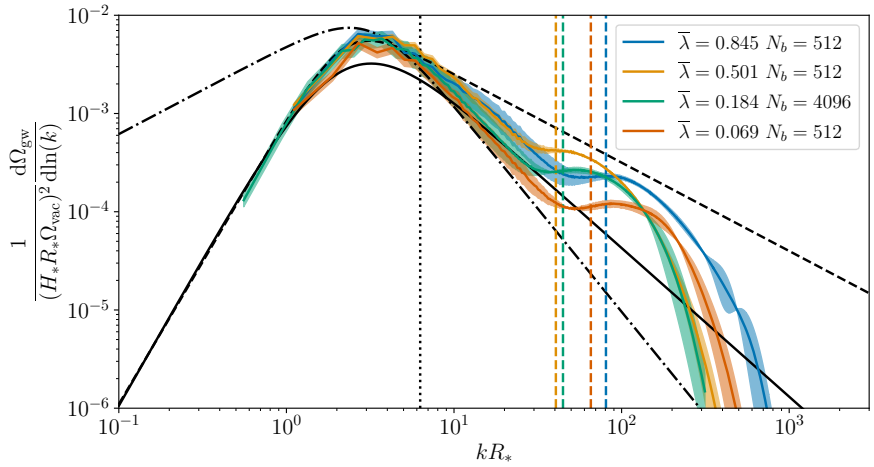

(b) $t/R_* = 1.6$

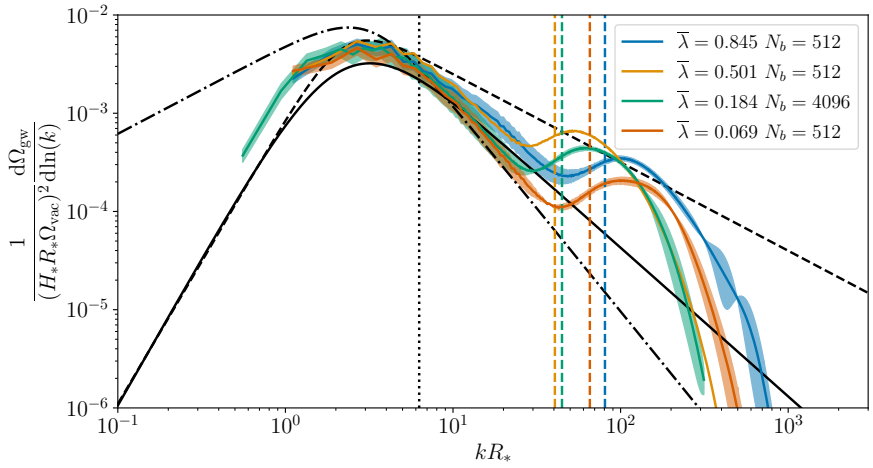

(c) $t/R_* = 2.5$

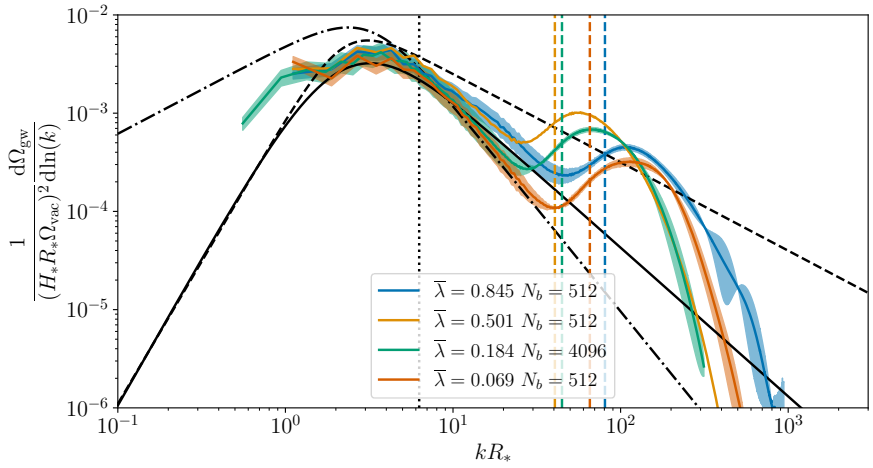

(d) $t/R_* = 4.0$

Figure 5.10: Evolution of the gravitational-wave power spectrum for the largest simulations performed for each $\overline{\lambda}$. Each simulation uses a simultaneous nucleation scenario, and the Lorentz factor of the wall of a bubble with diameter R_* is $\gamma_* = 4.0$. We plot the power spectra at four different times, early collision phase (a), late collision phase (b), early oscillation phase (c), later in the oscillation phase (d). The black dashed line gives the result from the envelope approximation [122], the black dash-dot line gives the prediction from the bulk flow model [122], and the solid black line indicates the previous fit provided in Ref. [1]. The envelope approximation and bulk flow model fits are for an exponential nucleation rate. The vertical dotted line gives the location of $k = 2\pi/R_*$, whereas the coloured dashed lines indicate where $k = M_{\rm b}$. For each simulation we shade a region corresponding to $\pm$ the difference in power between our high and medium resolution runs. At high wavenumbers the signal is overwhelmed by noise arising from single-precision floating point numerical errors. This noise is identified by comparing a smaller single-precision and double-precision run. We therefore apply a cut off in the UV at $k = \pi/2\Delta x$.

at a length scale associated with $M_{\rm b}$.

We can also use these simulations to calculate the growth rate of $\Omega_{\rm gw}$ during the oscillation phase. We plot $\Omega_{\rm gw}$ for our late time simulations in Fig. 5.12. From this plot, we can see that the growth rate is fairly similar for all $\overline{\lambda}$. The rate appears to be slower than linear. Note that the growth of gravitational waves shown in our simulations are in effect an upper bound, as in reality other effects will come into play such as the decay of the scalar field into other particles and damping of the scalar field gradients due to the effects of expansion.

We find that the calculation of the growth of $\Omega_{\rm gw}$ during the oscillation phase is similar for all $\overline{\lambda}$ to that found in Ref. [1]. Therefore, upon extrapolation to a realistic separation of scales, the gravitational wave energy density will be dominated by the production in the collision phase providing $M_b \ll m_{\rm Pl}$, with $m_{\rm Pl}$ the Plank mass.

5.6.1 Fitting

In order to attempt to distinguish between the resulting power spectra for different $\overline{\lambda}$ we calculate fits for the spectrum. We do this for the largest simulation performed for each $\overline{\lambda}$. We choose to fit according to the following function,

$$\frac{d\Omega_{\rm gw}}{d\ln(k)} = \tilde{\Omega}_{\rm GW}\frac{(a+b)\tilde{k}^b k^a}{b\tilde{k}^{(a+b)} + ak^{(a+b)}}, \tag{5.55}$$

where a, b, $\tilde{k}$ and $\tilde{\Omega}_{\rm GW}$ are the fitting parameters. The fit is calculated using the difference in power between the high resolution and medium resolution runs as the one sigma uncertainty for each bin.

We are able to see from Fig. 5.10 that there appears to be some indication of time dependence in the power spectra, even after the bubbles have finished colliding. This is also indicated due to the evolution of $\mathcal{P}_T$ shown in Fig.5.8. We, therefore, choose to perform our fit throughout the simulation and track how the fitting parameters evolve. We fit for values of k up to $k = M_{\rm b}/2$ in order to avoid the UV power law being affected by the growing bump associated with oscillations in the scalar field about the mass scale.

In Fig. 5.13, we plot how all four fitting parameters a, b, $\tilde{k}$ and $\tilde{\Omega}_{\rm GW}$ evolve for the largest simulation for each $\overline{\lambda}$ in Table 5.2. We include lines to illustrate the predictions for each parameter by the envelope approximation and by the bulk flow model.

Note that the envelope and bulk flow predictions are taken from simulations with an exponential nucleation rate, whereas our simulations use simultaneous nucleation. This could result in a discrepancy between the peak frequency and amplitude [66], though the power law exponents are not typically affected by the nucleation scenario. In previous

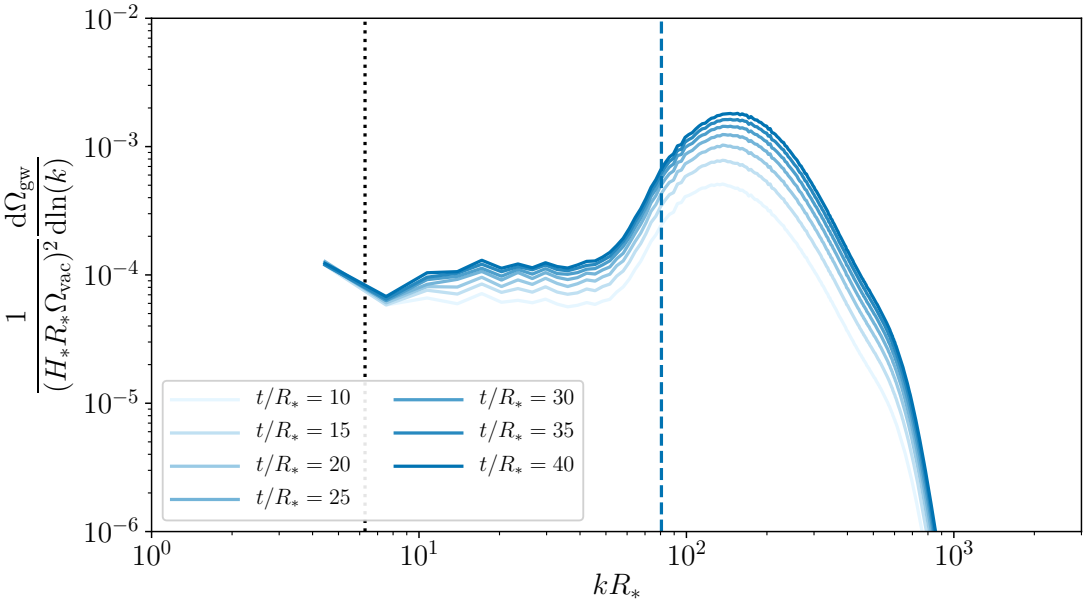

(a) $\overline{\lambda} = 0.84$, $N_{\rm b} = 8$

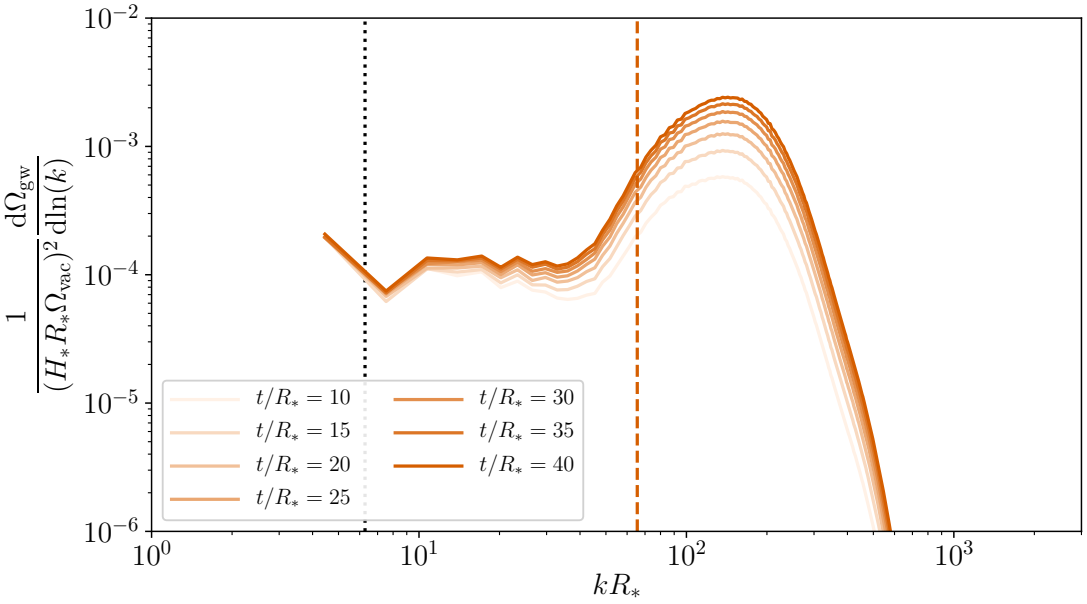

(b) $\overline{\lambda} = 0.07$, $N_{\rm b} = 8$

Figure 5.11: The power spectrum of the gravitational wave energy density parameter for two of the simulations listed in Table 5.3. In these simulations the metric perturbations are only turned on after the bubbles have finished colliding, at $t/R_* = 2.5$. In each plot darker shades indicate later times. The vertical black dotted line shows the location of $k = 2\pi/R_*$, whereas the vertical dashed coloured line shows the location of $k = M_{\rm b}$.

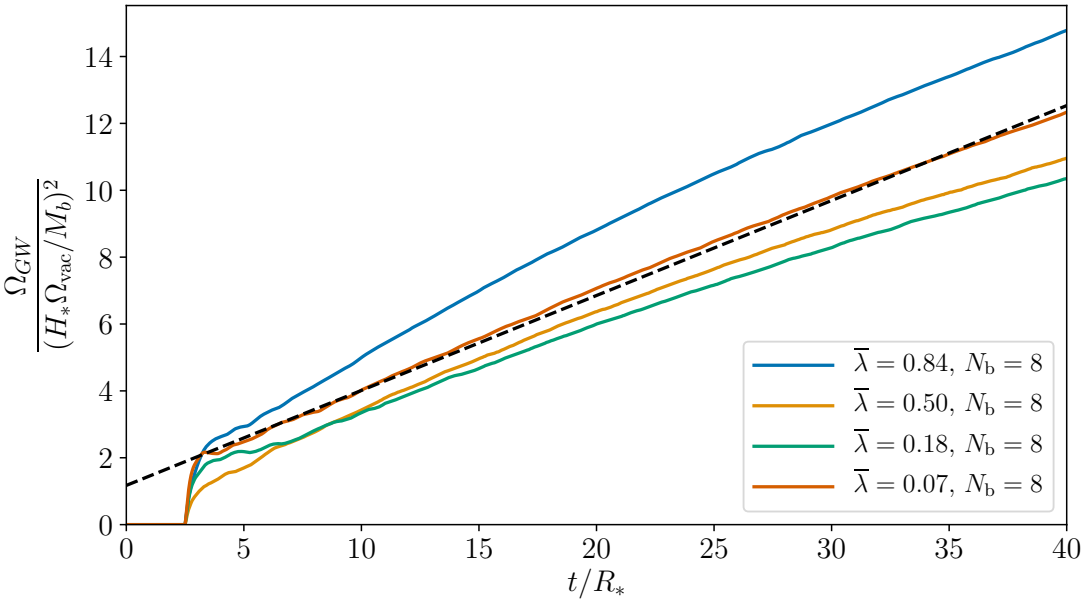

Figure 5.12: Evolution of the total gravitational wave energy density parameter $\Omega_{\rm gw}$ for a series of $\overline{\lambda}$. These are the simulations listed in Table 5.3, in which the evolution of h_{ij}^{TT} is only turned on at $t/R_* = 2.5$. The black dashed line represents a linear fit to the data with slope $\frac{d\Omega_{\rm gw}}{dt} \sim 0.28(H_*\Omega_{\rm vac}/M_{\rm b})^2/R_*$.

lattice simulations conducted in Ref. [1], no strong dependence on the nucleation rate was seen in the peak amplitude or frequency.

At early times the peak frequency is slightly more than $\tilde{k} \sim 2\pi/R_*$, but as the bubbles finish colliding this shifts to smaller values, closer to $\tilde{k} \sim \pi/R_*$. This behaviour is consistent across all $\overline{\lambda}$. In all cases, the final value of $\tilde{k}$ is larger than predicted for an exponential rate in the bulk flow model and slightly larger than the envelope approximation prediction.

The peak gravitational-wave amplitude is obtained around the time of $t/R_* = 1.5$. At later times, the peak amplitude drops as the power spectrum becomes more broad. We observe that there is some deviation between $\overline{\lambda}$ with the peak gravitational-wave power larger for the two thin wall potentials, and smaller for the two thick wall potentials. This effect is overall quite small, and $\tilde{\Omega}_{\rm gw}$ is the fitting parameter most sensitive to lattice effects, see App. 5.8.1. The peak amplitude is smaller than that predicted for an exponential nucleation rate in the envelope approximation, which in turn is smaller than the amplitude predicted in the bulk flow model.

We see that at early times, for all $\overline{\lambda}$, the IR power law is close to a white noise spectrum of k^3. After the bubbles finish colliding, the IR power law decreases. This indicates that gravitational waves are being sourced on scales larger than R_*. This agrees with what we have seen in both $\mathcal{P}_T$ and Fig. 5.10. There is some indication of the IR power law

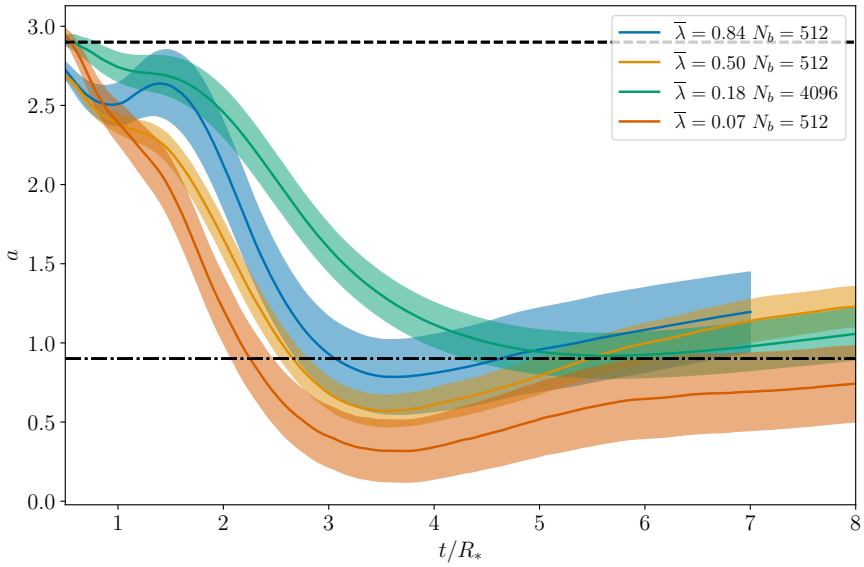
$\overline{\lambda} = 0.84$ $N_b = 512$
$\overline{\lambda} = 0.50$ $N_b = 512$
$\overline{\lambda} = 0.18$ $N_b = 4096$
$\overline{\lambda} = 0.07$ $N_b = 512$
a
t/R_*

(a)

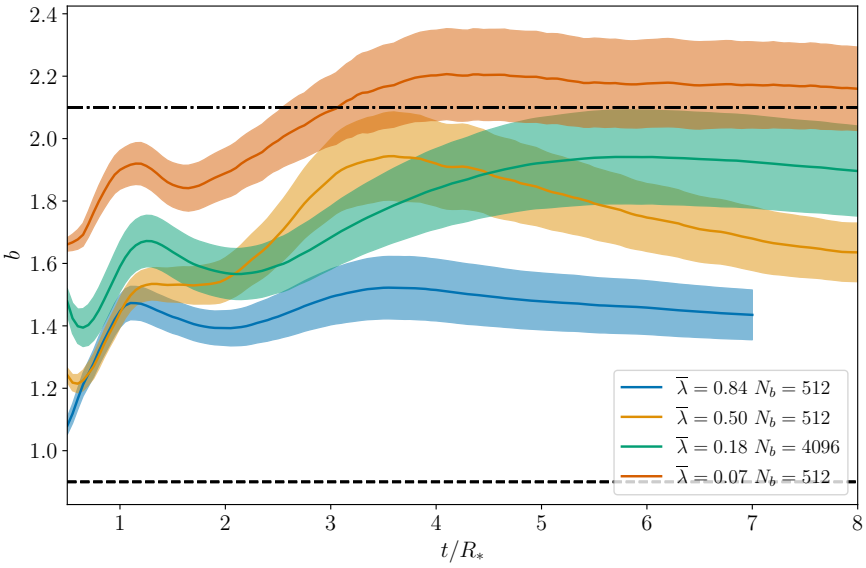
$\overline{\lambda} = 0.84$ $N_b = 512$
$\overline{\lambda} = 0.50$ $N_b = 512$
$\overline{\lambda} = 0.18$ $N_b = 4096$
$\overline{\lambda} = 0.07$ $N_b = 512$
b
t/R_*

(b)

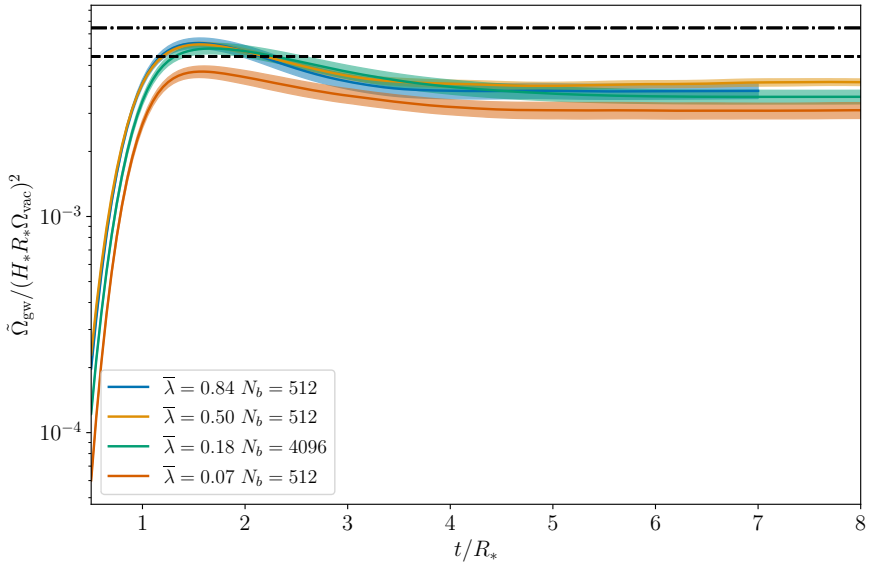

(c)

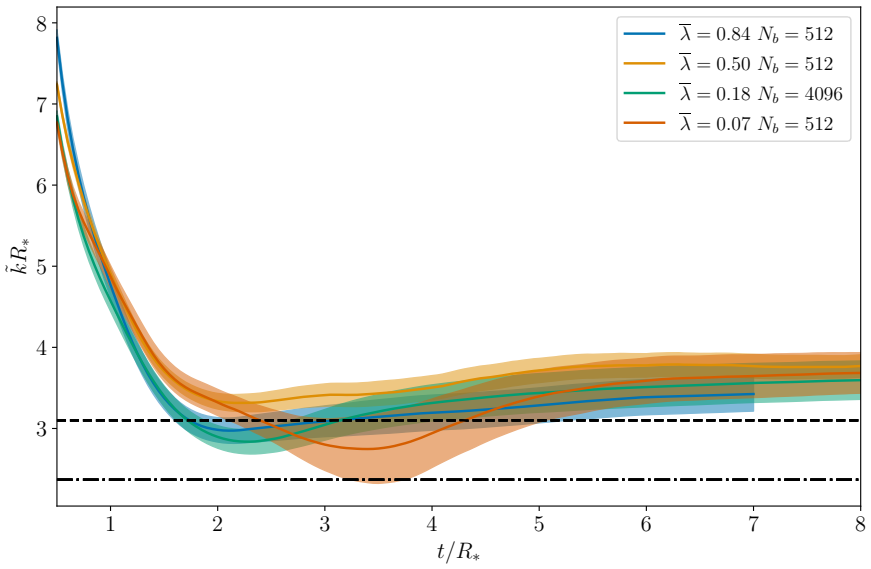

(d)

Figure 5.13: Plot of the values of all the fitting parameters in Eq. 5.55 for a simultaneous nucleation rate. These have been found using the largest simulation for each $\overline{\lambda}$ in Table 5.2. We plot how these values vary with time during the simulations. In (a) we show the IR power law a, in (b) we show the UV power law b, in (c) we plot the peak amplitude $\tilde{\Omega}_{\rm GW}$ and in (d) we plot the peak frequency $\tilde{k}$. The coloured bands show the region corresponding to one standard deviation on the fitting parameters. In each plot we highlight the prediction for each parameter for an exponential nucleation rate in the envelope approximation by a horizontal dashed black line, and in the bulk flow model by a dash-dot black line.

exponent a growing towards the end of the simulations. Our limited resolution in the IR and the small number of modes in the bins with smallest k values mean that we cannot evaluate accurately the value of a, particularly at late times where the peak frequency is smallest. However, the data that we do have does show a strong indication of an IR power law that becomes shallower than k^3 at late times after the bubbles have finished colliding. This is particularly true in the case of $\overline{\lambda} = 0.18$ which has the largest number of bubbles, $N_{\rm b} = 4096$. For all $\overline{\lambda}$, the final value of the IR power law is close to $a = 1$ as predicted by the bulk flow model. We do see some indication that, as $\overline{\lambda}$ increases, the final IR power law becomes steeper.

At early times, the UV power law exponent b grows for all $\overline{\lambda}$. At late times we see that there is also a consistent trend in b according to $\overline{\lambda}$, with the UV power law becoming steeper as $\overline{\lambda}$ decreases. The final value of b for $\overline{\lambda} = 0.07$ is close to that of the bulk flow model prediction. As $\overline{\lambda} \to 1$, the value of b decreases, moving towards the value predicted in the envelope approximation, though it does not reach it for the values of $\overline{\lambda}$ we study.

There is some indication that there is a slow decrease in b at late times. This is in part because a and b are anti-correlated around the peak of the spectrum, and as a grows b decreases. The limited separation of scales we obtain between R_* and $1/M_{\rm b}$ increases the influence of a on b. This effect is strongest for $\overline{\lambda} = 0.50$ where the peak in the spectrum from bubble collisions and that from oscillations in the scalar field are closest together. Forcing a to be fixed leads to a more stable value of b at the end of the simulation, though a worse fit overall. In order to obtain a more accurate fit for b, we need to improve our resolution in the IR to obtain a better estimate on a. Alternatively, we could increase the separation between R_* and $1/M_{\rm b}$ by increasing γ_*. Both of these options require larger simulations and a dynamic range currently unavailable to us.

In Table 5.4 we provide the late time values of the fitting parameters for each $\overline{\lambda}$. These are taken at the end of the simulation, corresponding to $t/R_* = 7.0$ for $\overline{\lambda} = 0.84$ and $t/R_* = 8.0$ for the other $\overline{\lambda}$. Caution should be taken when using these values, as from Fig. 5.13 it can be seen that the exponents a and b have not completely settled by the end of our simulations.

5.7 Conclusions

In this work, we have investigated whether the underlying potential for a vacuum phase transition can affect the resulting gravitational-wave signal. We note that, for a quartic effective potential with a cubic term, the effect of the potential on the dynamics of the

$\overline{\lambda}$	$\tilde{\Omega}_{\rm GW}/(H_* R_* \Omega_{\rm vac})^2$	$\tilde{k} R_*$	a	b
0.84	$(3.81 \pm 0.30) \times 10^{-3}$	3.42 ± 0.21	1.20 ± 0.25	1.44 ± 0.08
0.50	$(4.18 \pm 0.15) \times 10^{-3}$	3.77 ± 0.14	1.23 ± 0.13	1.64 ± 0.09
0.18	$(3.56 \pm 0.26) \times 10^{-3}$	3.60 ± 0.24	1.06 ± 0.16	1.90 ± 0.14
0.07	$(3.10 \pm 0.26) \times 10^{-3}$	3.68 ± 0.25	0.742 ± 0.241	2.16 ± 0.13

Table 5.4: Final values of fitting parameter values in Eq. 5.55 which gives gravitational-wave power spectrum arising from bubble collisions. These are calculated for the largest simulation for all $\overline{\lambda}$ given in Table 5.2. The values supplied here are taken at the end of the simulations, which corresponds to $t/R_* = 7.0$ for $\overline{\lambda} = 0.84$ and $t/R_* = 8.0$ for the other values of $\overline{\lambda}$. Uncertainties on the fitting parameters are calculated taking the one sigma uncertainty on each power spectrum bin to be given by the difference between its value in our medium and high resolution runs.

scalar field is determined through a single parameter, $\overline{\lambda}$. When $\overline{\lambda} \to 1$, we are in the thin wall limit, and the critical profile can be approximated by a tanh function. The thick wall limit is approached for $\overline{\lambda} \to 0$, and in this case, the critical profile is approximated well by a gaussian.

The dynamics of the scalar field in the overlap region between colliding bubbles depends on the value of $\overline{\lambda}$. When $\overline{\lambda}$ is close to one, after bubbles collide, the scalar field rebounds in the overlap region towards the symmetric phase. The rebound is reduced as $\overline{\lambda} \to 0$ for fixed γ_*.

We have explored a range of $\overline{\lambda}$ in a series of simulations with up to 4800^3 lattice sites in which as many as 4096 bubbles are nucleated simultaneously. From these, we evaluate the transverse traceless shear-stress T_{ij}^{TT} and compute the power spectrum $\mathcal{P}_T$. We find evidence that even after the bubbles have finished colliding, gravitational waves continue to be sourced at scales larger than R_*. This could be as a result of energy density in the bubble walls continuing to propagate after collision. Continued propagation of shells of energy density after collision is a violation of one of the assumptions of the envelope approximation and matches closer to the bulk flow model.

After the bubbles have finished colliding, we enter an oscillation phase during which the scalar field is oscillating around ϕ_b. This produces a peak in $\mathcal{P}_T$ around $k \sim M_{\rm b}$, and at very late times this develops a white noise IR power law of k^3. While this feature is very long-lasting within our simulations, we would expect that in reality, the amplitude would decay as the scalar field gradients decrease due to quantum processes and Hubble

friction.

During the oscillation phase, gravitational waves are sourced by a feature in $\mathcal{P}_{TTT}$ with a peak around $k \sim M_{\rm b}$. This behaviour was already noted in Refs. [1, 118]. This feature produces a bump in the gravitational-wave power spectrum around $k \sim M_{\rm b}$ for all $\overline{\lambda}$. The growth rate of the $\Omega_{\rm gw}$ during the oscillation phase is slightly slower than linear. As our simulations do not account for damping from Hubble friction or allow for the scalar field to decay via quantum processes, this should be taken as an upper bound on the growth rate for $\Omega_{\rm gw}$. Our results on the growth rate are consistent with those in Ref. [1], where it was shown that the total gravitational-wave power from the oscillation phase will be suppressed compared to that arising from bubble collisions providing that $M_{\rm b} \ll m_{\rm P}$.

We also compute the gravitational wave energy density parameter power spectrum $d\Omega_{\rm gw}/d\ln(k)$. We perform a fit for the spectrum arising from bubble collisions using Eq. 5.55. We calculate how the fitting parameters vary during our simulations.

There are some indications that $\overline{\lambda}$ can affect the resulting gravitational-wave power spectrum. The peak power of the gravitational-wave power spectrum varies according to $\overline{\lambda}$, though the variation is probably not significant enough to be observable. The values of $\tilde{\Omega}_{\rm GW}$ found at the end of our simulations are larger for $\overline{\lambda} > 0.5$, and decreases for smaller $\overline{\lambda}$. The peak amplitude $\tilde{\Omega}_{\rm GW}/(H_* R_* \Omega_{\rm vac})^2$ varies between 4.2×10^{-3} for $\overline{\lambda} = 0.50$, and 3.1×10^{-3} for $\overline{\lambda} = 0.07$.

More hopeful is the possibility that we could distinguish vacuum transitions with different potentials due to the UV power law. The UV power laws we find at the end of the simulations become steeper as $\overline{\lambda}$ decreases. The gravitational-wave power spectrum falls as $k^{-1.4}$ for $\overline{\lambda} = 0.84$ and $k^{-2.2}$ for $\overline{\lambda} = 0.07$.

The IR power law is close to k^3 when bubbles start to collide, with a peak in the spectrum around $k \sim 2\pi/R_*$. At later times the peak shifts slightly towards the IR. The section of the IR power law that we can resolve appears to become shallower with an exponent < 3. Our limited resolution in the IR means that we can only infer the power law from the first few bins in our power spectrum. We find that at the end of our simulations the IR power law is shallower for smaller $\overline{\lambda}$, varying between $k^{1.2}$ for $\overline{\lambda} = 0.84$ and $k^{0.7}$ for $\overline{\lambda} = 0.07$. Presumably, at larger scales than we can resolve within our simulations, the power law turns over to a white noise spectrum as causality dictates.

We find that neither the envelope approximation or the bulk flow model correctly predict the final gravitational-wave power spectrum. For all $\overline{\lambda}$, the peak power is slightly smaller than predicted by the envelope approximation which is itself smaller than the

bulk flow model predicts. The peak location is closer to that predicted by the envelope approximation. The UV power law is similar to the bulk flow model for small $\overline{\lambda}$, and moves towards the envelope approximation prediction as $\overline{\lambda}$ increases. The value of the IR power law also seems to be closer to the bulk flow model, though as $\overline{\lambda}$ increases, it does become steeper, shifting towards the envelope approximation value. This roughly follows the picture proposed in Ref. [116]. It remains to be determined if simulations with larger $\overline{\lambda}$ become even closer to the envelope approximation, and whether at larger γ_* the proposal of Ref. [116] becomes more exact.

Overall, we have shown that for vacuum phase transitions, the underlying effective potential can affect the resulting gravitational wave power spectrum. In particular, we have seen that, for the quartic potential that we investigated, the UV power law appears sensitive to $\overline{\lambda}$. The IR power law is challenging to resolve with our simulations, but we see some indication that it may be shallower than a k^3 spectrum, and it appears to be evolving long after the bubbles have finished colliding. Further explorations into the IR power law and behaviour of the gravitational-wave power spectrum as we extrapolate to larger γ_* will require new techniques as we have reached the limit of the computing resources available to us.

Acknowledgements

We thank Oliver Gould, Rysuke Jinno, Thomas Konstandin, Eugene Lim, Satumaaria Sukuvaara and Essi Vilhonen for useful discussions. DC, DJW, and MH would like to thank Nordita for their hospitality during the "Gravitational Waves from the Early Universe" workshop. Our simulations were carried out at the Finnish Centre for Scientific Computing CSC. DC (ORCID ID 0000-0002-7395-7802) is supported by a Science and Technology Facilities Council Studentship and the University of Sussex. EGE was supported by the Academy of Finland, grant 320123. EGE and DJW were supported by the Research Funds of the University of Helsinki. DJW (ORCID ID 0000-0001-6986-0517) was supported by a Science and Technology Facilities Council Ernest Rutherford Fellowship, grant no. ST/R003904/1, and by the Academy of Finland, grants 324882 and 328958. MH was supported by the Science and Technology Facilities Council (grant number ST/P000819/1) and the Academy of Finland (grant number 286769).

5.8 Appendix

5.8.1 Convergence tests

Gravitational waves

Our convergence tests for the gravitational-wave power spectrum consist of performing a series of simulations in which the bubbles are nucleated in the same position, but the lattice spacing Δx is varied while keeping the timestep $\Delta t = \Delta x/5$. We refer to the value of Δx used in the main paper as $\Delta x_{\rm ref}$. Tables 5.2 and 5.3 contain the values of this and other important simulation parameters. The captions to these tables are also useful as reminders of the symbols used in the following discussion.

In Fig. 5.14 we plot the gravitational-wave power spectrum at $t/R_* = 8.0$ for $\overline{\lambda} = 0.18$ with $N_{\rm b} = 4096$. We do this for $\Delta x/\Delta x_{\rm ref}$ equal to 1, 2, and 4. From this plot, we can see that the gravitational-wave power generated by oscillations around the mass scale is well behaved at these lattice spacings. The spectrum due to bubble collisions varies more substantially. The peak location remains fairly fixed, and the IR and UV power laws seem consistent across lattice spacings. The amplitude of the spectrum increases as Δx is decreased. From this, we can clearly see that it is the total gravitational-wave power rather than the peak location or power law exponents that is most sensitive to the lattice spacing.

From our convergence tests, we can estimate the lattice errors on the fitting parameters reported in Table 5.4. In order to do this, we must vary the lattice spacing of the simulations with the most bubbles. This corresponds to $N_{\rm b} = 4096$ for $\overline{\lambda} = 0.18$, and $N_{\rm b} = 512$ for all other $\overline{\lambda}$. We perform additional simulations with $\Delta x/\Delta x_{\rm ref} = 2$ and 4. We find the fitting parameters in Eq. 5.55 at the end of each simulation. We then plot how the fitting parameters vary with Δx in Fig. 5.15. Differences between the parameter values at $\Delta x_{\rm ref}$ and the values quoted in Table 5.4 arise as we use a uniform uncertainty across all bins[1]. This differs to the results listed in the main body of the paper where the difference in power at each bin between high and mid resolutions runs was used as the uncertainty.

We see that the change in a, b and $\tilde{k}$ between $\Delta x/\Delta x_{\rm ref} = 2$ and $\Delta x/\Delta x_{\rm ref} = 1$ is at the $\sim 1\%$ level, whereas it is at the $\sim 10\%$ level for $\tilde{\Omega}_{\rm gw}$. Extrapolating a linear fit on $\tilde{\Omega}_{\rm gw}$ as a function of Δx to the continuum shows us that the error on $\tilde{\Omega}_{\rm gw}$ at $\Delta x_{\rm ref}$ is on the

[1] We use the SciPy library function `optimize.curve_fit` with arguments `sigma=None` and `absolute_sigma=False`. This weights each bin power spectrum bin used in the fit equally with a uniform uncertainty.

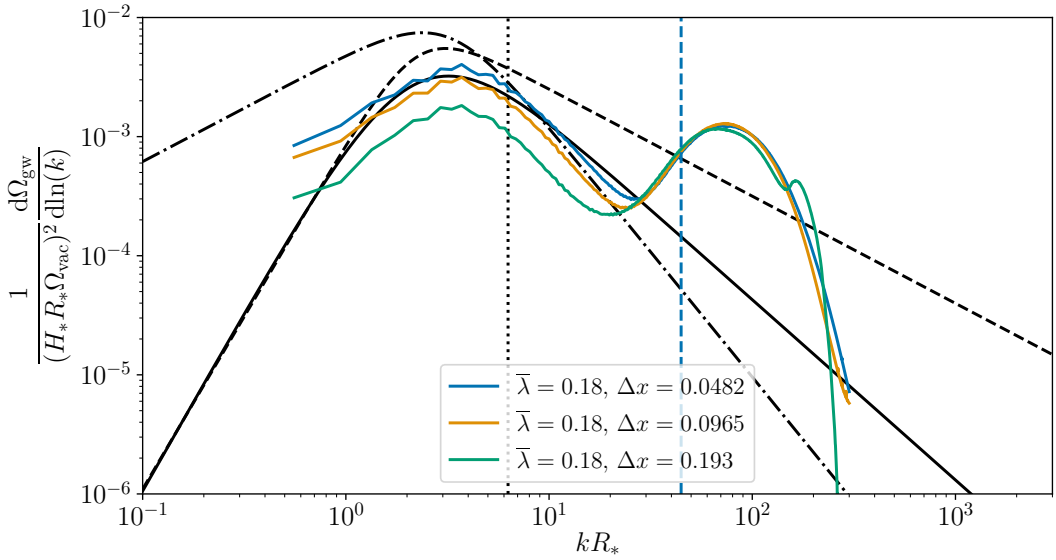

Figure 5.14: Variation of the gravitational-wave power spectrum with lattice spacing at $t/R_* = 8.0$ for $\overline{\lambda} = 0.18$ with $N_{\rm b} = 4096$. The black dashed line gives the result from the envelope approximation [122], the black dash-dot line gives the prediction from the bulk flow model [122], and the solid black line indicates the previous fit provided in Ref. [1]. The vertical dotted line gives the location of $k = 2\pi/R_*$, whereas the red dashed line indicates where $k = M_{\rm b}$. At high wavenumbers the signal is overwhelmed by single-precision white noise in the power spectrum from the fast Fourier transforms. For this reason we apply a cut off in the UV.

order of 10%. Even in the continuum limit $\tilde{\Omega}_{\rm gw}$ is smaller than the envelope prediction.

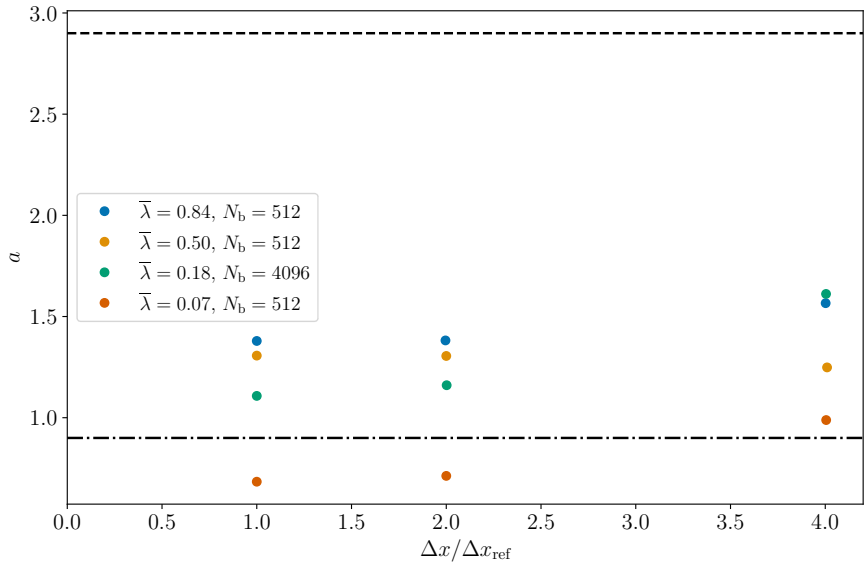

(a)

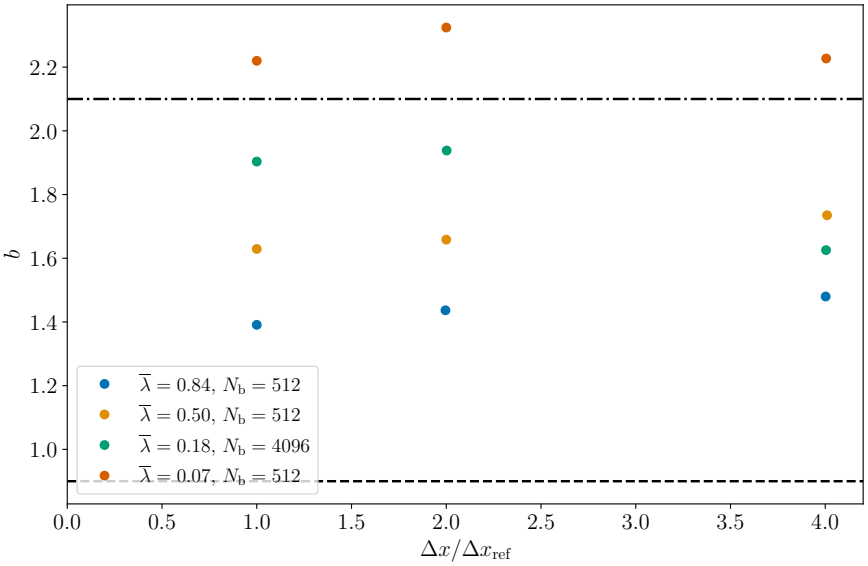

(b)

In order to check the behaviour of the gravitational-wave power spectrum for $\Delta x/\Delta x_{\rm ref} < 1$, we must reduce the size of the simulations and number of bubbles. We perform a series of simulations with $N_{\rm b} = 8$ for each $\overline{\lambda}$. In this case we can no longer fit the power spectrum according to Eq. 5.55, as the peak of the spectrum is not resolved. Instead we fit the UV power law according to the following equation,

$$\frac{d\Omega_{\rm gw}}{d\ln(k)} = A\left(\frac{R_*}{2\pi}k\right)^{-b}, \tag{5.56}$$

where b is the UV power law exponent and A corresponds to the amplitude of the spectrum at $k = 2\pi/R_*$. We provide the resulting evaluation of A and b at $t/R_* = 8.0$ in Fig. 5.16.

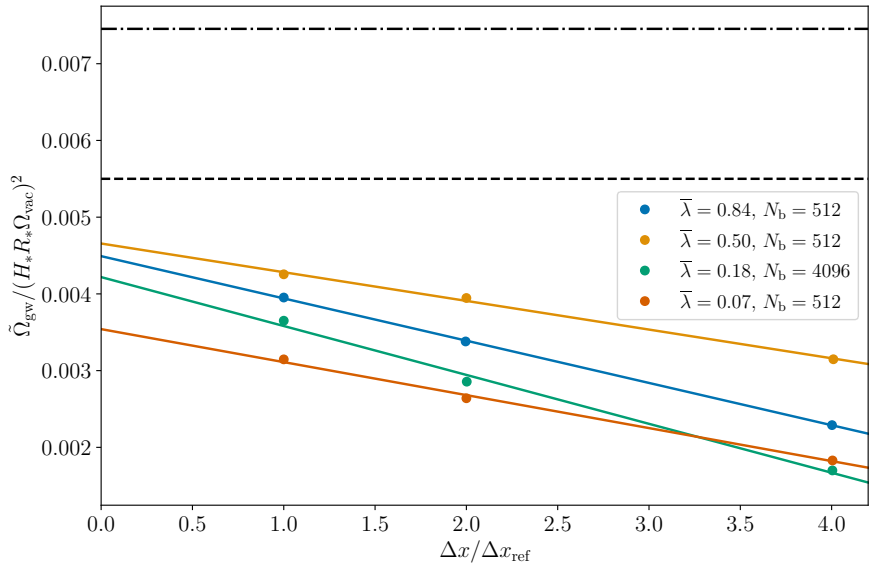

(c)

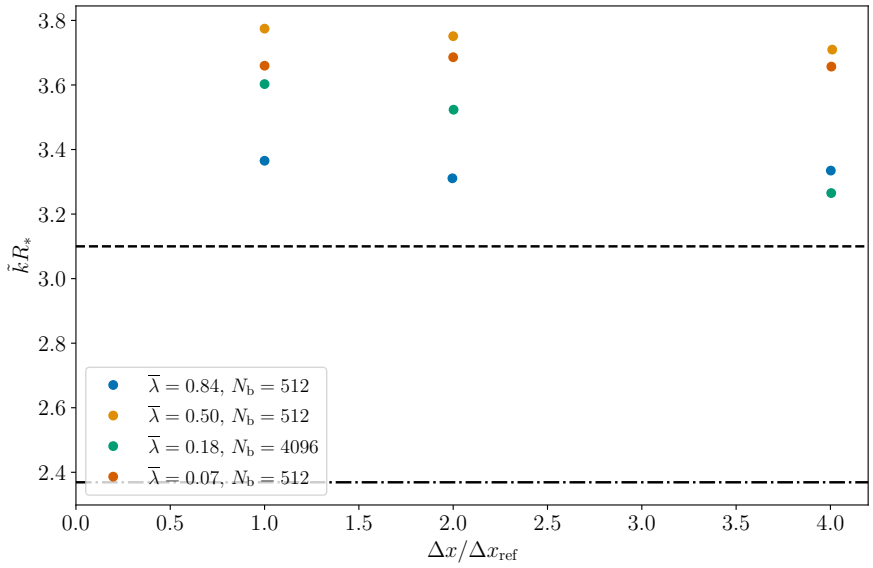

(d)

Figure 5.15: Convergence of the fitting parameters in Eq. 5.55 calculated at the end of each simulation. We plot how the fitting parameters vary with $\Delta x/\Delta x_{\rm ref}$, where $\Delta x_{\rm ref}$ corresponds to the value of Δx used in Table 5.2. In (a) we show the IR power law a, in (b) we show the UV power law b, in (c) we plot the peak amplitude $\tilde{\Omega}_{\rm gw}$, and in (d) we plot the peak frequency $\tilde{k}$. For the peak amplitude we also plot a linear fit to the continuum value. In each plot, we highlight the prediction for each parameter by the envelope approximation by a horizontal dashed black line, and for the bulk flow model by a dash-dot black line.

We do not see any indication of a change in behaviour at smaller lattice spacing than Δx_{ref}.

Scalar field

In order to study the effect of the lattice spacing on the scalar field, we perform a series of simulations of isolated bubbles. We do this both in a simplified 1D code with spherical symmetry and compare the results to an isolated bubble expanding in our 3D code. From this, we are able to measure the deviation of the scalar field profile from its expected behaviour outlined in Section 5.2.3. The deviation then provides some measure of the lattice effects. We show the deviation of bubble radius parameters r_{in}, r_{out} and r_{mid} for a series of lattice spacings and two $\overline{\lambda}$ in Fig. 5.17.

We calculate an effective Lorentz factor of the bubble wall via the contraction of the bubble wall width, $\gamma_{\text{sim}} = l_{\text{w}}/(r_{\text{out}} - r_{\text{in}})$. The effect of the lattice on γ as estimated from the wall thickness is shown in Fig. 5.18.

We see that even a small deviation in r_{in}, r_{out} and r_{mid} can result in a large change in the measured value of γ_{sim}. The finer the lattice spacing the larger γ can grow with γ_{sim} remaining close to the theoretical value. We also see that for the same lattice spacing, the 3D runs show smaller lattice effects during expansion. For large $\overline{\lambda}$, as γ increases $\gamma_{\text{sim}}/\gamma$ will decrease, whereas for small $\overline{\lambda}$ we see that first, the lattice effects cause the ratio $\gamma_{\text{sim}}/\gamma$ to grow before eventually it also decreases below unity.

5.8.2 Slices

In Fig. 5.19 and Fig. 5.20 we show slices through simulations with $\overline{\lambda} = 0.07$ and $\overline{\lambda} = 0.84$ respectively. Both simulations have $N_{\text{b}} = 64$, and $\gamma_* = 4$. The slices show ϕ, ρ_{gw} and $\sqrt{T_{ij}^{TT} T_{ij}^{TT}}$ at t/R_* equal to 0.5, 1.0 and 4.0.

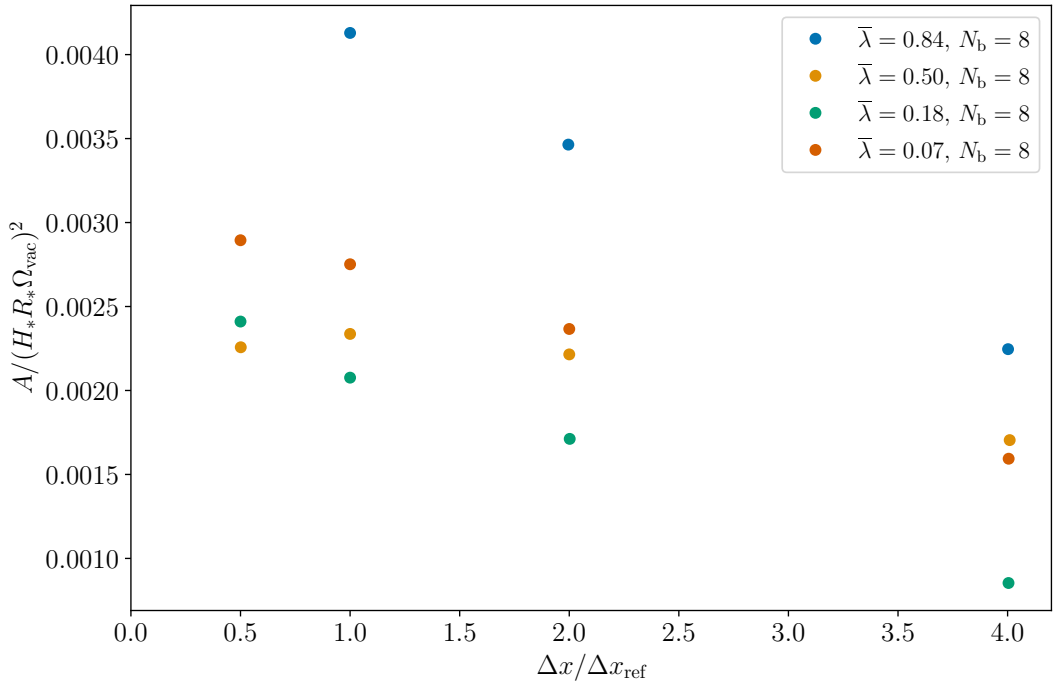

(a)

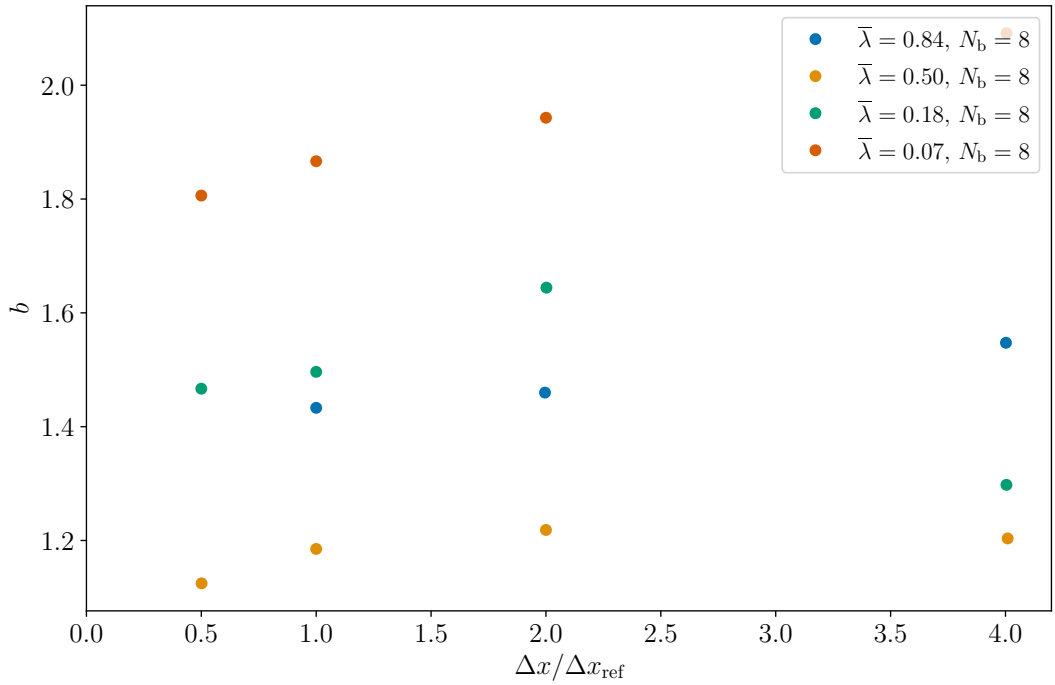

(b)

Figure 5.16: Convergence of the fitting parameters in Eq. 5.56 calculated at the end of each simulation. We plot how the fitting parameters vary with $\Delta x/\Delta x_\mathrm{ref}$, where Δx_ref corresponds to the value of Δx used in Table 5.2. In (a) we plot the amplitude of the power spectrum at $k = 2\pi/R_*$, A and in (b) we show the UV power law b.

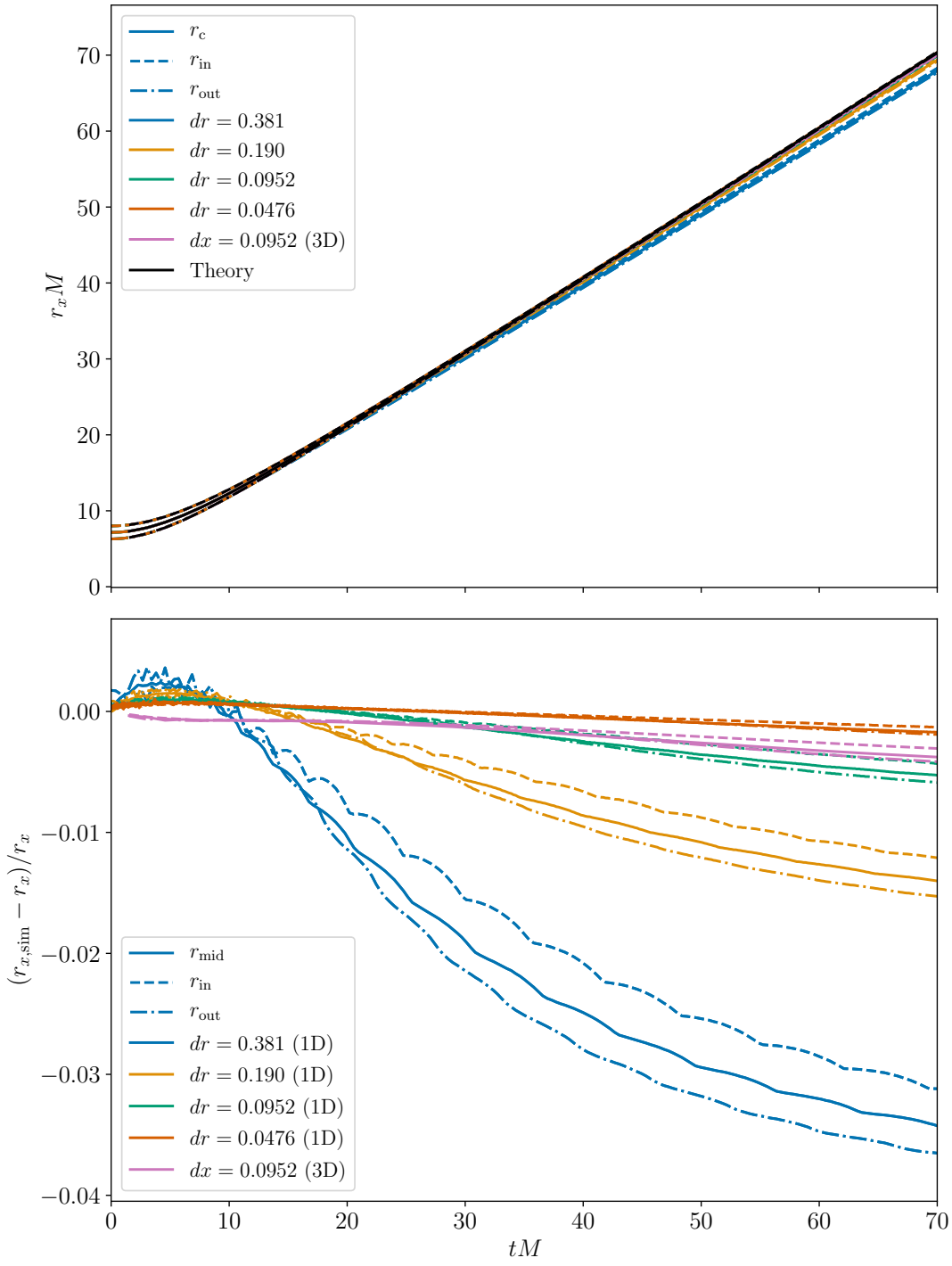

(a) $\overline{\lambda} = 0.84$

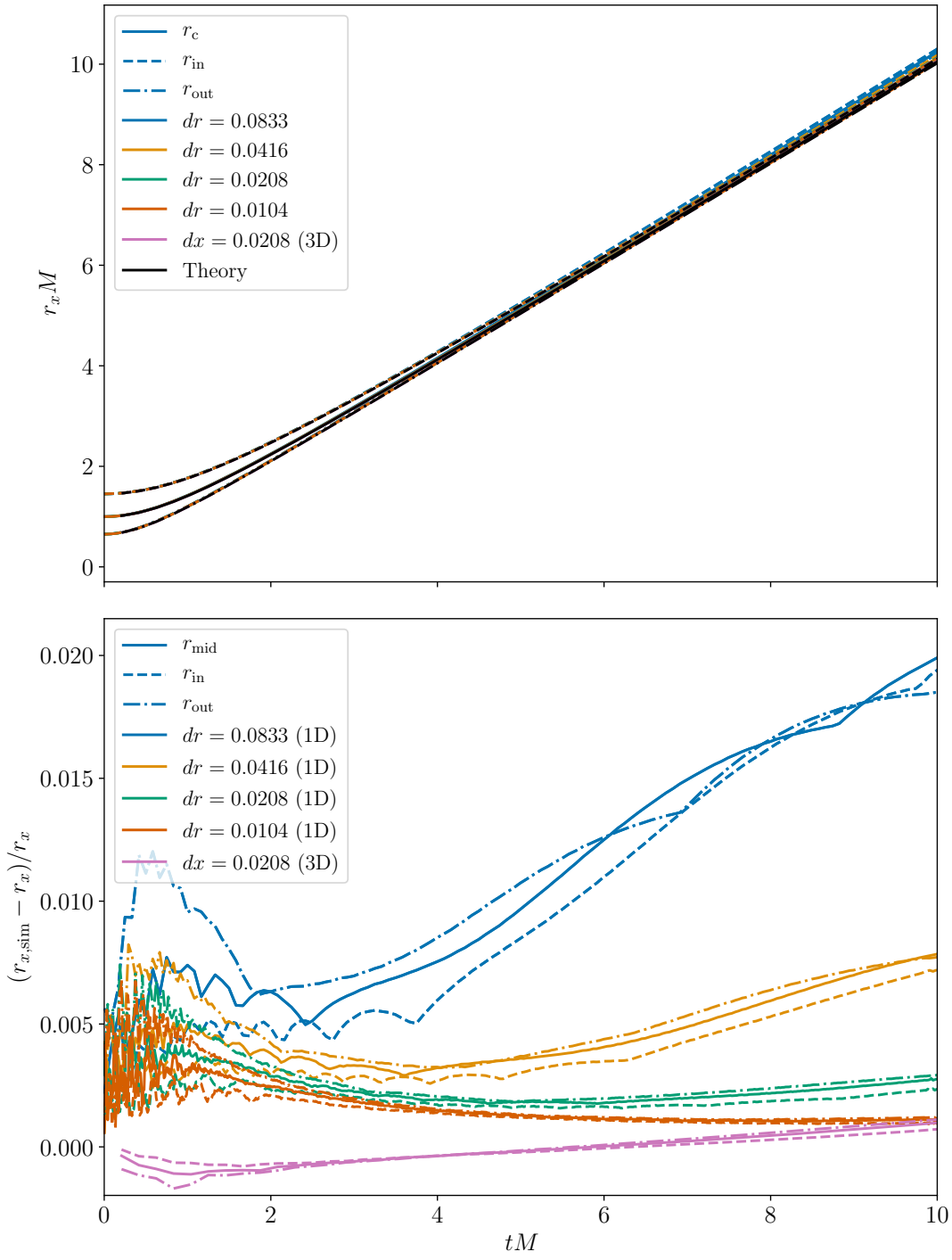

(b) $\overline{\lambda} = 0.07$

Figure 5.17: In the top plots we show the evolution of the bubble radius parameters r_{mid}, r_{in} and r_{out} (defined in subsection 5.2.2) for an isolated bubble. These are given for 1D simulations with various lattice spacings as well as the theoretical behaviour. The bottom panels give the fractional deviation from the theoretical value for each lattice spacing. We also include the result of an isolated bubble left to expand in a 3D simulation.

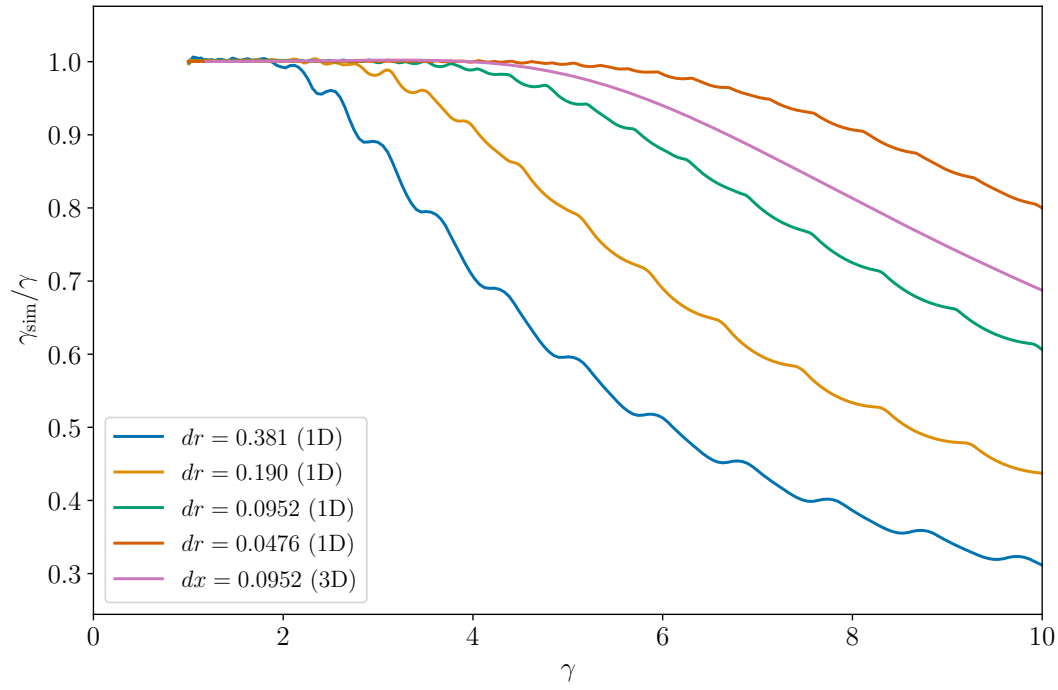

(a) $\overline{\lambda} = 0.84$

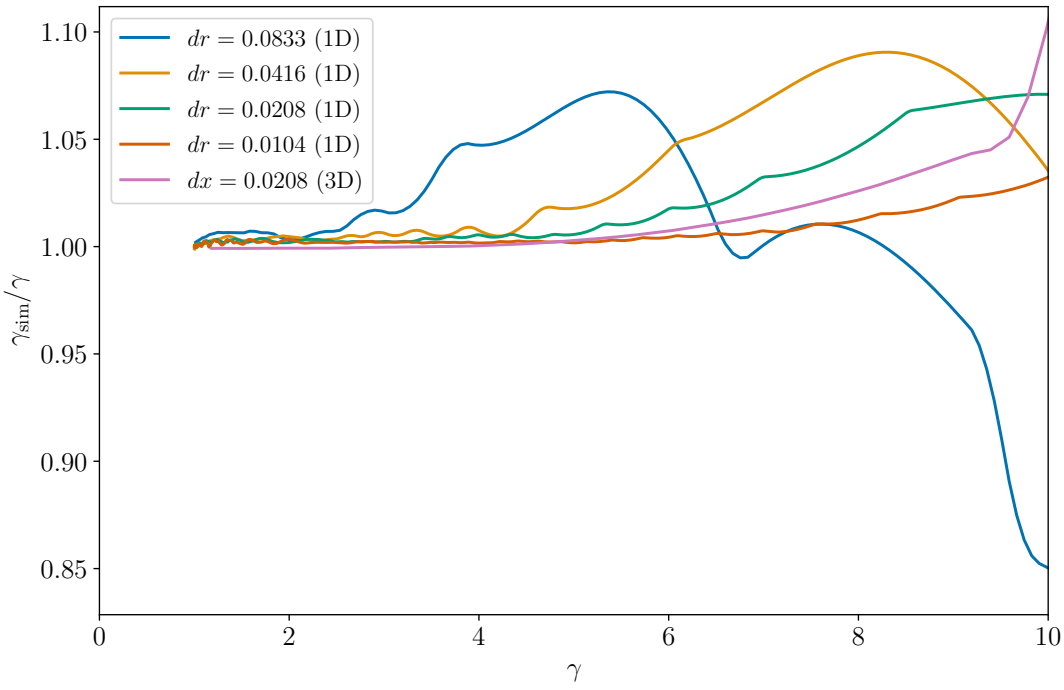

(b) $\overline{\lambda} = 0.07$

Figure 5.18: Deviation of the bubble wall Lorentz factor γ from its theoretical value in 1D simulations of isolated bubbles for a variety of lattice spacings. We also include the result of an isolated bubble left to expand in a 3D simulation.

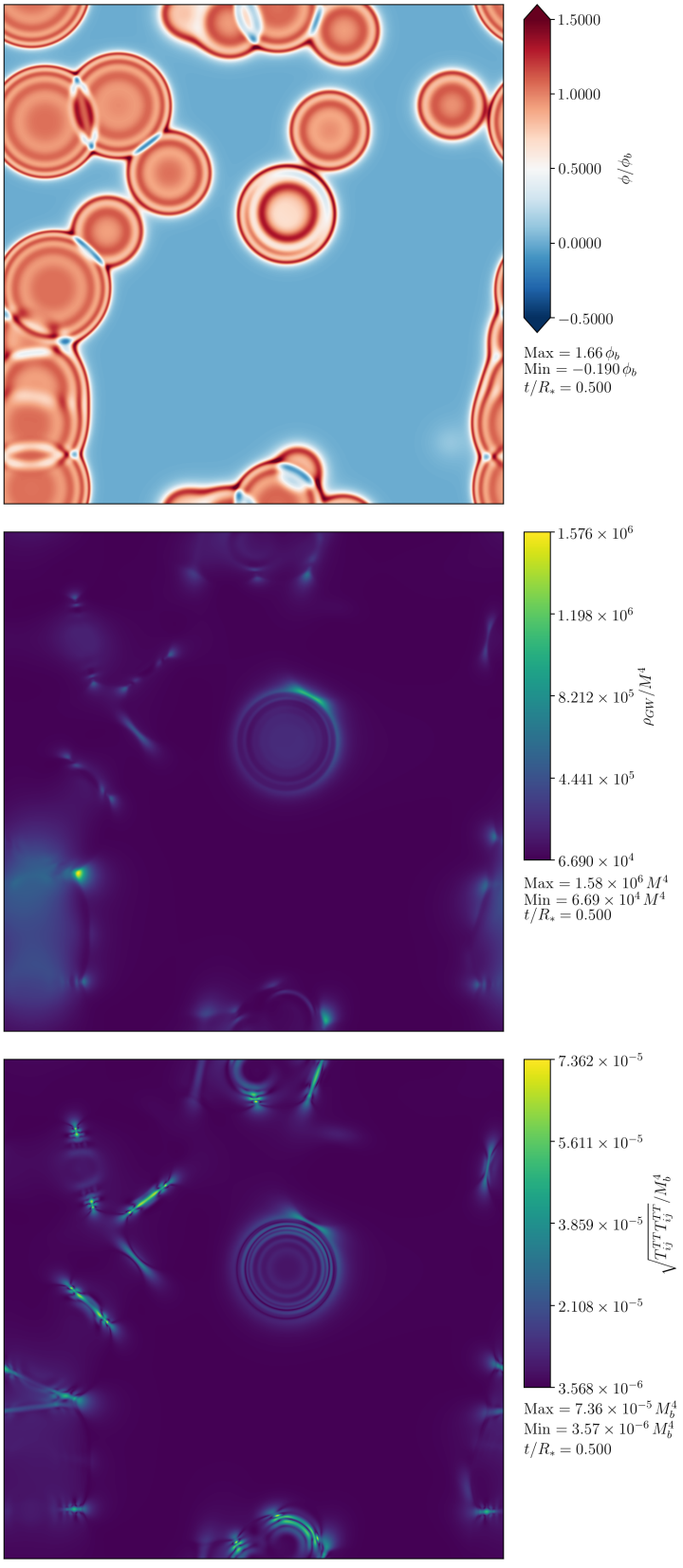
1.5000
1.0000
0.5000
0.0000
−0.5000
ϕ/ϕ_b
Max = 1.66 ϕ_b
Min = −0.190 ϕ_b
$t/R_* = 0.500$
1.576×10^6
1.198×10^6
8.212×10^5
4.441×10^5
6.690×10^4
ρ_{GW}/M^4
Max = $1.58 \times 10^6 M^4$
Min = $6.69 \times 10^4 M^4$
$t/R_* = 0.500$
7.362×10^{-5}
5.611×10^{-5}
3.859×10^{-5}
2.108×10^{-5}
3.568×10^{-6}
$\sqrt{T^{rr}T^{rr} + T^{ij}T^{ij}}/M_b^4$
Max = $7.36 \times 10^{-5} M_b^4$
Min = $3.57 \times 10^{-6} M_b^4$
$t/R_* = 0.500$

(a) $t/R_* = 0.5$

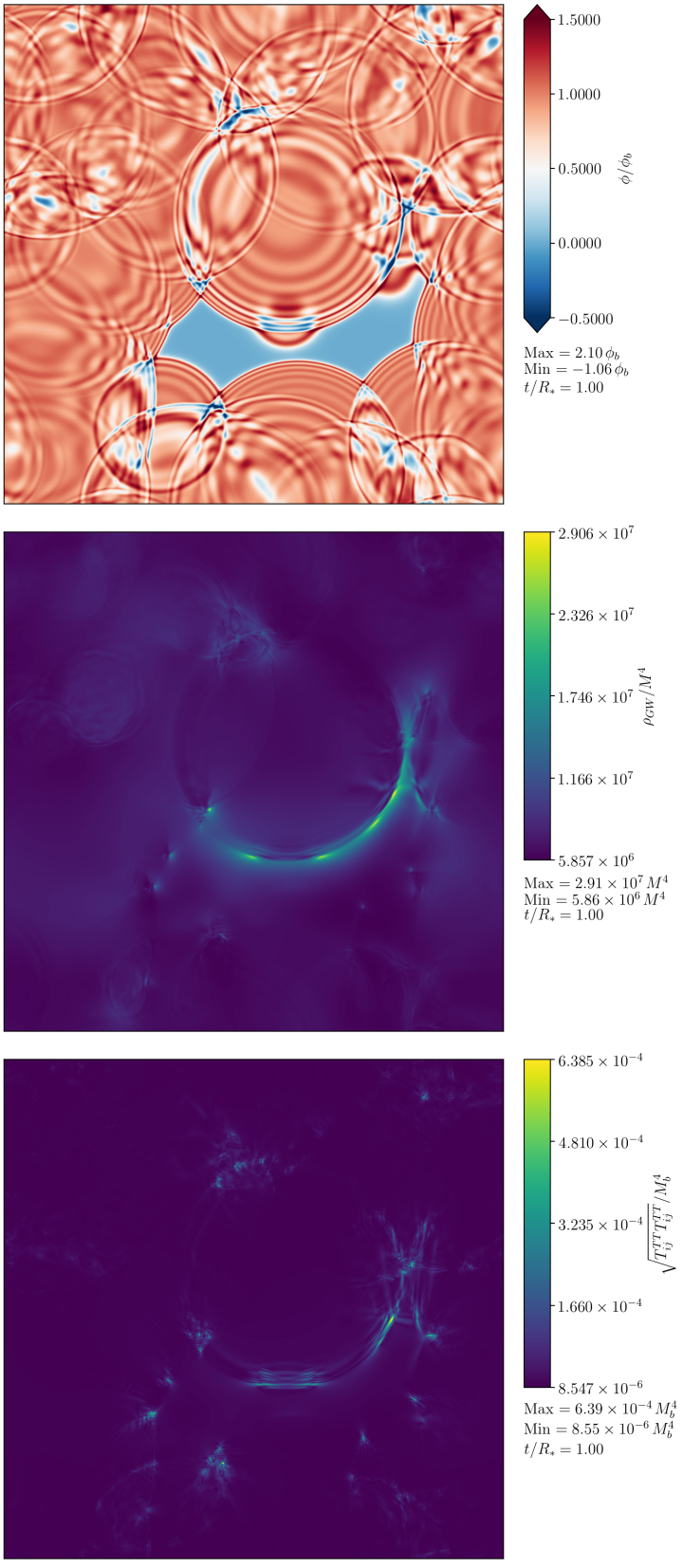
1.5000
1.0000
0.5000
0.0000
−0.5000
ϕ/ϕ_b
Max = 2.10 ϕ_b
Min = −1.06 ϕ_b
$t/R_* = 1.00$
2.906×10^7
2.326×10^7
1.746×10^7
1.166×10^7
5.857×10^6
ρ_{GW}/M^4
Max = $2.91 \times 10^7\, M^4$
Min = $5.86 \times 10^6\, M^4$
$t/R_* = 1.00$
6.385×10^{-4}
4.810×10^{-4}
3.235×10^{-4}
1.660×10^{-4}
8.547×10^{-6}
$\sqrt{T^{rT}T^{rT} + T^{rr}T^{rr}}/M_b^4$
Max = $6.39 \times 10^{-4}\, M_b^4$
Min = $8.55 \times 10^{-6}\, M_b^4$
$t/R_* = 1.00$

(b) $t/R_* = 1.0$

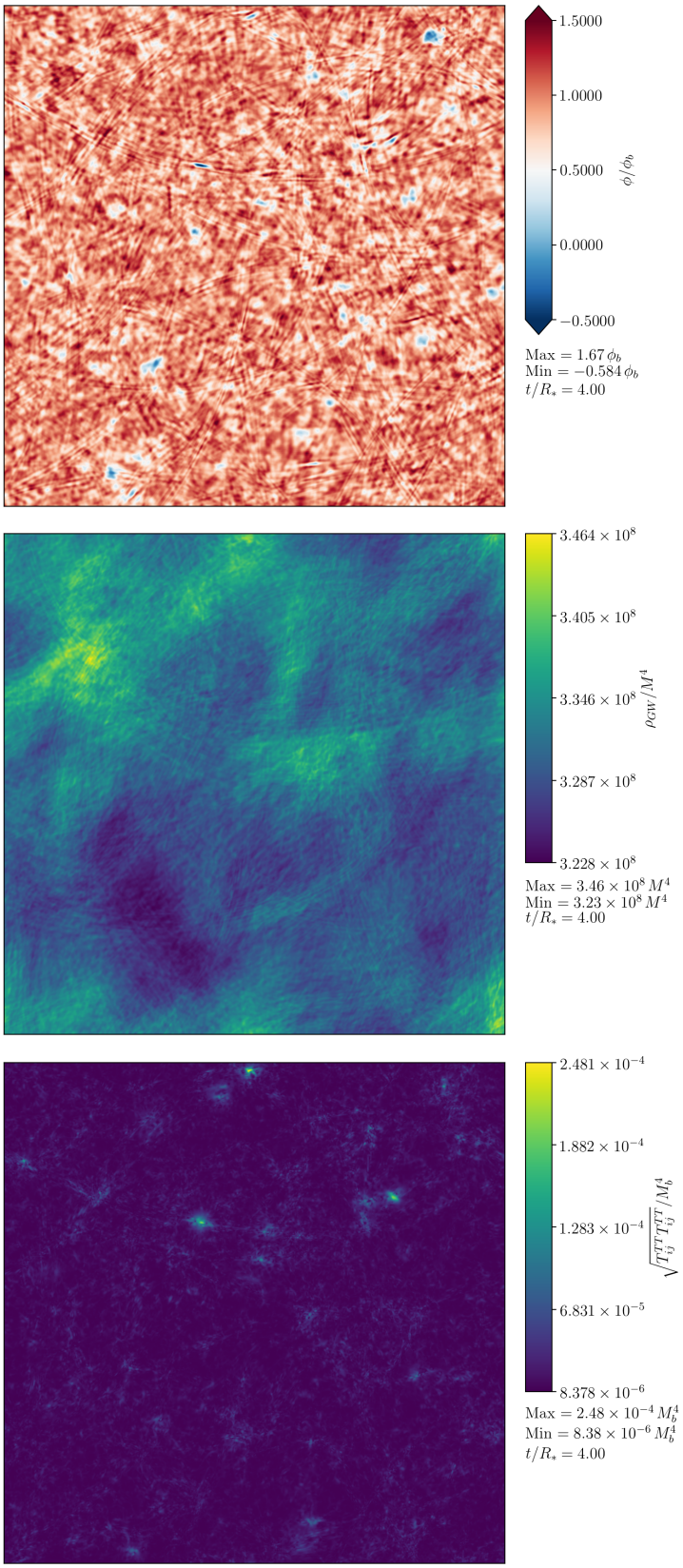

(c) $t/R_* = 4.0$

Figure 5.19: Slices $(0, y, z)$ for a simulation with $\overline{\lambda} = 0.07$ and $N_{\rm b} = 64$. In the top plot of each subfigure we show the scalar field normalised by the broken phase value. The middle plot shows the energy density in gravitational waves $\rho_{\rm gw}$. The bottom plot shows the modulus of the transverse traceless shear-stress.

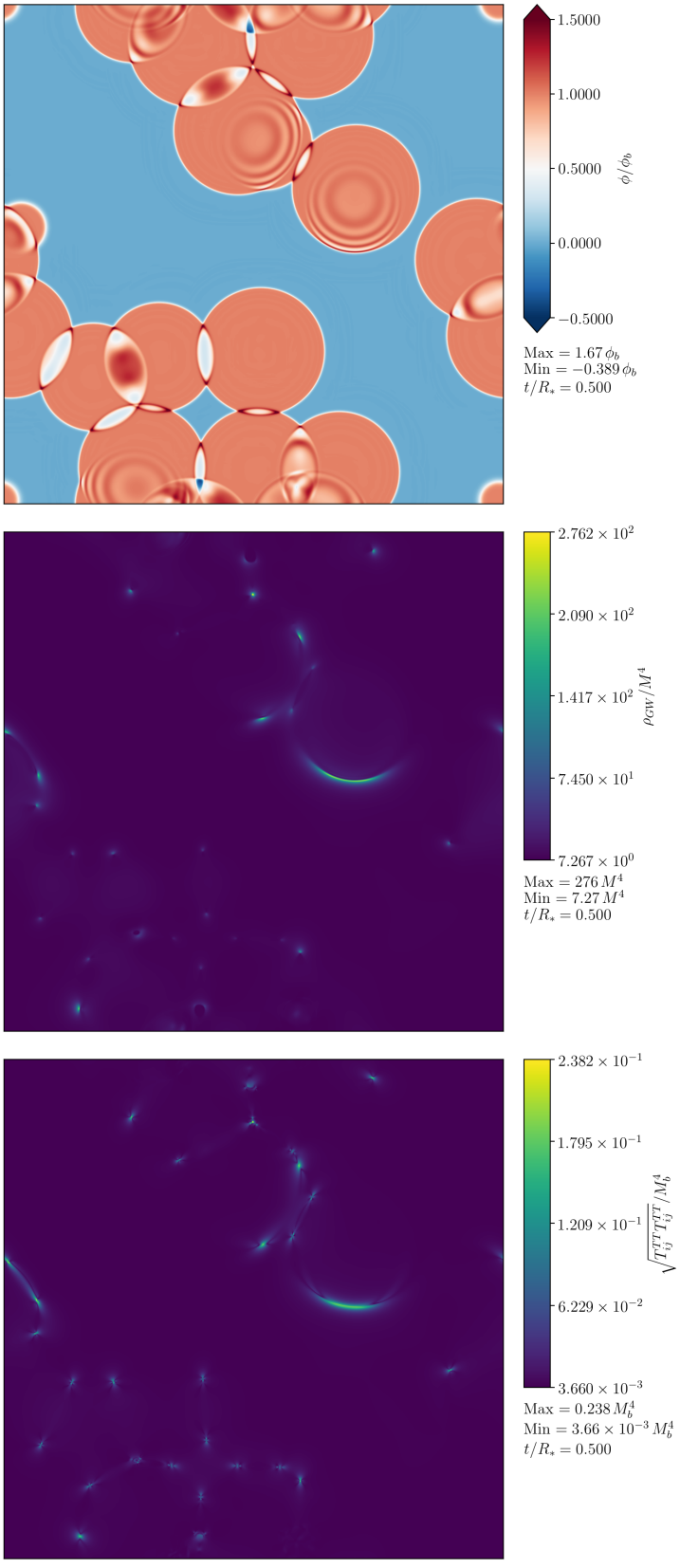
1.5000
1.0000
0.5000
0.0000
−0.5000
ϕ/ϕ_b
Max = 1.67 ϕ_b
Min = −0.389 ϕ_b
$t/R_* = 0.500$
2.762×10^2
2.090×10^2
1.417×10^2
7.450×10^1
7.267×10^0
ρ_{GW}/M^4
Max = 276 M^4
Min = 7.27 M^4
$t/R_* = 0.500$
2.382×10^{-1}
1.795×10^{-1}
1.209×10^{-1}
6.229×10^{-2}
3.660×10^{-3}
$\sqrt{T^{rr}T^{rr} + T^{r\theta}_{ij}T^{r\theta}_{ij}}/M_b^4$
Max = 0.238 M_b^4
Min = 3.66×10^{-3} M_b^4
$t/R_* = 0.500$

(a) $t/R_* = 0.5$

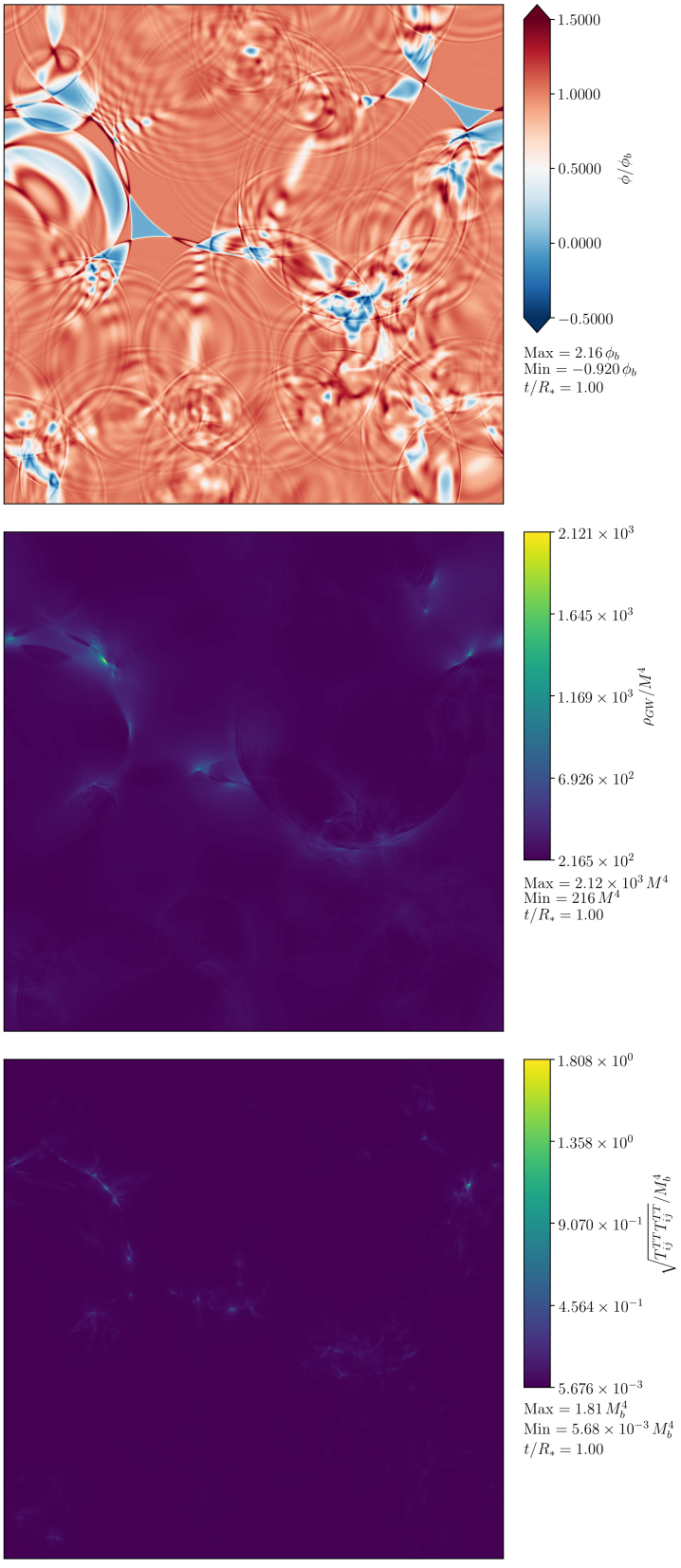
1.5000
1.0000
0.5000
0.0000
−0.5000
ϕ/ϕ_b
Max = 2.16 ϕ_b
Min = −0.920 ϕ_b
$t/R_* = 1.00$
2.121×10^3
1.645×10^3
1.169×10^3
6.926×10^2
2.165×10^2
ρ_{GW}/M^4
Max = $2.12 \times 10^3\, M^4$
Min = $216\, M^4$
$t/R_* = 1.00$
1.808×10^0
1.358×10^0
9.070×10^{-1}
4.564×10^{-1}
5.676×10^{-3}
$\sqrt{T^{rT}T^{rT} + T^{rT}T^{rT}}/M_b^4$
Max = $1.81\, M_b^4$
Min = $5.68 \times 10^{-3}\, M_b^4$
$t/R_* = 1.00$

(b) $t/R_* = 1.0$

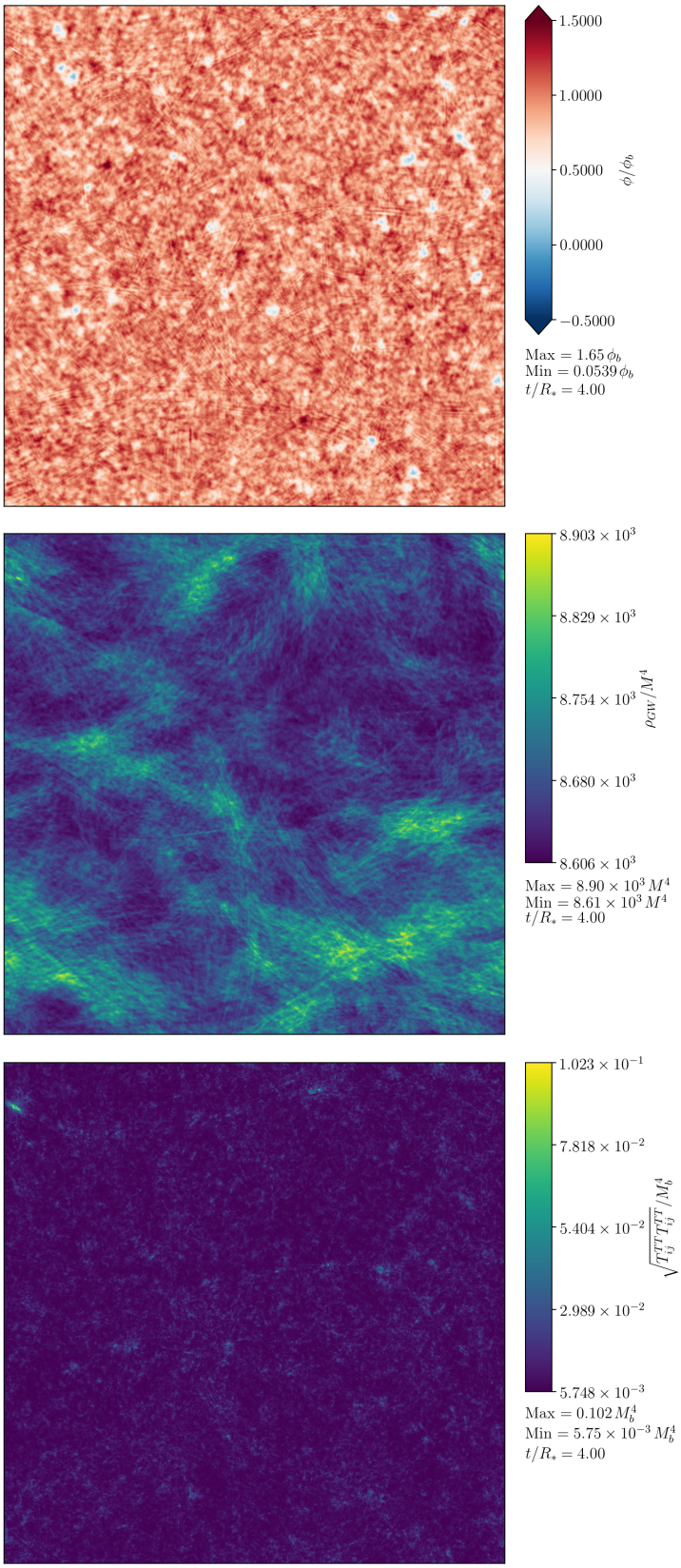

(c) $t/R_* = 4.0$

Figure 5.20: Slices $(0, y, z)$ for a simulation with $\overline{\lambda} = 0.84$ and $N_\mathrm{b} = 64$. In the top plot of each subfigure we show the scalar field normalised by the broken phase value. The middle plot shows the energy density in gravitational waves ρ_gw. The bottom plot shows the modulus of the transverse traceless shear-stress.

Chapter 6

Vorticity, kinetic energy, and suppressed gravitational wave production in strong first-order phase transitions

Daniel Cutting[a,b], Mark Hindmarsh[a,b] and David Weir[b,c]

[a] *Department of Physics and Astronomy, University of Sussex, Falmer, Brighton, BN1 9QH, U.K.*

[b] *Department of Physics and Helsinki Institute of Physics, PL 64, FI-00014, University of Helsinki, Finland*

[c] *School of Physics and Astronomy, University of Nottingham, Nottingham, NG7 2RD, U.K.*

Abstract

We have performed the first 3-dimensional simulations of strong first-order thermal phase transitions in the early Universe. For deflagrations, we find that the rotational component of the fluid velocity increases as the transition strength is increased. For detonations, however, the rotational velocity component remains constant and small. We also find that the efficiency with which kinetic energy is transferred to the fluid falls below theoretical expectations as we increase the transition strength. The probable origin of the kinetic energy deficit is the formation of reheated droplets of the metastable phase during the collision, slowing the bubble walls. The rate of increase in the gravitational wave energy density for deflagrations in strong transitions is suppressed compared to that predicted in earlier work. This is largely accounted for by the reduction in kinetic energy. Current modelling therefore substantially overestimates the gravitational wave signal for strong transitions with deflagrations, in the most extreme case by a factor of 10^3. Detonations are less affected.

6.1 Introduction

The Laser Interferometer Space Antenna (LISA), scheduled for launch in 2034, will open the mHz band of the emerging field of gravitational wave astronomy [137]. One of the most exciting goals of LISA is to probe the early universe by searching for gravitational wave signals from a first-order phase transition.

While the Standard Model is a cross-over [19, 20], there are many extensions with first-order phase transitions. These range from adding a scalar singlet [25–28, 33] or doublet [29–31], to models with spontaneously broken conformal symmetry [46–52]. There are also models with phase transitions in hidden sectors [37–43]. Non-perturbative methods are sometimes necessary to establish the order of the phase transition [158–160].

An important parameter of a first-order phase transition is the trace anomaly difference, which quantifies the energy available for conversion to shear stress, and hence the power of the gravitational wave signal. If the trace anomaly difference is comparable to the radiation energy density of the universe, we call the transition 'strong'. We denote the ratio of the trace anomaly to the thermal energy α, in which case a strong transition has $\alpha \sim 1$. We call $\alpha \gg 1$ 'very strong'; our results do not access this region.

Substantial progress has been made in understanding gravitational wave production from first-order transitions with weak ($\alpha \sim 10^{-2}$) to intermediate ($\alpha \sim 10^{-1}$) strength using numerical simulations [60–63], as well as modelling [64, 121, 122]. While the fluid motion is well-described as a linear superposition of sound waves after a weak transition [60], rotational modes and turbulence are expected in stronger transitions [53, 67], which could substantially affect the gravitational wave signal [58, 68–72].

At the same time, investigation of the underlying particle physics models indicates that intermediate to strong transitions are common in conservative extensions of the Standard Model [91, 98], and very strong transitions are possible in models of composite Higgs and nearly conformal potentials [46–52]. It is also clear that LISA will be most likely to observe transitions where nonlinear effects like shocks and turbulence become important [63]. Recent work tackling the non-linear regime includes gravitational wave production from magnetohydrodynamic turbulence [73] and studies of shock collisions using a mixture of 1-dimensional simulations and modelling [155].

In this paper, we present results from the first numerical simulations of strong first-order phase transitions. We measure the fraction of the fluid kinetic energy in rotational modes, as traced by the mean-square velocity. As we increase the strength of the transition, this proportion grows substantially for deflagrations, with up to 65% of the mean square

velocity found in rotational motion. The rotational proportion is far less for detonations, remaining roughly constant for all transition strengths.

As the transition strength α is increased, the efficiency of fluid kinetic energy production decreases below expectation. For deflagrations, this is associated with reduced wall speeds for expanding bubbles and reheating of the region in front of the walls, reducing the pressure difference [67, 161, 162]. The kinetic energy loss leads to a suppression in the gravitational wave power, by a factor which can be as small as $\mathrm{O}(10^{-3})$. This means that current models substantially overestimate gravitational wave production from strong transitions with deflagrations. Detonations are less affected.

6.2 Methods

We model the phase transition with a real scalar field ϕ, coupled to a perfect fluid. We assume that there is no extra physics generating a magnetic field either before or during the phase transition. The model follows that used in previous work [62, 63, 101], differing by a change in the effective potential and therefore the equation of state. Our previous work used the high-temperature expansion of the one-loop thermal effective potential, and we found that in stronger transitions, the total energy could drop below the scalar potential energy, which is unphysical. In this scenario, our algorithm would compute the temperature to be imaginary, causing a crash. Indeed, the high-temperature expansion is known to fail well below T_c; for example, the speed of sound diverges and then becomes imaginary. To fix this we have introduced a simpler bag model equation of state, described below. The new equation of state changes only how the relevant thermodynamic parameters α and v_w are realised in terms of the parameters of the potential and field-fluid coupling term. The flows around the expanding bubbles, and hence the gravitational wave spectrum, depend on the underlying theory only through α and the wall speed v_w, with the overall frequency scale set by the redshifted mean bubble separation.

Our coupled field-fluid system has energy-momentum tensor

$$T^{\mu\nu} = \partial^\mu\phi\partial^\nu\phi - \frac{1}{2}g^{\mu\nu}(\partial\phi)^2 + (\epsilon + p)U^\mu U^\nu + g^{\mu\nu}p \tag{6.1}$$

where $U = \gamma(1, \mathbf{v})$, with fluid 3-velocity $\mathbf{v}$ and associated Lorentz factor γ. The internal energy ϵ and pressure p are

$$\epsilon = 3a(\phi)T^4 + V_0(\phi), \qquad p = a(\phi)T^4 - V_0(\phi), \tag{6.2}$$

and the enthalpy is $w = \epsilon + p$.

The zero-temperature effective potential is

$$V_0(\phi) = \frac{1}{2}M^2\phi^2 - \frac{1}{3}\mu\phi^3 + \frac{1}{4}\lambda\phi^4 - V_c, \tag{6.3}$$

where V_c is chosen such that $V_0(\phi_b) = 0$, and ϕ_b is the value of ϕ in the broken phase at $T = 0$. We denote the potential energy difference between the vacua by $\Delta V_0 = V_0(0) - V_0(\phi_b)$.

We write the thermal effective potential of our bag model as

$$V(\phi, T) = V_0(\phi) - T^4 \left(a(\phi) - a_0\right), \tag{6.4}$$

where $a(\phi)$ models the change in degrees of freedom during the transition. We take

$$a(\phi) = a_0 - \frac{\Delta V_0}{T_c^4}\left[3\left(\frac{\phi}{\phi_b}\right)^2 - 2\left(\frac{\phi}{\phi_b}\right)^3\right], \tag{6.5}$$

where $a_0 = (\pi^2/90)g_*$ with g_* the effective number of relativistic degrees of freedom in the symmetric phase. Both $\phi = 0$ and $\phi = \phi_b$ are stationary points of the function for all T. For our choice of $a(\phi)$ the minima of V become degenerate at $T = T_c$, as required.

The energy-momentum tensor can be decomposed into field and fluid parts, coupled through a friction term,

$$\partial_\mu T^{\mu\nu}_\phi = -\partial_\mu T^{\mu\nu}_f = \eta U^\mu \partial_\mu \phi \partial^\nu \phi. \tag{6.6}$$

Ref. [63] used a field- and temperature-dependent friction parameter $\eta = \tilde{\eta}\phi^2/T$[1]. Although this models high temperature physics more accurately [163], strong transitions can reach small temperatures and again the high-temperature approximation fails. With small temperatures we also find numerical instabilities and so revert to using a constant η.

The phase transition strength is parametrised by the trace anomaly difference

$$\Delta\theta(T) = \frac{1}{4}\frac{d}{dT}\Delta V - \Delta V, \tag{6.7}$$

where $\Delta V = V(0, T) - V(\phi_b, T)$. The strength parameter is then

$$\alpha = \Delta\theta(T_n)/\epsilon_r(T_n). \tag{6.8}$$

where T_n is the nucleation temperature and $\epsilon_r = 3w/4$ the radiation energy density.

[1]It has been pointed out to the authors that instead of taking η to be proportional to ϕ^2 with ϕ the background field value, the fluctuation-dissipation theorem suggests that instead the friction coupling should be proportional to the variance of the field away from an equilibrium value. This would be interesting to investigate, but is beyond the scope of this work and will therefore be left to a future study.

We assume that the duration of the phase transition is much less than the Hubble time $H_{\rm n}^{-1}$, and neglect the effect of expansion. This is comparable to the statement that $H_{\rm n}R_* \ll 1$, where R_* is the mean bubble separation. In this regime the contribution of bubble collisions to the gravitational wave signal is negligible. To neglect expansion the final simulation time $t_{\rm fin}$ must also be much smaller than $H_{\rm n}^{-1}$. For all our simulations $t_{\rm fin} \leq 10\, R_*$.

The mean gravitational wave energy density is

$$\rho_{\rm gw} = \frac{1}{32\pi G}\frac{1}{\mathcal{V}}\int_{\mathcal{V}} {\rm d}^3x\, \overline{\dot{h}_{ij}^{\rm TT}\dot{h}_{ij}^{\rm TT}}, \tag{6.9}$$

where $\mathcal{V}$ is the simulation volume, $h_{ij}^{\rm TT}$ is the transverse traceless metric perturbation and the line indicates averaging over a characteristic period of the gravitational waves. We find $h_{ij}^{\rm TT}$ in Fourier space by a standard technique [60, 62, 147], sourced only by the fluid, the dominant contribution when $\alpha \lesssim 1$ and $H_{\rm n}R_* \ll 1$ [60, 62, 63].

We express the gravitational wave energy density in terms of the parameter $\Omega_{\rm gw} = \rho_{\rm gw}/\rho_{\rm c}$, with $\rho_{\rm c}$ the critical energy density. Our assumptions on α and $H_{\rm n}R_*$ ensure that $\Omega_{\rm gw} \ll 1$ at all times. They also ensure that the gravitational backreaction is negligible compared to the pressure forces, as the wavelength of the density perturbations $\sim R_*$ is much less than the Jeans length $\sim c_{\rm s}/H_{\rm n}\sqrt{\delta}$, where δ is the energy density contrast averaged over the wavelength being considered[2]. We leave a deeper analysis of gravitational backreaction in the case $H_{\rm n}R_* \sim c_{\rm s}/\sqrt{\delta}$ to a later study.

6.3 Simulations

We perform a series of three-dimensional simulations of the field-fluid system. The simulation code is the same as used in Ref. [63] except for the above changes.

We scan over α for three subsonic deflagrations with asymptotic wall speeds $v_{\rm w} = \{0.24, 0.44, 0.56\}$, and two detonations with $v_{\rm w} = \{0.82, 0.92\}$. The asymptotic wall speeds, and their fluid profiles, are found with a spherically symmetric version of the code [62, 63, 111, 113], run with the same parameters until $t = 10000T_{\rm c}^{-1}$. As we increase α, the maximum velocity of the asymptotic fluid profile $v_{\rm p}$ increases. For each $v_{\rm w}$, there is a maximum $v_{\rm p}$, and hence a maximum strength $\alpha_{\rm max}$, above which solutions either do not exist (subsonic deflagrations), or change into hybrids. We do not consider hybrids here.

[2]For the parameter space we consider, we determined that the variation of the energy density is at most a factor of twenty in the asymptotic fluid profile that develops around an expanding bubble; δ will be less than this due to averaging over a given wavelength.

The values of η needed for these wall speeds are given in the supplemental material. By comparison, the Standard Model estimate is $\eta \simeq 3\,\phi_{\rm b}^2/T_{\rm c}$ [107, 108, 163].

All simulations have the number of bubbles $N_{\rm b} = 8$, lattice spacing $\delta x = 1.0\,T_{\rm c}^{-1}$, timestep $\delta t = 0.2\,T_{\rm c}^{-1}$, and $L^3 = 960^3$ lattice sites, giving a mean bubble separation $R_* = L\,\delta x/N_{\rm b}^{1/3} = 480\,T_{\rm c}^{-1}$. All bubbles are nucleated simultaneously with a gaussian profile at the same locations at the start of each simulation. The initial profile of the bubbles is insignificant as they approach the same asymptotic profile.

We fix $g_* = 106.75$, $M^2 = 0.0427\,T_{\rm c}^2$, $\mu = 0.168\,T_{\rm c}$ and $\lambda = 0.0732$, in turn fixing $\phi_{\rm b} = 2.0\,T_{\rm c}$. This sets the relative change in degrees of freedom to $[a(\phi_{\rm b}) - a_0]/a_0 = 5.9 \times 10^{-3}$. To change the transition strength we vary $T_{\rm n}$.

We output slices of the temperature T, fluid speed v and vorticity magnitude $|\nabla \times \mathbf{v}|$. Movies created from these slices are available at [164]. Selected stills are included in the supplemental material.

We measure the RMS fluid 3-velocity $\overline{v}$, and its irrotational and rotational parts $\overline{v}_{\parallel}$ and $\overline{v}_{\perp}$. We also track the enthalpy-weighted RMS four-velocity $\overline{U}_{\rm f}$ defined as

$$\overline{U}_{\rm f}^2 = \frac{1}{\overline{w}\mathcal{V}} \int_{\mathcal{V}} {\rm d}^3x\, w\gamma^2 v^2, \tag{6.10}$$

where $\overline{w}$ the mean enthalpy density. This gives an indication of the magnitude of the shear stress, the source of gravitational waves.

A similar quantity $\overline{U}_{\phi}$ can be constructed to track the progress of the phase transition

$$\overline{U}_{\phi}^2 = \frac{1}{\overline{w}\mathcal{V}} \int_{\mathcal{V}} {\rm d}^3x\, \partial_i\phi\partial_i\phi, \tag{6.11}$$

proportional to the total area of the phase boundary. We call the time when $\overline{U}_{\phi}$ reaches its maximum the peak collision time, $t_{\rm pc}$. Note that $t_{\rm pc} \propto R_*/v_{\rm w}$. To see how these global quantities evolve during a detonation and a deflagration see Fig. 6.10 in the supplemental material.

To check the dependence of our key observables on lattice spacing, we perform simulations with the same physical volume and various lattice spacings $\delta x\,T_{\rm c} = \{2.0, 1.5, 1.0, 0.75, 0.5\}$ for $v_{\rm w} = 0.24$ and $v_{\rm w} = 0.92$ and $\alpha = 0.5$. We find that $\overline{v}_{\perp,\rm max}^2$, $\overline{U}_{\rm f,max}$, and $\Omega_{\rm gw}$ converge with lattice spacing. We perform a quadratic fit with δx for each quantity, finding that $\overline{U}_{\rm f,max}$ and $\Omega_{\rm gw}$ differ from the continuum limit by O(1%). The quantity that is most sensitive to the grid is $\overline{v}_{\perp,\rm max}^2$ which we underestimate from the continuum limit by $\simeq 25\%$. We also test convergence of key observables with timestep, finding in all cases that convergence is better for δt than for δx. It is important to check how close the colliding bubbles are to their asymptotic profile. We find that spherically

symmetric bubbles with diameter R_c have at worst $\overline{U}_f$ within 20% of the asymptotic $\overline{U}_f$. In the supplemental material we show our convergence test results and the deviation from asymptotic $\overline{U}_f$ for all v_w and α considered here.

6.4 Results

From our simulations we see that a rotational component of velocity is generated during the bubble collision phase. In order to gauge the relative amount of kinetic energy in the rotational component of velocity, we consider the ratio of the maxima of mean square 3-velocities $\overline{v}^2_{\perp,\max}/\overline{v}^2_{\max}$. We plot this in Fig. 6.1. As we increase α for the deflagrations, we see that the proportion of the velocity found in rotational modes increases dramatically, whereas for detonations it stays constant. The deflagrations with smaller wall velocities have a larger proportion of the velocity in rotational modes. For $v_w = 0.24$, $\alpha = 0.34$ the ratio $\overline{v}^2_{\perp,\max}/\overline{v}^2_{\max} = 0.65$, and if we naively extrapolate the trend in the last few points up to $\alpha_{\max}$ this increases to 0.95.

Fig. 6.11 of the supplemental material shows that the vorticity is generated inside the bubbles, not outside where the fluid shells first interact.

To better understand transfer of energy from the scalar field to the fluid, we plot how $\overline{U}_\phi$ and $\overline{U}_f$ change as we increase α for detonations with $v_w = 0.92$ and deflagrations with $v_w = 0.44$ (Fig. 6.2). When $\overline{U}_\phi$ reaches its maximum, the volumes in each phase are approximately equal. As the phase boundary sweeps out the remaining regions of metastable phase, $\overline{U}_\phi$ relaxes to zero. It is striking that for deflagrations the relaxation takes longer as we increase α, whereas for detonations the shape of $\overline{U}_\phi$ remains unchanged. The phase boundaries in a deflagration must therefore move more slowly in the later stages, as the transition strength increases.

The reason for the slowing is that the metastable phase is reheated by the fluid shells in front of the bubble walls [67, 161, 162]. Towards the end of the transition the remaining metastable phase forms into hot droplets (see Fig. 6.11 in the supplemental material). The higher pressure inside the droplets opposes their collapse.

For detonations, where the fluid shell develops behind the bubble wall, shrinking regions of the metastable phase are not reheated (see Fig. 6.12 in the supplemental material).

Fig. 6.2 also shows that $\overline{U}_f$ increases with α, as one expects from the increasing scalar potential energy. However, the maximum is below that expected from a single bubble, which is a good estimate of $\overline{U}_f$ at low α [62, 63].

To obtain the single-bubble estimate, simulations of expanding spherical bubbles are

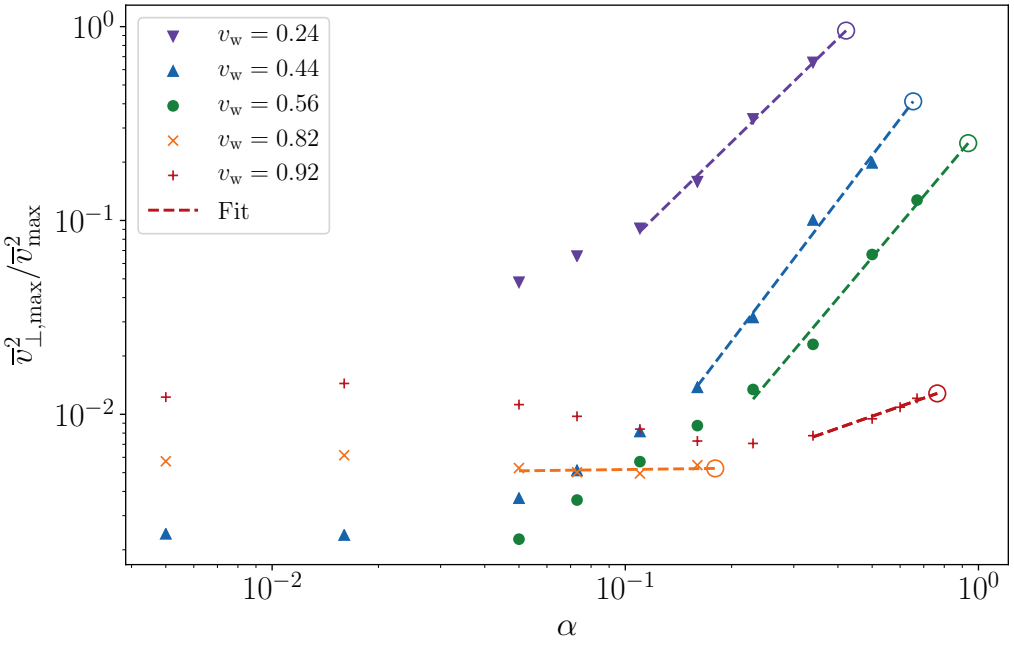

Figure 6.1: Proportion of mean square fluid velocity in the rotational modes. We plot the ratio of $\overline{v}_{\perp,\max}$ to $\overline{v}_{\max}$ against α. Dashed lines give a linear fit for the last four simulation points. The fits are extrapolated to $\alpha_{\max}$ for deflagrations, or to the largest α for which a wall speed corresponds to a detonation (hollow circles).

performed, and the expected enthalpy-weighted RMS velocity $\overline{U}_{\mathrm{f,exp}}$ is that of the fluid shell when the wall reaches a diameter of R_*. We then take the ratio with the maximum of $\overline{U}_{\mathrm{f}}$ in each simulation, shown in Fig. 6.3. Note that due to finite volume effects $\overline{U}_{\mathrm{f}}$ oscillates in our simulations, giving an O(10%) uncertainty to this estimate.

For all wall speeds, the ratio of $\overline{U}_{\mathrm{f,max}}$ to $\overline{U}_{\mathrm{f,exp}}$ decreases as we increase the transition strength. However, for deflagrations the decrease in the kinetic efficiency is more dramatic, and more rapid for slower walls: in the slowest deflagration ($v_{\mathrm{w}} = 0.24$), $\overline{U}_{\mathrm{f,max}}/\overline{U}_{\mathrm{f,exp}}$ reaches 0.3. The decrease is approximately linear; a naive linear extrapolation to the maximum possible strength is indicated by open circles. The loss of kinetic energy is probably a result of the slowing discussed above, limiting the transfer of energy.

The deficit in kinetic energy can be expected to reduce the gravitational wave signal. In current modelling [63, 77], the expected gravitational wave density parameter from a flow with $\overline{U}_{\mathrm{f,exp}}$ at time $t \ll H_{\mathrm{n}}^{-1}$ is

$$\Omega_{\mathrm{gw,exp}} = 3\,\tilde{\Omega}_{\mathrm{gw}} \left(\frac{\overline{w}}{\overline{\epsilon}}\right)^2 \overline{U}^4_{\mathrm{f,exp}} (H_{\mathrm{n}} t)(H_{\mathrm{n}} R_*), \tag{6.12}$$

where $\tilde{\Omega}_{\mathrm{gw}}$ has been shown to be a constant of $\mathrm{O}(10^{-2})$ in weak and intermediate trans-

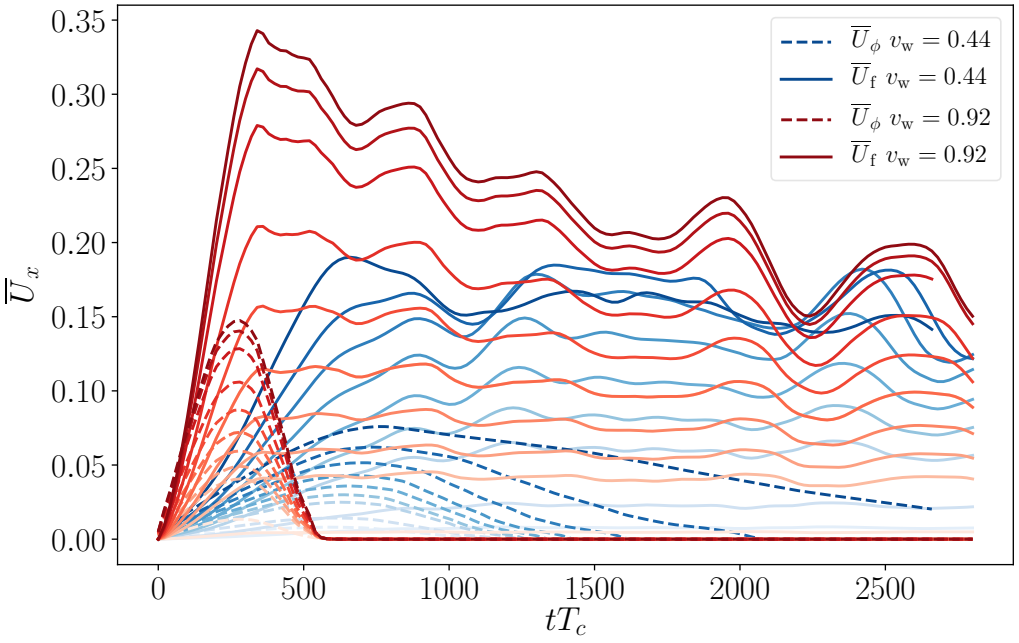

Figure 6.2: The evolution of $\overline{U}_\phi$ (dashed lines) and $\overline{U}_f$ (solid lines) for simulations with increasing α (darker shades). In blue we show deflagrations with $v_w = 0.44$ whereas red lines show detonations with $v_w = 0.92$.

itions. Here, we take $\tilde{\Omega}_{gw} = 10^{-2}$. In Fig. 6.4 we plot the ratio of Ω_{gw}/t to $\Omega_{gw,exp}/t$, where Ω_{gw}/t is averaged over the final $\Delta t = 2R_*$ of the simulation. In the most extreme case, $v_w = 0.24$ and $\alpha = 0.34$, the ratio is 2×10^{-3}. This is even less than the kinetic energy suppression suggests, a factor of $(\overline{U}_{f,max}/\overline{U}_{f,exp})^4 \simeq 8 \times 10^{-3}$.

A table of simulation parameters and measured quantities can be found in the supplemental material.

6.5 Conclusions

We have performed the first 3-dimensional simulations of strong first-order phase transitions, with the strength parameter α up to an order of magnitude larger than those previously studied [63].

A rotational component of velocity $\overline{v}_\perp$ is generated during the collision phase. For deflagrations, the ratio $\overline{v}^2_{\perp,max}/\overline{v}^2_{max}$ grows rapidly with α, reaching 0.65 for $v_w = 0.24$. For detonations, the ratio is $O(10^{-2})$—showing no consistent trend with α.

For stronger phase transitions a smaller proportion of the scalar potential energy is transferred into fluid kinetic energy than is expected from the behaviour of isolated

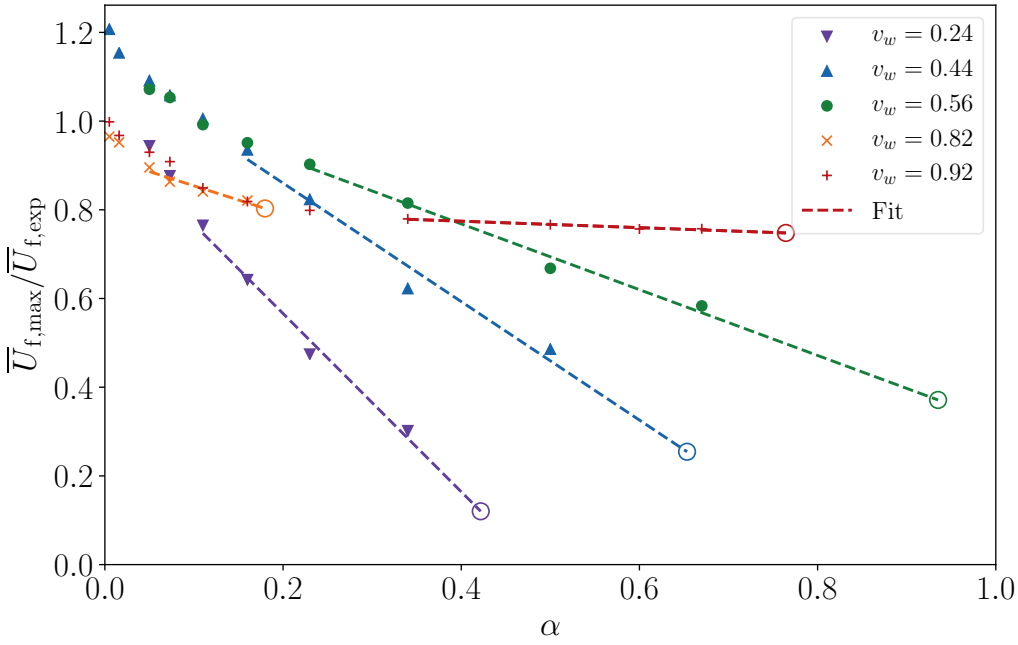

Figure 6.3: Comparison between the maximum value of $\overline{U}_{\mathrm{f}}$ in each simulation and that predicted by [88] for the given v_{w} and α. Dashed lines give a linear fit for the last four simulation points. Hollow circles show the extrapolation to α_{max} for deflagrations, or up to to the largest α for which the wall speed corresponds to a detonation.

bubbles. For deflagrations, we suppose that the deficit is due to reheating of the metastable phase slowing the bubble walls during the collision phase. The deficit can be substantial, with $\overline{U}_{\mathrm{f,max}}/\overline{U}_{\mathrm{f,exp}}$ falling to ~ 0.3 for $v_{\mathrm{w}} = 0.24$ in our simulations, and could fall as low as 0.1 using a naive linear extrapolation to the maximum possible strength at that wall speed.

The gravitational wave intensity is lower than expected, by a factor of order 10^{-3} for the strongest deflagration with the lowest wall speed. This can mostly be accounted for by the kinetic energy deficit. Detonations do not suffer such a dramatic suppression, with the smallest suppression factor about 0.2 for $v_{\mathrm{w}} = 0.92$.

Our results have important consequences for gravitational waves from phase transitions. They indicate that the current model [63, 77] overestimates the gravitational wave power spectrum for strong transitions, by a factor of a few for detonations, and by an order of magnitude or more for deflagrations. We estimate[3] that to obtain a signal to

[3]We use PTPlot `v1.01`, `http://www.ptplot.org/ptplot/`[90], to compute and plot signal to noise ratio (SNR) curves from first-order phase transitions for LISA. We choose $g_* = 106.75$ and an optimistic $T_{\mathrm{n}} = 100\,\mathrm{GeV}$. The resulting plot shows that an SNR of 10 requires $\overline{U}_{\mathrm{f}}$ of at least 0.07 for all $H_{\mathrm{n}}R_*$.

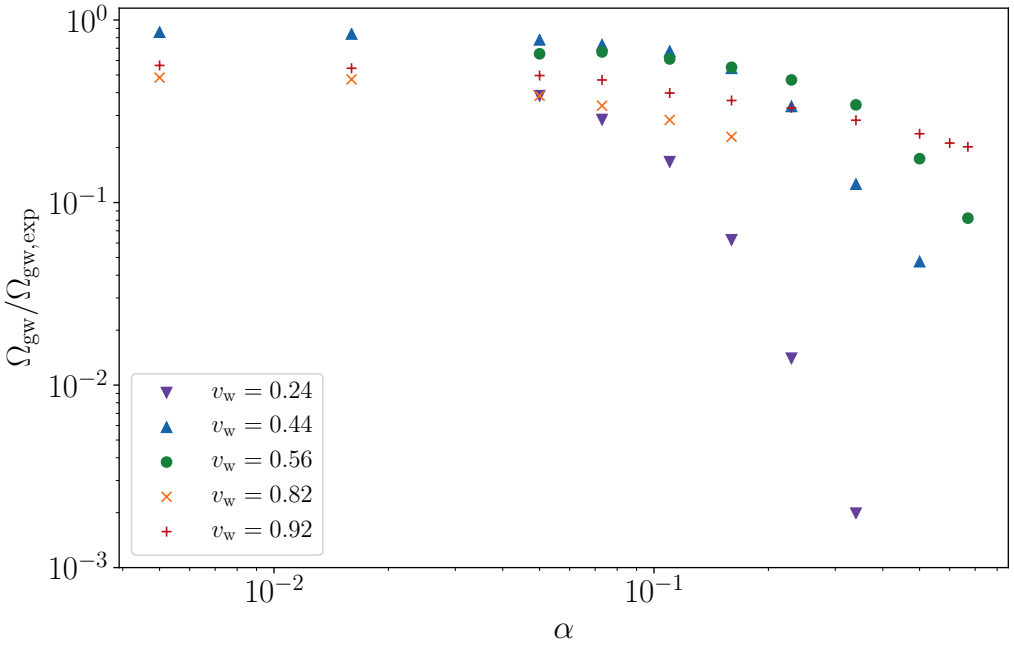

Figure 6.4: Comparison of the gravitational waves produced in our simulations against that predicted by Eq. (6.12) using $\overline{U}_{\rm f,exp}$ found from $v_{\rm w}$ and α.

noise ratio of 10 $\overline{U}_{\rm f}$ must be at least 0.07. Therefore the kinetic energy suppression we observe will probably render transitions with $v_{\rm w} = 0.24$ unobservable except for within a very small region of parameter space. Faster walls suffer less suppression, though the observable parameter space is still reduced.

We plan larger simulations to characterise more precisely the suppression, and its effect on observability.

Acknowledgements

The authors would like to thank Chiara Caprini, Kari Rummukainen, and Danièle Steer for helpful discussions. Our simulations made use of the resources of the Finnish Centre for Scientific Computing CSC. DC (ORCID ID 0000-0002-7395-7802) is supported by an STFC Studentship. MH (ORCID ID 0000-0002-9307-437X) acknowledges support from the Science and Technology Facilities Council, grant no. ST/P000819/1. DJW (ORCID ID 0000-0001-6986-0517) is supported by an Science and Technology Facilities Council Ernest Rutherford Fellowship, grant no. ST/R003904/1, by the Research Funds of the University of Helsinki, and by the Academy of Finland, grant no. 286769.

6.6 Supplemental Material

6.6.1 Field and fluid equations of motion

In order to obtain the equations of motion for our field and fluid system we focus on the coupling between the field and fluid parts of our energy momentum tensor. The current of the energy-momentum tensor can be split into field and fluid parts and coupled through a dissipative friction term,

$$[\partial_\mu T^{\mu\nu}]_{\text{field}} = (\partial_\mu \partial^\mu \phi)\partial^\nu \phi - \frac{\partial V}{\partial \phi}\partial^\nu \phi = \delta^\nu, \tag{6.13}$$

$$[\partial_\mu T^{\mu\nu}]_{\text{fluid}} = \partial_\mu[(\epsilon + p)U^\mu U^\nu] + \partial^\nu p + \frac{\partial V}{\partial \phi}\partial^\nu \phi = -\delta^\nu. \tag{6.14}$$

We can then write this coupling term as

$$\delta^\nu = \eta U^\mu \partial_\mu \phi \partial^\nu \phi. \tag{6.15}$$

From these two equations we can extract the equation of motion for our system. By taking Eq (6.13) and dividing through by $\delta^\nu \phi$ we obtain

$$-\ddot{\phi} + \nabla^2 \phi - \frac{\partial V}{\partial \phi} = \eta\gamma(\dot{\phi} + v^i \partial_i \phi). \tag{6.16}$$

We find the equation of motion for the fluid energy density $E = \gamma\epsilon$ by contracting Eq (6.14) with U_ν giving

$$\begin{aligned} \dot{E} + \partial_i(E v^i) + p[\dot{\gamma} + \partial(\gamma v^i)] - \frac{\partial V}{\partial \phi}\gamma(\dot{\phi} + v^i \partial_i \phi) \\ = \eta\gamma^2(\dot{\phi} + v^i \partial_i \phi)^2. \end{aligned} \tag{6.17}$$

Finally we obtain an expression for the fluid momentum density $Z_i = \gamma(\epsilon + p)U_i$ by considering the spatial components of Eq (6.14),

$$\dot{Z} + \partial_j(Z_i v^j) + \partial_i p + \frac{\partial V}{\partial \phi}\partial_i \phi = -\eta\gamma(\dot{\phi} + v^j \partial_j \phi)\partial_i \phi. \tag{6.18}$$

6.6.2 Gravitational waves

To obtain the gravitational wave energy density we must first calculate the transverse traceless perturbations in the metric, h_{ij}^{TT}. We operate in linearised gravity and therefore

the equation of motion for h_{ij}^{TT} is

$$\Box h_{ij}^{TT} = -16\pi G T_{ij}^{TT}, \tag{6.19}$$

where T_{ij}^{TT} is the transverse traceless projection of the energy-momentum tensor.

Due to the numerical cost of computing the transverse traceless components of the energy-momentum tensor, it is useful to instead track an auxiliary tensor u_{ij} [147] which evolves according to

$$\Box u_{ij} = -16\pi G T_{ij}. \tag{6.20}$$

Then to obtain h_{ij}^{TT} from u_{ij} we apply the transverse traceless projector in wave space,

$$\tilde{h}_{ij}^{TT}(\mathbf{k}, t) = \Lambda_{ij,lm}(\mathbf{k})\tilde{u}_{lm}(\mathbf{k}, t), \tag{6.21}$$

where

$$\Lambda_{ij,lm}(\mathbf{k} = P_{im}(\mathbf{k})P_{jl}(\mathbf{k}) - \frac{1}{2}P_{ij}(\mathbf{k})P_{lm}(\mathbf{k}), \tag{6.22}$$

and

$$P_{ij}(\mathbf{k}) = \delta_{ij} - \hat{k}_i\hat{k}_j. \tag{6.23}$$

This method then allows us to only need to perform the necessary Fourier transforms and projections to calculate the gravitational wave energy density at regular intervals rather than every timestep.

6.6.3 Resolution convergence

To ensure the validity of our simulations we performed a series of lattice resolution checks. To do this we repeated two simulations with $v_\mathrm{w} = 0.44$ and $v_\mathrm{w} = 0.92$ and $\alpha = 0.5$ for a variety of different lattice spacings and timesteps while keeping the total physical volume and duration of the simulations fixed. We plot the convergence of several key quantities with δx in Fig. 6.5 through Fig. 6.7. We also plot a quadratic fit for the convergence of each quantity with δx. We can see that all quantities converge. The worst convergence is for $\overline{v}^2_{\perp,\mathrm{max}}$ which for $\delta x = 1.0\,T_\mathrm{c}^{-1}$ we underestimate by up to 25% from the extrapolation to the continuum limit. We also performed tests for convergence of our simulations with δt. For $\delta t = 0.2T_\mathrm{c}^{-1}$ the error from our simulations is within $\sim 1\%$ from the continuum limit for $\overline{(\Omega_\mathrm{gw}/H_\mathrm{n}t)}(1/H_\mathrm{n}R_\mathrm{c})$ and $\overline{U}_\mathrm{f,max}$ and $\sim 5\%$ for $\overline{v}^2_{\perp,\mathrm{max}}$.

6.6.4 Convergence to asymptotic fluid flow

In addition to testing convergence with lattice spacing, we also check how close the fluid shells around colliding bubbles in our simulation are to the final asymptotic profiles. To

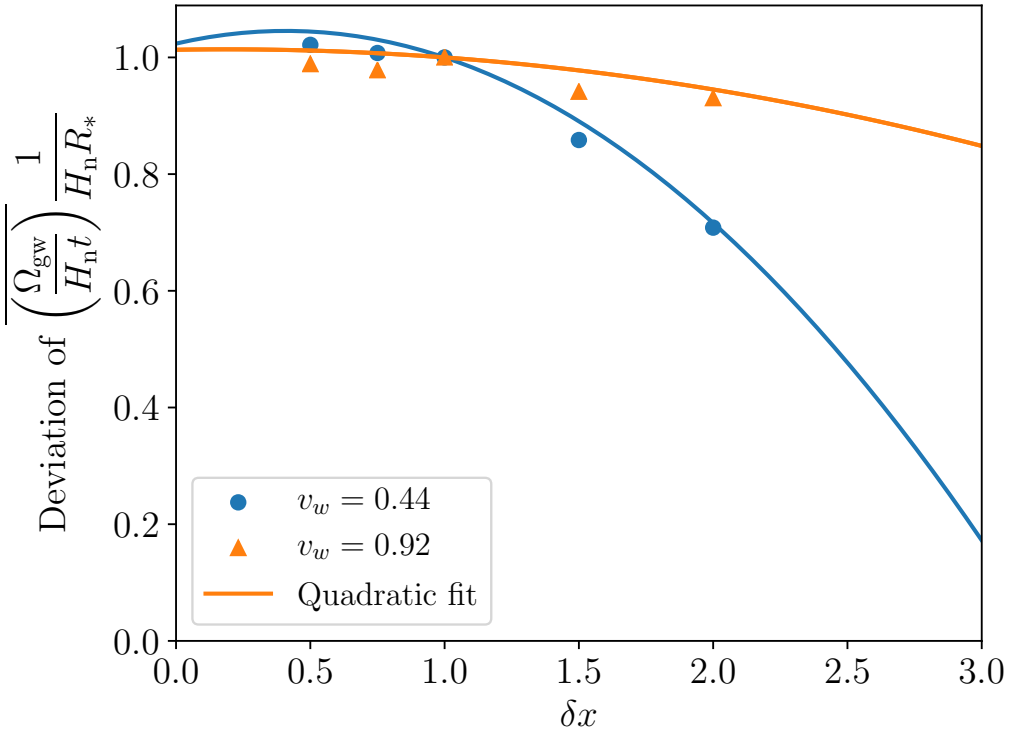

Figure 6.5: Variation of gravitational wave energy density with δx for $v_{\rm w} = 0.44$ and $v_{\rm w} = 0.92$ and transition strength of $\alpha = 0.5$. We normalise the y-axis by dividing by the result from the simulation presented in the paper ($\delta x = 1.0$). Note that $\overline{(\Omega_{\rm gw}/H_{\rm n}t)}$ signifies that we average the quantity inside the brackets over the final $\Delta t = 2R_*$ of the simulation.

do this we perform spherically symmetric 1D simulations of isolated bubbles and calculate $\overline{U}_{\rm f,exp}$ from the fluid shell when the bubble has diameter R_*. We then compare this to $\overline{U}_{\rm f,exp}$ calculated from the fluid shell at $t = 10000T_{\rm c}^{-1}$, i.e when the diameter is $\gg R_{\rm c}$ and the profile has reached its asymptotic solution. We plot the ratio of these two quantities for all α and $v_{\rm w}$ in Fig. 6.8. We can see that the bubbles colliding with the diameter of the average bubble separation are within 20% of the asymptotic $\overline{U}_{\rm f}$ for all simulations. We believe this to be sufficient for this study, and save a further investigation on the convergence with increasing $R_{\rm c}$ for a future work.

6.6.5 Parameter space

In order to understand the regions of parameter space mapped out by our simulations, it can be illuminating to plot the asymptotic maximum fluid flow velocity $v_{\rm p}$ against the wall velocity $v_{\rm w}$ for each simulation point. We do this in Fig. 6.9. Plotting the parameter space in this manner separates subsonic-deflagrations, supersonic-deflagrations,

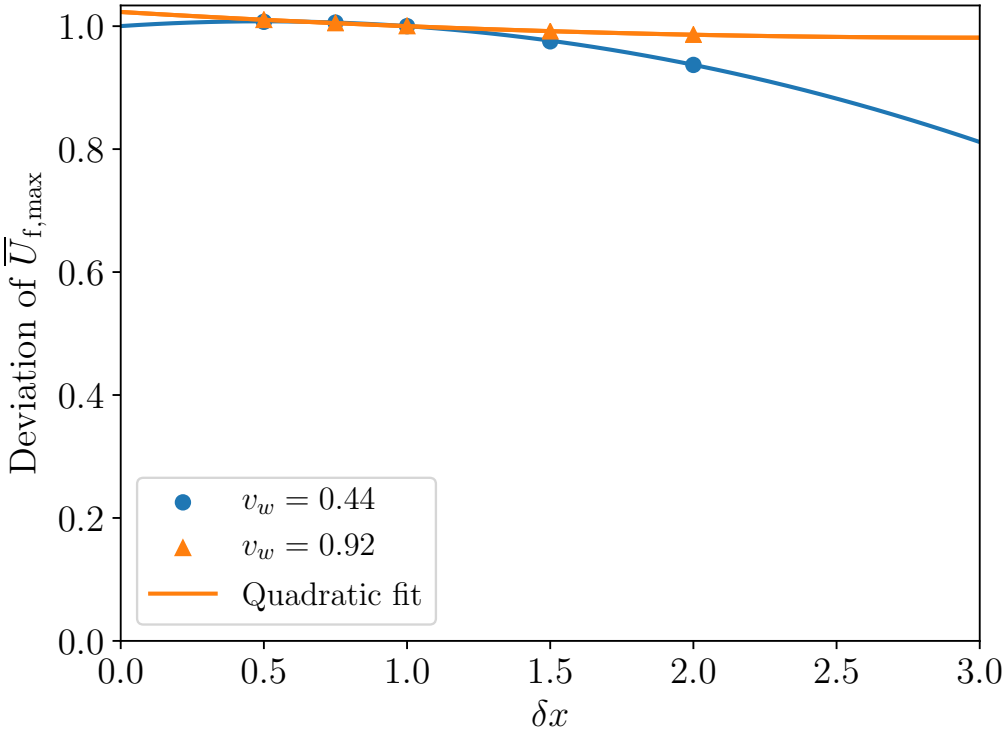

Figure 6.6: Variation of $\overline{U}_{\mathrm{f,max}}$ with δx for $v_{\mathrm{w}} = 0.44$ and $v_{\mathrm{w}} = 0.92$ and transition strength of $\alpha = 0.5$. We normalise the y-axis by dividing by the result from the simulation presented in the paper ($\delta x = 1.0$).

and detonations. Stronger phase transitions with the same wall velocity have a larger value of v_{p}. Transitions with $v_{\mathrm{p}} > v_{\mathrm{w}}$ are forbidden as this would mean that in the wall frame fluid was flowing out from the bubble. We additionally colour each simulation point by the suppression factor in gravitational waves found in our study.

6.6.6 Evolution of global quantities

In Fig. 6.10 we plot how $\overline{U}_{\mathrm{f}}$ and $\overline{U}_{\phi}$ evolve for a deflagration and a detonation, both with strength $\alpha = 0.5$. We see that a rotational component of velocity $\overline{v}_{\perp}$ is generated during the bubble collision phase, and that the deflagration generates $\overline{v}_{\perp}$ more efficiently than the detonation. We also see that, for the deflagration, $\overline{U}_{\phi}$ decreases more slowly than it increases, indicating a slowing down of the phase boundary.

6.6.7 Simulation slice stills

In this supplemental material we include various stills taken from movies of our simulations of strong phase transitions in the early universe, which can be seen in Fig. 6.11 and

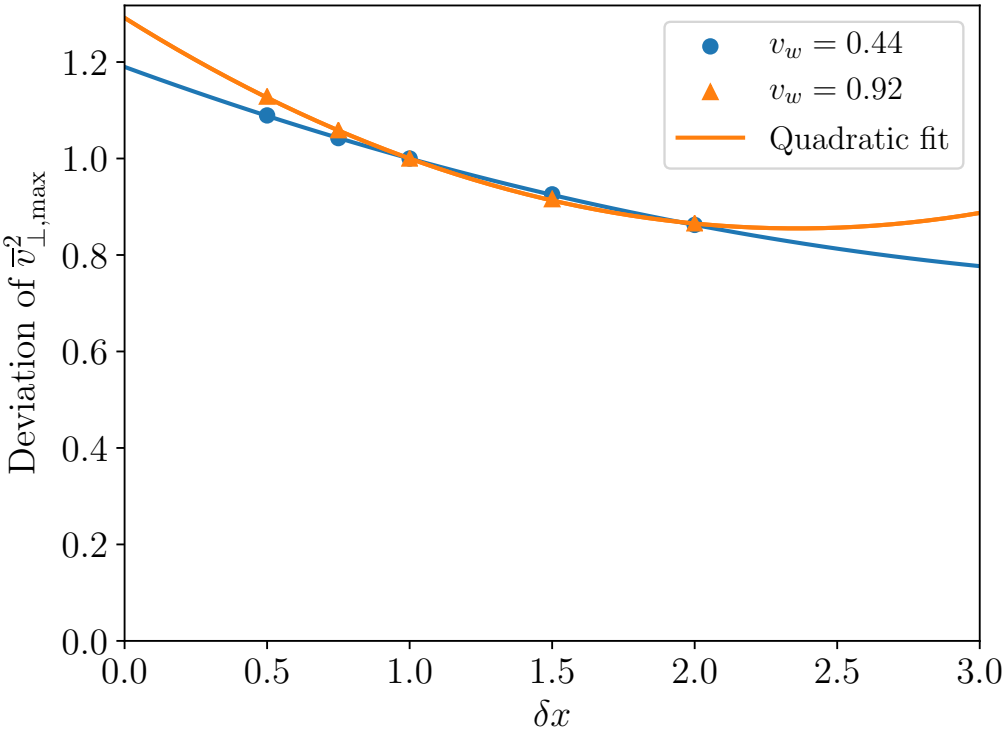

Figure 6.7: Variation of $\overline{v}_{\perp,\max}$ with δx for $v_\mathrm{w} = 0.44$ and $v_\mathrm{w} = 0.92$ and transition strength of $\alpha = 0.5$. We normalise the y-axis by dividing by the result from the simulation presented in the paper ($\delta x = 1.0$).

Fig. 6.12. The movies these stills have been taken from can be found in a Vimeo album [164].

6.6.8 Simulation parameters and measurements

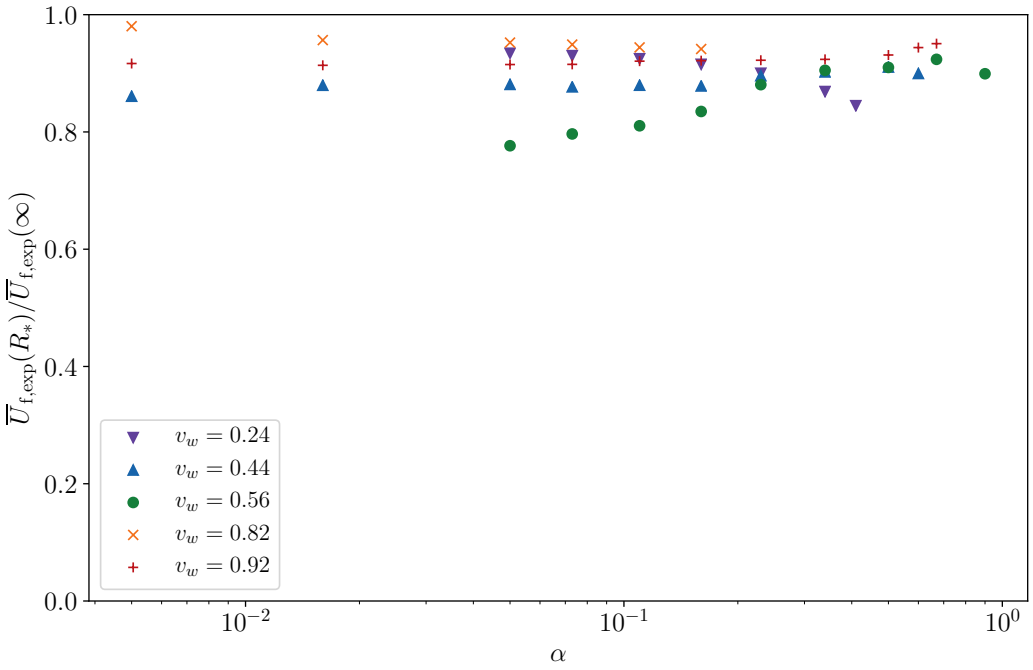

Figure 6.8: Plot comparing $\overline{U}_{\mathrm{f,exp}}$ calculated for an isolated bubble when the diameter of the bubble is R_* to late times ($t = 10000\, T_{\mathrm{c}}^{-1}$) where it has reached the asymptotic profile.

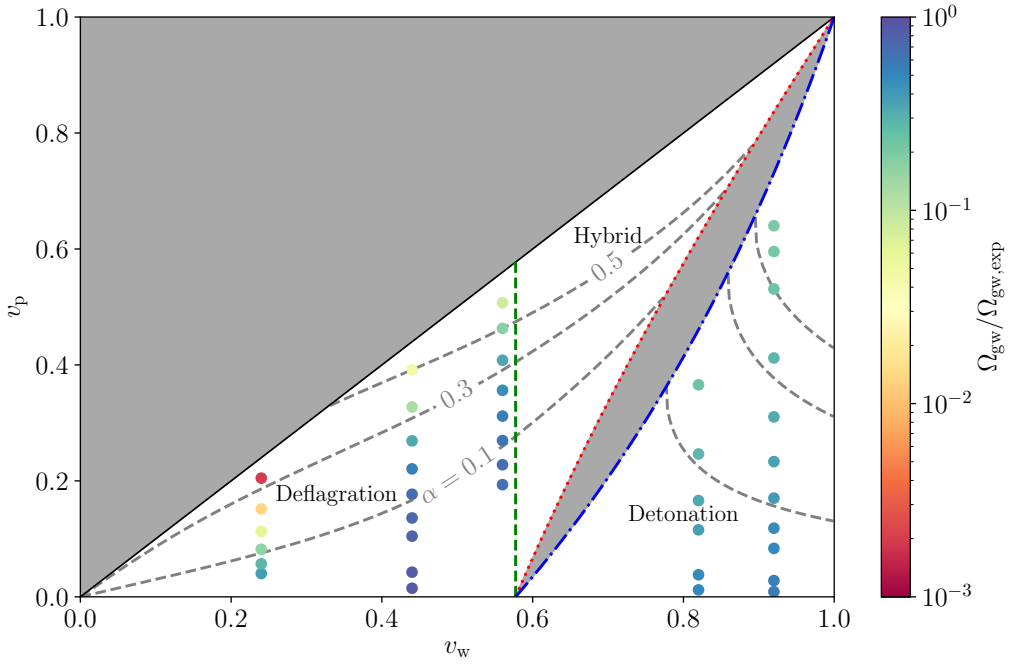

Figure 6.9: Plot of maximum fluid flow velocity for the asymptotic profile v_p against the wall velocity. The green dashed line separates subsonic-deflagrations from supersonic-deflagrations. The blue dotted line gives the minimum v_p for a hybrid. Similarly the red dashed line shows the maximum v_p for a detonation. In the grey regions there are no solutions. See Fig. 7 of [88] for more details. Each point has been coloured according to the suppression in gravitational waves given in Table 6.1. Lines of constant α are shown in dashed grey.

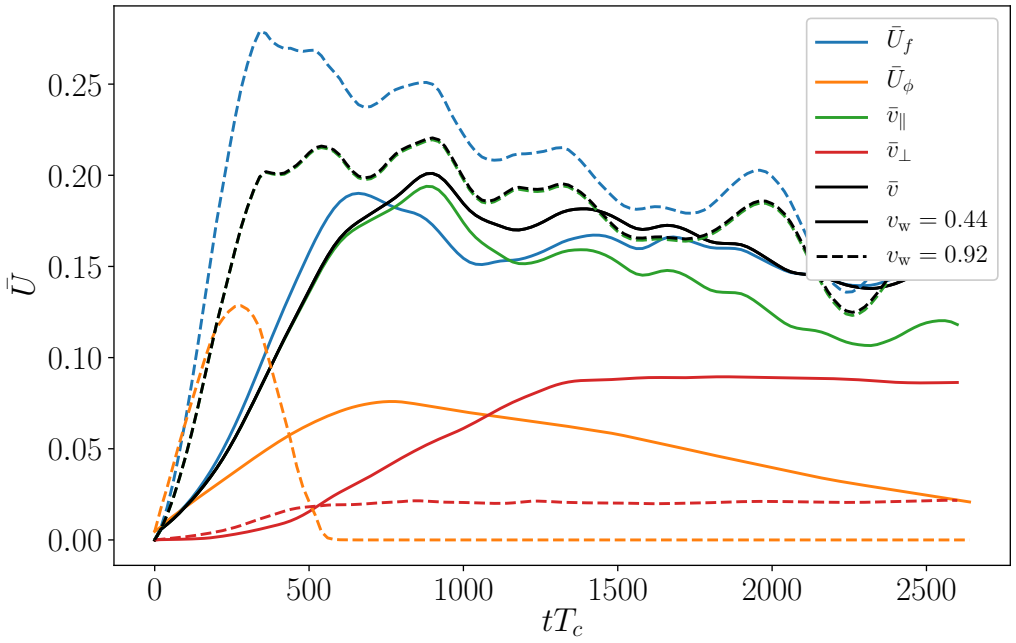

Figure 6.10: The RMS fluid velocities decomposed into irrotational and rotational modes, plotted against time. We also plot the quantities $\overline{U}_\mathrm{f}$ and $\overline{U}_\phi$. Solid lines show a subsonic deflagration with $\alpha = 0.5$, $v_\mathrm{w} = 0.44$, and dashed lines a detonation with $\alpha = 0.5$, $v_\mathrm{w} = 0.92$.

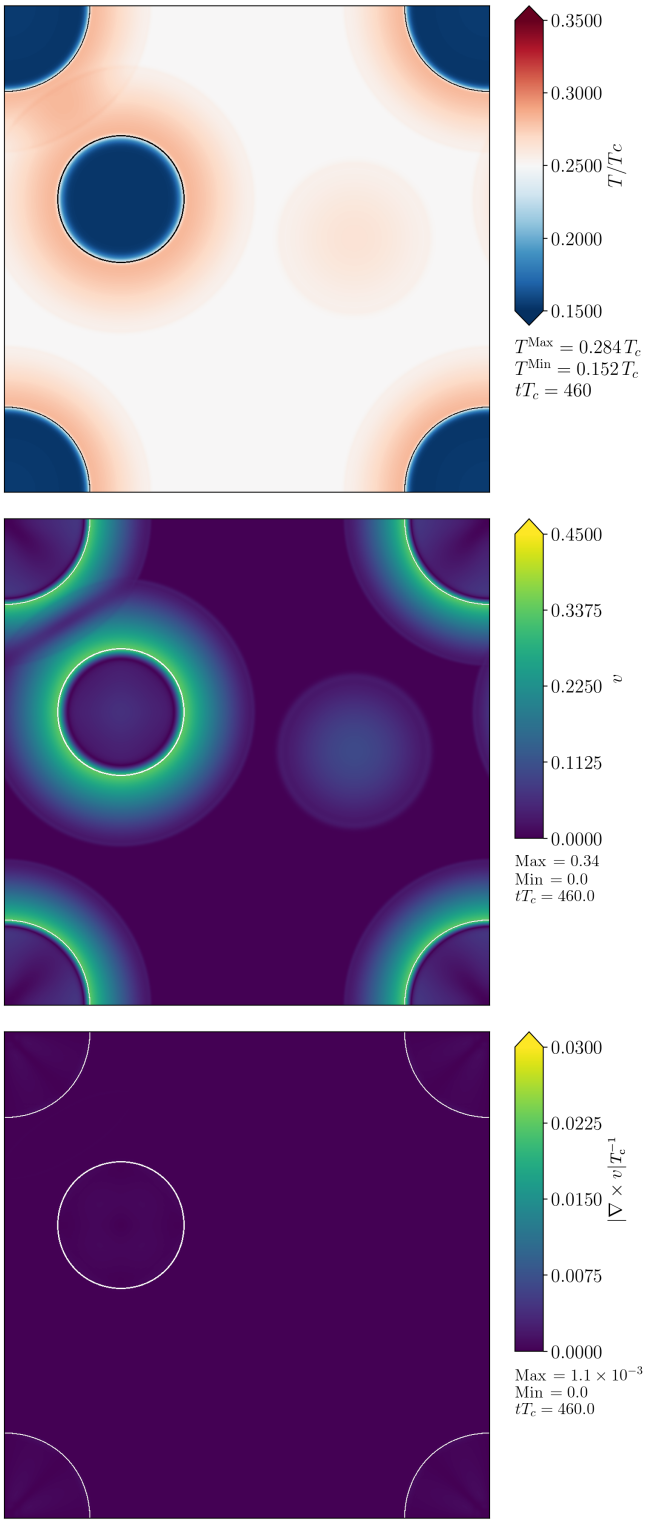
0.3500
0.3000
0.2500
0.2000
0.1500
T/T_c
$T^{\mathrm{Max}} = 0.284\,T_c$
$T^{\mathrm{Min}} = 0.152\,T_c$
$tT_c = 460$
0.4500
0.3375
0.2250
0.1125
0.0000
v
Max $= 0.34$
Min $= 0.0$
$tT_c = 460.0$
0.0300
0.0225
0.0150
0.0075
0.0000
$|\nabla \times v|T_c^{-1}$
Max $= 1.1 \times 10^{-3}$
Min $= 0.0$
$tT_c = 460.0$

(a) $tT_c = 460$

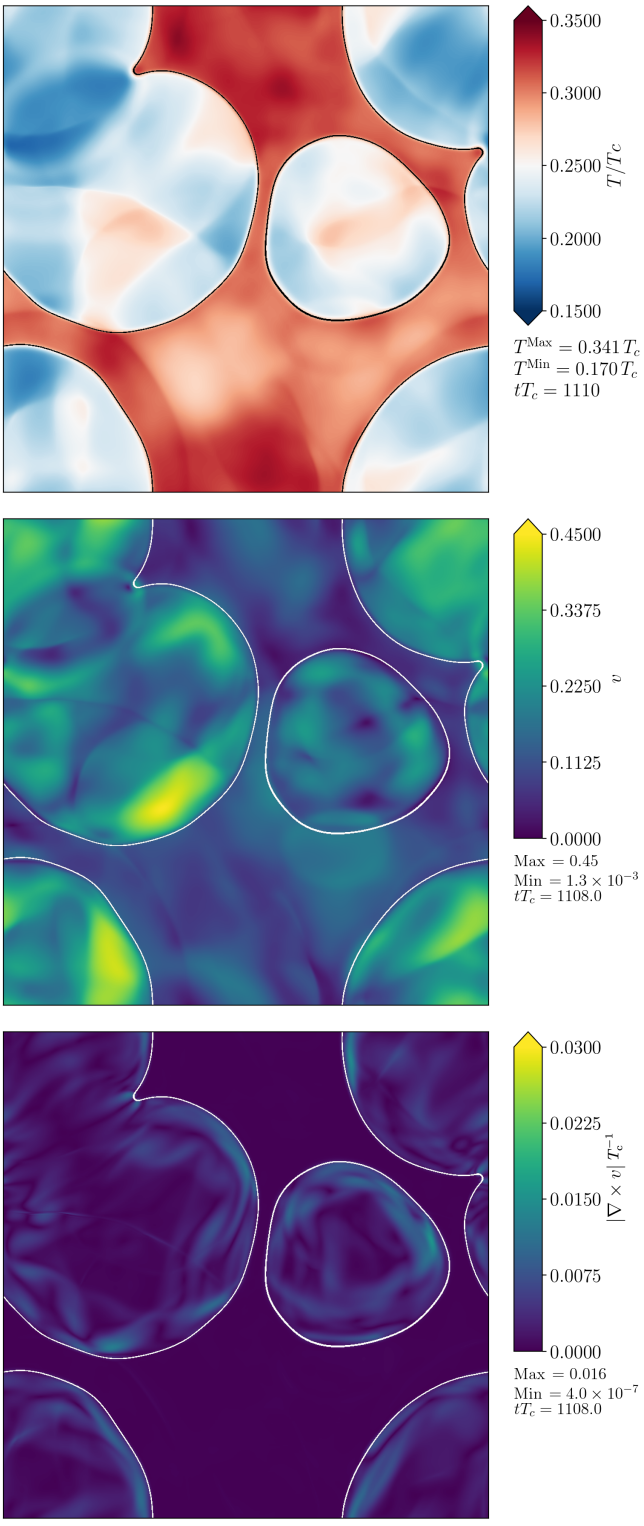

(b) $tT_{\mathrm{c}} = 1110$

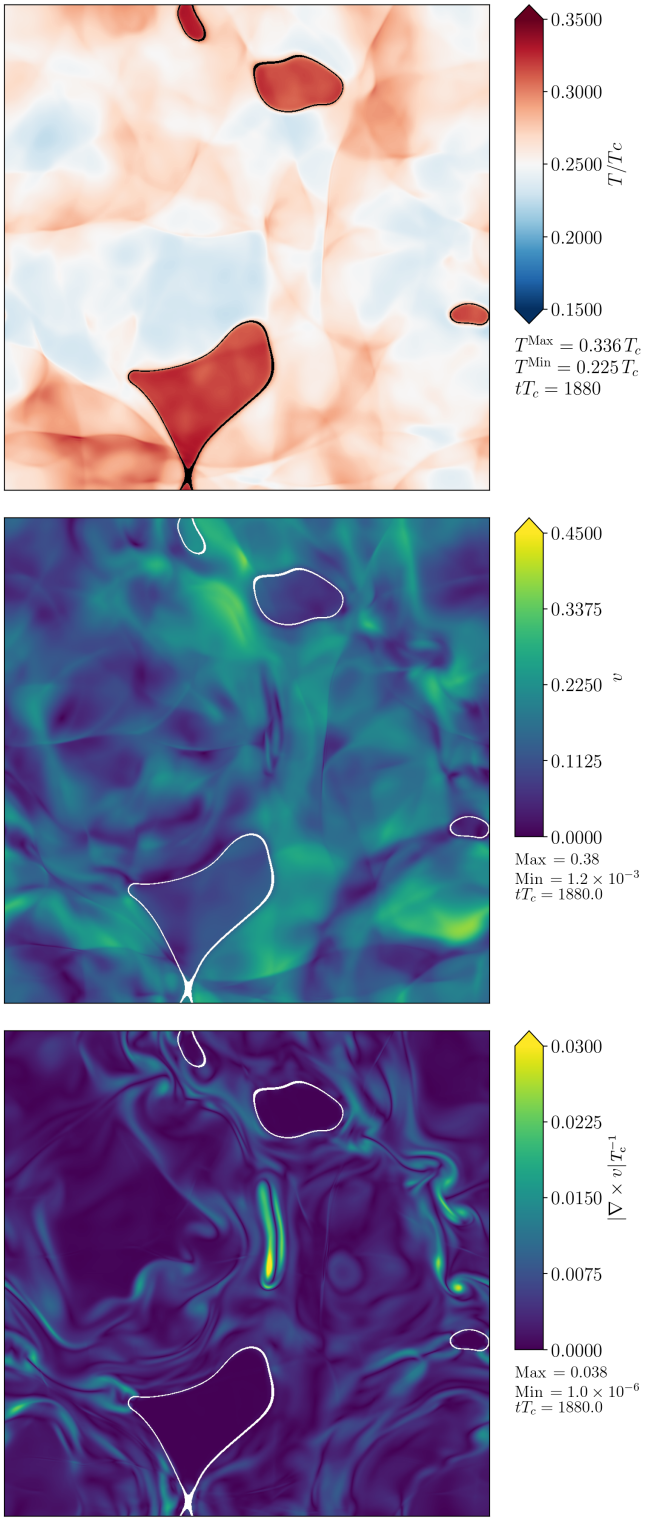

(c) $tT_{\mathrm{c}} = 1880$

Figure 6.11: Slices through $(0, y, z)$ for a simulation with $v_{\mathrm{w}} = 0.44$, $\alpha = 0.5$, corresponding to a deflagration. In the top plot of each subfigure, we plot the temperature T/T_{c}. The midpoint of this colormap corresponds to T_{n}. The middle plot shows the fluid velocity v. The bottom plot shows the vorticity $|\nabla \times v|$. The bubble walls are shaded in black for the top plot, and white for the middle and bottom plots.

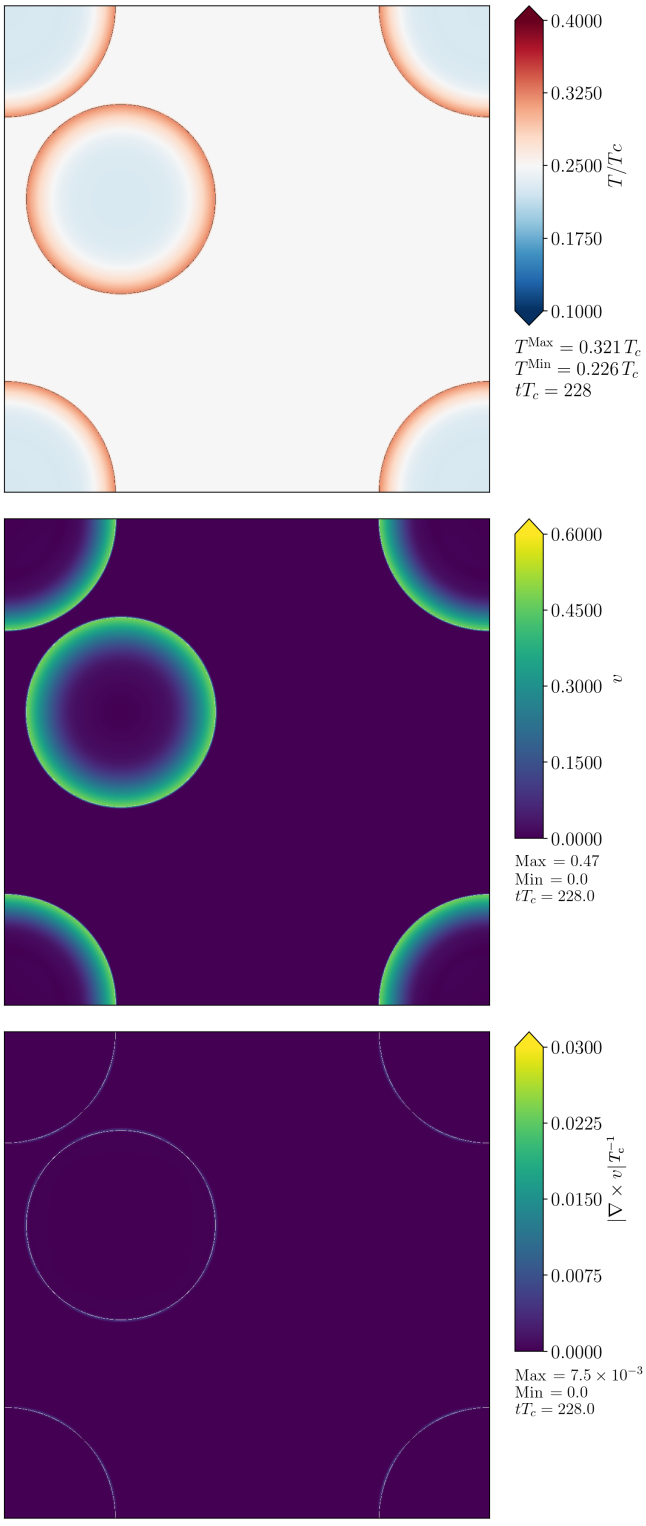
0.4000
0.3250
0.2500
0.1750
0.1000
T/T_c
$T^{\mathrm{Max}} = 0.321\,T_c$
$T^{\mathrm{Min}} = 0.226\,T_c$
$tT_c = 228$
0.6000
0.4500
0.3000
0.1500
0.0000
v
Max = 0.47
Min = 0.0
$tT_c = 228.0$
0.0300
0.0225
0.0150
0.0075
0.0000
$|\nabla \times v|\,T_c^{-1}$
Max = 7.5×10^{-3}
Min = 0.0
$tT_c = 228.0$

(a) $tT_c = 228$

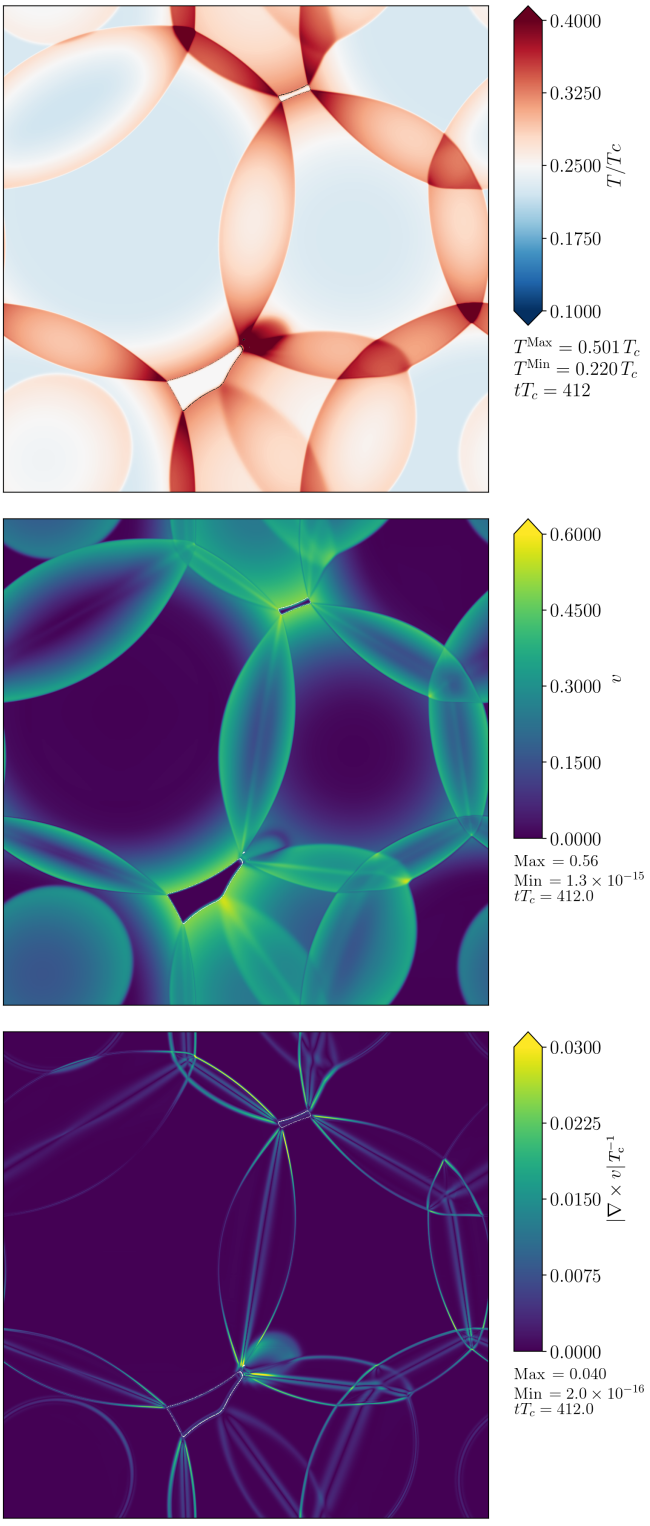
0.4000
0.3250
0.2500
0.1750
0.1000
T/T_c
$T^{\mathrm{Max}} = 0.501\,T_c$
$T^{\mathrm{Min}} = 0.220\,T_c$
$tT_c = 412$
0.6000
0.4500
0.3000
0.1500
0.0000
v
Max $= 0.56$
Min $= 1.3 \times 10^{-15}$
$tT_c = 412.0$
0.0300
0.0225
0.0150
0.0075
0.0000
$|\nabla \times v|\,T_c^{-1}$
Max $= 0.040$
Min $= 2.0 \times 10^{-16}$
$tT_c = 412.0$

(b) $tT_c = 412$

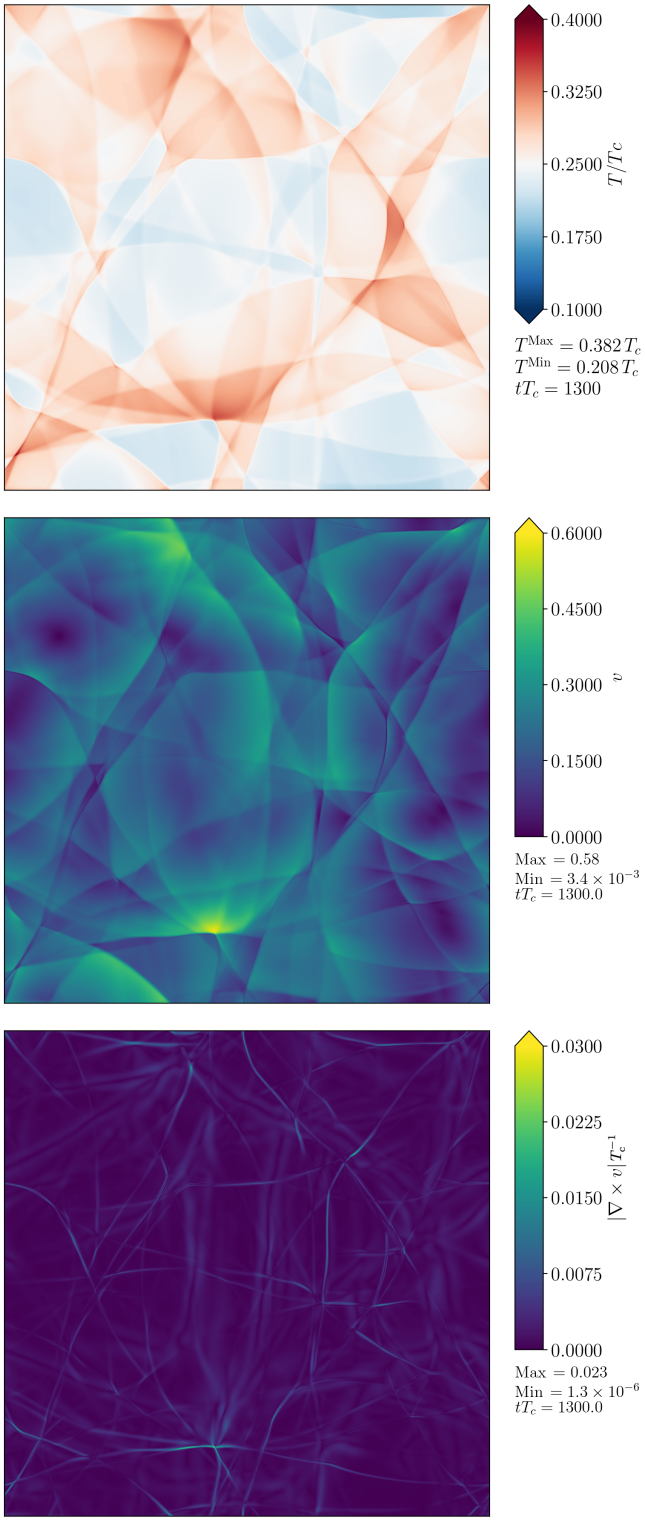

(c) $tT_{\mathrm{c}} = 1300$

Figure 6.12: Slices through $(0, y, z)$ for a simulation with $v_{\mathrm{w}} = 0.92$, $\alpha = 0.5$, corresponding to a detonation. In the top plot of each subfigure, we plot the temperature T/T_{c}. The midpoint of this colormap corresponds to T_{n}. The middle plot shows the fluid velocity v. The bottom plot shows the vorticity $|\nabla \times v|$. The bubble walls are shaded in black for the top plot, and white for the middle and bottom plots.

v_w	α	T_n/T_c	$t_{fin}T_c$	η/T_c	$\overline{U}_{f,max}$	$\overline{U}_{f,exp}$	$\bar{v}_\perp^2$	$\bar{v}^2$	$\overline{\left(\frac{\Omega_{gw}}{H_n t}\right)}\frac{1}{H_n R_*}$	$\frac{\Omega_{gw,exp}}{H_n t}\frac{1}{H_n R_*}$
0.24	0.050	0.45	4.8×10^3	1.2	0.036	0.039	6.4×10^{-5}	1.3×10^{-3}	4.6×10^{-8}	1.2×10^{-7}
0.24	0.073	0.41	4.8×10^3	1.3	0.048	0.055	1.5×10^{-4}	2.3×10^{-3}	1.4×10^{-7}	5.0×10^{-7}
0.24	0.11	0.37	4.8×10^3	1.5	0.063	0.082	3.7×10^{-4}	4.1×10^{-3}	4.1×10^{-7}	2.4×10^{-6}
0.24	0.16	0.33	4.8×10^3	1.8	0.074	0.12	9.1×10^{-4}	5.7×10^{-3}	6.0×10^{-7}	9.5×10^{-6}
0.24	0.23	0.30	4.8×10^3	2.4	0.075	0.16	2.0×10^{-3}	5.9×10^{-3}	4.6×10^{-7}	3.3×10^{-5}
0.24	0.34	0.28	4.8×10^3	5.1	0.066	0.22	2.9×10^{-3}	4.4×10^{-3}	2.3×10^{-7}	1.2×10^{-4}
0.44	0.0050	0.79	2.4×10^3	0.34	0.0083	0.0069	1.7×10^{-7}	6.9×10^{-5}	1.0×10^{-10}	1.2×10^{-10}
0.44	0.016	0.59	2.4×10^3	0.52	0.025	0.021	1.4×10^{-6}	6.0×10^{-4}	9.1×10^{-9}	1.1×10^{-8}
0.44	0.050	0.45	2.4×10^3	0.66	0.066	0.061	1.6×10^{-5}	4.3×10^{-3}	5.6×10^{-7}	7.2×10^{-7}
0.44	0.073	0.41	2.4×10^3	0.71	0.090	0.085	4.0×10^{-5}	7.8×10^{-3}	2.0×10^{-6}	2.8×10^{-6}
0.44	0.11	0.37	2.4×10^3	0.81	0.12	0.12	1.1×10^{-4}	1.3×10^{-2}	7.0×10^{-6}	1.0×10^{-5}
0.44	0.16	0.33	2.4×10^3	0.94	0.15	0.16	3.0×10^{-4}	2.1×10^{-2}	2.0×10^{-5}	3.7×10^{-5}
0.44	0.23	0.30	2.4×10^3	1.2	0.18	0.22	1.0×10^{-3}	3.2×10^{-2}	4.3×10^{-5}	1.3×10^{-4}
0.44	0.34	0.28	2.4×10^3	1.7	0.18	0.30	3.6×10^{-3}	3.6×10^{-2}	5.2×10^{-5}	4.2×10^{-4}
0.44	0.50	0.25	2.4×10^3	3.5	0.19	0.39	8.0×10^{-3}	4.0×10^{-2}	5.8×10^{-5}	1.2×10^{-3}
0.56	0.050	0.45	2.8×10^3	0.53	0.080	0.075	1.3×10^{-5}	5.6×10^{-3}	1.1×10^{-6}	1.7×10^{-6}
0.56	0.073	0.41	2.8×10^3	0.59	0.10	0.10	3.5×10^{-5}	9.6×10^{-3}	3.6×10^{-6}	5.3×10^{-6}
0.56	0.11	0.37	2.8×10^3	0.67	0.14	0.14	9.2×10^{-5}	1.6×10^{-2}	1.2×10^{-5}	2.0×10^{-5}
0.56	0.16	0.33	2.8×10^3	0.76	0.18	0.19	2.4×10^{-4}	2.7×10^{-2}	3.6×10^{-5}	6.4×10^{-5}
0.56	0.23	0.30	2.8×10^3	0.90	0.22	0.25	5.8×10^{-4}	4.3×10^{-2}	9.3×10^{-5}	2.0×10^{-4}
0.56	0.34	0.28	2.8×10^3	1.2	0.27	0.33	1.5×10^{-3}	6.4×10^{-2}	2.1×10^{-4}	6.2×10^{-4}
0.56	0.50	0.25	2.8×10^3	1.7	0.28	0.43	5.2×10^{-3}	7.8×10^{-2}	3.1×10^{-4}	1.8×10^{-3}
0.56	0.67	0.23	2.8×10^3	2.9	0.30	0.51	1.1×10^{-2}	9.0×10^{-2}	3.0×10^{-4}	3.7×10^{-3}
0.82	0.0050	0.79	2.8×10^3	0.11	0.0064	0.0066	2.3×10^{-7}	4.0×10^{-5}	4.8×10^{-11}	1.0×10^{-10}
0.82	0.016	0.59	2.8×10^3	0.16	0.019	0.020	2.2×10^{-6}	3.6×10^{-4}	4.3×10^{-9}	9.1×10^{-9}
0.82	0.050	0.45	2.8×10^3	0.18	0.055	0.061	1.5×10^{-5}	2.8×10^{-3}	2.9×10^{-7}	7.6×10^{-7}
0.82	0.073	0.41	2.8×10^3	0.19	0.076	0.088	2.6×10^{-5}	5.2×10^{-3}	1.1×10^{-6}	3.2×10^{-6}
0.82	0.11	0.37	2.8×10^3	0.20	0.11	0.13	4.7×10^{-5}	9.4×10^{-3}	4.1×10^{-6}	1.4×10^{-5}
0.82	0.16	0.33	2.8×10^3	0.22	0.15	0.18	8.4×10^{-5}	1.6×10^{-2}	1.2×10^{-5}	5.5×10^{-5}
0.92	0.0050	0.79	2.4×10^3	0.053	0.0051	0.0051	3.2×10^{-7}	2.6×10^{-5}	2.0×10^{-11}	3.6×10^{-11}
0.92	0.016	0.59	2.4×10^3	0.086	0.015	0.016	3.4×10^{-6}	2.4×10^{-4}	1.9×10^{-9}	3.6×10^{-9}
0.92	0.050	0.45	2.4×10^3	0.099	0.045	0.049	2.2×10^{-5}	1.9×10^{-3}	1.5×10^{-7}	3.0×10^{-7}
0.92	0.073	0.41	2.4×10^3	0.10	0.064	0.070	3.6×10^{-5}	3.7×10^{-3}	6.0×10^{-7}	1.3×10^{-6}
0.92	0.11	0.37	2.4×10^3	0.10	0.087	0.10	5.8×10^{-5}	6.9×10^{-3}	2.4×10^{-6}	6.0×10^{-6}
0.92	0.16	0.33	2.4×10^3	0.11	0.12	0.14	8.8×10^{-5}	1.2×10^{-2}	8.4×10^{-6}	2.3×10^{-5}
0.92	0.23	0.30	2.4×10^3	0.11	0.16	0.20	1.4×10^{-4}	2.0×10^{-2}	2.6×10^{-5}	8.0×10^{-5}
0.92	0.34	0.28	2.4×10^3	0.12	0.21	0.27	2.5×10^{-4}	3.2×10^{-2}	8.1×10^{-5}	2.9×10^{-4}
0.92	0.50	0.25	2.4×10^3	0.13	0.28	0.36	4.6×10^{-4}	4.9×10^{-2}	2.2×10^{-4}	9.3×10^{-4}
0.92	0.60	0.24	2.4×10^3	0.14	0.32	0.42	6.3×10^{-4}	5.8×10^{-2}	3.5×10^{-4}	1.6×10^{-3}
0.92	0.67	0.23	2.4×10^3	0.15	0.34	0.45	7.8×10^{-4}	6.5×10^{-2}	4.5×10^{-4}	2.2×10^{-3}

Table 6.1: Key simulation parameters and measured quantities used to generate the graphs in this paper. Note that $\overline{\left(\frac{\Omega_{gw}}{H_n t}\right)}$ signifies that we average the quantity inside the brackets over the final $\Delta t = 2R_*$ of the simulation.

Chapter 7

Conclusions

Within this thesis we have studied first-order phase transitions in the early universe, with a focus on the gravitational wave signals they can produce. We began with a review of general relativity, basic cosmology and linearised gravity in Chapter 2, where we introduced the concept of gravitational waves.

In Chapter 3, we discussed the dynamics of first-order phase transitions, from bubble nucleation through to the eventual production of gravitational waves. A distinction was made between thermal transitions, in which bubbles of the true vacuum nucleate among a relativistic plasma, and vacuum transitions. We showed how thermal transitions can be modelled using a coupled fluid-field model. As bubbles expand in a thermal transition, shells of perturbed fluid develop around the bubble wall. The form of the fluid shell can be classified according to the bubble wall speed, with subsonic deflagrations, supersonic deflagrations, and detonations possible. We showed how the energy budget of the transition can be estimated from the asymptotic fluid profile of an expanding bubble. It is possible that bubble walls in thermal transitions can undergo a runaway acceleration, in which case the vast majority of the free energy released during the transition can be deposited into the motion of the bubble wall, similar to in a vacuum transition. We explained the scenarios in which runaway transitions may occur and the dynamics of the scalar field unique to runaways and vacuum transitions. Finally, we outlined the gravitational wave power spectra that are produced from bubble collisions, sound waves, and turbulence.

The remaining chapters contained the original research of this thesis. They focused on the results from classical lattice field theory simulations of first-order phase transitions. Chapter 4 reported on the results from simulations of many bubbles in a vacuum transition with a quartic potential. When studying the scalar field dynamics, it could be seen that the scalar field initially rebounded to the false vacuum in the overlap region of colliding bubbles. This violated one of the assumptions in the so called envelope approximation, that energy momentum of the scalar field disappeared on collision of the bubble wall.

Comparison between the gravitational wave power spectrum produced from bubble collisions in the lattice simulations and the envelope approximation revealed that while the peak frequency and peak amplitude were comparable, the high frequency power law fell as $f^{-1.5}$ instead of the f^{-1} predicted in the envelope approximation. After the bubbles finished colliding, the scalar field continued to oscillate around the broken phase value for a substantial time. During this period gradients in the scalar field continued to source gravitational waves. While this behaviour had been noted in a previous study, we showed that the length scale of the gravitational waves produced are associated with the scalar field mass rather than the mean bubble separation. As a result, if the separation of scales were extrapolated to realistic values found in real world cosmological phase transitions, the signal from the oscillation phase would be subdominant and at a length scale inaccessible to gravitational wave detectors.

Within Chapter 5, the parameter space of the quartic potential was explored in more detail with further simulations. It was shown that the dependence of the scalar field dynamics on the potential could be reduced to a single parameter $\overline{\lambda} = M^2/M_c^2$ with M the symmetric phase mass of the scalar field and M_c the critical mass. Varying $\overline{\lambda}$ changes the thickness of the critical bubble wall and how degenerate the minimas in the potential are in comparison to the potential barrier. For larger values of $\overline{\lambda}$, the scalar field rebounded temporarily into the false vacuum upon collision, whereas for small values of $\overline{\lambda}$ the rebound was substantially reduced. Analysis of the transverse-traceless shear stress and gravitational wave power spectrum revealed that gravitational waves continued to be sourced at the length scale of the mean bubble separation for some time after the bubbles finished colliding. The gravitational wave power spectrum was fitted using a broken power law and the peak frequency, peak amplitude, and power law exponents were tracked during the simulation. There was evidence that the infrared power law became shallower than the f^3 predicted by causality. The ultraviolet power laws at the end of the simulations became steeper as $\overline{\lambda} \to 0$, varying between $f^{-1.4}$ and $f^{-2.3}$ for the $\overline{\lambda}$ we considered. The simulation results were compared to the expectations from the envelope approximation and bulk flow model, but it was found that neither fully predicted the shape of the resulting gravitational wave power spectrum.

Our attention turned towards thermal transitions in Chapter 6. In this chapter, simulations of strongly first-order phase transitions in a coupled field-fluid model with a bag-like equation of state were conduted. A scan across wall velocities and transition strengths was performed, with both subsonic deflagrations and detonations represented. It was found

that for subsonic deflagrations the ratio of rotational kinetic energy to compressional kinetic energy directly after the transition, $\epsilon_{\rm turb}$, grew as the transition strength increased. For detonations $\epsilon_{\rm turb}$ remained approximately constant. It appeared that vorticity was generated when fluid passed through the phase transition boundary. This could not occur in detonations, as the fluid is at rest in front of the bubble wall. For deflagrations in a strong transition, the fluid ahead of the bubble wall was heated substantially above the nucleation temperature. Hot, high pressure regions of the metastable state formed into droplets which resisted collapse, slowing down the advance of the phase boundary. This led to a substantial deficit in the overall kinetic energy in the fluid when comparing to that predicted from the asymptotic fluid profile of an expanding bubble. Again this process does not occur in detonations as the fluid is at rest ahead of the bubble wall. The kinetic energy deficit resulted in a suppression in the gravitational wave signal when compared to the naive calculation using the asymptotic fluid profile to estimate the kinetic energy. The vorticity generation and suppression in gravitational waves was largest for the strongest and slowest of the deflagrations we considered. For the simulation with $v_{\rm w} = 0.24$ and $\alpha_\theta = 0.34$, the ratio of the mean square velocity in rotational modes to the total mean square velocity was $\overline{v}_\perp^2/\overline{v}^2 = 0.66$, and the suppression in the gravitational wave signal was $\Omega_{\rm gw}/\Omega_{\rm gw,exp} = 1.9 \times 10^{-3}$. In other words, for certain regions in the parameter space the ansatz provided by the LISA Cosmology Working Group in Ref. [77] could overestimate the gravitational wave signal by up to a factor of a thousand. Furthermore, the presence of substantial vorticity immediately after the completion of the phase transition could lead to a more rapid development of turbulence and decay of the sound wave signal, futher modifying the predicted signal. In order to establish the capability of LISA to detect or rule out BSM physics, further careful studies will be required to develop our understanding of strong phase transitions.

The results we have presented within this thesis give us further understanding of the gravitational waves produced during a first-order phase transition. However, much remains to be clarified before LISA flies in the early 2030s. In order to link particle physics models with first-order phase transitons to any gravitational wave signal seen at LISA, it is crucial we are able to characterise the background accurately. An area in particular need of investigation is the generation of non-linear effects in the flow and the subsequent decay of sound waves. We have shown in Chapter 6 that it is possible to simulate strong transitions and further simulations that follow the decay of the sound waves are necessary to deduce the overall strength of the gravitational wave signal.

A logical follow up to the research on strong transitions conducted in Chapter 6 is to analyse in detail the shape of the velocity power spectrum and the gravitational wave power spectrum to see how they are modified in strong phase transitions. This will require larger simulations with more bubbles to obtain a greater dynamic range so that the peak of the spectra may be seen. We already have some indication that the power spectra will be modified for deflagrations as there are substantial amounts of vorticity produced during strong transitions.

In Section 3.2, we showed that supersonic deflagrations have the largest kinetic efficiency for a given transition strength and wall velocity, but we also showed that the appearance of supersonic deflagrations depends on the form of the effective potential and equation of state. It would be interesting to further investigate whether supersonic deflagrations can exist in realisitic particle physics models. If supersonic deflagrations do exist, simulations should be performed to deduce the shape of the gravitational wave signal they produce.

So far all of our simulations of thermal phase transitions have assumed there is no magnetic field present during the transition. If there is a seed field prior to the transition, or magnetic fields can be generated during the transition itself, it could result in a modification to the fluid behavior during the transition. Adding magnetic fields into our simulations would be a very interesting research project. It would also allow us to study the effect of magnetic fields during bubble collisions and the development of magnetohydrodynamical turbulence after the transition completed.

We have also performed simulations of vacuum phase transitions in Chapters 4 and 5. We showed that the envelope approximation does not accurately predict the gravitational wave power spectrum. We provided fits for the gravitational wave power spectrum for a substantial region of the parameter space for a quartic potential. One future area of study could be to generalise to other potential shapes. We were limited in our ability to explore collisions with $\gamma_* \gtrsim 4$ using the dynamic range possible with the computational resources available to us. Similarly, it was a challenge to deduce the infrared power law. A different approach will likely prove necessary to push to higher values of γ_* and also to find the infrared spectral shape. One possibility would be to perform deeper studies of the parameter space in two bubble collisions, where extra symmetries can be exploited to reduce the computational demands.

All of the simulations conducted within this thesis have been performed in the weak gravity limit using linearised gravity. While we expect this to be a valid approximation for

the parameter space we consider, simulations within full numerical general relativity would be useful to confirm this. Furthermore, there are very interesting regions of parameter space where full numerical general relativity will be required, for example within very strong phase transitions with $\alpha_\theta > 1$ and for transitions where the size of the bubbles upon collision approach the Hubble length. These limits are particularly interesting for the production of gravitational waves or even the formation of primordial black holes. While numerical relativity simulations represent a significant challenge, the potential rewards are also substantial, with a strong possibility of novel results.

With the launch of a funded space based gravitational wave detector on the horizon, the future is bright for the field of early universe first-order phase transitions. As outlined within this chapter, there is a huge variety of interesting topics to explore, even just within the scope of phase transition dynamics and the production of gravitational waves. Working in this field over the last four years has been a fascinating and rewarding experience for me. While much remains to be understood before the LISA mission begins, if we are lucky, it might provide us with a glimpse of the conditions at the origin of our universe.

Bibliography

[1] D. Cutting, M. Hindmarsh and D. J. Weir, "Gravitational waves from vacuum first-order phase transitions: from the envelope to the lattice", *Phys. Rev.*, vol. D97, no. 12, p. 123 513, 2018. DOI: 10.1103/PhysRevD.97.123513. arXiv: 1802.05712 [astro-ph.CO].

[2] ——, "Vorticity, kinetic energy, and suppressed gravitational wave production in strong first order phase transitions", Jun. 2019. arXiv: 1906.00480 [hep-ph].

[3] D. Cutting, E. G. Escartin, M. Hindmarsh and D. J. Weir, "Gravitational waves from vacuum first order phase transitions II: from thin to thick walls", May 2020. arXiv: 2005.13537 [astro-ph.CO].

[4] S. R. Coleman, "The Fate of the False Vacuum. 1. Semiclassical Theory", *Phys. Rev.*, vol. D15, pp. 2929–2936, 1977, [Erratum: Phys. Rev.D16,1248(1977)]. DOI: 10.1103/PhysRevD.15.2929.

[5] A. D. Linde, "Decay of the False Vacuum at Finite Temperature", *Nucl.Phys.*, vol. B216, p. 421, 1983. DOI: 10.1016/0550-3213(83)90293-6.

[6] P. J. Steinhardt, "Relativistic detonation waves and bubble growth in false vacuum decay", *Phys.Rev.*, vol. D25, p. 2074, 1982. DOI: 10.1103/PhysRevD.25.2074.

[7] C. G. Callan Jr. and S. R. Coleman, "The Fate of the False Vacuum. 2. First Quantum Corrections", *Phys. Rev.*, vol. D16, pp. 1762–1768, 1977. DOI: 10.1103/PhysRevD.16.1762.

[8] A. D. Linde, "Phase Transitions in Gauge Theories and Cosmology", *Rept.Prog.Phys.*, vol. 42, pp. 389–437, 1979. DOI: 10.1088/0034-4885/42/3/001.

[9] A. Sakharov, "Violation of CP Invariance, C asymmetry, and baryon asymmetry of the universe", *Sov. Phys. Usp.*, vol. 34, no. 5, pp. 392–393, 1991. DOI: 10.1070/PU1991v034n05ABEH002497.

[10] V. Kuzmin, V. Rubakov and M. Shaposhnikov, "On the Anomalous Electroweak Baryon Number Nonconservation in the Early Universe", *Phys. Lett. B*, vol. 155, p. 36, 1985. DOI: 10.1016/0370-2693(85)91028-7.

[11] M. Shaposhnikov, "Possible Appearance of the Baryon Asymmetry of the Universe in an Electroweak Theory", *JETP Lett.*, vol. 44, pp. 465–468, 1986.

[12] ——, "Baryon Asymmetry of the Universe in Standard Electroweak Theory", *Nucl. Phys. B*, vol. 287, pp. 757–775, 1987. DOI: 10.1016/0550-3213(87)90127-1.

[13] D. E. Morrissey and M. J. Ramsey-Musolf, "Electroweak baryogenesis", *New J. Phys.*, vol. 14, p. 125 003, 2012. DOI: 10.1088/1367-2630/14/12/125003. arXiv: 1206.2942 [hep-ph].

[14] J. M. Cline, "Is electroweak baryogenesis dead?", *Phil. Trans. Roy. Soc. Lond. A*, vol. 376, no. 2114, E. Auge, J. Dumarchez and J. Tran Thanh Van, Eds., p. 20 170 116, 2018. DOI: 10.1098/rsta.2017.0116. arXiv: 1704.08911 [hep-ph].

[15] A. Bochkarev, S. Kuzmin and M. Shaposhnikov, "Electroweak baryogenesis and the Higgs boson mass problem", *Phys. Lett. B*, vol. 244, pp. 275–278, 1990. DOI: 10.1016/0370-2693(90)90069-I.

[16] A. G. Cohen, D. B. Kaplan and A. E. Nelson, "Weak scale baryogenesis", *Phys. Lett. B*, vol. 245, pp. 561–564, 1990. DOI: 10.1016/0370-2693(90)90690-8.

[17] ——, "Baryogenesis at the weak phase transition", *Nucl. Phys. B*, vol. 349, pp. 727–742, 1991. DOI: 10.1016/0550-3213(91)90395-E.

[18] N. Turok and J. Zadrozny, "Electroweak baryogenesis in the two doublet model", *Nucl. Phys. B*, vol. 358, pp. 471–493, 1991. DOI: 10.1016/0550-3213(91)90356-3.

[19] K. Kajantie, M. Laine, K. Rummukainen and M. E. Shaposhnikov, "Is there a hot electroweak phase transition at m(H) larger or equal to m(W)?", *Phys.Rev.Lett.*, vol. 77, pp. 2887–2890, 1996. DOI: 10.1103/PhysRevLett.77.2887. arXiv: hep-ph/9605288 [hep-ph].

[20] ——, "A Nonperturbative analysis of the finite T phase transition in SU(2) x U(1) electroweak theory", *Nucl.Phys.*, vol. B493, pp. 413–438, 1997. DOI: 10.1016/S0550-3213(97)00164-8. arXiv: hep-lat/9612006 [hep-lat].

[21] Y. Aoki, G. Endrődi, Z. Fodor, S. D. Katz and K. K. Szabó, "The order of the quantum chromodynamics transition predicted by the standard model of particle physics", *Nature*, vol. 443, no. 7112, pp. 675–678, 2006, ISSN: 1476-4687. DOI: 10.1038/nature05120. [Online]. Available: http://dx.doi.org/10.1038/nature05120.

[22] M. Pietroni, "The Electroweak phase transition in a nonminimal supersymmetric model", *Nucl. Phys. B*, vol. 402, pp. 27–45, 1993. DOI: 10.1016/0550-3213(93)90635-3. arXiv: hep-ph/9207227.

[23] A. Davies, C. Froggatt and R. Moorhouse, "Electroweak baryogenesis in the next-to-minimal supersymmetric model", *Phys. Lett. B*, vol. 372, pp. 88–94, 1996. DOI: 10.1016/0370-2693(96)00076-7. arXiv: hep-ph/9603388.

[24] W. Huang, Z. Kang, J. Shu, P. Wu and J. M. Yang, "New insights in the electroweak phase transition in the NMSSM", *Phys. Rev. D*, vol. 91, no. 2, p. 025 006, 2015. DOI: 10.1103/PhysRevD.91.025006. arXiv: 1405.1152 [hep-ph].

[25] S. Profumo, M. J. Ramsey-Musolf and G. Shaughnessy, "Singlet Higgs phenomenology and the electroweak phase transition", *JHEP*, vol. 08, p. 010, 2007. DOI: 10.1088/1126-6708/2007/08/010. arXiv: 0705.2425 [hep-ph].

[26] J. R. Espinosa, T. Konstandin and F. Riva, "Strong Electroweak Phase Transitions in the Standard Model with a Singlet", *Nucl. Phys.*, vol. B854, pp. 592–630, 2012. DOI: 10.1016/j.nuclphysb.2011.09.010. arXiv: 1107.5441 [hep-ph].

[27] S. Profumo, M. J. Ramsey-Musolf, C. L. Wainwright and P. Winslow, "Singlet-catalyzed electroweak phase transitions and precision Higgs boson studies", *Phys. Rev.*, vol. D91, no. 3, p. 035 018, 2015. DOI: 10.1103/PhysRevD.91.035018. arXiv: 1407.5342 [hep-ph].

[28] A. Beniwal, M. Lewicki, M. White and A. G. Williams, "Gravitational waves and electroweak baryogenesis in a global study of the extended scalar singlet model", *JHEP*, vol. 02, p. 183, 2019. DOI: 10.1007/JHEP02(2019)183. arXiv: 1810.02380 [hep-ph].

[29] M. Kakizaki, S. Kanemura and T. Matsui, "Gravitational waves as a probe of extended scalar sectors with the first order electroweak phase transition", *Phys. Rev.*, vol. D92, no. 11, p. 115 007, 2015. DOI: 10.1103/PhysRevD.92.115007. arXiv: 1509.08394 [hep-ph].

[30] G. C. Dorsch, S. J. Huber, T. Konstandin and J. M. No, "A Second Higgs Doublet in the Early Universe: Baryogenesis and Gravitational Waves", *JCAP*, vol. 1705, no. 05, p. 052, 2017. DOI: 10.1088/1475-7516/2017/05/052. arXiv: 1611.05874 [hep-ph].

[31] P. Basler, M. Krause, M. Muhlleitner, J. Wittbrodt and A. Wlotzka, "Strong First Order Electroweak Phase Transition in the CP-Conserving 2HDM Revisited", *JHEP*, vol. 02, p. 121, 2017. DOI: 10.1007/JHEP02(2017)121. arXiv: 1612.04086 [hep-ph].

[32] H. H. Patel and M. J. Ramsey-Musolf, "Stepping Into Electroweak Symmetry Breaking: Phase Transitions and Higgs Phenomenology", *Phys. Rev. D*, vol. 88, p. 035 013, 2013. DOI: 10.1103/PhysRevD.88.035013. arXiv: 1212.5652 [hep-ph].

[33] J. M. Cline and K. Kainulainen, "Electroweak baryogenesis and dark matter from a singlet Higgs", *JCAP*, vol. 1301, p. 012, 2013. DOI: 10.1088/1475-7516/2013/01/012. arXiv: 1210.4196 [hep-ph].

[34] M. Fairbairn and R. Hogan, "Singlet Fermionic Dark Matter and the Electroweak Phase Transition", *JHEP*, vol. 09, p. 022, 2013. DOI: 10.1007/JHEP09(2013)022. arXiv: 1305.3452 [hep-ph].

[35] N. Craig, H. K. Lou, M. McCullough and A. Thalapillil, "The Higgs Portal Above Threshold", *JHEP*, vol. 02, p. 127, 2016. DOI: 10.1007/JHEP02(2016)127. arXiv: 1412.0258 [hep-ph].

[36] W. Chao, H.-K. Guo and J. Shu, "Gravitational Wave Signals of Electroweak Phase Transition Triggered by Dark Matter", *JCAP*, vol. 09, p. 009, 2017. DOI: 10.1088/1475-7516/2017/09/009. arXiv: 1702.02698 [hep-ph].

[37] P. Schwaller, "Gravitational Waves from a Dark Phase Transition", *Phys. Rev. Lett.*, vol. 115, no. 18, p. 181 101, 2015. DOI: 10.1103/PhysRevLett.115.181101. arXiv: 1504.07263 [hep-ph].

[38] M. Aoki, H. Goto and J. Kubo, "Gravitational Waves from Hidden QCD Phase Transition", *Phys. Rev.*, vol. D96, no. 7, p. 075 045, 2017. DOI: 10.1103/PhysRevD.96.075045. arXiv: 1709.07572 [hep-ph].

[39] A. Addazi and A. Marciano, "Gravitational waves from dark first order phase transitions and dark photons", *Chin. Phys.*, vol. C42, no. 2, p. 023 107, 2018. DOI: 10.1088/1674-1137/42/2/023107. arXiv: 1703.03248 [hep-ph].

[40] D. Croon, V. Sanz and G. White, "Model Discrimination in Gravitational Wave spectra from Dark Phase Transitions", *JHEP*, vol. 08, p. 203, 2018. DOI: 10.1007/JHEP08(2018)203. arXiv: 1806.02332 [hep-ph].

[41] M. Breitbach, J. Kopp, E. Madge, T. Opferkuch and P. Schwaller, "Dark, Cold, and Noisy: Constraining Secluded Hidden Sectors with Gravitational Waves", 2018. arXiv: 1811.11175 [hep-ph].

[42] N. Okada and O. Seto, "Probing the seesaw scale with gravitational waves", *Phys. Rev.*, vol. D98, no. 6, p. 063 532, 2018. DOI: 10.1103/PhysRevD.98.063532. arXiv: 1807.00336 [hep-ph].

[43] T. Hasegawa, N. Okada and O. Seto, "Gravitational waves from the minimal gauged $U(1)_{B-L}$ model", *Phys. Rev.*, vol. D99, no. 9, p. 095 039, 2019. DOI: 10.1103/PhysRevD.99.095039. arXiv: 1904.03020 [hep-ph].

[44] D. J. Schwarz and M. Stuke, "Lepton asymmetry and the cosmic QCD transition", *JCAP*, vol. 11, p. 025, 2009, [Erratum: JCAP 10, E01 (2010)]. DOI: 10.1088/1475-7516/2009/11/025. arXiv: 0906.3434 [hep-ph].

[45] D. Croon, J. N. Howard, S. Ipek and T. M. Tait, "QCD baryogenesis", *Phys. Rev. D*, vol. 101, no. 5, p. 055 042, 2020. DOI: 10.1103/PhysRevD.101.055042. arXiv: 1911.01432 [hep-ph].

[46] L. Randall and G. Servant, "Gravitational waves from warped spacetime", *JHEP*, vol. 05, p. 054, 2007. DOI: 10.1088/1126-6708/2007/05/054. arXiv: hep-ph/0607158 [hep-ph].

[47] T. Konstandin, G. Nardini and M. Quiros, "Gravitational backreaction effects on the holographic phase transition", *Phys. Rev. D*, vol. 82, p. 083 513, 8 2010. DOI: 10.1103/PhysRevD.82.083513. [Online]. Available: https://link.aps.org/doi/10.1103/PhysRevD.82.083513.

[48] T. Konstandin and G. Servant, "Cosmological Consequences of Nearly Conformal Dynamics at the TeV scale", *JCAP*, vol. 1112, p. 009, 2011. DOI: 10.1088/1475-7516/2011/12/009. arXiv: 1104.4791 [hep-ph].

[49] B. von Harling and G. Servant, "QCD-induced Electroweak Phase Transition", *JHEP*, vol. 01, p. 159, 2018. DOI: 10.1007/JHEP01(2018)159. arXiv: 1711.11554 [hep-ph].

[50] B. M. Dillon, B. K. El-Menoufi, S. J. Huber and J. P. Manuel, "Rapid holographic phase transition with brane-localized curvature", *Phys. Rev.*, vol. D98, no. 8, p. 086 005, 2018. DOI: 10.1103/PhysRevD.98.086005. arXiv: 1708.02953 [hep-th].

[51] E. Megías, G. Nardini and M. Quirós, "Cosmological Phase Transitions in Warped Space: Gravitational Waves and Collider Signatures", *JHEP*, vol. 09, p. 095, 2018. DOI: 10.1007/JHEP09(2018)095. arXiv: 1806.04877 [hep-ph].

[52] S. Bruggisser, B. Von Harling, O. Matsedonskyi and G. Servant, "Electroweak Phase Transition and Baryogenesis in Composite Higgs Models", *JHEP*, vol. 12, p. 099, 2018. DOI: 10.1007/JHEP12(2018)099. arXiv: 1804.07314 [hep-ph].

[53] E. Witten, "Cosmic Separation of Phases", *Phys.Rev.*, vol. D30, pp. 272–285, 1984. DOI: 10.1103/PhysRevD.30.272.

[54] C. J. Hogan, "Gravitational radiation from cosmological phase transitions", *MNRAS*, vol. 218, pp. 629–636, 1986.

[55] A. Kosowsky, M. S. Turner and R. Watkins, "Gravitational radiation from colliding vacuum bubbles", *Phys.Rev.*, vol. D45, pp. 4514–4535, 1992. DOI: 10.1103/PhysRevD.45.4514.

[56] ——, "Gravitational waves from first order cosmological phase transitions", *Phys.Rev.Lett.*, vol. 69, pp. 2026–2029, 1992. DOI: 10.1103/PhysRevLett.69.2026.

[57] A. Kosowsky and M. S. Turner, "Gravitational radiation from colliding vacuum bubbles: envelope approximation to many bubble collisions", *Phys.Rev.*, vol. D47, pp. 4372–4391, 1993. DOI: 10.1103/PhysRevD.47.4372. arXiv: astro-ph/9211004 [astro-ph].

[58] M. Kamionkowski, A. Kosowsky and M. S. Turner, "Gravitational radiation from first order phase transitions", *Phys.Rev.*, vol. D49, pp. 2837–2851, 1994. DOI: 10.1103/PhysRevD.49.2837. arXiv: astro-ph/9310044 [astro-ph].

[59] S. J. Huber and T. Konstandin, "Gravitational Wave Production by Collisions: More Bubbles", *JCAP*, vol. 0809, p. 022, 2008. DOI: 10.1088/1475-7516/2008/09/022. arXiv: 0806.1828 [hep-ph].

[60] M. Hindmarsh, S. J. Huber, K. Rummukainen and D. J. Weir, "Gravitational waves from the sound of a first order phase transition", *Phys.Rev.Lett.*, vol. 112, p. 041 301, 2014. DOI: 10.1103/PhysRevLett.112.041301. arXiv: 1304.2433 [hep-ph].

[61] J. T. Giblin and J. B. Mertens, "Gravitional radiation from first-order phase transitions in the presence of a fluid", *Phys.Rev.*, vol. D90, no. 2, p. 023 532, 2014. DOI: 10.1103/PhysRevD.90.023532. arXiv: 1405.4005 [astro-ph.CO].

[62] M. Hindmarsh, S. J. Huber, K. Rummukainen and D. J. Weir, "Numerical simulations of acoustically generated gravitational waves at a first order phase transition", *Phys. Rev.*, vol. D92, no. 12, p. 123 009, 2015. DOI: 10.1103/PhysRevD.92.123009. arXiv: 1504.03291 [astro-ph.CO].

[63] ——, "Shape of the acoustic gravitational wave power spectrum from a first order phase transition", *Phys. Rev.*, vol. D96, no. 10, p. 103 520, 2017. DOI: 10.1103/PhysRevD.96.103520. arXiv: 1704.05871 [astro-ph.CO].

[64] M. Hindmarsh, "Sound shell model for acoustic gravitational wave production at a first-order phase transition in the early Universe", *Phys. Rev. Lett.*, vol. 120, no. 7, p. 071 301, 2018. DOI: 10.1103/PhysRevLett.120.071301. arXiv: 1608.04735 [astro-ph.CO].

[65] M. Hindmarsh and M. Hijazi, "Gravitational waves from first order cosmological phase transitions in the Sound Shell Model", *JCAP*, vol. 12, no. 12, p. 062, 2019. DOI: 10.1088/1475-7516/2019/12/062. arXiv: 1909.10040 [astro-ph.CO].

[66] D. J. Weir, "Revisiting the envelope approximation: gravitational waves from bubble collisions", *Phys. Rev.*, vol. D93, no. 12, p. 124 037, 2016. DOI: 10.1103/PhysRevD.93.124037. arXiv: 1604.08429 [astro-ph.CO].

[67] H. Kurki-Suonio, "Deflagration bubbles in the quark - hadron phase transition", *Nucl.Phys.*, vol. B255, p. 231, 1985. DOI: 10.1016/0550-3213(85)90135-X.

[68] C. Caprini, R. Durrer and G. Servant, "Gravitational wave generation from bubble collisions in first-order phase transitions: An analytic approach", *Phys.Rev.*, vol. D77, p. 124 015, 2008. DOI: 10.1103/PhysRevD.77.124015. arXiv: 0711.2593 [astro-ph].

[69] G. Gogoberidze, T. Kahniashvili and A. Kosowsky, "The Spectrum of Gravitational Radiation from Primordial Turbulence", *Phys.Rev.*, vol. D76, p. 083 002, 2007. DOI: 10.1103/PhysRevD.76.083002. arXiv: 0705.1733 [astro-ph].

[70] C. Caprini, R. Durrer and G. Servant, "The stochastic gravitational wave background from turbulence and magnetic fields generated by a first-order phase transition", *JCAP*, vol. 0912, p. 024, 2009. DOI: 10.1088/1475-7516/2009/12/024. arXiv: 0909.0622 [astro-ph.CO].

[71] C. Caprini, R. Durrer, T. Konstandin and G. Servant, "General Properties of the Gravitational Wave Spectrum from Phase Transitions", *Phys.Rev.*, vol. D79,

p. 083 519, 2009. DOI: 10.1103/PhysRevD.79.083519. arXiv: 0901.1661 [astro-ph.CO].

[72] P. Niksa, M. Schlederer and G. Sigl, "Gravitational Waves produced by Compressible MHD Turbulence from Cosmological Phase Transitions", *Class. Quant. Grav.*, vol. 35, no. 14, p. 144 001, 2018. DOI: 10.1088/1361-6382/aac89c. arXiv: 1803.02271 [astro-ph.CO].

[73] A. R. Pol, S. Mandal, A. Brandenburg, T. Kahniashvili and A. Kosowsky, "Numerical Simulations of Gravitational Waves from Early-Universe Turbulence", 2019. arXiv: 1903.08585 [astro-ph.CO].

[74] B. P. Abbott *et al.*, "Observation of Gravitational Waves from a Binary Black Hole Merger", *Phys. Rev. Lett.*, vol. 116, no. 6, p. 061 102, 2016. DOI: 10.1103/PhysRevLett.116.061102. arXiv: 1602.03837 [gr-qc].

[75] P. A. Seoane *et al.*, "The Gravitational Universe", 2013. arXiv: 1305.5720 [astro-ph.CO].

[76] C. Caprini and D. G. Figueroa, "Cosmological Backgrounds of Gravitational Waves", 2018. arXiv: 1801.04268 [astro-ph.CO].

[77] C. Caprini *et al.*, "Science with the space-based interferometer eLISA. II: Gravitational waves from cosmological phase transitions", *JCAP*, vol. 1604, no. 04, p. 001, 2016. DOI: 10.1088/1475-7516/2016/04/001. arXiv: 1512.06239 [astro-ph.CO].

[78] B. P. Abbott, R. Abbott, T. D. Abbott *et al.*, "Gw170817: Observation of gravitational waves from a binary neutron star inspiral", *Phys. Rev. Lett.*, vol. 119, p. 161 101, 16 2017. DOI: 10.1103/PhysRevLett.119.161101. [Online]. Available: https://link.aps.org/doi/10.1103/PhysRevLett.119.161101.

[79] B. P. Abbott, R. Abbott, T. D. Abbott *et al.*, "Multi-messenger observations of a binary neutron star merger", *The Astrophysical Journal*, vol. 848, no. 2, p. L12, 2017, ISSN: 2041-8213. DOI: 10.3847/2041-8213/aa91c9. [Online]. Available: http://dx.doi.org/10.3847/2041-8213/aa91c9.

[80] B. P. Abbott *et al.*, "Gravitational Waves and Gamma-rays from a Binary Neutron Star Merger: GW170817 and GRB 170817A", *Astrophys. J.*, vol. 848, no. 2, p. L13, 2017. DOI: 10.3847/2041-8213/aa920c. arXiv: 1710.05834 [astro-ph.HE].

[81] M. Maggiore, *Gravitational Waves: Volume 1: Theory and Experiments*, ser. Gravitational Waves. OUP Oxford, 2008, ISBN: 9780198570745. [Online]. Available: https://books.google.co.uk/books?id=AqVpQgAACAAJ.

[82] S. Weinberg, *Gravitation and Cosmology: Principles and Applications of the General Theory of Relativity*. New York: John Wiley and Sons, 1972, ISBN: 978-0-471-92567-5, 978-0-471-92567-5.

[83] M. P. Hobson, G. P. Efstathiou and A. N. Lasenby, *General Relativity: An Introduction for Physicists*. Cambridge University Press, 2006. DOI: 10.1017/CBO9780511790904.

[84] S. M. Carroll, *Spacetime and Geometry: An Introduction to General Relativity*. Cambridge University Press, 2019. DOI: 10.1017/9781108770385.

[85] R. A. Isaacson, "Gravitational Radiation in the Limit of High Frequency. I. The Linear Approximation and Geometrical Optics", *Phys. Rev.*, vol. 166, pp. 1263–1271, 1968. DOI: 10.1103/PhysRev.166.1263.

[86] ——, "Gravitational Radiation in the Limit of High Frequency. II. Nonlinear Terms and the Effective Stress Tensor", *Phys. Rev.*, vol. 166, pp. 1272–1279, 1968. DOI: 10.1103/PhysRev.166.1272.

[87] D. Bodeker and G. D. Moore, "Electroweak Bubble Wall Speed Limit", 2017. arXiv: 1703.08215 [hep-ph].

[88] J. R. Espinosa, T. Konstandin, J. M. No and G. Servant, "Energy Budget of Cosmological First-order Phase Transitions", *JCAP*, vol. 1006, p. 028, 2010. DOI: 10.1088/1475-7516/2010/06/028. arXiv: 1004.4187 [hep-ph].

[89] D. Bodeker and G. D. Moore, "Can electroweak bubble walls run away?", *JCAP*, vol. 0905, p. 009, 2009. DOI: 10.1088/1475-7516/2009/05/009. arXiv: 0903.4099 [hep-ph].

[90] C. Caprini *et al.*, "Detecting gravitational waves from cosmological phase transitions with LISA: an update", *JCAP*, vol. 2003, no. 03, p. 024, 2020. DOI: 10.1088/1475-7516/2020/03/024. arXiv: 1910.13125 [astro-ph.CO].

[91] J. Ellis, M. Lewicki, J. M. No and V. Vaskonen, "Gravitational wave energy budget in strongly supercooled phase transitions", 2019. arXiv: 1903.09642 [hep-ph].

[92] S. R. Coleman and E. J. Weinberg, "Radiative Corrections as the Origin of Spontaneous Symmetry Breaking", *Phys. Rev. D*, vol. 7, pp. 1888–1910, 1973. DOI: 10.1103/PhysRevD.7.1888.

[93] L. Dolan and R. Jackiw, "Symmetry Behavior at Finite Temperature", *Phys. Rev. D*, vol. 9, pp. 3320–3341, 1974. DOI: 10.1103/PhysRevD.9.3320.

[94] M. Quiros, "Finite temperature field theory and phase transitions", in *ICTP Summer School in High-Energy Physics and Cosmology*, Jan. 1999, pp. 187–259. arXiv: hep-ph/9901312.

[95] A. D. Linde, "Fate of the False Vacuum at Finite Temperature: Theory and Applications", *Phys. Lett. B*, vol. 100, pp. 37–40, 1981. DOI: 10.1016/0370-2693(81)90281-1.

[96] K. Enqvist, J. Ignatius, K. Kajantie and K. Rummukainen, "Nucleation and bubble growth in a first order cosmological electroweak phase transition", *Phys.Rev.*, vol. D45, pp. 3415–3428, 1992. DOI: 10.1103/PhysRevD.45.3415.

[97] A. H. Guth and E. J. Weinberg, "Could the Universe Have Recovered from a Slow First Order Phase Transition?", *Nucl. Phys. B*, vol. 212, pp. 321–364, 1983. DOI: 10.1016/0550-3213(83)90307-3.

[98] J. Ellis, M. Lewicki and J. M. No, "On the Maximal Strength of a First-Order Electroweak Phase Transition and its Gravitational Wave Signal", *JCAP*, vol. 04, p. 003, 2019. DOI: 10.1088/1475-7516/2019/04/003. arXiv: 1809.08242 [hep-ph].

[99] S. J. Huber and T. Konstandin, "Production of gravitational waves in the nMSSM", *JCAP*, vol. 0805, p. 017, 2008. DOI: 10.1088/1475-7516/2008/05/017. arXiv: 0709.2091 [hep-ph].

[100] M. E. Carrington and J. I. Kapusta, "Dynamics of the electroweak phase transition", *Phys. Rev. D*, vol. 47, pp. 5304–5315, 1993. DOI: 10.1103/PhysRevD.47.5304.

[101] J. Ignatius, K. Kajantie, H. Kurki-Suonio and M. Laine, "The growth of bubbles in cosmological phase transitions", *Phys.Rev.*, vol. D49, pp. 3854–3868, 1994. DOI: 10.1103/PhysRevD.49.3854. arXiv: astro-ph/9309059 [astro-ph].

[102] T. Konstandin, G. Nardini and I. Rues, "From Boltzmann equations to steady wall velocities", *JCAP*, vol. 1409, no. 09, p. 028, 2014. DOI: 10.1088/1475-7516/2014/09/028. arXiv: 1407.3132 [hep-ph].

[103] A. Megevand and A. D. Sanchez, "Velocity of electroweak bubble walls", *Nucl.Phys.*, vol. B825, pp. 151–176, 2010. DOI: 10.1016/j.nuclphysb.2009.09.019. arXiv: 0908.3663 [hep-ph].

[104] A. Megevand and F. A. Membiela, "Stability of cosmological deflagration fronts", *Phys. Rev.*, vol. D89, no. 10, p. 103 507, 2014. DOI: 10.1103/PhysRevD.89.103507. arXiv: 1311.2453 [astro-ph.CO].

[105] G. C. Dorsch, S. J. Huber and T. Konstandin, "Bubble wall velocities in the Standard Model and beyond", *JCAP*, vol. 12, p. 034, 2018. DOI: 10.1088/1475-7516/2018/12/034. arXiv: 1809.04907 [hep-ph].

[106] S. J. Huber and M. Sopena, "An efficient approach to electroweak bubble velocities", 2013. arXiv: 1302.1044 [hep-ph].

[107] G. D. Moore and T. Prokopec, "How fast can the wall move? A Study of the electroweak phase transition dynamics", *Phys.Rev.*, vol. D52, pp. 7182–7204, 1995. DOI: 10.1103/PhysRevD.52.7182. arXiv: hep-ph/9506475 [hep-ph].

[108] P. John and M. G. Schmidt, "Do stops slow down electroweak bubble walls?", *Nucl. Phys.*, vol. B598, pp. 291–305, 2001, [Erratum: Nucl. Phys.B648,449(2003)]. DOI: 10.1016/S0550-3213(00)00768-9,10.1016/S0550-3213(02)01014-3. arXiv: hep-ph/0002050 [hep-ph].

[109] J. Kozaczuk, "Bubble Expansion and the Viability of Singlet-Driven Electroweak Baryogenesis", *JHEP*, vol. 10, p. 135, 2015. DOI: 10.1007/JHEP10(2015)135. arXiv: 1506.04741 [hep-ph].

[110] L. Rezzolla and O. Zanotti, *Relativistic Hydrodynamics*, ser. EBSCO ebook academic collection. OUP Oxford, 2013, ISBN: 9780198528906. [Online]. Available: https://books.google.co.uk/books?id=KU2oAAAAQBAJ.

[111] H. Kurki-Suonio and M. Laine, "Supersonic deflagrations in cosmological phase transitions", *Phys.Rev.*, vol. D51, pp. 5431–5437, 1995. DOI: 10.1103/PhysRevD.51.5431. arXiv: hep-ph/9501216 [hep-ph].

[112] D. Cutting, *private communication*, 2017.

[113] H. Kurki-Suonio and M. Laine, "On bubble growth and droplet decay in cosmological phase transitions", *Phys.Rev.*, vol. D54, pp. 7163–7171, 1996. DOI: 10.1103/PhysRevD.54.7163. arXiv: hep-ph/9512202 [hep-ph].

[114] S. Hawking, I. Moss and J. Stewart, "Bubble Collisions in the Very Early Universe", *Phys.Rev.*, vol. D26, p. 2681, 1982. DOI: 10.1103/PhysRevD.26.2681.

[115] J. Braden, J. R. Bond and L. Mersini-Houghton, "Cosmic bubble and domain wall instabilities I: parametric amplification of linear fluctuations", *JCAP*, vol. 1503, no. 03, p. 007, 2015. DOI: 10.1088/1475-7516/2015/03/007. arXiv: 1412.5591 [hep-th].

[116] R. Jinno, T. Konstandin and M. Takimoto, "Relativistic bubble collisions—a closer look", *JCAP*, vol. 09, p. 035, 2019. DOI: 10.1088/1475-7516/2019/09/035. arXiv: 1906.02588 [hep-ph].

[117] M. Lewicki and V. Vaskonen, "On bubble collisions in strongly supercooled phase transitions", Dec. 2019. arXiv: 1912.00997 [astro-ph.CO].

[118] H. L. Child and J. Giblin John T., "Gravitational Radiation from First-Order Phase Transitions", *JCAP*, vol. 1210, p. 001, 2012. DOI: 10.1088/1475-7516/2012/10/001. arXiv: 1207.6408 [astro-ph.CO].

[119] P. A. R. Ade *et al.*, "Planck 2015 results. XIII. Cosmological parameters", *Astron. Astrophys.*, vol. 594, A13, 2016. DOI: 10.1051/0004-6361/201525830. arXiv: 1502.01589 [astro-ph.CO].

[120] J. C. Mather, D. J. Fixsen, R. A. Shafer, C. Mosier and D. T. Wilkinson, "Calibrator design for the COBE far infrared absolute spectrophotometer (FIRAS)", *Astrophys. J.*, vol. 512, pp. 511–520, 1999. DOI: 10.1086/306805. arXiv: astro-ph/9810373 [astro-ph].

[121] R. Jinno and M. Takimoto, "Gravitational waves from bubble collisions: analytic derivation", *Phys. Rev.*, vol. D95, no. 2, p. 024 009, 2017. DOI: 10.1103/PhysRevD.95.024009. arXiv: 1605.01403 [astro-ph.CO].

[122] T. Konstandin, "Gravitational radiation from a bulk flow model", *JCAP*, vol. 1803, no. 03, p. 047, 2018. DOI: 10.1088/1475-7516/2018/03/047. arXiv: 1712.06869 [astro-ph.CO].

[123] R. Jinno and M. Takimoto, "Gravitational waves from bubble dynamics: Beyond the Envelope", *JCAP*, vol. 01, p. 060, 2019. DOI: 10.1088/1475-7516/2019/01/060. arXiv: 1707.03111 [hep-ph].

[124] U.-L. Pen and N. Turok, "Shocks in the Early Universe", *Phys. Rev. Lett.*, vol. 117, no. 13, p. 131 301, 2016. DOI: 10.1103/PhysRevLett.117.131301. arXiv: 1510.02985 [astro-ph.CO].

[125] J. Ellis, M. Lewicki and J. M. No, "Gravitational waves from first-order cosmological phase transitions: lifetime of the sound wave source", Mar. 2020. arXiv: 2003.07360 [hep-ph].

[126] T. Vachaspati, "Magnetic fields from cosmological phase transitions", *Phys. Lett. B*, vol. 265, pp. 258–261, 1991. DOI: 10.1016/0370-2693(91)90051-Q.

[127] T. Kibble and A. Vilenkin, "Phase equilibration in bubble collisions", *Phys. Rev. D*, vol. 52, pp. 679–688, 1995. DOI: 10.1103/PhysRevD.52.679. arXiv: hep-ph/9501266.

[128] E. J. Copeland, P. Saffin and O. Tornkvist, "Phase equilibration and magnetic field generation in U(1) bubble collisions", *Phys. Rev. D*, vol. 61, p. 105 005, 2000. DOI: 10.1103/PhysRevD.61.105005. arXiv: hep-ph/9907437.

[129] T. Stevens and M. B. Johnson, "Theory of Magnetic Seed-Field Theory of Magnetic Seed-Field Generation during the Cosmological First-Order Electroweak Phase Transition", Jan. 2010. arXiv: 1001.3694 [astro-ph.CO].

[130] Y. Zhang, T. Vachaspati and F. Ferrer, "Magnetic field production at a first-order electroweak phase transition", *Phys. Rev. D*, vol. 100, no. 8, p. 083 006, 2019. DOI: 10.1103/PhysRevD.100.083006. arXiv: 1902.02751 [hep-ph].

[131] A. Kolmogorov, "The Local Structure of Turbulence in Incompressible Viscous Fluid for Very Large Reynolds' Numbers", *Akademiia Nauk SSSR Doklady*, vol. 30, pp. 301–305, Jan. 1941.

[132] A. Kosowsky, A. Mack and T. Kahniashvili, "Gravitational radiation from cosmological turbulence", *Phys.Rev.*, vol. D66, p. 024 030, 2002. DOI: 10.1103/PhysRevD.66.024030. arXiv: astro-ph/0111483 [astro-ph].

[133] C. Caprini and R. Durrer, "Gravitational waves from stochastic relativistic sources: Primordial turbulence and magnetic fields", *Phys.Rev.*, vol. D74, p. 063 521, 2006. DOI: 10.1103/PhysRevD.74.063521. arXiv: astro-ph/0603476 [astro-ph].

[134] R. H. Kraichnan, "Approximations for steady-state isotropic turbulence", *The Physics of Fluids*, vol. 7, no. 8, pp. 1163–1168, 1964. DOI: 10.1063/1.1711357. eprint: https://aip.scitation.org/doi/pdf/10.1063/1.1711357. [Online]. Available: https://aip.scitation.org/doi/abs/10.1063/1.1711357.

[135] T. Kahniashvili, L. Campanelli, G. Gogoberidze, Y. Maravin and B. Ratra, "Gravitational radiation from primordial helical inverse cascade magnetohydrodynamic turbulence", *Phys. Rev. D*, vol. 78, p. 123 006, 12 2008. DOI: 10.1103/PhysRevD.78.123006. [Online]. Available: https://link.aps.org/doi/10.1103/PhysRevD.78.123006.

[136] B. P. Abbott *et al.*, "GW151226: Observation of Gravitational Waves from a 22-Solar-Mass Binary Black Hole Coalescence", *Phys. Rev. Lett.*, vol. 116, no. 24,

p. 241 103, 2016. DOI: 10.1103/PhysRevLett.116.241103. arXiv: 1606.04855 [gr-qc].

[137] H. Audley *et al.*, "Laser Interferometer Space Antenna", 2017. arXiv: 1702.00786 [astro-ph.IM].

[138] D. J. Weir, "Gravitational waves from a first order electroweak phase transition: a brief review", in *Phil. Trans. R. Soc. A 2018 376 20170126*, vol. A2018, 2017, p. 376. DOI: 10.1098/rsta.2017.0126. arXiv: 1705.01783 [hep-ph]. [Online]. Available: http://inspirehep.net/record/1598112/files/arXiv:1705.01783.pdf.

[139] K. Enqvist, J. Ignatius, K. Kajantie and K. Rummukainen, "Nucleation and bubble growth in a first-order cosmological electroweak phase transition", *Phys. Rev. D*, vol. 45, pp. 3415–3428, 10 1992. DOI: 10.1103/PhysRevD.45.3415. [Online]. Available: https://link.aps.org/doi/10.1103/PhysRevD.45.3415.

[140] R. Jinno, S. Lee, H. Seong and M. Takimoto, "Gravitational waves from first-order phase transitions: Towards model separation by bubble nucleation rate", *JCAP*, vol. 1711, no. 11, p. 050, 2017. DOI: 10.1088/1475-7516/2017/11/050. arXiv: 1708.01253 [hep-ph].

[141] I. Garcia Garcia, S. Krippendorf and J. March-Russell, "The String Soundscape at Gravitational Wave Detectors", 2016. arXiv: 1607.06813 [hep-ph].

[142] S. W. Hawking, I. G. Moss and J. M. Stewart, "Bubble collisions in the very early universe", *Phys. Rev. D*, vol. 26, pp. 2681–2693, 10 1982. DOI: 10.1103/PhysRevD.26.2681. [Online]. Available: https://link.aps.org/doi/10.1103/PhysRevD.26.2681.

[143] J. Zhang and Y.-S. Piao, "Preheating in Bubble Collision", *Phys. Rev.*, vol. D82, p. 043 507, 2010. DOI: 10.1103/PhysRevD.82.043507. arXiv: 1004.2333 [hep-th].

[144] G. Aarts, G. F. Bonini and C. Wetterich, "On Thermalization in classical scalar field theory", *Nucl. Phys.*, vol. B587, pp. 403–418, 2000. DOI: 10.1016/S0550-3213(00)00447-8. arXiv: hep-ph/0003262 [hep-ph].

[145] R. Micha and I. I. Tkachev, "Relativistic turbulence: A Long way from preheating to equilibrium", *Phys. Rev. Lett.*, vol. 90, p. 121 301, 2003. DOI: 10.1103/PhysRevLett.90.121301. arXiv: hep-ph/0210202 [hep-ph].

[146] A. Arrizabalaga, J. Smit and A. Tranberg, "Equilibration in phi**4 theory in 3+1 dimensions", *Phys. Rev.*, vol. D72, p. 025 014, 2005. DOI: 10.1103/PhysRevD.72.025014. arXiv: hep-ph/0503287 [hep-ph].

[147] J. Garcia-Bellido, D. G. Figueroa and A. Sastre, "A Gravitational Wave Background from Reheating after Hybrid Inflation", *Phys.Rev.*, vol. D77, p. 043 517, 2008. DOI: 10.1103/PhysRevD.77.043517. arXiv: 0707.0839 [hep-ph].

[148] J. F. Dufaux, A. Bergman, G. N. Felder, L. Kofman and J.-P. Uzan, "Theory and Numerics of Gravitational Waves from Preheating after Inflation", *Phys. Rev.*, vol. D76, p. 123 517, 2007. DOI: 10.1103/PhysRevD.76.123517. arXiv: 0707.0875 [astro-ph].

[149] D. Daverio, M. Hindmarsh and N. Bevis, "Latfield2: A c++ library for classical lattice field theory", 2015. arXiv: 1508.05610 [physics.comp-ph].

[150] J. A. Combs and S. Yip, "Single-kink dynamics in a one-dimensional atomic chain: A nonlinear atomistic theory and numerical simulation", *Phys. Rev. B*, vol. 28, pp. 6873–6885, 12 1983. DOI: 10.1103/PhysRevB.28.6873. [Online]. Available: https://link.aps.org/doi/10.1103/PhysRevB.28.6873.

[151] M. Peyrard and M. D. Kruskal, "Kink dynamics in the highly discrete sine-Gordon system", *Physica*, vol. 14D, pp. 88–102, 1984.

[152] R. Durrer and C. Caprini, "Primordial magnetic fields and causality", *JCAP*, vol. 0311, p. 010, 2003. DOI: 10.1088/1475-7516/2003/11/010. arXiv: astro-ph/0305059 [astro-ph].

[153] E. Hall, T. Konstandin, R. McGehee and H. Murayama, "Asymmetric Matters from a Dark First-Order Phase Transition", Nov. 2019. arXiv: 1911.12342 [hep-ph].

[154] E. Hall, T. Konstandin, R. McGehee, H. Murayama and G. Servant, "Baryogenesis From a Dark First-Order Phase Transition", *JHEP*, vol. 04, p. 042, 2020. DOI: 10.1007/JHEP04(2020)042. arXiv: 1910.08068 [hep-ph].

[155] R. Jinno, H. Seong, M. Takimoto and C. M. Um, "Gravitational waves from first-order phase transitions: Ultra-supercooled transitions and the fate of relativistic shocks", *JCAP*, vol. 10, no. 10, p. 033, 2019. DOI: 10.1088/1475-7516/2019/10/033. arXiv: 1905.00899 [astro-ph.CO].

[156] R. Watkins and L. M. Widrow, "Aspects of reheating in first order inflation", *Nucl. Phys. B*, vol. 374, pp. 446–468, 1992. DOI: 10.1016/0550-3213(92)90362-F.

[157] E. Lim, private communication, 2020.

[158] T. Gorda, A. Helset, L. Niemi, T. V. I. Tenkanen and D. J. Weir, "Three-dimensional effective theories for the two Higgs doublet model at high temperature", *JHEP*, vol. 02, p. 081, 2019. DOI: 10.1007/JHEP02(2019)081. arXiv: 1802.05056 [hep-ph].

[159] O. Gould, J. Kozaczuk, L. Niemi *et al.*, "Nonperturbative analysis of the gravitational waves from a first-order electroweak phase transition", *Phys. Rev. D*, vol. 100, no. 11, p. 115 024, 2019. DOI: 10.1103/PhysRevD.100.115024. arXiv: 1903.11604 [hep-ph].

[160] K. Kainulainen, V. Keus, L. Niemi *et al.*, "On the validity of perturbative studies of the electroweak phase transition in the Two Higgs Doublet model", 2019. arXiv: 1904.01329 [hep-ph].

[161] T. Konstandin and J. M. No, "Hydrodynamic obstruction to bubble expansion", *JCAP*, vol. 1102, p. 008, 2011. DOI: 10.1088/1475-7516/2011/02/008. arXiv: 1011.3735 [hep-ph].

[162] A. Mégevand and S. Ramírez, "Bubble nucleation and growth in slow cosmological phase transitions", *Nucl. Phys.*, vol. B928, pp. 38–71, 2018. DOI: 10.1016/j.nuclphysb.2018.01.012. arXiv: 1710.06279 [astro-ph.CO].

[163] B.-H. Liu, L. D. McLerran and N. Turok, "Bubble nucleation and growth at a baryon number producing electroweak phase transition", *Phys. Rev.*, vol. D46, pp. 2668–2688, 1992. DOI: 10.1103/PhysRevD.46.2668.

[164] D. Cutting, See movies of strong phase transitions available at https://vimeo.com/album/5968055, 2019.